CHALMERS UNIVERSITY OF TECHNOLOGY
Gothenburg, Sweden
www.chalmers.se

PHD THESIS

Ever-growing energy consumption and CO_2 emissions due to the increase in road transport are major challenges that attract international attention, especially policy makers, logistic service providers and customers considering environmental, ecological and economic issues. Other negative side-effects caused by the growth of the road transport are the extensive costs because of traffic congestion. Thus, there is a strong motivation to investigate possible ways of improving transport efficiency aiming at achieving a sustainable transport, e.g. by finding the best compromise between resource consumption and logistics performance. The transport efficiency can be improved by optimal planning of the transport mission, which can be interpreted as optimising mission start and/or finish time and increasing storage-to-meter energy efficiency. Furthermore, there has been a recent paradigm shift within the automotive industry towards battery electric vehicles (BEV). The main disadvantages of BEVs, however, compared to conventional vehicles, are limited driving range and long recharge times, particularly at cold or warm temperatures. To address the issues of driving range and long recharge times, it is possible to combine energy and thermal management of BEVs. The objective is to develop a high-level supervisory controller that can take a holistic approach, based on real-time data from navigation system and charging infrastructure, and consider both climatization, driving and charging aspects over long-distance trips. Example of potential control signals are: heating/cooling of compartment and battery, charging power, and cruise control set speed.
To achieve above-mentioned goals, this thesis proposes a mission planner for vehicles over long-distance trips. The mission planner consists of three components, i.e. logistics planner, eco-driving supervisor, and thermal and charging supervisor.

CHALMERS
UNIVERSITY OF TECHNOLOGY

AHAD HAMEDNIA

AHAD HAMEDNIA • On Optimal Mission Planning for Vehicles over Long-distance Trips • 2022

On Optimal Mission Planning for Vehicles over Long-distance Trips

AHAD HAMEDNIA

DEPARTMENT OF ELECTRICAL ENGINEERING
CHALMERS UNIVERSITY OF TECHNOLOGY
Gothenburg, Sweden 2022
www.chalmers.se

THESIS FOR THE DEGREE OF DOCTOR OF PHILOSOPHY

On Optimal Mission Planning for Vehicles over Long-distance Trips

Ahad Hamednia

CHALMERS
UNIVERSITY OF TECHNOLOGY

Department of Electrical Engineering
Chalmers University of Technology
Gothenburg, Sweden, 2022

On Optimal Mission Planning for Vehicles over Long-distance Trips

Ahad Hamednia
ISBN: 978-91-7905-788-6

Doktorsavhandlingar vid Chalmers tekniska högskola
Ny serie nr 5254
ISSN 0346-718X
This thesis has been prepared using LaTeX.

Department of Electrical Engineering
Chalmers University of Technology
SE-412 96 Gothenburg, Sweden
Phone: +46 (0)31 772 1000
www.chalmers.se

Printed by Chalmers Reproservice
Gothenburg, Sweden, 2022

To my family

Abstract

This thesis proposes a mission planner for vehicles over long-distance trips, for finding the optimal trade-off between trip time, energy efficiency, and driver comfort, subject to road information, traffic situations, and weather conditions. The mission planner consists of three components, i.e. logistics planner, eco-driving supervisor, and thermal and charging supervisor. The logistics planner aims at optimising the mission start and/or finish time by minimising energy consumption and trip time. The eco-driving supervisor computes the velocity profile of the driving vehicle, by optimising the energy consumption and penalising driver discomfort. To do so, an online-capable algorithm has been formulated in a model predictive control framework, subject to road and traffic information, and the pre-optimised mission start and/or finish time. This algorithm is computationally efficient and enables the driving vehicle to adapt and optimally respond to predicted disturbances within a short amount of time. Eco-driving has also been achieved for a vehicle confronted with wind, by applying stochastic dynamic programming method. The thermal and charging supervisor regulates battery temperature and state of charge by coordinating the energy use of different thermal components. Within the thermal and charging supervisor design, a heat pump has been included for waste heat recovery purposes. Also, the charging stops have been optimally planned, in favour of energy efficiency and trip time. The performance of the proposed algorithms over a road with a hilly terrain is assessed using simulations. According to the simulation results, it is observed that total travel time is reduced up to 5.5 % by optimising the mission start time, when keeping an average cruising speed of about 75 km/h. Also, compared to standard cruise control, the energy savings of using this algorithm is up to 11.6 %. Furthermore, total charging time and energy consumption are reduced by up to 19.4 % and 30.6 %, respectively by developing the thermal and charging supervisor, compared to a case without the heat pump activated and without charge point optimisation.

Keywords: Energy efficiency, Mission planning, Logistics planning, Eco-driving, Thermal and charging management, Optimal control, Nonlinear programming, Model predictive control, Stochastic dynamic programming

List of Publications

This thesis is based on the following publications:

[A] **Ahad Hamednia**, Nikolce Murgovski, and Jonas Fredriksson, "Time optimal and eco-driving mission planning under traffic constraints". 23rd *IEEE International Conference on Intelligent Transportation Systems (ITSC)*, Rhodos, Greece, Sep 2020.

[B] **Ahad Hamednia**, Nalin K.Sharma, Nikolce Murgovski, Jonas Fredriksson, "Computationally efficient algorithm for eco-driving over long look-ahead horizons". *IEEE Transactions on Intelligent Transportation Systems*, Feb 2021.

[C] **Ahad Hamednia**, Maryam Razi, Nikolce Murgovski, and Jonas Fredriksson, "Electric vehicle eco-driving under wind uncertainty". 24rd *IEEE International Conference on Intelligent Transportation Systems (ITSC)*, Indianapolis, IN, United States, Sep 2021.

[D] **Ahad Hamednia**, Nikolce Murgovski, Jonas Fredriksson, Jimmy Forsman, Mitra Pourabdollah, and Viktor Larsson, "Optimal thermal management, charging, and eco-driving of battery electric vehicles". Re-submitted the revised version to *IEEE Transactions on Vehicular Technology* in Oct 2022.

[E] **Ahad Hamednia**, Victor Hanson, Jiaming Zhao, Nikolce Murgovski, Jimmy Forsman, Mitra Pourabdollah, Viktor Larsson, and Jonas Fredriksson, "Optimal thermal management and charging of battery electric vehicles over long trips". Submitted to *IEEE Transactions on Vehicular Technology* in Sep 2022.

Other publications by the author, not included in this thesis, are:

[F] **A. Hamednia**, N. Murgovski, and J.Fredriksson, "Predictive velocity control in a hilly terrain over a long look-ahead horizon". 5th *IFAC Conference on Engine and Powertrain Control, Simulation and Modeling (E-CoSM)*, Changchun, China, Sep 2018.

[G] S. E. T. Jacobsen, A. Gustafsson, N. Vu, S. Madhusudhana, **A. Hamednia**, N. K. Sharma, and N. Murgovski, "Predictive cruise control behind a stationary or slow moving object". 30^{th} *IEEE Intelligent Vehicles Symposium (IV)*, Paris, France, Jun 2019.

[H] N. K. Sharma, **A. Hamednia**, N. Murgovski, E. R. Gelso, and J. Sjöberg, "Optimal eco-driving of a heavy-duty vehicle behind a leading heavy-duty vehicle". *IEEE Transactions on Intelligent Transportation Systems (ITS)*, vol. 22, no. 12, pp. 7792–7803, 2020.

[I] K. Keykhosravi, **A. Hamednia**, N. Murgovski, H. Rastegarfar, and E. Agrell, "Data preprocessing for machine-learning-based adaptive data center transmission". *ICT Express*, vol. 8, issue. 1, pp. 37–43, 2022.

[J] **A. Hamednia**, J. Forsman, N. Murgovski, V. Larsson, and J. Fredriksson, "Optimal pre-conditioning of battery electric vehicles before fast charging". Submitted to *22nd IFAC World Congress*, Yokohama, Japan, Jul 2023..

Acknowledgments

As a PhD student who is approaching the end of a journey at Chalmers, I would like to take a moment to acknowledge those whom I had the privilege to work with and learn from.

First and foremost, my supervisor Associate Professor Nikolce Murgovski. I would like to express my sincere gratitude to you, for your guidance, encouragement, and advice throughout these years. Also, I would like to thank my co-supervisor Professor Jonas Fredriksson for many fruitful discussions, which greatly helped me to gain deeper understanding about my research field.

Many thanks to Dr. Nalin Kumar Sharma and Dr. Maryam Razi for your time and helpful discussions during the first half of my PhD period. Honestly, I've learned a considerable amount from you both.

Dr. Viktor Larsson, Mats Bohman, Dr. Mitra Pourabdollah, Jimmy Forsman, Victor Hanson, and Jiaming Zhao from Volvo Car Corporation (VCC) deserve a particular recognition. Without your expertise and insight, this thesis would have been very different. I am deeply grateful for sharing your wisdom and for having deep talks about my topic. I also highly appreciate the understanding and patience of my current manager at VCC Ole-Fredrik Dunderberg and the product owner Anette Westerlund, letting finalize my PhD thesis while I was working.

A big thanks goes to my past and present office-mates, Changfu, Julio, Ivan, Wenhao, and Maximilian. Maxi I'm so lucky to have you as a great friend of mine. I never forget all the talks, walks, and laughter we had together. Still, I'm not a fan of Bayern Munich though:)

I also want to thank all the great seniors and colleagues at the department, including the past and present SYSCON PhD students and Post-Docs. You truly made the last five years for me.

My Iranian friends at Chalmers, in Sweden, in Iran, and all over the world; you are of my invaluable assets in life. I am so proud of you all and I respect all the moments we've experienced joy and pain together.

My parents, Roghayeh and Majid! I would like to give the most heartfelt thanks to you for your unconditional love and encouragement. It would not have been possible for me to pursue my studies without the endless support of you and my lovely sister Mahdieh. I am indebted for your sacrifices, though it is always a void in my heart that I've been living far from you for the past years.

Last but by no means least, my wife! You have brought ever-growing love and happiness to my life, and you have given me through the ups-and-downs of the past couple of years. I love you Nazanin. I also try to keep the nagging due to PhD life down:)

Sincerely,
Ahad Hamednia,
Göteborg, 2022

Acronyms

GDP:	Gross Domestic Product
NDC:	Nationally Determined Contributions
HDV:	Heavy Duty Vehicles
R&D:	Research and Development
MPC:	Model Predictive Control
ICE:	Internal Combustion Engine
EM:	Electric Machine
OCP:	Optimal Control Problem
EV:	Electrified Vehicle
CAGR:	Compound Annual Growth Rate
LFP:	Lithium Iron Phosphate
HEV:	Hybrid Electric Vehicle
PHEV:	Plug-in Hybrid Electric Vehicle
BEV:	Battery Electric Vehicle
Li-ion:	Lithium-ion
SoC:	State of Charge
HP:	Heat Pump
WHR:	Waste Heat Recovery
ED:	Electric Drivetrain
PE:	Power Electronic
BSFC:	Brake Specific Fuel Consumption

HVAC:	Heating, Ventilation, and Air Conditioning
HVCH:	High Voltage Coolant Heater
CoP:	Coefficient of Performance
NLP:	Nonlinear Program
DP:	Dynamic Programming
SDP:	Stochastic Dynamic Programming
PMP:	Pontryagin's Maximum Principle
TPBVP:	Two-point Boundary Value Problem
MHMPC:	Moving Horizon Model Predictive Control
SHMPC:	Shrinking Horizon Model Predictive Control
RTI:	Real-time Iteration
SQP:	Sequential Quadratic Programming
QP:	Quadratic Program
MINLP:	Mixed-integer Nonlinear Program

Contents

Part I

Overview

CHAPTER 1

Introduction

1.1 Motivation

Transport demand is linked with several factors, such as economic environment, political will, and technological advance. In particular, the economic environment, characterized as gross domestic product (GDP), international trade, and oil prices, plays a central role in the development of a transportation system. The growth of GDP has been historically identified as a major contributor to the extension of both freight and passenger transport, i.e. greater rise in goods production can lead to greater transport distances travelled [1]. Also, international trade among different countries and people, outlined as a crucial matter for the development of civilizations, is enabled by the means of transport. The volume of international trade has grown twenty-seven-fold in the post-war era between 1950 and 2007, three times faster than the growth of world GDP [1].

Among all transport modes, road and rail (surface) transport include around 30 % of the freight transport demand and around 86 % of the passenger transport demand [1]. In a baseline scenario, defined as an extrapolation of the trends about current policy developments, surface freight demand is projected

to grow from 32 000 to 83 000 billion tonne-kilometers between 2015 to 2050, accounting road freight demand for about 60 % of the total, see Figure 1.1(a). Also, global surface passenger demand is expected to increase from 43 500 billion passenger-kilometers in 2015 to around 92 800 billion passenger-kilometers in 2050, see Figure 1.1(b), where road passenger-kilometers are estimated to account over 80 % of the total. Although surface transport is increasing, its growth rate is not the same in all countries. In this context, the future progression path of the countries in service-oriented economies highly influences the surface transport sector [1].

Excessive energy consumption and CO_2 emissions caused by the growth of road transport are alarming concerns for policy makers, logistic service providers, and customers due to economic, environmental, and ecological issues. The nationally determined contributions (NDC) underline the necessity of reducing vehicular energy consumption and fleet decarbonisation by addressing the important role of fuel-efficient technologies and development of electromobility [1]. In 2015, energy consumption due to the road transport in Europe amounted to around 11.5 million terajoules. Also, the calculated volume of the emissions is 60 % higher compared to the total amount in 1990 and is estimated to increase by more than 70 % until 2050 [2]. In relation to the oil prices, the risk of abandoning the commitments made against climate change is reduced by current high oil prices, thus encouraging less fossil fuel burning. In the long term, the chance for clean investments may be raised further, as future possible cost-effective clean mobility solutions may win the competition against conventional fuel [1].

Extensive costs, e.g. economic and social, due to traffic congestion are other negative side effects caused by the increase in road transport. In 2010, the estimated cost due to the traffic congestion is $115 billion over 439 urban areas of the United States [3]. The traffic congestion engenders mainly because the traffic volume is too close to the maximum capacity of a road or network for certain hours of a day. Current official forecasts point out that congestion will grow considerably within future decades [4]. In public opinion, the growing traffic congestion on motorways is indicated as a waste of money and time, which can be resolved by means of building more roads. However, road construction is not always cost-effective and can cause serious environmental issues. Thus, due to the enormous increase in the energy consumption, CO_2 emissions, and traffic congestion costs, there is a strong incentive to achieve

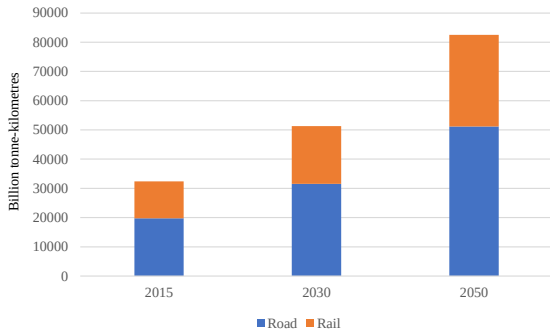

(a) Surface freight transport demand by mode.

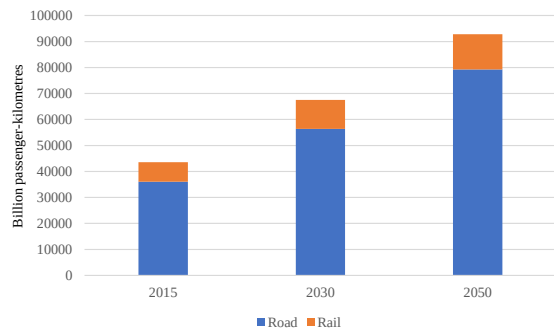

(b) Surface passenger transport demand by mode.

Figure 1.1: Surface transport demand including freight and passenger, baseline scenario. Data are extracted from [1].

a sustainable transport by improving transport efficiency, which can be interpreted as providing service with less consumption of resources and not losing *logistics performance*, i.e. costs and delivery service [5].

Transport efficiency can be improved by optimal planning the transport mission. To do so, it is essential to optimise the mission start and/or finish time, and increase the efficiency of *storage-to-meter*, referring to the conversion of energy drawn from a storage, e.g. fuel or electrical grid, into potential and kinetic energy required for displacement, and accompanied losses [6]. The storage-to-meter efficiency can be improved in several ways by, e.g. better usage of vehicle components, reducing the vehicle mass, choosing the most energy-efficient route, or providing the vehicle's energy-efficient drive, so-called *eco-driving* [7]–[9]. In particular, it is revealed in [6] that there is a high potential of eco-driving in improving the storage-to-meter efficiency without having any requirement for structural changes in the vehicle. To achieve eco-driving, it is necessary to optimally plan the velocity profile of the vehicle, subject to road and traffic flow information. One important factor in optimising the velocity profile is the speed limits, which are imposed by not only legal speed limits but also dynamic constraints [10], [11]. For instance, surrounding traffic enforces such dynamic constraints due to the presence of e.g. traffic lights, intersections, ramps and junctions. Another example that dynamically affects the speed limits is the linking of two or more trucks in convoy in order to increase the energy efficiency [12]. As dynamic speed limits depend on day and time of day, the total trip time depends not only on the planned velocity profile, but also on the mission start time. The traffic jam could be avoided by optimising the mission start time [13].

In case of non-urban road transport, there is a great potential of improving the energy efficiency and reducing CO_2 when driving in a hilly terrain, especially for heavy-duty vehicles (HDVs), due to their large kinetic and potential energy buffers [14]. Accordingly, the vehicle accelerates when driving downhill and decelerates when climbing uphill. This leads to less waste of non-recuperable energy compared to driving with constant speed [15]. To implement such behaviour over complex road topographies, advanced optimal control strategies [6] can be employed that maximise energy efficiency by optimal coordination of energy sources, utilizing information of the road topography.

In addition to the aforementioned solutions, another well-known way for

increasing the storage-to-meter efficiency is to utilise alternative powertrains, focusing on counteracting increasingly stringent legislation against greenhouse gas emissions, and achieving more sustainable and environmentally friendly vehicles [16], [17]. Thus, research and development (R&D) of electrified vehicles (EVs) have recently gained extensive interest among researchers and manufacturers, by adding a secondary energy source to conventional powertrains with an internal combustion engine (ICE) [18]. Batteries, fuel cells, pneumatic and hydraulic reservoirs, flywheels, and supercapacitors are known as the major additional energy carriers [19]. Depending on the size of the electric energy source, the electrified powertrains can be classified into various configurations, i.e. hybrid electric vehicles (HEVs), plug-in HEVs (PHEVs) [18], [20], and all-electric vehicles generally referred to as battery electric vehicles (BEVs) [21]. In HEVs and PHEVs, ICE together with an electric machine (EM) provide propulsion power at the wheel side of the vehicle, whereas in BEVs, EM is the only actuator to do so.

The EV market has had a steep increase over the last decade, such that several car companies have set a goal of pure electric production in near future [22]. In 2020, worldwide BEV Market size worth 150 billion US Dollars, which is forecasted to rise at a compound annual growth rate (CAGR) of over 10 % from 2021 to 2027 [23]. Tax rebate possibility and rapid investments in R&D of advanced battery technologies are identified as other principal reasons that can highly foster the market growth, in addition to the environmentally friendly feature of the EVs. In 2021, Tesla publicized the use of Lithium Iron Phosphate (LFP) based batteries in all of its produced cars, aiming at achieving longer battery life expectancy, improved charge/discharge capability, reduced vehicle weight, and zero maintenance costs. Furthermore, it is easier to recycle the LFP batteries compared to nickel-cobalt aluminum battery packs [24].

In 2020, overall automotive industry including the EV market inevitably suffered from the negative impacts of the COVID-19 pandemic, due to unavailability of electric components, shutdown of manufacturing facilities, and contracted consumer demand followed by massive lockdowns and strict travel banns [25]. This also led to a deferral in launching new BEVs, thus decreasing the BEV market revenue. Although, the EV market growth has been shrunk in the short-term because of the COVID-19 outbreak, the industry is stimulated enough to grow steadily in the long run, as a consequence of supportive

government policies and the restrictive emission standards [23].

Despite promising contributions in improving the energy efficiency and reducing destructive emissions, EVs still confront several challenges impeding their widespread adoption. Energy management, limited distance range, long charging times, and thermal management are among those major challenges, which become even more crucial to ponder in case of planning for long distance trips, i.e. longer than the vehicle's distance range [26]–[28]. Range anxiety, a driver's fear associated with running out of the battery energy before reaching a planned destination or a suitable charging point, is a psychological side effect of the BEVs' limited range. Depending on a car model, the range can vary over a large distance window [29]. The current range may meet most consumers' short to medium-distance mobility needs, revealed by recent investigations about actual driving profiles of BEVs [30], [31]. However, such capabilities still fail to fully meet the range requirement of long-distance trips, highlighting the significance of reducing total energy consumption as well as promoting fast-charging technology for BEV customer acceptance. Lately, a high-power fast-charging technology has been introduced, aiming at recharging a battery up to 80 % state of charge (SoC) within several minutes, in order to provide more convenient long-distance trip experiences [32].

In addition to the charger's rated power, charging time can also be highly shaped by fast charging properties of the battery. This is mostly related to the battery chemistry, aging, SoC, and temperature, implying that the charging may not necessarily perform with a full rate [33]. Thus, solutions associated with the BEV's fast charging are required to incorporate various aspects rather than just focusing on increasing the maximum power provided by the charger [34].

A crucial factor that directly affects charging time as well as total energy consumption is the thermal management system targeting the satisfaction of safety, durability, and performance requirements, especially in harsh climates [35]. Lithium-ion (Li-ion) batteries, as a widely used alternative in the market, are highly temperature sensitive. At high battery temperatures, corrosion and even explosion can occur in the battery pack by creating bubbles, bulge, sparks, and flames, due to overexposure of the battery to heat. Furthermore, at sub-zero temperatures, the battery performance is deteriorated due to a slowed electro-chemical process within the battery cells. This yields a severe reduction in the cell's available power and energy, thereby significantly

increasing the charging time [36]. Moreover, to enhance the awareness about total energy consumption of the vehicle, it is essential to incorporate the thermal management system in optimising the storage-to-meter energy efficiency of the BEV, since the demanded power for the thermal management system components are supplied by the battery [37], [38].

1.2 Research gaps and questions

Although extensive research has been conducted on improving the transport efficiency over the past years, still the inherent autonomy of the vehicle as well as logistical service, over long distances are questionable due to the vehicle's limited range. During such long-distance trips, the range is highly dependent on the driving behaviour, road topography, traffic situations, and weather conditions. However, providing the logistic performance and achieving online-capable eco-driving algorithms for long-distance trip cases are not properly addressed in the technical literature. Developing the online-capable algorithms are essential, as the vehicle requires to react adequately against potential disturbances and events along the driving route. Furthermore, reducing the long charging time together with designing a suitable thermal management system, in order to experience an energy efficient and yet convenient long-distance trips, have not thoroughly been studied.

The main research questions of this thesis are summarised as:

1. How to attain the logistics performance in terms of energy efficiency and/or time?
2. How to develop a computationally efficient supervisory controller for eco-driving of a vehicle over long look-ahead horizons?
3. How to develop a stochastic controller for eco-driving of a vehicle under wind uncertainty?
4. How to develop an algorithm for combined eco-driving, charging, and thermal management on long-distance trips?
5. What are the benefits of including a heat pump in the thermal management system?
6. How to choose the charging locations in favor of achieving optimality in time, energy, or a compromise of both?

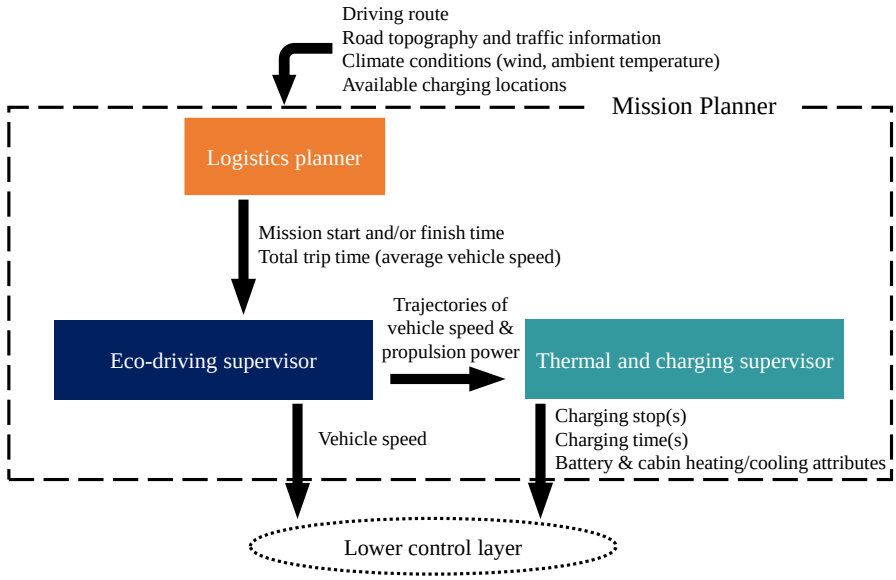

Figure 1.2: Structure of the mission planner, which consists of a logistics planner, eco-driving supervisor, and thermal and charging supervisor.

1.3 Thesis focus and contributions

The focus of this thesis is on the development of an optimal mission planner for a vehicle over long-distance trips, subject to predictive information about the driving road, traffic situations, climate conditions, and available charging locations along the road. As depicted in Figure 1.2, the mission planner consists of three components, i.e. logistics planner, eco-driving supervisor, and thermal and charging supervisor. Several goals have stimulated us to design such a multi-component structure, for e.g. reducing computational complexity, providing modularity and the ability to reject possible disturbances. Thus, each component has specific tasks, which are performed by solving an optimal control problem (OCP).

The logistics planner computes the optimal mission start and/or finish time by offline optimising energy consumption and trip time. It also generates a reference velocity profile and, thus, an estimate of the time for reaching sparsely assigned positions along the route, at intervals of about 250 m. To do so, the

logistics planner uses road information together with traffic situation. The energy-efficient and time-optimal solution provided by the logistics planner offers the logistics service providers a promising investigation, which is useful for the coordination of the shipping and receiving of goods, supplies, foods and people.

When solving the logistics planning OCP offline, reducing the computational time is often not the major bottleneck, since the problem solving is allowed to take a considerable amount of time. However, the offline implementation has drawbacks in situations where the disturbances and/or constraints, for e.g. traffic situation, change unpredictably and the vehicle is no longer able to exactly follow the planned solution. In such situations an alternative controller is needed to provide an adequate solution, where in each instance the estimations and predictions of the vehicle and environment are utilised. Thus, an online-capable eco-driving supervisor has been developed in a model predictive control (MPC) fashion for look-ahead horizons of up to hundreds of kilometers, subject to the pre-optimised mission start and/or finish time, and the reference velocity profile.

Eco-driving is also achieved for a vehicle when confronted with wind, e.g. headwind, tailwind crosswind. The wind speed has a stochastic behaviour in general, leading to an unsteady driving environment. Thus, an OCP has been formulated, aiming at improving energy efficiency and trip time, under the wind uncertainty. The dimension of the formulated problem has been reduced, by adjoining the trip time dynamics to the objective. This can considerably boost the computational efficiency. Also, to cope with the stochastic wind disturbance, stochastic dynamic programming (SDP) has been applied to find the global optimum of the problem. Furthermore, soft constraints on speed limits (kinetic energy) have been enforced to the problem by including sharp penalties to the objective, in order to study potential constraints violations on trip time and/or speed limits.

To increase awareness on total demanded power of the vehicle, and to further improve the source-to-meter energy efficiency, eco-driving is combined with optimal thermal management and charging of the vehicle. To do so, an OCP has been formulated, with the goal of at finding the optimal trade-off between trip time and energy efficiency. The formulated problem is then transformed into a hybrid dynamical system, where the dynamics in driving and charging modes are modelled with different functions and possibly with

different state and control vectors. The formulated problem resembles realistic driving situations, as it captures the vehicle's both driving and charging modes. Also, multiple charging options are incorporated along the driving route to achieve scalability of the developed algorithm. Furthermore, the benefits of including a heat pump (HP) in the thermal management system for waste heat recovery (WHR) purposes have been investigated. WHR refers to an energy recovery process by transferring heat from one part to another part within the vehicle and, thus, improve the energy efficiency. Moreover, the charging locations are planned, in favour of obtaining optimality in time, energy, or their trade-off.

The main contributions of this thesis are summarised as:

- Developing an logistics planner to attain the logistics performance, by optimising start and/or finish time of the vehicle mission, under legal speed limits and dynamic speed limits imposed by surrounding traffic (Chapter 3 and Paper A).
- Developing an eco-driving supervisor as a predictive supervisory controller that employs communication and prediction abilities of modern transportation to anticipate future events and react against potential disturbances (Chapter 3 and Paper B).
- Developing a stochastic controller for eco-driving of a vehicle under wind uncertainty, to achieve robustness against potential constraints violations of total trip time and/or speed limits (Chapter 3 and Paper C).
- Developing a thermal and charging supervisor combined with eco-driving of the vehicle, to further improve the storage-to-meter efficiency and reduce trip time (Chapter 3 and Paper D).
- Extending the scope of thermal and charging supervisor by including an HP in the thermal management system for WHR, and charge point planning to obtain optimality in time, energy, or their trade-off (Chapter 3 and Paper E).

1.4 Thesis outline

This thesis is divided into two parts. Part I consists of five chapters and serves as an introduction to papers that are appended in Part II. The following paragraph describes the outline of Part I.

Chapter 2 describes the studied vehicle powertrain and its driving mission

over long-distance trips. Chapter 3 addresses the tools used for solving the optimisation problem of each component of the mission planner. Chapter 4 provides a short summary for each of the appended papers. Finally, the last chapter of introductory part concludes the thesis and presents the possible directions for future extensions of current research.

CHAPTER 2

Vehicle powertrain and driving mission

This chapter addresses a multi-domain configuration of the vehicle powertrain, i.e. for a combustion engine vehicle or a BEV. Later, a long-distance driving mission of the vehicle is demonstrated as a driving route accompanied with the road topography, speed limits, wind effect, and available charging locations along the route.

2.1 Vehicle powertrain

A schematic diagram of the studied powertrain is depicted in Figure 2.1, illustrating the connection of the powertrain components via mechanical, electrical, and thermal paths. The powertrain comprises propulsion components, namely an energy supply/storage unit, e.g. fuel tank or battery, an actuator, e.g. ICE or EM, and a transmission system, as well as a thermal management system. Note that the electrical and thermal domains are addressed for BEVs in this thesis, to model the electrical and thermal behaviours of the electric powertrain, in favour of achieving performance, safety, and durability requirements [39]. The three powertrain domains are explained in the following sections.

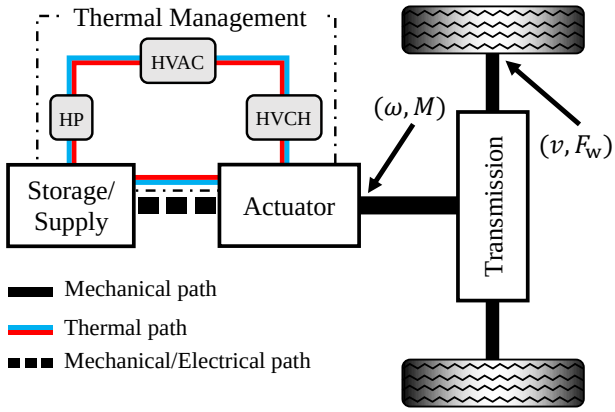

Figure 2.1: Powertrain schematic diagram, which consists of an energy storage/supply unit, an actuator, a transmission system, and a thermal management system. The transmission translates shaft torque and rotating speed to traction force and vehicle speed. The thermal management system may include an HVCH, an HVAC, and an HP, which are employed for actively regulating the battery pack and cabin compartment temperatures.

Mechanical domain

The actuators in Figure 2.1 are modelled with static relations based on steady-state measurements. An example of efficiency maps of the ICE and EM for a given pair of rotational speed and torque at the shaft between the actuator and transmission are shown in Figure. 2.2.

The negative torque limit, shown in Figure 2.2(a), corresponds to a lower bound on negative torque due to an additional braking by a retarder, a compression release, engine brake, and/or an exhaust pressure governor. The additional braking is preferred over the service braking in order to reduce wear and avoid lockup of the braking pads. In Figure 2.2(b), the positive and negative torque regions indicate the motoring and the generating modes of operation, respectively. For a combustion engine vehicle, the storage is connected to the ICE through a mechanical path. The traction power provided by the actuator is delivered to the wheels of the vehicle via the transmission system through a mechanical path, by transforming the shaft torque and rotational speed into traction force and vehicle speed, respectively. More details

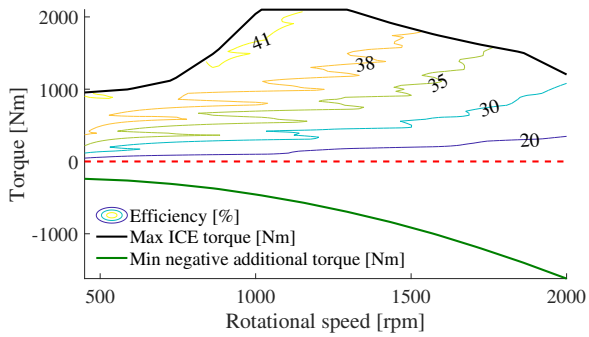

(a) Steady-state efficiency map together with ICE torque limits.

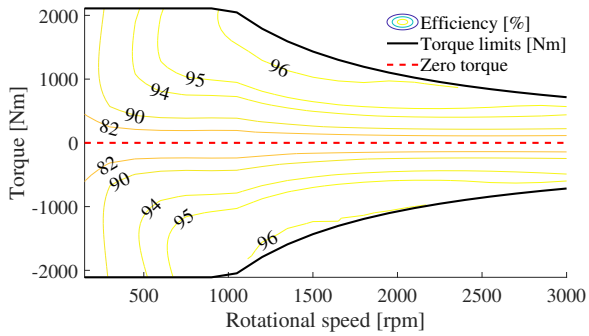

(b) Steady-state efficiency map together with EM torque limits.

Figure 2.2: Steady-state efficiency map together with actuator torque limits.

on modelling the propulsion components are given in Paper B.

Electrical domain

As depicted in Figure. 2.1, the electric power flow between the battery and EM is bidirectional via the electrical path, depending on the EM's operating mode, i.e. generating or motoring. Accordingly, the electrical energy is supplied to the EM during the motoring mode, or stored in the battery throughout the generating mode. In this thesis, the battery is modelling using an equivalent circuit, including a voltage source known as open-circuit voltage, and an internal resistance of the battery. The open-circuit voltage is generally proportional to the battery SoC. The internal resistance is usually a nonlinear monotonically decreasing function of the battery temperature [40]. As the battery temperature increases, the ions inside the battery cells get more energized, resulting in less internal resistance against the ions' movement.

Thermal domain

The dynamical variations of the battery pack's temperature is generally because of the convective heat exchange rate between the battery pack and ambient air and/or the chassis of the vehicle, and the heat generated/removed by means of two groups of sources, i.e. passive and active, as explained in the remainder of this section. Note that uneven conductive distribution of the battery pack temperature associated with the diffusion is neglected in this thesis, to avoid increasing unnecessary complexity of the thermal model. Thus, the core and crust battery pack temperatures are assumed to be identical.

Passive heating

The passive heat generation is due to: 1) the heat induced by the battery internal resistive losses, so called *irreversible ohmic Joule heat*; and 2) the conversion of electric drivetrain (ED) power losses into heat, which is generally dependent on the propulsion power demand. Power electronic (PE) devices and EM are the two major heat generating components within the ED circuit. For cold climate operation, it is desirable to harvest the heat from the ED to increase the temperature in the battery and/or cabin compartment. However, in warm climate operation, it is most likely favourable to detach the ED components from the battery by a valve, and cool them down, using various

components, namely radiator, HP, or heating, ventilation, and air conditioning (HVAC).

Active heating/cooling

The active heat generation/removal is due to: 1) high voltage coolant heater (HVCH) power conversion for heating the battery pack and/or cabin, 3) HVAC power conversion for cooling the battery pack, and 3) the heat transferred from the battery as a source at low temperature to the cabin as a sink at high temperature, by a heat pumping cycle. To perform the cycle, work is required, as the heat cannot spontaneously flow from a colder place to a warmer one, according to the second law of thermodynamics [41]. In the technical literature, as a merit of the HP, a coefficient of performance (CoP) is defined as a ratio of useful heat provided (e.g. for the cabin compartment) to the work required [42].

2.2 Vehicle driving mission

Consider a vehicle that starts its long-distance trip from point A in Figure. 2.3, and is driving a planned route in a hilly terrain. The main factors influencing the total energy consumption and trip time of the vehicle can be summarised as road topography, driving style, speed limits, and weather conditions. If the driving vehicle is a BEV, then it is essential to make sure that there are available charging locations along the route, in order to finish the vehicle's mission. This also raises the significance of the thermal and charging management of the battery with the goal of enhancing the energy efficiency and/or trip time of the vehicle.

Vehicle longitudinal motion

According to the Newton's law of motion, longitudinal movement of the vehicle can be described as the traction and resistive forces exerted to the vehicle, as depicted in Figure. 2.4. Thus, the net force at wheels of the vehicle is equal to the subtraction of braking force, aerodynamic drag, and roll drag, from the traction force. The braking force generally includes the force by the additional braking. The aerodynamic drag is proportional to the vehicle speed relative to the wind speed, the ambient air density, frontal area of the vehicle, and a

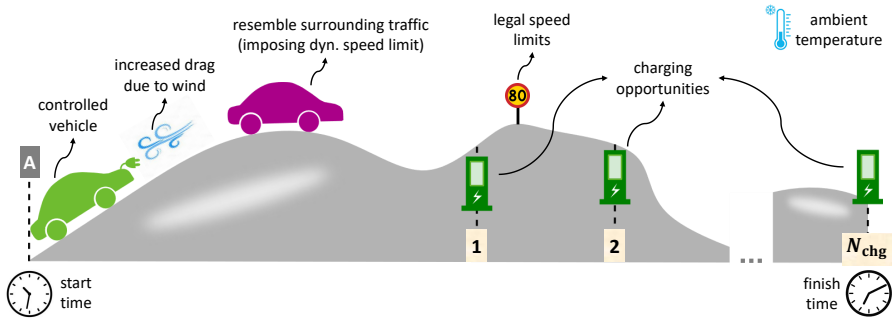

Figure 2.3: Long-distance mission of the vehicle driving on a road with a hilly terrain. Driving behaviour, speed limits, road topography, and charging/discharging properties of the battery are among major elements that affect the energy efficiency of the vehicle.

drag coefficient, referred to as a dimensionless factor used to quantify the drag or resistance of an object in a fluid environment. Furthermore, the roll drag corresponds to resistive forces that depend on the vehicle mass, gravitational acceleration, and the road gradient. At lower relative speeds, the rolling resistance is the dominant element of the resistive forces. However, a threshold is crossed somewhere in the 50-100 km/h speed window above which the air drag becomes the dominant element. Note that this threshold is dependent on the weight and configuration of the vehicle.

Hilly terrain

In the context of energy efficiency when driving in a hilly terrain, the combustion engine vehicles burn extra fuel to climb an uphill, then continue with burning less fuel on the way down, usually by idling and/or braking. However, the BEVs can gain a considerable portion of the energy used for driving the uphill, by the regenerative braking when rolling a downhill. Note that the additional braking mechanism in combustion engine vehicles is only able to reduce wear of the braking pads, and to prevent their overheating.

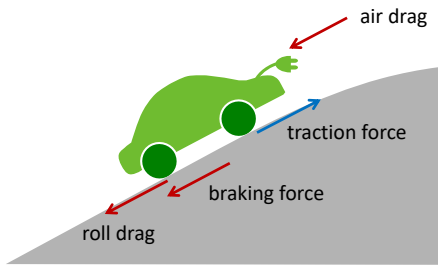

Figure 2.4: Longitudinal motion of the vehicle. Traction force, braking force, aerodynamic drag, and roll drag are mainly the forces that are applied to the vehicle.

Speed limits

Maximum total speed limit $v_{\max}$ for a given pair of travel distance and time of day is computed as minimum value of the maximum legal speed limit, $v_{\max}^{\text{lg}}$, and maximum dynamic speed limit, $v_{\max}^{\text{dyn}}$, as

$$v_{\max}(s,t) = \min\left(v_{\max}^{\text{lg}}(s), v_{\max}^{\text{dyn}}(s,t)\right), \tag{2.1}$$

where s is travelled distance, t is time of day. The maximum legal speed limit can generally change abruptly for different segments of the driving road, see Figure. 2.5(a). However, the dynamic speed limits generally vary smoothly in terms of s and t, see Figure. 2.5(b), since there is no instantaneous change in traffic flow neither in terms of s, nor in terms of t. Thus, the maximum dynamic speed limit is modelled by a smooth function in terms of t. New modern technologies, e.g. e-horizon systems, can provide the information about legal and dynamic speed limits and the road slope [43].

Charge/discharge characteristics

Charging/discharging characteristics of the battery are mostly related to the charger's rated power and maximum available battery power while charging. Maximum power delivered by the ith charger for $i \in \mathcal{I} = \{1, 2, \ldots, N_{\text{chg}}\}$ is

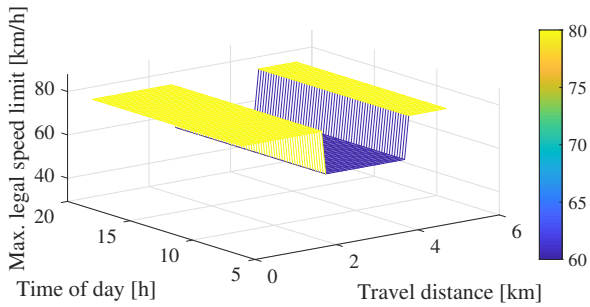

(a) Maximum dynamic speed limit.

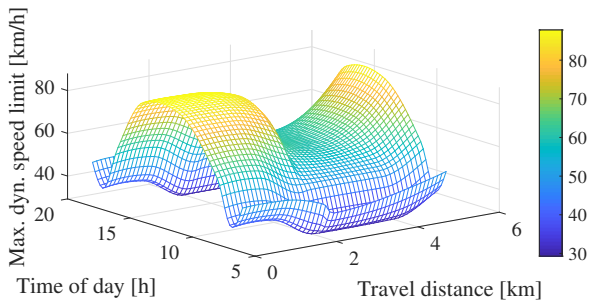

(b) Maximum legal speed limit.

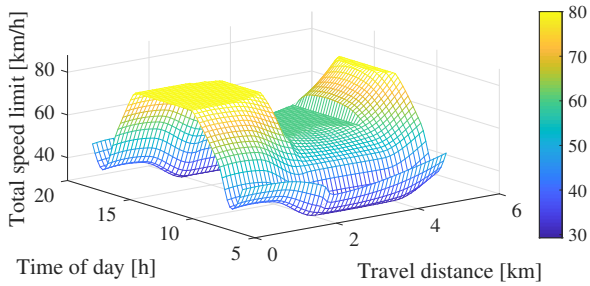

(c) Total speed limit as a minimum of legal and dynamic speed limit.

Figure 2.5: Maximum speed limits in terms of travel distance and time of day. The legal speed limits can change abruptly in terms of travel distance, however dynamic speed limits vary smoothly in terms of travel distance and time of day.

given by

$$P^{i}_{\text{grid}}(s) \in \begin{cases} \{0\}, & s \in \mathcal{S}_{\text{drv}}, \\ [0, P^{i,\max}_{\text{grid}}], & s \in \mathcal{S}^{i}_{\text{chg}} \end{cases} \tag{2.2}$$

where i is charger index, N_{chg} is total number of available charging locations along the driving route, $P^{i,\max}_{\text{grid}}$ is rated power of the ith charger, and $\mathcal{S}_{\text{drv}}$ and $\mathcal{S}_{\text{chg}}$ denote sets of driving and charging distance instances, respectively. Furthermore, an example of the battery charging power limit is demonstrated in Figure 2.6(a), for a given combination of battery temperature and SoC. Accordingly, the bound on the battery charge power is proportional to the battery temperature and inverse of SoC level. Furthermore, the maximum battery discharge power is also of interest, since it can limit the provided traction power while driving. As depicted in Figure 2.6(b), the discharge power limit is proportional to both the battery temperature and SoC level. Thus, the battery power limits can be modelled by nonlinear functions of the battery temperature and SoC, as

$$P_{\text{b}}(s) \in \begin{cases} [P^{\min}_{\text{b,chg}}(\text{soc}(s), T_{\text{b}}(s)), P^{\max}_{\text{b,dchg}}(\text{soc}(s), T_{\text{b}}(s))], & s \in \mathcal{S}_{\text{drv}} \\ [P^{\min}_{\text{b,chg}}(\text{soc}(s), T_{\text{b}}(s)), 0], & s \in \mathcal{S}^{i}_{\text{chg}} \end{cases} \tag{2.3}$$

where $P^{\max}_{\text{b,dchg}} > 0$ and $P^{\min}_{\text{b,chg}} < 0$ are the discharge and charge power limits, respectively. It is deduced from (2.3) that the battery power during driving can also take negative values due to regenerative braking, referred to as a mechanism that transforms the vehicle's kinetic energy into electrical energy to be stored in the battery. Also, the charging power limit generally may differ in driving and charging modes.

Trip time

The vehicle's total trip time includes the driving and charging times together with a detour time from the main route to a charging stop and back. The driving time depends directly on the vehicle average speed constrained by the legal and dynamic speed limits. Also, the charging time is influenced by the

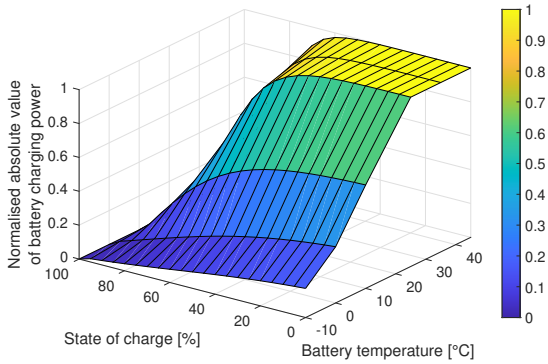

(a) Battery charge power limit.

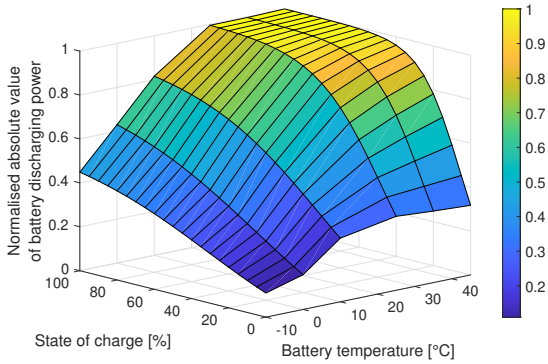

(b) Battery discharge power limit.

Figure 2.6: Normalised absolute value of battery charge and discharge power limits for a given pair of battery temperature and SoC.

charger's maximum delivered power as well as the battery's power availability shaped by the battery temperature and SoC, according to Figure. 2.6. This implies that the thermal management also plays an important role in achieving a reduced charging time, as both the battery temperature and SoC can be directly affected by the thermal management system. Furthermore, optimal charge point planning is another way to reduce the total trip time. More details on impacts of the thermal management system and charge point planning on total trip time are given in Paper D and Paper E.

CHAPTER 3

Optimisation tools

This chapter gives an overview of the optimisation methods used for solving the OCP formulated in Paper A-E.

3.1 Optimal control problem

The OCP is summarised as

$$\min_{\mathbf{u}\in\mathcal{U}} \left(S(\mathbf{x}(\mathrm{s_f}), \mathrm{s_f}) + \int_{\mathrm{s_0}}^{\mathrm{s_f}} V(\mathbf{x}(s), \mathbf{u}(s), s)\mathrm{d}s \right) \tag{3.1a}$$

subject to:

$$\frac{\mathrm{d}\mathbf{x}(s)}{\mathrm{d}s} = f(\mathbf{x}(s), \mathbf{u}(s), s) \tag{3.1b}$$

$$g(\mathbf{x}(s), \mathbf{u}(s), s) \leq 0 \tag{3.1c}$$

$$\mathbf{x}(s) \in \mathcal{X}(s) \tag{3.1d}$$

$$\mathbf{u}(s) \in \mathcal{U}(s) \tag{3.1e}$$

$$\mathbf{x}(\mathrm{s_0}) \in \mathcal{X}_0(s_0) \tag{3.1f}$$

$$\mathbf{x}(\mathrm{s_f}) \in \mathcal{X}_\mathrm{f}(s_\mathrm{f}) \tag{3.1g}$$

where $\mathrm{s_0}$ is initial position, $\mathrm{s_f}$ is final position, and S and V, respectively known as terminal and running costs, form the objective function of the OCP. The objective function may differ for the mission planner components. However, it may generally include total energy consumption, charging cost, and penalised trip time and/or driver discomfort. The energy consumption in combustion engine vehicles corresponds to consumed fossil fuel, while in BEVs it refers to the electricity usage. Other objective functions that the OCP can accept are found in [44]–[48], and the references therein. The vectors $\mathbf{x}$ and $\mathbf{u}$ gather the state variables and control inputs, respectively. The vectors f and g include nonlinear functions in terms of the states, control inputs, and travelled distance, where f denotes the system dynamics on for e.g. trip time, battery temperature and SoC, and longitudinal motion of the vehicle. Also, g represents system general constraints, which may correspond to the maximum dynamic speed limit, actuator bounds, or the battery power limits. Moreover, $\mathcal{X}$, $\mathcal{X}_0$, $\mathcal{X}_\mathrm{f}$ and $\mathcal{U}$ denote the feasible sets of states, allowed initial states at $\mathrm{s_0}$, target states at $\mathrm{s_f}$ and control inputs, respectively.

The problem (3.1) generally represents a mixed-integer nonlinear program (MINLP) if the set $\mathcal{U}$ is mixed-integer, otherwise it becomes a dynamic nonlinear program (NLP). As explained in Paper B, the set $\mathcal{U}$ includes an integer subset, because of choosing gear as an additional control input. Also, the optimal charge point planning performed in Paper E involves introducing an integer variable for each charging location, in order to decide to use or skip a charger. MINLPs are of the most general formats of optimisation problems. Despite a considerable development in software for MINLP solvers in the last twenty years, still solving such problems has proven to be challenging [49]. In the remainder of this chapter, the strategies used in this thesis for effectively solving the problem (3.1) have been briefly explained. These strategies include bi-level programming [50], model predictive control [51], Pontryagin's maximum principle (PMP) [52], sequential quadratic programming (SQP) [53], real-time iterations (RTI) [54], dynamic programming (DP) [55], and hybrid dynamical system reformulation [56].

3.2 Bi-level programming

Bi-level programming is an optimisation scheme, in which one problem (as a sub-problem) is embedded within another. Thus, the optimisation tasks are divided between outer (upper-level) and inner (lower-level) tasks. Likewise, the optimisation variables are categorised into the upper-level variables and the lower-level variables. Bi-level programming is used for energy management and optimal velocity control of vehicles, to overcome the computational burden of high-dimensional optimisation problems [57]–[59].

In Paper B, bi-level programming has been used for gear optimisation. Accordingly, the optimisation of integer variables, i.e. gear, are moved to the lower-level task, and all system dynamics reside in the top-level task which form a dynamic NLP. Static modelling of the actuator and transmission system allows separating the lower level and solving it offline, where the vehicle speed (or kinetic energy) and traction force are regarded as parameters, and optimal gear is computed as a function of these parameters.

To approach the offline-optimal gear selection that minimises energy consumption, it is first needed to translate the brake specific fuel consumption (BSFC) from the engine to the wheels. BSFC refers to the fuel efficiency of any prime mover that burns fuel and produces rotational, or shaft power. A given BSFC map of the engine translates to several equivalent maps at the wheels, one map for each gear. This is illustrated in Figure. 3.1(a), where BSFC is calculated over a grid of feasible vehicle speed and traction force. It can be noticed that map regions with the same speed and force overlap for different gears. Then, the optimal BSFC map for the overlapping regions is derived by calculating the minimum BSFC value for each pair of speed and traction force, see Figure. 3.1(b). Thus, the optimal gear is computed as the corresponding gear that has minimised the BSFC for the given pair of speed and traction force, see Figure. 3.1(c).

Gear selection is relevant even in the negative force region, where a retarder, a compression release engine brake and/or an exhaust pressure governor can be used for braking. The maximum braking force that these units can deliver, also referred to as the minimum additional force limit, is calculated as the minimum force at the wheels for a combination of speed and gear, as shown in Figure. 3.1(c). The goal is to use these units, and thus avoid wear of the service brakes. If the total negative demanded force is higher than the minimum negative additional force, the highest possible gear is selected, which

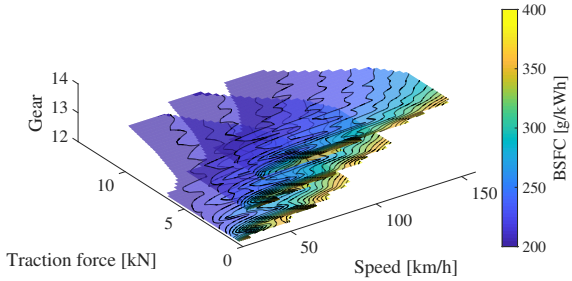

(a) BSFC map for feasible combinations of speed and traction force for gears 12, 13 and 14.

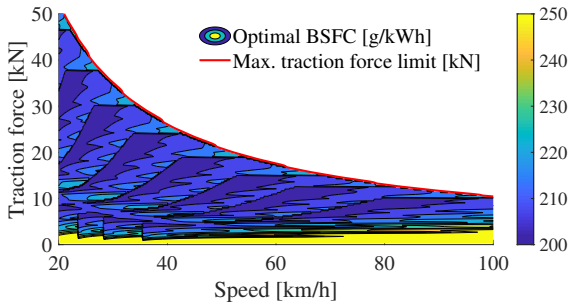

(b) Offline-optimised BSFC map with maximum traction force limit for the speed range of 20-100 km.

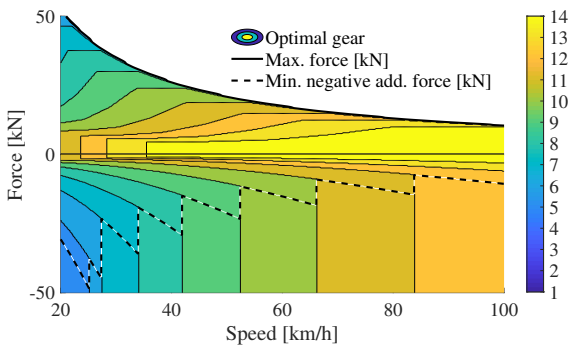

(c) Offline-optimised gear map together with maximum traction force and minimum negative additional force limits for the speed range of 20-100 km.

Figure 3.1: Gear optimisation procedure.

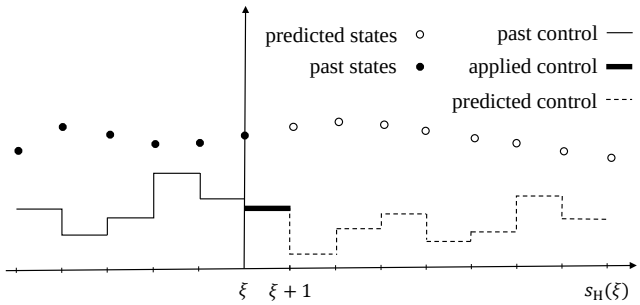

Figure 3.2: Concept of a model predictive controller in discrete domain, where ζ is current instance and s_H is prediction horizon length.

avoids unnecessary down-shifting. On the other hand, if total demanded force is lower than the minimum negative additional force, the lowest possible gear is selected, since it provides the most possible negative additional force and thus reduces the need for using the service brakes.

3.3 Model predictive control

MPC is an online-capable framework that iteratively solves (3.1). The main advantage of MPC is that it engages future instances in optimising the current instance. In other words, a finite horizon of instances is optimised, but only the optimal solution of current instance is implemented. This process repeatedly continues up to the end of the horizon. Thus, MPC is able to anticipate future events, e.g. disturbances, and can take adequate control action accordingly. MPC is a commonly used scheme with high amount of academic literature in the areas of energy management [60]–[62], eco-driving [63]–[65] and optimal thermal management and charging [66], [67]. The concept of MPC in discrete domain is demonstrated in Figure. 3.2.

In Paper B, the eco-driving supervisor has been developed using MPC framework that allows horizons to cover the entire route. As computational resources are always limited, we impose an upper bound on horizon length, s_{Hmax}, hopefully in the range of hundreds of kilometers. Thus, the eco-driving supervision OCP can be solved in a moving horizon MPC (MHMPC)

framework if $s_{\mathrm{Hmax}} < \mathrm{s_f}$, or in a shrinking horizon MPC (SHMPC) framework if $s_{\mathrm{Hmax}} \geq \mathrm{s_f}$. The optimisation variables are predicted at samples $s \in [\zeta, \zeta + s_{\mathrm{H}}]$, given information of the actual vehicle's states at ζ. Thus, the actual horizon length can be computed as

$$s_{\mathrm{H}}(\zeta) = \min\{s_{\mathrm{Hmax}}, \mathrm{s_f} - \zeta\}. \tag{3.2}$$

The problem can now be summarised as follows

$$\min_{\mathbf{u}\in\mathcal{U}} \left(S(\mathbf{x}(s_{\mathrm{H}}|\zeta), s_{\mathrm{H}}) + \int_{\zeta+\mathrm{s_0}}^{\zeta+s_{\mathrm{H}}(\zeta)} V(\mathbf{x}(s|\zeta), \mathbf{u}(s|\zeta), s)\mathrm{d}s \right) \tag{3.3a}$$

subject to:

$$\frac{\mathrm{d}\mathbf{x}(s|\zeta)}{\mathrm{d}s} = f(\mathbf{x}(s|\zeta), \mathbf{u}(s|\zeta), s) \tag{3.3b}$$

$$g(\mathbf{x}(s|\zeta), \mathbf{u}(s|\zeta), s) \leq 0 \tag{3.3c}$$

$$\mathbf{x}(s|\zeta) \in \mathcal{X}(s|\zeta) \tag{3.3d}$$

$$\mathbf{u}(s|\zeta) \in \mathcal{U}(s|\zeta). \tag{3.3e}$$

$$\mathbf{x}(\mathrm{s_0}|\zeta) \in \mathcal{X}_0(s_0|\zeta) \tag{3.3f}$$

$$\mathbf{x}(\mathrm{s_f}|\zeta) \in \mathcal{X}_{\mathrm{f}}(s_{\mathrm{f}}|\zeta) \tag{3.3g}$$

The full statements of problem (3.3) is given in Paper B.

3.4 Insights from necessary PMP optimality conditions

A way to reduce the computational complexity of the high-dimensional optimisation problems is done by adjoining system dynamics to the objective function and neglecting or adjoining constraints on state variables, suggested by the PMP approach [52]. This is a well-known strategy that has been extensively used for optimising the vehicle speed, gear selection, and energy use of vehicles [10], [61], [68]–[72].

In this thesis, the above-mentioned strategy has been used, which involves moving the dynamics on trip time to the objective function of the optimisation problem. The new extended objective, i.e. the Hamiltonian [73], [74], is

defined as

$$\mathcal{H}(s, \mathbf{x}, \mathbf{u}_\mathrm{r}, \lambda) = V(\mathbf{x}(s), \mathbf{u}_\mathrm{r}(s), s) + \lambda^T f(\mathbf{x}(s), \mathbf{u}_\mathrm{r}(s), s), \tag{3.4}$$

where $\mathbf{u}_\mathrm{r}$ is the top-level real-valued decision vector, including the vehicle jerks and mechanical force. Also, λ denotes the vector of Lagrange multipliers known as costate vector to the state vector $\mathbf{x}$. The Hamiltonian (3.4) detailed in Paper B is not an explicit function of trip time, thus optimal time costate, λ_t^*, i.e. the value for λ_t that satisfies maximum trip time constraint, is a constant value, i.e.

$$\lambda_\mathrm{t}^{*}(s) = -\left(\frac{\partial \mathcal{H}(\cdot)}{\partial t}\right)^{*} = 0. \tag{3.5}$$

Furthermore, the trip time is a strictly monotonically increasing function that may activate the maximum trip time constraint only at the final instance. Consequently, if λ_t^* is known, it will be possible to adjoin the nonlinear dynamics on trip time to the objective function. The optimal λ_t^* can be calculated by solving a two-point boundary value problems (TPBVP). To do so, it is considered that the optimal energy consumption corresponds in general to driving slow, so it can be assumed that the vehicle will use the entire trip time, i.e. $t^*(\lambda_\mathrm{t}, s_\mathrm{H}) \approx t_\mathrm{H}$, where t^* is optimised trip time and t_H is desired trip time at final position of the horizon, obtained by the logistic planner. Thus, it is possible to try different values for λ_t and then use search methods, e.g. Newton or bisection, that minimises the cost

$$\min_{\lambda_\mathrm{t}} ||t^*(\lambda_\mathrm{t}, s_\mathrm{H}|\zeta) - t_\mathrm{H}(\zeta)|| \tag{3.6}$$

where $||\cdot||$ may indicate any norm. For more details on finding λ_t^* see Paper B.

3.5 Sequential quadratic programming

Let an NLP be formulated as

$$\min_{\mathbf{d}\in\mathcal{D}} F(\mathbf{d}) \tag{3.7a}$$

subject to:

$$G(\mathbf{d}) \leq 0 \tag{3.7b}$$

$$H(\mathbf{d}) = 0 \tag{3.7c}$$

$$\mathbf{d} \in \mathcal{D} \subseteq \mathbb{R}^n \tag{3.7d}$$

where $\mathbf{d}$ is a vector of decision variables that are feasible within a set of $\mathcal{D}$, and n is a positive integer. Also, the objective F is a nonlinear function, and G and H are vector nonlinear functions representing inequality and equality constraints, respectively. The Lagrangian of the problem (3.7) is defined as

$$\mathcal{L}(\mathbf{d}, \lambda, \sigma) = F(\mathbf{d}) - \lambda^T G(\mathbf{d}) - \sigma^T H(\mathbf{d}), \tag{3.8}$$

where λ and σ are Lagrange multipliers.

If the functions F, G, and H are assumed to be twice continuously differentiable, the NLP (3.7) can be solved efficiently using SQP method. Accordingly, a quadratic version of the problem can be obtained, by linearising the inequality constraints (3.7b) and equality constraints (3.7c). Solving the resultant QP generally gives an approximate solution to the NLP (3.7). However, the accuracy of the solution can be improved, by modifying the objective function with the gradient of the original objective function and the Lagrangian of the constraints. Thus, the resultant problem is a convex quadratic program (QP), as

$$\min_{\Delta\mathbf{d}} F(\mathbf{d}_k) + \nabla F(\mathbf{d}_k)^T \Delta\mathbf{d} + \frac{1}{2}\Delta\mathbf{d}^T \nabla^2 F(\mathbf{d}_k)\Delta\mathbf{d} \tag{3.9a}$$

subject to:

$$G(\mathbf{d}_k) + \nabla G(\mathbf{d}_k)^T \Delta\mathbf{d} \leq 0 \tag{3.9b}$$

$$H(\mathbf{d}_k) + \nabla H(\mathbf{d}_k)^T \Delta\mathbf{d} = 0 \tag{3.9c}$$

where ∇ and ∇^2 denote the gradient and the hessian, respectively, and $\Delta\mathbf{d}$ is a search direction. The problem (3.9) referred to as a sub-problem is solved iteratively in a way that the current sub-problem is linearized around the previous solution. The $k+1 : th$ iterate of the sub-problem (3.9) is given by $\mathbf{d}_{k+1} = \mathbf{d}_k + \beta\Delta\mathbf{d}$, where $\mathbf{d}_k$ is the $k : th$ iterate, and $\beta \in (0, 1]$ is the search step length. The iterations continue until a stop criterion is satisfied, e.g. when the normed difference between two consecutive solutions is less than a defined tolerance. SQP has recently shown a considerable usage in the areas of energy management and eco-driving of vehicles [57], [75], [76].

In Paper B, SQP has been applied for solving the NLP derived as the top-level task of the bi-level program, where λ_t is also a given value.

Real-time iterations

The convex QPs are fast to solve, however, there is no guarantee for the number of sub-problems (3.9) required to be solved until the convergence is reached. This is a major drawback, especially when applying SQP in real-time scenarios, as it is crucial to obtain the solution fast enough. Another issue is that the solutions to the sub-problems (3.9) may be infeasible in the original NLP (3.7). Thus, as the SQP is stopped prematurely, it is essential to verify that the obtained solution by solving a single QP is also feasible in the original NLP. Feasibility can be guaranteed if the domain of the QP, obtained by linearizing nonlinear constraints, is inner approximation of the feasible set of the NLP. RTI [54] facilitates the convergence loop's removal, where the idea is to solve only a single QP per MPC update, without waiting for a full convergence. The obtained solution is possibly sub-optimal, but due to the contractivity of the RTI scheme as shown in [77], the real-time iterates quickly approach the optimal solution during the run-time of the process. The significant reduction of computation time has encouraged researchers to use RTI for real-time applications in automotive areas [57], [78].

Paper B uses RTI in order to boost the computational efficiency of solving the problem (3.9). The feasibility of the sub-problem solution has also been verified in Paper B.

3.6 Dynamic programming

DP [55] is a well-known strategy commonly used for optimal control of vehicles, due to its potential to guarantee global optimum for non-convex, nonlinear and mixed-integer optimisation problems [44], [79]–[83]. DP uses Bellman's principle of optimality [55], where the complex full problem is broken down into simpler sub-problems and solved via backwards recursion handling the problem's nonlinearities and constraints in a straightforward way. Major drawback of using DP is the *curse of dimensionality*, which denotes to a fact that computational time increases exponentially with the number of state variables and control signals [55].

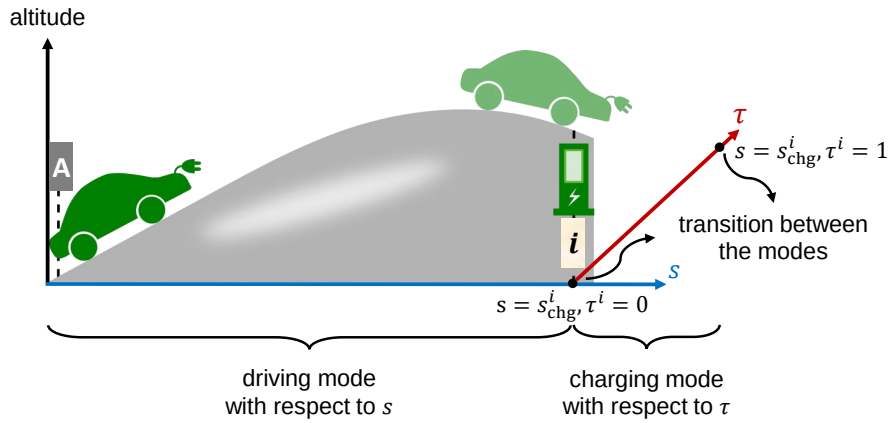

Figure 3.3: Hybrid dynamical system demonstration including driving mode, charging mode and transition between these two modes. During the driving and charging modes decisions are planned with respect to s and τ^i, $i \in \mathcal{I}$, respectively.

DP has been used in Paper C for studying the influence of wind uncertainty on eco-driving of the vehicle. Here, the goal is to derive an optimal policy, i.e. a policy prescribing how to act optimally in the face of the wind uncertainty. Furthermore, to improve the computational efficiency, the dimension of the problem has been reduced by appending trip time dynamics to the objective function, followed by PMP.

3.7 Hybrid dynamical system

A hybrid dynamical system generally refers to a system that encompasses both continuous and discrete dynamical behavior [56]. The structure of hybrid dynamical systems has the advantage of including a vast class of systems, providing more flexibility in the system modelling. This has strongly encouraged using the form of hybrid dynamical system for modelling and control of vehicles [84]–[87].

The Hybrid dynamical system has been used in Paper D, which addresses the thermal management and charging design combined with eco-driving over a long-distance trip with multiple charging options along the route, as illustrated in Figure. 2.3. Accordingly, an hybrid dynamical system has been

formulated, where the driving dynamics are modelled in a spatial domain, i.e. decisions are made along the travelled distance. Also, charging dynamics are modelled in a temporal domain, i.e. decisions are made along a normalized charging time. The actual charging time is optimised together with the optimal state and control trajectories, for both charging and driving modes. The demonstration of the hybrid dynamical system is shown in Figure. 3.3.

The thermal management and charging design in Paper D has been extended in Paper E, by studying the impacts of the optimal charge point planning and including an HP in the thermal management system, on the energy efficiency and trip time.

CHAPTER 4

Summary of included papers

This chapter provides a summary of the included papers. Full versions of the papers are appended in Part II. The layout of the papers has been revised to obey the layout of the rest of the thesis.

4.1 Paper A

Ahad Hamednia, Nikolce Murgovski, and Jonas Fredriksson
Time optimal and eco-driving mission planning under traffic constraints
23rd *IEEE International Conference on Intelligent Transportation Systems (ITSC)* .

This paper describes a methodology for achieving desired logistics performance, i.e. providing service with reduced energy consumption and fulfilling requested shipping and delivery time. The methodology is developed and implemented in a tool, i.e. the logistics planner, by controlling the mission start and/or finish time as well as the velocity profile of a vehicle driving in a hilly terrain. In other words, logistics planner generates a reference velocity profile and, thus, an estimate of the time for reaching sparsely assigned positions along the route, at intervals of about 250 m. Inputs to logistics planner, road

topography and total speed limits, are given by the user, where the total speed limits have been calculated as the minimum value of the legal and dynamic speed limits derived from the traffic information. Furthermore, the trade-off between energy consumption and trip time has been investigated in Paper A, while allowing a flexibility in starting time and a certain variation of vehicle speed around an average. This gives a valuable information to the logistics service provider, to optimally coordinate the shipping and delivering of supplies, foods, goods, and people. It is observed that total trip time is reduced up to 5.5% by adjusting the mission start time, when keeping an average cruising speed of about 75 km/h.

4.2 Paper B

Ahad Hamednia, Nalin K.Sharma, Nikolce Murgovski, Jonas Fredriksson
Computationally efficient algorithm for eco-driving over long look-ahead horizons
IEEE Transactions on Intelligent Transportation Systems .

This paper addresses developing eco-driving supervisor, which aims at obtaining a velocity profile for the entire route such that the trip time is upper bounded and the total energy consumption is minimised. The upper bound on trip time is computed by logistics planner from Paper A, subject to the road and traffic flow information. Thus, an online-capable algorithm has been developed in an MPC framework for long prediction horizons of up to hundreds of kilometers. The controller is capable of using communication and prediction abilities of modern transportation to anticipate future events and disturbances. This implies that the controller is able to re-optimise the velocity profile online, considering possible changes in the condition of the vehicle and/or the driving road. As a central concern for such online-implementable supervisor, the computational efficiency has been considered by developing a bi-level algorithm where integer variable, i.e. gear, is decoupled from the real-valued variables. In the bottom level, the optimal gear map is derived in a way that the total energy consumption is minimised. In the top level, the remaining nonlinear problem has been solved by gaining insights from PMP conditions for optimality and real-time iterations SQP. To provide more comfortable way of driving, acceleration and jerk of the vehicle have been ap-

pended to the top level's objective function. The proposed algorithm is able to solve the optimisation in a very short amount of time, i.e. for a horizon length of 118 km with the sampling interval kept at about 250 m, the computation time is less than 20 ms. Compared to standard cruise control, the energy savings of using this algorithm is up to 11.6 %. Also, Pareto frontier illustrating the trade-off between energy efficiency and driver comfort has been presented, which provides valuable information for vehicle manufacturers to customise the vehicle's performance for a desired energy use and comfort.

4.3 Paper C

Ahad Hamednia, Maryam Razi, Nikolce Murgovski, and Jonas Fredriksson
Electric vehicle eco-driving under wind uncertainty
24rd *IEEE International Conference on Intelligent Transportation Systems (ITSC)* .

This paper addresses eco-driving under wind speed uncertainty, subject to road topography and legal and dynamic speed limits. Thus, an OCP has been formulated, where the trip time dynamics has been adjoined to the objective function, in order to boost the computational efficiency. To find the global optimum of the problem, DP method has been applied, which copes with the stochastic wind disturbance. DP has been approached by discretizing the problem in continuous spatial domain, and gridding the feasible sets of state variable (kinetic energy) and control input (traction acceleration). Moreover, soft constraints on speed limits (kinetic energy) have been enforced to the problem by including sharp penalties to the objective, in order to study potential constraints violations. Subsequently, a deterministic controller and a stochastic controller have been obtained. The deterministic controller has been derived for a fixed wind speed, whereas for the stochastic controller, the wind speed can have a value from a bounded and discretized normal distribution. The performance of the stochastic controller has been evaluated in comparison to the deterministic controller, on uncertain wind profiles. For a fixed energy consumption and average trip time, the constraint violation on speed due to the wind speed uncertainty is 21 % for the deterministic controller, whereas the stochastic controller is robust against such violations. Also, the percentage of violated maximum allowed trip time is 25 % for the

deterministic controller.

4.4 Paper D

Ahad Hamednia, Nikolce Murgovski, Jonas Fredriksson, Jimmy Forsman, Mitra Pourabdollah, and Viktor Larsson
Optimal thermal management, charging, and eco-driving of battery electric vehicles
Re-submitted the revised version to IEEE Transactions on Vehicular Technology in Oct 2022 .

In this paper, a tool has been developed for the thermal management and charging combined with eco-driving of a BEV experiencing a long-distance trip. To do so, a hybrid dynamical system has been formulated, where the total energy consumption and trip time are minimised, subject to predictive information about the driving road, traffic situations, climate conditions, and available charging locations along the road. Within the hybrid dynamical system, the dynamics in driving and charging modes are modelled with different functions and with different state and control vectors. Such hybrid problem formulation allows for reduced computational burden, by modelling the driving dynamics in a spatial domain, i.e. decisions are made along the traveled distance. Also, charging dynamics are modelled in a temporal domain, where decisions are made along a normalized charging time. The actual charging time is modelled as a scalar variable that is optimized simultaneously with the optimal state and control trajectories, for both charging and driving modes. The developed tool provides the satisfaction of safety and battery power availability requirements in extreme climates, as well as convenient trip experiences due to reduced charging times and less range anxiety. The performance of the proposed algorithm has been assessed via several simulations, where it is observed that the total trip time including driving and charging times, is reduced by 44 %, compared to a case without battery active heating/cooling.

4.5 Paper E

Ahad Hamednia, Victor Hanson, Jiaming Zhao, Nikolce Murgovski, Jimmy Forsman, Mitra Pourabdollah, Viktor Larsson, and Jonas Fredriks-

son
Optimal thermal management and charging of battery electric vehicles over long trips
Submitted to IEEE Transactions on Vehicular Technology in Sep 2022 .

The thermal management and charging developed in Paper D has been extended in Paper E, with a focus on potential benefits of including an HP in the TM system for WHR, and charging point planning in a way to achieve optimality in time, energy, or their trade-off. Thus, similar to Paper D, a hybrid dynamical system has been formulated, where charging dynamics are modelled in the domain of normalized charging time. Driving dynamics can be modelled in either of the trip time or travel distance domains, as the vehicle speed is assumed to be known a priori, and the vehicle is only stopping at charging locations. Within the hybrid dynamical system, a binary variable is introduced for each charging location, in order to decide to use or skip a charger. This problem is solved numerically, and simulations are performed to evaluate the performance in terms of energy efficiency and time. Within the simulations, Pareto frontiers describing the trade-off between energy efficiency and time are derived versus different features, e.g. a heat pump, charging stops, and ambient temperature. Such graphs provide a wide range of choices for car manufacturers as well as grid service providers to gain more insight into the design and development of TM and charging systems. Furthermore, various car users can customise their trips according to the information given within these graphs. According to the obtained results, energy consumption and the time needed for charging are reduced by up to 19.4 % and 30.6 %, respectively, by including an HP in the TM system. By including optimal charge point planning in the form of binary decision variables, the solution depends on factors such as the priority between time and energy, the availability of an HP, and ambient temperature.

CHAPTER 5

Conclusion and future work

In this chapter, the thesis is concluded by addressing the research goals and possible directions for future research.

5.1 Concluding remarks

Automotive industry leaders and transport service providers constantly consider reducing ever-growing energy consumption and CO_2 emissions by improving transport efficiency and logistics performance. This thesis has investigated how these goals are achievable by optimal planning of the vehicle's mission, which is characterized as optimising the start and/or finish time of vehicle driving mission and increasing the storage-to-meter efficiency. It has been shown that optimising the vehicle's longitudinal drive has a significant impact on enhancing the storage-to-meter efficiency. Thus, the core idea has been introduced as formulating a driving mission as an optimal control problem. To do so, several factors have been considered that strongly influence solving the optimal control problem, such as speed limits, trip time, weather conditions, driver comfort, future events and disturbances, and the battery power availability during driving and charging modes of the vehicle.

In order to increase feasibility in realistic driving situations, the control problem incorporates speed limits that include not only legal, but also dynamic limits using the information about the road and traffic available. Surrounding traffic can impose such dynamic constraints on the vehicle speed due to presence of e.g. traffic lights, intersections, ramps and junctions. Furthermore, the trade-offs between the energy efficiency and trip time, and between the energy efficiency and driver comfort, are considered in the control problem, i.e. lower energy cost generally yields non-smooth saw-tooth shape velocity profiles and longer trip times. Moreover, predictive controllers are developed that employ communication and prediction abilities of modern transportation to anticipate future contradiction events and disturbances.

To improve the transport efficiency and not lose the logistics performance, with all above-mentioned factors considered, a mission planner. The mission planner consists of a logistics planner, an eco-driving supervisor, and a thermal and charging supervisor. The logistics planner provides the optimal mission start and/or finish time by offline optimising energy consumption and trip time. It also provides a reference speed profile and, thus, an estimate of the time for reaching sparsely assigned positions along the route, at intervals of about 250 m. To do so, the logistics planner uses road information as well as traffic situation characterized as a map of total maximum speed limits given in terms of travel distance and time of day. Here, the trade-off between energy efficiency and total trip time has been investigated, which offers the logistics service provider a valuable information to tailor the vehicle's trip in terms of energy costs and delivery service. It is observed that total trip time is reduced up to 5.5 % by adjusting the mission start time, when keeping an average cruising speed of about 75 km/h.

In cases that the traffic situation and/or the driving road change unpredictably for any reason, an algorithm is needed to generate a valid solution by solving the optimal control problem, and consequently should be real-time implementable. To achieve this, an online-capable algorithm for the eco-driving supervisor has been developed in an MPC fashion, subject to the pre-optimised mission start and/or finish time, and the reference velocity profile. It obtains a velocity profile by optimising the energy consumption and penalising driver discomfort. The algorithm is able to solve the optimisation in a very short amount of time, i.e. for a horizon length of 118 km with the sampling interval kept at about 250 m, the computation time is less than 20 ms. For on-line ap-

plications, such small computation time can strongly enhance the optimality, since the suggested optimal state of vehicle can be updated more frequently. Also, this algorithm is applicable to offline analysis of multi-path problems, where the optimal path of the driving vehicle in terms of energy consumption can be obtained by iteratively solving the eco-driving problem within a small amount of time. Compared to standard cruise control, the proposed algorithm provides the energy savings of up to 11.6 %. Also, Pareto frontier describing the trade-off between energy efficiency and comfortable driving has been presented. This offers a wide range of choices for vehicle manufacturers to customise the vehicle's performance for a desired energy use and comfort.

To achieve the vehicle's eco-driving in the face of wind uncertainty, an analysis has been carried out, using dynamic programming. Thus, a stochastic controller has been derived, where the wind speed takes a value from a bounded and discretized normal distribution. The performance of the stochastic controller has been compared later to a deterministic controller on 100 stochastic wind profiles, where the energy consumption and average trip time are fixed. For obtaining the deterministic controller, the wind speed is a fixed (average of the distribution) value. Accordingly, the speed limits are violated for 21 % of the wind profiles, in the deterministic controller case. However, the stochastic controller is robust against such violations. Such robustness is due to the fact that the stochasticity of the wind speed has been already taken into account when obtaining the stochastic controller.

To further improve the energy efficiency, the thermal management and charging has been designed, capturing both driving and charging modes of the vehicle. Within the thermal management and charging, the benefits of a heat pump system as a mechanism for waste heat recovery has been investigated. According to the results, total charging time and energy consumption are reduced by up to 19.4 % and 30.6 %, respectively by incorporating a heat pump in the thermal management and charging design. It is worth mentioning that the improvement varies noticeably with ambient temperature, however as long as there is a heating demand for the cabin compartment, it is more time and energy efficient in the case with the HP activated. Note that using a heat pump may be beneficiary in cases where there are constraints on discharge power capability of the battery at low battery temperature and SoC regions, or the waste heat available within the battery pack is limited. Furthermore, the charging stops have been optimally planned, which allows for a

holistic solution of a long-distance trip in a BEV in terms of energy consumption and total trip time. The solution depends on factors such as the priority between time and energy, the availability of an HP, and ambient temperature characterised as the cabin heating demand.

5.2 Future work

In this section, several possible directions for future research on the topic mission planning are presented.

Optimal mission planning of HEVs

The current developed mission planner can also be extended to be applicable to HEVs. To this end, an optimisation problem can be formulated, which aims at planning optimal velocity trajectory for the entire route, in a way that total energy consumption is minimised, trip time is upper bounded, and battery SoC at final position is specified. Having the fixed trip time and the battery SoC at the end of the route, indicate that the mission planning of HEVs is also a long-horizon type of problem. Thus, the problem can be treated by using an SHMPC considering the information to the end of the driving route per each MPC update. This results in gradual battery depletion and reaching the desired battery SoC at end of the route. Note that an important step in designing the mission planner for HEVs is the offline gear optimisation, where both fuel and electricity consumption are required to be incorporated in finding the optimal gear map.

Stochastic charging coordination of electrified vehicles

The current developed mission planner can also be extended with a new functionality that optimally coordinates electricity charging of multiple BEVs over long-distance trips, subject to road and traffic information and systems dynamics. A key factor is to incorporate uncertain information on electricity pricing that may vary from charger to charger and time of day, costs for overstay at charging locations and charging capabilities. When the uncertainties are bounded, robust MPC can be designed to guarantee that constraints on system states and control inputs are always respected. If the uncertainties are unbounded, stochastic MPC can be employed to ensure that constraints

are satisfied on average or with a given probability. The main challenge in stochastic optimization over long horizons is in the development of efficient numerical methods to comply to the real-time requirements and limitations of computational units. Another crucial issue is to find a good balance between optimality, robustness and real-time computational feasibility. Thus, current investigations on mathematical transformations, such as bi-level formulation, variable changes and time-to-space coordinate transformation can be extended by studying implications on conservativeness, convexity, accuracy and optimality.

References

[1] I. T. Forum, *ITF Transport Outlook 2017*. 2017, p. 224.

[2] I. E. Agency, *World Energy Outlook 2015*. 2015, p. 600.

[3] D. Schrank, B. Eisele, and T. Lomax, "Tti's 2012 urban mobility report," *Texas A&M Transportation Institute. The Texas A&M University System*, vol. 4, 2012.

[4] C. Lee, Y. Kim, S. M. Jin, *et al.*, "A visual analytics system for exploring, monitoring, and forecasting road traffic congestion," *IEEE transactions on visualization and computer graphics*, 2019.

[5] H. Aronsson and M. H. Brodin, "The environmental impact of changing logistics structures," *The international journal of logistics management*, 2006.

[6] A. Sciarretta, G. D. Nunzio, and L. L. Ojeda, "Optimal ecodriving control: Energy-efficient driving of road vehicles as an optimal control problem," *IEEE Control Systems Magazine*, vol. 35, no. 5, pp. 71–90, 2015.

[7] M. A. S. Kamal, M. Mukai, J. Murata, and T. Kawabe, "Model predictive control of vehicles on urban roads for improved fuel economy," *IEEE Transactions on control systems technology*, vol. 21, no. 3, pp. 831–841, 2012.

[8] M. Vajedi and N. L. Azad, "Ecological adaptive cruise controller for plug-in hybrid electric vehicles using nonlinear model predictive control," *IEEE Transactions on Intelligent Transportation Systems*, vol. 17, no. 1, pp. 113–122, 2015.

[9] Y. Luo, T. Chen, S. Zhang, and K. Li, "Intelligent hybrid electric vehicle acc with coordinated control of tracking ability, fuel economy, and ride comfort," *IEEE Transactions on Intelligent Transportation Systems*, vol. 16, no. 4, pp. 2303–2308, 2015.

[10] M. Held, O. Flärdh, and J. Mårtensson, "Optimal speed control of a heavy-duty vehicle in urban driving," *IEEE Transactions on Intelligent Transportation Systems*, vol. 20, no. 4, pp. 1562–1573, 2018.

[11] R. Basso, P. Lindroth, B. Kulcsár, and B. Egardt, "Traffic aware electric vehicle routing," in *2016 IEEE 19th International Conference on Intelligent Transportation Systems (ITSC)*, IEEE, 2016, pp. 416–421.

[12] A. Alam, B. Besselink, J. Mårtensson, and K. H. Johansson, "Heavy-duty vehicle platooning for sustainable freight transportation: A cooperative method to enhance safety and efficiency," *IEEE Control Systems Magazine*, vol. 35, no. 6, pp. 34–56, 2015.

[13] M. Gendreau, G. Ghiani, and E. Guerriero, "Time-dependent routing problems: A review," *Computers & operations research*, vol. 64, pp. 189–197, 2015.

[14] OECD, *Moving Freight with Better Trucks*. 2011, p. 360.

[15] J. N. Barkenbus, "Eco-driving: An overlooked climate change initiative," *Energy Policy*, vol. 38, no. 2, pp. 762–769, 2010.

[16] R. R. Kumar and K. Alok, "Adoption of electric vehicle: A literature review and prospects for sustainability," *Journal of Cleaner Production*, vol. 253, p. 119 911, 2020.

[17] C. M. Martinez, X. Hu, D. Cao, E. Velenis, B. Gao, and M. Wellers, "Energy management in plug-in hybrid electric vehicles: Recent progress and a connected vehicles perspective," *IEEE Transactions on Vehicular Technology*, vol. 66, no. 6, pp. 4534–4549, 2016.

[18] X. Hu, J. Han, X. Tang, and X. Lin, "Powertrain design and control in electrified vehicles: A critical review," *IEEE Transactions on Transportation Electrification*, vol. 7, no. 3, pp. 1990–2009, 2021.

[19] K. van Berkel, S. Rullens, T. Hofman, B. Vroemen, and M. Steinbuch, "Topology and flywheel size optimization for mechanical hybrid powertrains," *IEEE Transactions on Vehicular Technology*, vol. 63, no. 9, pp. 4192–4205, 2014.

[20] T. Liu, X. Tang, H. Wang, H. Yu, and X. Hu, "Adaptive hierarchical energy management design for a plug-in hybrid electric vehicle," *IEEE Transactions on Vehicular Technology*, vol. 68, no. 12, pp. 11 513–11 522, 2019.

[21] D.-D. Tran, M. Vafaeipour, M. El Baghdadi, R. Barrero, J. Van Mierlo, and O. Hegazy, "Thorough state-of-the-art analysis of electric and hybrid vehicle powertrains: Topologies and integrated energy management strategies," *Renewable and Sustainable Energy Reviews*, vol. 119, p. 109 596, 2020.

[22] A. M. Andwari, A. Pesiridis, S. Rajoo, R. Martinez-Botas, and V. Esfahanian, "A review of battery electric vehicle technology and readiness levels," *Renewable and Sustainable Energy Reviews*, vol. 78, pp. 414–430, 2017.

[23] G. M. Insights, *Battery Electric Vehicle Market Size, By Vehicle (Electric Cars, Electric Buses, Electric Trucks, Electric Motorcycles & Scooters, E-bikes), By Battery Type (SLA, Li-ion, NiMH), COVID-19 Impact Analysis, Regional Outlook, Growth Potential, Competitive Market Share & Forecast, 2021 – 2027*. 2021, p. 210.

[24] L. Ulrich, "Tesla inside: The land rover defender gets an electric makeover," *IEEE Spectrum*, vol. 59, no. 5, pp. 44–49, 2022.

[25] W. Wen, S. Yang, P. Zhou, and S. Gao, "Impacts of covid-19 on the electric vehicle industry: Evidence from china," *Renewable and Sustainable Energy Reviews*, vol. 144, p. 111 024, 2021.

[26] J. A. Sanguesa, V. Torres-Sanz, P. Garrido, F. J. Martinez, and J. M. Marquez-Barja, "A review on electric vehicles: Technologies and challenges," *Smart Cities*, vol. 4, no. 1, pp. 372–404, 2021.

[27] B. O. Varga, A. Sagoian, and F. Mariasiu, "Prediction of electric vehicle range: A comprehensive review of current issues and challenges," *Energies*, vol. 12, no. 5, p. 946, 2019.

[28] A. Donkers, D. Yang, and M. Viktorović, "Influence of driving style, infrastructure, weather and traffic on electric vehicle performance," *Transportation research part D: transport and environment*, vol. 88, p. 102 569, 2020.

[29] C. Suarez and W. Martinez, "Fast and ultra-fast charging for battery electric vehicles–a review," in *2019 IEEE Energy Conversion Congress and Exposition (ECCE)*, IEEE, 2019, pp. 569–575.

[30] M. A. Melliger, O. P. van Vliet, and H. Liimatainen, "Anxiety vs reality–sufficiency of battery electric vehicle range in switzerland and finland," *Transportation Research Part D: Transport and Environment*, vol. 65, pp. 101–115, 2018.

[31] C. J. Meinrenken, Z. Shou, and X. Di, "Using gps-data to determine optimum electric vehicle ranges: A michigan case study," *Transportation Research Part D: Transport and Environment*, vol. 78, p. 102 203, 2020.

[32] M. M. Mahfouz and M. R. Iravani, "Grid-integration of battery-enabled dc fast charging station for electric vehicles," *IEEE Transactions on Energy Conversion*, vol. 35, no. 1, pp. 375–385, 2019.

[33] J. Jaguemont, M. Abdel-Monem, N. Omar, J. Van Mierlo, and P. Van Den Bossche, "Thermal effect of fast-charging profiles on lithium-ion batteries," in *2018 21st International Conference on Electrical Machines and Systems (ICEMS)*, IEEE, 2018, pp. 2127–2132.

[34] M. Keyser, A. Pesaran, Q. Li, *et al.*, "Enabling fast charging–battery thermal considerations," *Journal of Power Sources*, vol. 367, pp. 228–236, 2017.

[35] J. Jaguemont, L. Boulon, P. Venet, Y. Dubé, and A. Sari, "Lithium-ion battery aging experiments at subzero temperatures and model development for capacity fade estimation," *IEEE Transactions on Vehicular Technology*, vol. 65, no. 6, pp. 4328–4343, 2015.

[36] J. Jeffs, "An investigation into the optimal operation of a complex heat pump for the complete thermal management of an electric vehicle in cold climates," Ph.D. dissertation, University of Warwick, 2019.

[37] M. R. Amini, H. Wang, X. Gong, D. Liao-McPherson, I. Kolmanovsky, and J. Sun, "Cabin and battery thermal management of connected and automated hevs for improved energy efficiency using hierarchical model predictive control," *IEEE Transactions on Control Systems Technology*, vol. 28, no. 5, pp. 1711–1726, 2019.

[38] B. Chen, X. Li, S. A. Evangelou, and R. Lot, "Joint propulsion and cooling energy management of hybrid electric vehicles by optimal control," *IEEE Transactions on Vehicular Technology*, vol. 69, no. 5, pp. 4894–4906, 2020.

[39] M. A. Hannan, M. M. Hoque, A. Hussain, Y. Yusof, and P. J. Ker, "State-of-the-art and energy management system of lithium-ion batteries in electric vehicle applications: Issues and recommendations," *Ieee Access*, vol. 6, pp. 19 362–19 378, 2018.

[40] C. Zhu, F. Lu, H. Zhang, and C. C. Mi, "Robust predictive battery thermal management strategy for connected and automated hybrid electric vehicles based on thermoelectric parameter uncertainty," *IEEE Journal of Emerging and Selected Topics in Power Electronics*, vol. 6, no. 4, pp. 1796–1805, 2018.

[41] M. J. Moran, H. N. Shapiro, D. D. Boettner, and M. B. Bailey, *Fundamentals of engineering thermodynamics*. John Wiley & Sons, 2010.

[42] B. Chen, C. Wulff, K. Etzold, *et al.*, "A comprehensive thermal model for system-level electric drivetrain simulation with respect to heat exchange between components," in *2020 19th IEEE Intersociety Conference on Thermal and Thermomechanical Phenomena in Electronic Systems (ITherm)*, IEEE, 2020, pp. 558–567.

[43] O. Lindgärde, M. Söderman, A. Tenstam, and L. Feng, "Optimal complete vehicle control for fuel efficiency," *Transportation Research Procedia*, vol. 14, pp. 1087–1096, 2016.

[44] E. Hellström, M. Ivarsson, J. Åslund, and L. Nielsen, "Look-ahead control for heavy trucks to minimize trip time and fuel consumption," *Control Engineering Practice*, vol. 17, no. 2, pp. 245–254, 2009.

[45] B. Passenberg, P. Kock, and O. Stursberg, "Combined time and fuel optimal driving of trucks based on a hybrid model," in *European Control Conference*, Budapest, Hungary, 2009, pp. 4955–4960.

[46] N. Murgovski, B. Egardt, and M. Nilsson, "Cooperative energy management of automated vehicles," *Control Engineering Practice*, vol. 57, pp. 84–98, 2016.

[47] H. Rakha and R. K. Kamalanathsharma, "Eco-driving at signalized intersections using v2i communication," in *2011 14th international IEEE conference on intelligent transportation systems (ITSC)*, IEEE, 2011, pp. 341–346.

[48] G. Heppeler, M. Sonntag, and O. Sawodny, "Fuel efficiency analysis for simultaneous optimization of the velocity trajectory and the energy management in hybrid electric vehicles," *IFAC Proceedings Volumes*, vol. 47, no. 3, pp. 6612–6617, 2014.

[49] S. Sager, *Numerical methods for mixed-integer optimal control problems*. Der Andere Verlag Lübeck, 2005.

[50] L. N. Vicente and P. H. Calamai, "Bilevel and multilevel programming: A bibliography review," *Journal of Global optimization*, vol. 5, no. 3, pp. 291–306, 1994.

[51] E. F. Camacho and C. B. Alba, *Model predictive control*. Springer science & business media, 2013.

[52] L. S. Pontryagin, V. G. Boltyanskii, R. V. Gamkrelidze, and E. F. Mishchenko, *The Mathematical Theory of Optimal Processes*. Interscience Publishers, 1962.

[53] P. T. Boggs and J. W. Tolle, "Sequential quadratic programming," *Acta numerica*, vol. 4, pp. 1–51, 1995.

[54] M. Diehl, "Real-time optimization for large scale nonlinear processes," Ph.D. dissertation, University of Heidelberg, 2001.

[55] R. Bellman, *Dynamic Programming*. New Jersey: Princeton Univ Pr, 1957.

[56] R. Goebel, R. G. Sanfelice, and A. R. Teel, "Hybrid dynamical systems," *IEEE control systems magazine*, vol. 29, no. 2, pp. 28–93, 2009.

[57] S. Uebel, N. Murgovski, B. Baker, and J. Sjoberg, "A 2-level MPC for energy management including velocity control of hybrid electric vehicle," *IEEE Transactions on Vehicular Technology*, 2019.

[58] X. Zhang, L. Guo, N. Guo, Y. Zou, and G. Du, "Bi-level energy management of plug-in hybrid electric vehicles for fuel economy and battery lifetime with intelligent state-of-charge reference," *Journal of Power Sources*, vol. 481, p. 228 798, 2021.

[59] T. Liu and X. Hu, "A bi-level control for energy efficiency improvement of a hybrid tracked vehicle," *IEEE Transactions on Industrial Informatics*, vol. 14, no. 4, pp. 1616–1625, 2018.

[60] M. Khodabakhshian, L. Feng, S. Börjesson, O. Lindgärde, and J. Wikander, "Reducing auxiliary energy consumption of heavy trucks by onboard prediction and real-time optimization," *Applied Energy*, vol. 188, pp. 652–671, 2017.

[61] T. Liu, "Computationally efficient energy management for a hybrid electric racing car by binary model predictive control and pontryagin's minimum principle," in *34th International Electric Vehicle Symposium and Exhibition (EVS34)*, AVERE. European Association for Battery, Hybrid and Fuel Cell Electric Road ..., 2021.

[62] A. Ritter, F. Widmer, P. Duhr, and C. H. Onder, "Long-term stochastic model predictive control for the energy management of hybrid electric vehicles using pontryagin's minimum principle and scenario-based optimization," *Applied Energy*, vol. 322, p. 119 192, 2022.

[63] G. P. Incremona and P. Polterauer, "Design of a switching nonlinear mpc for emission aware ecodriving," *IEEE Transactions on Intelligent Vehicles*, 2022.

[64] F. Ma, Y. Yang, J. Wang, *et al.*, "Eco-driving-based cooperative adaptive cruise control of connected vehicles platoon at signalized intersections," *Transportation Research Part D: Transport and Environment*, vol. 92, p. 102 746, 2021.

[65] Z. Nie and H. Farzaneh, "Role of model predictive control for enhancing eco-driving of electric vehicles in urban transport system of japan," *Sustainability*, vol. 13, no. 16, p. 9173, 2021.

[66] Q. Hu, M. R. Amini, I. Kolmanovsky, J. Sun, A. Wiese, and J. B. Seeds, "Multihorizon model predictive control: An application to integrated power and thermal management of connected hybrid electric vehicles," *IEEE Transactions on Control Systems Technology*, vol. 30, no. 3, pp. 1052–1064, 2021.

[67] Q. Hu, M. R. Amini, A. Wiese, J. B. Seeds, I. Kolmanovsky, and J. Sun, "A multirange vehicle speed prediction with application to model predictive control-based integrated power and thermal management of connected hybrid electric vehicles," *Journal of Dynamic Systems, Measurement, and Control*, vol. 144, no. 1, 2022.

[68] E. Hellström, J. Åslund, and L. Nielsen, "Management of kinetic and electric energy in heavy trucks," *SAE International Journal of Engines*, vol. 3, no. 1, pp. 1152–1163, 2010.

[69] T. van Keulen, B. de Jager, D. Foster, and M. Steinbuch, "Velocity trajectory optimization in hybrid electric trucks," in *American Control Conference*, Marriott Waterfront, Baltimore, MD, USA, 2010, pp. 5074–5079.

[70] T. van Keulen, B. de Jager, and M. Steinbuch, "Optimal trajectories for vehicles with energy recovery options," in *IFAC World Congress*, Milan, Italy, 2011, pp. 3831–3836.

[71] M. Held, "Fuel-efficient look-ahead control for heavy-duty vehicles with varying velocity demands," Ph.D. dissertation, KTH Royal Institute of Technology, 2020.

[72] P. Duhr, G. Christodoulou, C. Balerna, M. Salazar, A. Cerofolini, and C. H. Onder, "Time-optimal gearshift and energy management strategies for a hybrid electric race car," *Applied Energy*, vol. 282, p. 115 980, 2021.

[73] W. R. Hamilton, "On a general method in dynamics," *Philosophical Transactions of the Royal Society*, vol. 2, pp. 247–308, 1834.

[74] ——, "Second essay on a general method in dynamics," *Philosophical Transactions of the Royal Society*, vol. 1, pp. 95–144, 1835.

[75] Z. Khalik, G. Padilla, T. Romijn, and M. Donkers, "Vehicle energy management with ecodriving: A sequential quadratic programming approach with dual decomposition," in *2018 Annual American Control Conference (ACC)*, IEEE, 2018, pp. 4002–4007.

[76] C. Zhang, Y. Zhang, Z. Huang, *et al.*, "Real-time optimization of energy management strategy for fuel cell vehicles using inflated 3d inception long short-term memory network-based speed prediction," *IEEE Transactions on Vehicular Technology*, vol. 70, no. 2, pp. 1190–1199, 2021.

[77] M. Diehl, H. G. Bock, and J. P. Schlöder, "A real-time iteration scheme for nonlinear optimization in optimal feedback control," *SIAM Journal on control and optimization*, vol. 43, no. 5, pp. 1714–1736, 2005.

[78] J. V. Frasch, A. Gray, M. Zanon, *et al.*, "An auto-generated nonlinear mpc algorithm for real-time obstacle avoidance of ground vehicles," in *2013 European Control Conference (ECC)*, IEEE, 2013, pp. 4136–4141.

[79] E. Hellström, J. Åslund, and L. Nielsen, "Design of an efficient algorithm for fuel-optimal look-ahead control," *Control Engineering Practice*, vol. 18, no. 11, pp. 1318–1327, 2010.

[80] W. Dib, L. Serrao, and A. Sciarretta, "Optimal control to minimize trip time and energy consumption in electric vehicles," in *2011 IEEE Vehicle Power and Propulsion Conference*, IEEE, 2011, pp. 1–8.

[81] G. Heppeler, M. Sonntag, U. Wohlhaupter, and O. Sawodny, "Predictive planning of optimal velocity and state of charge trajectories for hybrid electric vehicles," *Control Engineering Practice*, vol. 61, pp. 229–243, 2016.

[82] H.-G. Wahl, K.-L. Bauer, F. Gauterin, and M. Holzäpfel, "A real-time capable enhanced dynamic programming approach for predictive optimal cruise control in hybrid electric vehicles," in *16th International IEEE Conference on Intelligent Transportation Systems (ITSC 2013)*, IEEE, 2013, pp. 1662–1667.

[83] L. Bühler, *Fuel-efficient platooning of heavy duty vehicles through road topography preview information*, 2013.

[84] R. Zhang and Y. Chen, "Control of hybrid dynamical systems for electric vehicles," in *Proceedings of the 2001 American Control Conference.(Cat. No. 01CH37148)*, IEEE, vol. 4, 2001, pp. 2884–2889.

[85] H. F. Ghavidel and A. A. Kalat, "Robust control for mimo hybrid dynamical system of underwater vehicles by composite adaptive fuzzy estimation of uncertainties," *Nonlinear Dynamics*, vol. 89, no. 4, pp. 2347–2365, 2017.

[86] X. Fu, Q. Zhang, C. Wang, and J. Tang, "Torque coordination control of hybrid electric vehicles based on hybrid dynamical system theory," *Electronics*, vol. 8, no. 6, p. 712, 2019.

[87] H. Banvait, J. Hu, and Y. Chen, "Energy management control of plug-in hybrid electric vehicle using hybrid dynamical systems," *IEEE Transactions on Intelligent Transportation Systems*, 2013.

Part II

Papers

PAPER A

Time optimal and eco-driving mission planning under traffic constraints

Ahad Hamednia, Nikolce Murgovski, and Jonas Fredriksson

23rd *IEEE International Conference on Intelligent Transportation Systems (ITSC)*

The layout has been revised.

Abstract

This paper addresses optimising a transport mission by controlling the mission start time and velocity profile of an electric vehicle (EV) driving in a hilly terrain, subject to legal and dynamic speed limits imposed by traffic congestion. To this end, a nonlinear program (NLP) is formulated, where the mission start time is allowed to vary within an interval and final time is kept free. The goal is to find the optimal trade-off between energy consumption and travel time, while allowing a flexibility in starting time and a certain variation of vehicle speed around an average. It is observed that total travel time is reduced up to 5.5% by adjusting the mission start time, when keeping an average cruising speed of about 75 km/h.

1 Introduction

Transportation plays an important role in the current global trade system, where the demand for transportation is highly connected to economic development. Particularly, road transportation's influence in the economy is crucial, since it includes nearly 60 % of all surface freight transportation [1]. Although the road transportation positively contributes to the economy, it is facing serious challenges, e.g. increasing energy consumption and CO_2 emissions.

In order to alleviate the destructive consequences from ever-growing CO_2 emissions, one promising alternative for future transportation systems is to electrify the vehicles ranging from hybrid to fully electric [2]. Furthermore, time loss due to traffic congestion is an additional negative side effect of the road transportation that greatly costs the society. The traffic congestion cost is estimated to $115 billion over 439 urban areas of the United States in 2010 [3]. Thus, there is a strong motivation to achieve a sustainable transportation system by improving transport efficiency, which can be interpreted as providing a service with less consumption of resources and not losing logistics performance, i.e. costs and delivery service [4].

Logistics service providers are considered among major actors that are involved in increasing the transport efficiency. *The service providers can optimally plan the transport mission by controlling the mission start time and*

following the principles of energy-efficient driving, referred to as eco-driving [5]–[7]. To achieve eco-driving it is necessary to optimally plan the velocity profile of a vehicle, subject to road and traffic flow information. One important factor in optimising the velocity profile is the knowledge about speed limits, which are imposed by not only legal speed limits, but also dynamic constraints [8], [9]. For instance, surrounding traffic sets such dynamic constraints due to presence of e.g. traffic lights, intersections, ramps and junctions. Another example that dynamically affects the speed limits is the linking of two or more trucks in convoy in order to increase the energy efficiency [10]. The dynamic speed limits make the travel time to be time-dependent, since the optimised speed can vary depending on time of the day [11].

In case of driving in a hilly terrain, preferably the optimal velocity varies within a bound, which originates from the legal and dynamic speed limits and the utilization of the road topography, i.e. the vehicle accelerates when driving downhill and decelerates when climbing uphill. This leads to less waste of non-recuperable energy compared to driving with constant speed [12]. To implement such behaviour over complex road topographies, advanced control strategies [13] could be employed that maximise energy efficiency by optimal coordination of energy sources, using information of the road topography and traffic flow.

Among the optimal control strategies, dynamic programming (DP) [14], which can handle mixed-integer, non-convex and nonlinear optimisation problems, is the most commonly used algorithm to optimise the velocity profile of a vehicle. For instance, information about the road topography ahead is used to optimise the velocity profile using DP in [15] to minimize fuel consumption and travel time.

Although DP is a powerful tool in solving optimal control problems, its main drawback is so-called *curse of dimensionality*, which refers to exponential increase in computational time with the increase in problem dimension [14]. The high computation burden due to using DP can be reduced by employing a heuristic method, which priorities exploring to the most promising solutions, utilizing the knowledge about considered problem [16]. As an alternative approach to DP, Pontryagin's Maximum Principle (PMP) [17] has been widely applied to the velocity optimisation of vehicles, especially in order to tackle the computational complexity due to high-dimensional optimisation problems. An algorithm for optimising the velocity profile is proposed in [18]

incorporating gear shifting, road grade constraints and speed limits. Necessary optimality conditions as stated by the PMP have been exploited in the well known equivalent consumption minimisation strategy (ECMS) to optimally manage energy flows in hybrid electric vehicles [19]. ECMS provides computational advantages by converting the optimisation problem to a two-point boundary-value program. However, for problems where states' bounds are frequently activated, multiple-shooting techniques are preferred, where the problem is directly transcribed to a nonlinear program (NLP) [20].

A combination of DP and other approaches for optimal control of vehicles have also been investigated. In [21]–[23], a mixture of DP and (sequential) convex optimisation is developed, where integer decisions, e.g. gear selection, are optimised by DP and real-valued decisions are taken by sequential convex optimisation. A PMP-DP method has been proposed in [24] to optimally plan the vehicle speed, gear selection, battery energy and ICE on/off state.

The combination of eco-driving and start time of the vehicle's mission by considering the dynamic speed limits is not addressed in the technical literature. This paper formulates a nonlinear program (NLP), which aims at optimal planning of the transport mission on long horizons that possibly stretches up to 100 km. The goal is to find a possible solution for energy-efficient driving considering both legal and dynamic speed limits, where the mission start time is allowed to vary within certain bounds. The method is demonstrated and applied on electric vehicle (EV) example.

2 Vehicle modelling

This section addresses modelling of the dynamics of an EV as a lumped mass, characteristics of EM and transmission system, and driving mission.

2.1 Travel time and longitudinal dynamics

Consider a vehicle driving on a planned route with a hilly terrain, where the vehicle does not stop or change direction of movement. This allows choosing travel distance, s, as an independent variable instead of travel time, t, i.e. decisions are taken with respect to s. The reason for such transformation is to alleviate high computational complexity due to nonlinearity in resistive force originating from roll resistance, which is shown in the following. Similar

transformations in the governing equations of the vehicle are done in [25]–[27] and references therein. Thus, the dynamics on travel time is

$$t'(s) = \frac{1}{v(s)}, \tag{A.1}$$

where v is longitudinal velocity.

Longitudinal dynamics of the vehicle, according to the Newton's law of motion, is

$$\mathrm{m}v(s)v'(s) = F(s) + F_{\mathrm{brk}}(s) - F_{\mathrm{air}}(v) - F_{\alpha}(s), \tag{A.2}$$

where $v' = \mathrm{d}v/\mathrm{d}s$ is the space derivative and $vv' = \mathrm{d}v/\mathrm{d}t$ denotes the longitudinal acceleration. Also, m is total lumped mass of the vehicle, F is EM force at the wheel side of the vehicle generated by the EM, and F_{brk} is non-positive mechanical braking force. The nominal aerodynamic drag, F_{air}, and the roll resistance, $F_{\alpha}(s)$, are defined as

$$F_{\mathrm{air}}(v) = \frac{\rho_{\mathrm{a}} \mathrm{c_d} \mathrm{A_f} v^2}{2}, \tag{A.3}$$

$$F_{\alpha}(s) = \mathrm{mg}\left(\sin(\alpha(s)) + \mathrm{c_r}\cos(\alpha(s))\right), \tag{A.4}$$

where α is road inclination, ρ_{a} is air density, $\mathrm{c_d}$ is aerodynamic drag coefficient, $\mathrm{A_f}$ is frontal area of the vehicle, g is the gravitational acceleration, and $\mathrm{c_r}$ is rolling resistance coefficient. Throughout this paper, all constants that are not dependent on s are displayed in upright letters, e.g. m, does not depend on s. Also, the dependency on s of the variables that are trajectories in terms of s, e.g. $F(s)$, is not shown in several places for simplicity.

2.2 Electric machine and transmission system

A schematic diagram of the studied fully electric powertrain is demonstrated in Fig. 1. The powertrain includes an electric battery as an energy storage unit, an EM, and a transmission system. The torque and rotational speed at the shaft between the electric machine and transmission are represented by M and ω, respectively.

The EM is represented using a steady-state model. The steady-state efficiency map of the EM for a given pair of rotational speed and torque is

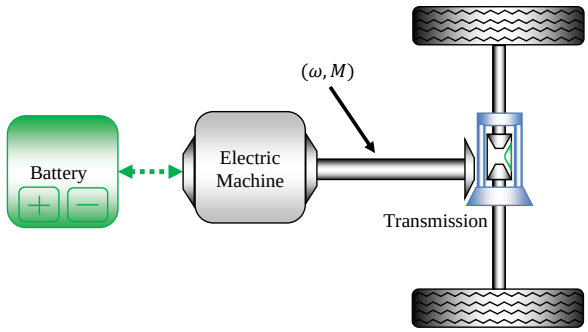

Figure 1: Schematic diagram of a fully electric powertrain. The powertrain consists of electric battery as energy storage unit, electric machine and transmission system, which transfers shaft torque, M, with rotating speed ω.

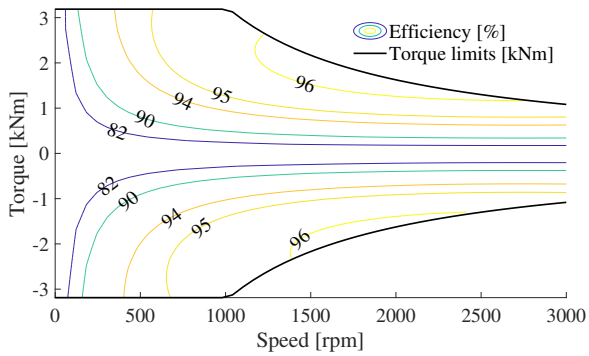

Figure 2: Steady-state efficiency map and torque limits of the electric machine.

shown in Fig. 2, where positive and negative torque regions correspond to the motoring and the generating modes of operation, respectively.

The transmission system for the studied powertrain is solely a final gear ratio, which translates the shaft torque and rotational speed to the EM force and longitudinal velocity respectively, as

$$F(s) = \frac{M(s)}{R}, \quad v(s) = \omega(s)R, \quad R = \frac{\mathrm{r_w}}{\mathrm{r_{fg}}} \tag{A.5}$$

where γ denotes selected gear, $\mathrm{r_w}$ is wheel radius and $\mathrm{r_{fg}}$ is final gear ratio respectively.

2.3 Driving mission

We describe a driving mission by a map of maximum dynamic speed limits for a given pair of travel distance and time of day, as given in Figure. 6.3(a) and the associated road topography, see Figure. 6.3(b). Figure. 6.3(a) includes a contour plot, where the lighter the contour color is, the greater the vehicle speed is. Figure. 6.3(b) is a double y-axis plot, where the left y-axis corresponds to the vehicle speed and the right axis is the road altitude, while the gray area represents the road topography. According to the max speed map, the vehicle's mission, characterised as the mission start time, total travel time and velocity profile, can be tailored in favour of the improved energy efficiency. One execution of the mission in terms of speed/time trajectory is also shown in Figure. 3, where the vehicle starts the mission at 10:00. It can be seen that the traffic speed drops to about 30 km/h in the congested area, at travel distance of about 25 km.

3 Problem statement

In this section an optimisation problem is formulated, which aims at planning optimal velocity trajectory for the entire mission, in a way that total energy consumption is minimised and the travel time is adjusted by a penalty factor. Note that the travel time at initial position of the route is not fixed, but is allowed to vary within a bound. Final travel time is kept free.

Based on the models derived in the previous section, the energy optimization problem can be formulated as:

$$\min_{F,F_{\mathrm{brk}}} \lambda_{\mathrm{t}} \left(t(\mathrm{s_f}) - t(\mathrm{s_0})\right) + \int_{\mathrm{s_0}}^{\mathrm{s_f}} \frac{P_{\mathrm{b}}(v,F)}{v(s)} \mathrm{d}s \tag{A.6a}$$

subject to:

$$t'(s) = \frac{1}{v(s)} \tag{A.6b}$$

$$\mathrm{m}v(s)v'(s) = F(s) + F_{\mathrm{brk}}(s) - F_{\mathrm{air}}(v) - F_{\alpha}(s) \tag{A.6c}$$

$$v(s) \in [v_{\min}(s,t), v_{\max}(s,t)] \tag{A.6d}$$

$$F(s) \in [F_{\min}(v), F_{\max}(v)] \tag{A.6e}$$

$$F_{\mathrm{brk}}(s) \leq 0 \tag{A.6f}$$

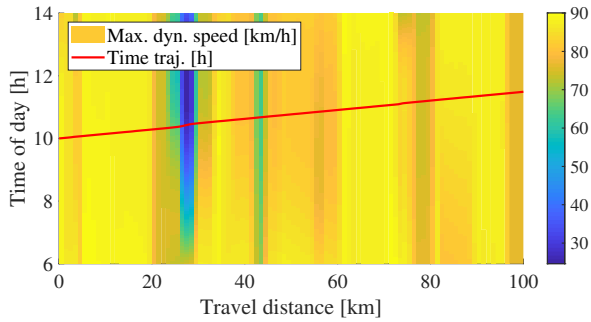

(a) Map of maximum dynamic speed limits together with one execution of the driving mission in terms of time trajectory.

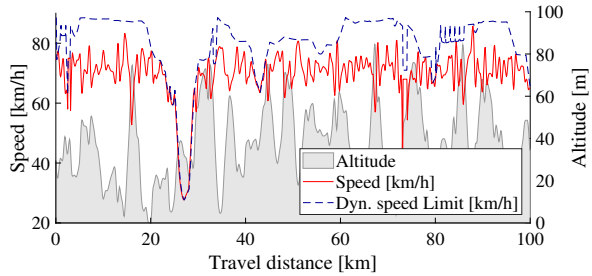

(b) Road topography with hilly terrain together with one execution of the driving mission in terms of longitudinal velocity and maximum dynamic speed limit.

Figure 3: Maximum dynamic speed limits map for a given pair of travel distance and time of day, together with associated road topography and one execution of the driving mission.

$$t(\mathrm{s}_0) \in [\mathrm{t}_0^{\min}, \mathrm{t}_0^{\max}], \quad v(\mathrm{s}_0) = \mathrm{v}_0 \tag{A.6g}$$

where $\mathrm{t}_0^{\min}$ is the minimum and $\mathrm{t}_0^{\max}$ is the maximum allowed initial time, and v_0 is initial longitudinal velocity. The longitudinal velocity limits including legal speed limits and dynamics constraints are shown by $v_{\min}(s,t)$ and $v_{\max}(s,t)$. Also, $F_{\min}(v)$ and $F_{\max}(v)$ represent the EM force limits for a given longitudinal velocity. In (A.6a), s_0 and s_f are initial and final positions of the driving vehicle respectively, and λ_t is a coefficient for penalising the travel time. The division of the battery power with speed in (A.6a) is obtained from

the time to space transformation, i.e.

$$\int P_{\mathrm{b}}(v, F)\mathrm{d}t = \int P_{\mathrm{b}}(v, F)/v(s)\,\mathrm{d}s.$$

The constraints (A.6b)-(A.6f) are enforced for all $s \in [\mathrm{s}_0, \mathrm{s}_\mathrm{f}]$. Problem (A.6) has two states, t and v, and two control inputs, F and F_{brk}.

4 Smooth nonlinear programming

In this paper we define an NLP to be smooth if it is not mixed-integer. On the other hand, if the program is non-smooth, i.e. it is mixed-integer NLP, then there is at least one non-smooth or discontinuous function in the program with unbounded derivative. Accordingly, the direction in which the function is decreasing (or increasing) cannot generally be determined by using its derivative or gradient information. Thus, having one feasible solution provides very little information about how to search for a better solution, which makes the NLP extremely difficult to solve. Therefore, there is a strong motivation to model the non-smooth functions within an optimisation program by smooth or piece-wise smooth functions to alleviate the computational complexity.

The limits on longitudinal velocity (A.6d) and EM force (A.6e) may not be smooth functions. Such problems may generally be solved with DP, with the cost of high computation effort, which is exponential in the number of system states. In addition to the two system states, travel time and longitudinal velocity, having free initial and final time requires solving DP in an additional loop, which is computationally equivalent to having a 3rd state in the problem. Moreover, the problem may need to be solved multiple times, for different values of the time penalty factor, or may involve additional states to model driving comfort. Thus, there is a strong incentive to solve problem (A.6) in a computationally efficient way. To this end, the EM force limits are modeled as piecewise functions, where each of the pieces is a smooth function, and speed limits are approximated by smooth functions. This allows the problem to be translated to a smooth NLP that can be solved efficiently with Newton-based methods.

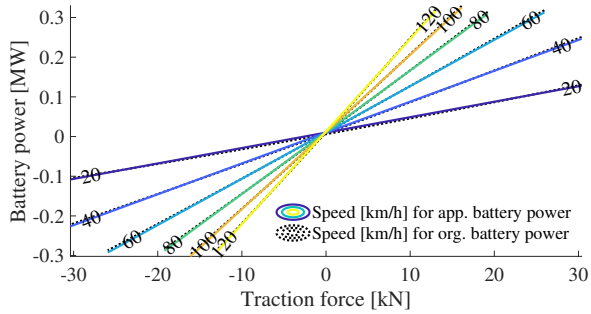

Figure 4: Measured and modelled electric battery power for a given longitudinal velocity and EM force.

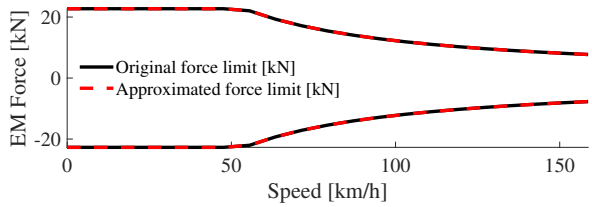

Figure 5: Measured and modelled EM force limits of the EM.

Electric battery power is modeled as

$$\begin{aligned} P(v,F) \approx \mathrm{p}_0 + \mathrm{p}_1 v(s) + \mathrm{p}_2 v^3(s) + \mathrm{p}_3 v^5(s) + \\ + \mathrm{p}_4 v(s) F(s) + \mathrm{p}_5 v(s) F^2(s), \end{aligned} \tag{A.7}$$

with $\mathrm{p}_0, \mathrm{p}_1, \mathrm{p}_2, \mathrm{p}_3, \mathrm{p}_4, \mathrm{p}_5 \geq 0$. Fig. 4 shows that the model fits well original steady-state measurements.

The EM force limits are modelled as piecewise functions

$$F_{\min}(v) \approx \max\left\{\underline{F}, \mathrm{x}_0 + \frac{\mathrm{x}_1}{v(s)}\right\} \tag{A.8}$$

$$F_{\max}(v) \approx \min\left\{\overline{F}, \mathrm{y}_0 + \frac{\mathrm{y}_1}{v(s)}\right\} \tag{A.9}$$

where $\underline{F}$ is constant minimum and $\overline{F}$ is constant maximum EM force, while the coefficients x_1 and y_1 denote maximum and minimum power limits. An illustration of the modelled and measured force limits is given in Fig. 5.

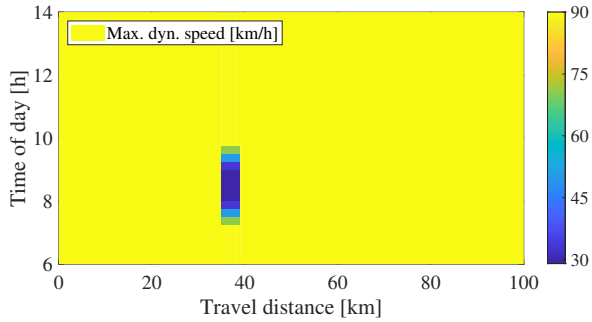

Figure 6: Map of maximum dynamic speed limits, a simple scenario.

The maximum speed limit is computed as the minimum between the maximum legal speed limit, $v_{\max}^{\text{lg}}$, and maximum dynamic speed limit that is modelled as a sum of sigmoidal functions

$$v_{\max}(s,t) = \min\left(v_{\max}^{\text{lg}}(s), \sum_i \frac{a_i(s)}{1+e^{b_i(s)t+c_i(s)}}\right), \tag{A.10}$$

using traffic information. The proposed model for maximum dynamic speed limit gives the flexibility to model flat regions, as well as steep and shallow transitions. Here, $a_i(s)$, $b_i(s)$ and $c_i(s)$ are distance dependant coefficients. Our analyses showed that (A.10) is able to model many realistic scenarios, but the proposed method can identically be applied for other functions, as long as the smoothness of the NLP (A.6) is preserved.

5 Case study and results

In this section, optimal planning of a driving mission is investigated for a particular case study. An EV is driving in a 100 km long hilly terrain, as illustrated in Fig. 6.3(b), subject to a legal speed limit of 90 km/h. For pedagogical purposes, a simple scenario is considered with a single traffic jam, occurring at about 35 km, see Fig. 6. The traffic jam imposes dynamic speed limits, which depend on the time of the day, may constrain EV speed down to 30 km/h. Vehicle and simulation parameters are given in Table 1.

The resulting NLP (A.6) is discretized using the forward Euler method with a sampling interval of 400 m. It is then solved in Matlab with the solver

Table 1: Simulation parameters

Gravitational acceleration	$g = 9.81\,m/s^2$
Air density	$\rho = 1.29\,kg/m^3$
Vehicle frontal area	$A_f = 10\,m^2$
Rolling resistance coefficient	$c_r = 0.006$
Vehicle mass	$m = 40\,000\,kg$
Aerodynamic drag coefficient	$c_d = 0.5$
Wheel radius	$r_w = 0.50\,m$
Final gear ratio	$r_{fg} = 3$
Cruising set speed	$v_{cru} = 75\,km/h$
Route length	$100\,km$
Number of samples	$N = 250$

IPOPT using the open source optimisation tool CasADi [28]. To alleviate computational complexity due to nonlinearity in terms of the longitudinal velocity in (A.3), kinetic energy, $E(s)$, is used instead of longitudinal velocity, as proposed in [27], using the one-to-one relation

$$E(s) = \frac{m v^2(s)}{2}. \tag{A.11}$$

The NLP is warm-started by providing an initial guess, further detailed in Appendix 1.

5.1 Choosing penalty factor for travel time

Penalising total travel time in (A.6a) strongly influences the electrical energy consumption. To investigate this, problem (A.6) is solved for a wide range of the time penalty factor, where the mission start time is allowed to vary within half-hour time intervals starting from 6:30. Fig. 7 shows a contour plot of upper bound on each half-hour mission start time for a given combination of the consumed electrical energy and total travel time. It is observed that there is a trade-off between the electrical energy consumption and travel time, i.e. by increasing the penalty factor, the travel time decreases, but it leads to higher electricity use. Unsurprisingly, the curves of electricity use versus travel time overlap for the start time intervals of 6:30-7:00 and 9:00-9:30, since the vehicle

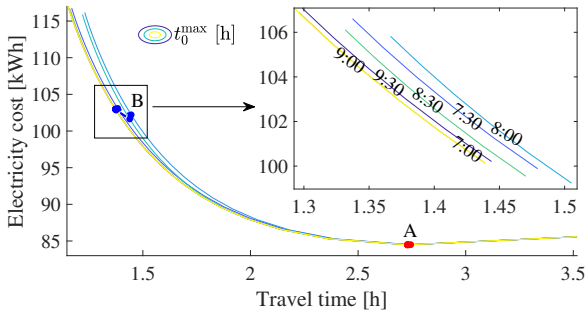

Figure 7: Contour plot of upper bound on each half-hour start time interval for a given pair of travel time and electricity use.

never encounters the traffic jam in either cases. The demonstrated profile in Fig. 7, provides promising information for e.g. logistics service managers, who have wide range of choices to customise the vehicle's mission. In this profile, the region A corresponds to $\lambda_t = 0$, i.e. the most energy efficient driving. By letting the penalty factor be negative, it is possible to further increase travel time, which will actually cause increase in energy consumption. This implies that there is a low speed threshold, here about 35 km/h, below which the benefit of reduced air drag is negated by the increased time of accumulating powertrain losses.

Region B in Fig. 7 corresponds to a positive penalty factor that results in keeping an average cruising speed of about $v_{cru} = 75$ km/h when traffic jam is avoided. For the remaining results in this paper, we use the time penalty factor that enables operation in region B. Optimal time trajectory for the region B, for each interval of the mission start time, is depicted in Fig. 8. It is observed that by applying the proposed algorithm, the vehicle tries to avoid the low speed area. The gray areas correspond to the infeasible time regions. The travel distance in Fig. 8 is divided into three segments; (1): before traffic congestion, (2): during traffic congestion and (3): after traffic congestion. The mean optimal speed values per each distance segment and mission start time interval together with electrical energy use and travel time are given in Table 2. For instance, by comparing the results of the intervals 6:30-7:00 and 7:30-8:00, travel time is reduced by 5.5%, when the mission starts at 6:30 instead of 8:00.

As an example, optimal longitudinal velocity profiles for the start time

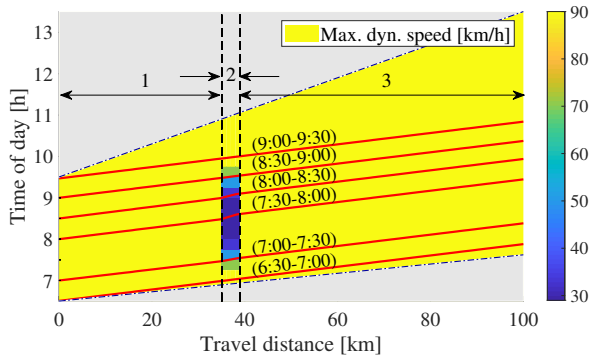

Figure 8: Optimal time trajectories for each mission start time interval; corresponding to region B.

Table 2: Mean optimal speed for given road segment and time interval together with electricity use and travel time, region B.

Start time interval	$\overline{v}_1$ [km/h]	$\overline{v}_2$ [km/h]	$\overline{v}_3$ [km/h]	Elec. [kWh]	Travel time [h]
6:30-7:00	73.07	74.00	73.08	102.99	1.37
7:00-7:30	75.34	55.75	73.08	103.09	1.38
7:30-8:00	72.92	40.33	73.08	102.22	1.45
8:00-8:30	70.93	45.27	73.08	101.64	1.44
8:30-9:00	72.93	71.64	73.08	102.86	1.38
9:00-9:30	73.07	74.00	73.08	102.99	1.37

intervals of 6:30-7:00 and 7:00-7:30 are shown in Fig. 9, together with their corresponding guess velocity profiles. It is observed that for the interval of 7:00-7:30 the vehicle speeds up in the first distance segment compared to the interval of 6:30-7:00 to avoid the traffic congestion. Optimal EM force and braking force trajectories are depicted in Fig. 6.10(a). Also, optimal force-speed operating points are given in Fig. 6.10(b). Note that Fig. 9 and Fig. 6.10(a) are shown for zoomed distance segment of 20 km-60 km.

6 Conclusion

In this paper, an NLP is formulated in order to improve the transport efficiency for an EV driving in a hilly terrain, by optimising the velocity profile and

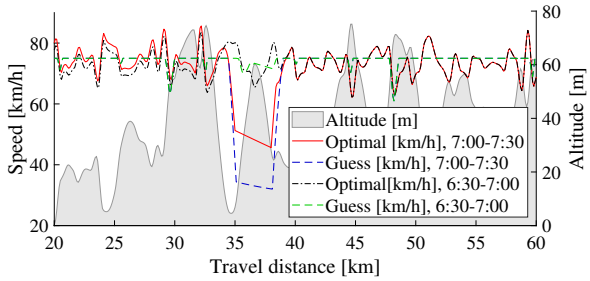

Figure 9: Optimal longitudinal velocity profiles for the start time intervals of 6:30-7:00 and 7:00-7:30 together with their corresponding guess velocity profiles.

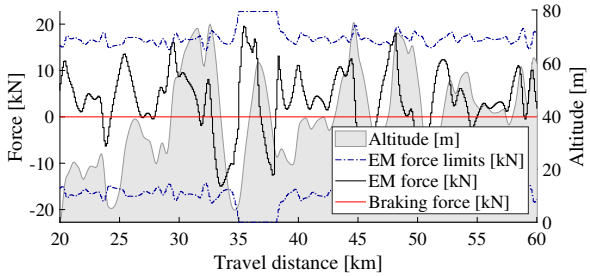

(a) Optimal EM force and braking force trajectories.

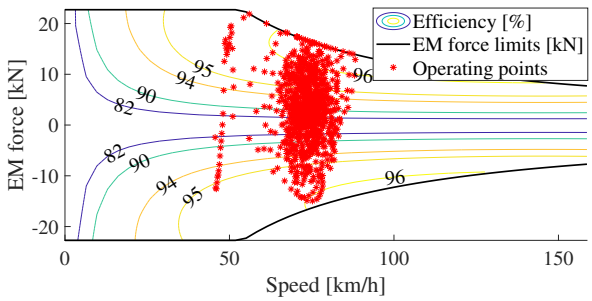

(b) Optimal force-speed points.

Figure 10: Optimal EM force and braking force trajectories together with optimal force-speed points, when the mission start time is allowed to vary over 7:00 to 7:30.

mission start time. To alleviate the computational complexity, non-smooth EM force and dynamic speed limits are modeled by smooth functions. The mission start time is allowed to vary over half-hour intervals starting from 6:30. For pedagogical purposes a scenario with a single traffic jam is studied. According to the simulation results, the proposed algorithm can find a possible solution such that the vehicle avoids the traffic jam.

1 Initial guess for warm-starting

An initial guess of speed limits

$$v^{\mathrm{g}}_{\mathrm{min}}(s,t) = \max\left\{v^{\mathrm{lg}}_{\mathrm{min}}(s), v^{\mathrm{dyn}}_{\mathrm{min}}(s,t)\right\}, \tag{A.12}$$

$$v^{\mathrm{g}}_{\mathrm{max}}(s,t) = \min\left\{v^{\mathrm{lg}}_{\mathrm{max}}(s), v^{\mathrm{dyn}}_{\mathrm{max}}(s,t)\right\}, \tag{A.13}$$

are obtained by considering legal speed limits of the road, $v^{\mathrm{lg}}_{\mathrm{min}}(s)$ and $v^{\mathrm{lg}}_{\mathrm{max}}(s)$, and dynamic speed limits, $v^{\mathrm{dyn}}_{\mathrm{min}}(s,t)$ and $v^{\mathrm{dyn}}_{\mathrm{max}}(s,t)$, for a given pair of travel distance and travel time. To initialize the problem (A.6), a velocity profile, $v_{\mathrm{g}}(s,t) \in [v^{\mathrm{g}}_{\mathrm{min}}(s,t), v^{\mathrm{g}}_{\mathrm{max}}(s,t)]$, can be derived as a guess by filtering cruising speed, $\mathrm{v_{cru}} \in [v^{\mathrm{lg}}_{\mathrm{min}}(s), v^{\mathrm{lg}}_{\mathrm{max}}(s)]$, where the cruising speed can be set manually by driver or automatically by a telemetry system. To compute $v_{\mathrm{g}}(s)$, the rated power of EM and legal/dynamic limits on speed are taken into consideration in filtering the cruise speed [22], i.e. the vehicle will try to maintain $\mathrm{v_{cru}}$ unless EM and/or speed limit is reached.

Let

$$F_{\mathrm{Wmax}}(v) = F_{\mathrm{max}}(v) - F_{\mathrm{air}}(v) - F_{\alpha}(s) \tag{A.14}$$

represent the maximum EM force to be delivered at the wheels, for the vehicle driving at the speed v. The guess longitudinal velocity, $v_{\mathrm{g}}(s)$, and travel time, $t_{\mathrm{g}}(s)$, are computed in discrete space domain using the forward Euler method as in Algorithm 1. In this algorithm, $\mathrm{t_{0g}}$ is a guess for the travel time at the first position, N is number of samples, $\mathrm{a_{max}}$ is the maximum allowed acceleration within a comfort zone, and Δs is the sampling interval.

Algorithm 1 Initial guess for warm-starting.

$t_{\mathrm{g}}^{0} \in [\mathrm{t}_{0}^{\min}, \mathrm{t}_{0}^{\max}]$
$v_{\mathrm{g}}^{0} = \mathrm{v}_{\mathrm{cru}}$
for $\mathrm{k} = 1, \ldots, \mathrm{N}$ **do**
    $v_{\mathrm{g}}^{\mathrm{k}} \leftarrow v_{\mathrm{g}}^{\mathrm{k}-1} + \frac{\Delta s}{v_{\mathrm{g}}^{\mathrm{k}-1}} \min \left\{ \mathrm{a}_{\max},\ \frac{F_{\mathrm{Wmax}}(v_{\mathrm{g}}^{\mathrm{k}-1})}{\mathrm{m}} \right\}$
    $v_{\mathrm{g}}^{\mathrm{k}} \leftarrow \min \left\{ \mathrm{v}_{\mathrm{cru}},\ v_{\mathrm{g}}^{\mathrm{k}} \right\}$
    $t_{\mathrm{g}}^{\mathrm{k}} \leftarrow t_{\mathrm{g}}^{\mathrm{k\text{-}1}} + \frac{\Delta s}{v_{\mathrm{g}}^{\mathrm{k}}}$
    $v_{\mathrm{g}}^{\mathrm{k}} \leftarrow \min \left\{ v_{\mathrm{g}}^{\mathrm{k}},\ v_{\max}^{\mathrm{dyn}}(s, t_{\mathrm{g}}^{\mathrm{k}}) \right\}$
    $t_{\mathrm{g}}^{\mathrm{k}} \leftarrow t_{\mathrm{g}}^{\mathrm{k\text{-}1}} + \frac{\Delta s}{v_{\mathrm{g}}^{\mathrm{k}}}$
end

References

[1] OECD/ITF, "ITF transport outlook 2013," 2013.

[2] S. PELLETIER, O. JABALI, and G. LAPORTE, "Goods distribution with electric vehicles: Review and research perspectives. montrál," Canada, 2014: Technical Report CIRRELT-2014-44, CIRRELT, Tech. Rep., 2014.

[3] D. Schrank, B. Eisele, and T. Lomax, "Tti's 2012 urban mobility report," *Texas A&M Transportation Institute. The Texas A&M University System*, vol. 4, 2012.

[4] H. Aronsson and M. H. Brodin, "The environmental impact of changing logistics structures," *The international journal of logistics management*, 2006.

[5] M. A. S. Kamal, M. Mukai, J. Murata, and T. Kawabe, "Model predictive control of vehicles on urban roads for improved fuel economy," *IEEE Transactions on control systems technology*, vol. 21, no. 3, pp. 831–841, 2012.

[6] M. Vajedi and N. L. Azad, "Ecological adaptive cruise controller for plug-in hybrid electric vehicles using nonlinear model predictive control," *IEEE Transactions on Intelligent Transportation Systems*, vol. 17, no. 1, pp. 113–122, 2015.

[7] Y. Luo, T. Chen, S. Zhang, and K. Li, "Intelligent hybrid electric vehicle acc with coordinated control of tracking ability, fuel economy, and ride comfort," *IEEE Transactions on Intelligent Transportation Systems*, vol. 16, no. 4, pp. 2303–2308, 2015.

[8] M. Held, O. Flärdh, and J. Mårtensson, "Optimal speed control of a heavy-duty vehicle in urban driving," *IEEE Transactions on Intelligent Transportation Systems*, vol. 20, no. 4, pp. 1562–1573, 2018.

[9] R. Basso, P. Lindroth, B. Kulcsár, and B. Egardt, "Traffic aware electric vehicle routing," in *2016 IEEE 19th International Conference on Intelligent Transportation Systems (ITSC)*, IEEE, 2016, pp. 416–421.

[10] A. Alam, B. Besselink, J. Mårtensson, and K. H. Johansson, "Heavy-duty vehicle platooning for sustainable freight transportation: A cooperative method to enhance safety and efficiency," *IEEE Control Systems Magazine*, vol. 35, no. 6, pp. 34–56, 2015.

[11] M. Gendreau, G. Ghiani, and E. Guerriero, "Time-dependent routing problems: A review," *Computers & operations research*, vol. 64, pp. 189–197, 2015.

[12] J. N. Barkenbus, "Eco-driving: An overlooked climate change initiative," *Energy Policy*, vol. 38, no. 2, pp. 762–769, 2010.

[13] A. Sciarretta, G. D. Nunzio, and L. L. Ojeda, "Optimal ecodriving control: Energy-efficient driving of road vehicles as an optimal control problem," *IEEE Control Systems Magazine*, vol. 35, no. 5, pp. 71–90, 2015.

[14] R. Bellman, *Dynamic Programming*. New Jersey: Princeton Univ Pr, 1957.

[15] E. Hellström, M. Ivarsson, J. Åslund, and L. Nielsen, "Look-ahead control for heavy trucks to minimize trip time and fuel consumption," *Control Engineering Practice*, vol. 17, no. 2, pp. 245–254, 2009.

[16] Z. Ajanović, M. Stolz, and M. Horn, "A novel model-based heuristic for energy-optimal motion planning for automated driving," *IFAC-PapersOnLine*, vol. 51, no. 9, pp. 255–260, 2018.

[17] L. S. Pontryagin, V. G. Boltyanskii, R. V. Gamkrelidze, and E. F. Mishchenko, *The Mathematical Theory of Optimal Processes*. Interscience Publishers, 1962.

[18] E. Ozatay, U. Ozguner, and D. Filev, "Velocity profile optimization of on road vehicles: Pontryagin's maximum principle based approach," *Control Engineering Practice*, vol. 61, pp. 244–254, 2017.

[19] A. Rezaei, J. B. Burl, and B. Zhou, "Estimation of the ecms equivalent factor bounds for hybrid electric vehicles," *IEEE Transactions on Control Systems Technology*, vol. 26, no. 6, pp. 2198–2205, 2017.

[20] H. W. Kuhn and A. W. Tucker, "Nonlinear programming," in *Traces and emergence of nonlinear programming*, Springer, 2014, pp. 247–258.

[21] L. Johannesson, M. Nilsson, and N. Murgovski, "Look-ahead vehicle energy management with traffic predictions," in *IFAC Workshop on Engine and Powertrain Control, Simulation and Modeling (E-COSM)*, vol. 48, Columbus, Ohio, USA, 2015, pp. 244–251.

[22] N. Murgovski, B. Egardt, and M. Nilsson, "Cooperative energy management of automated vehicles," *Control Engineering Practice*, vol. 57, pp. 84–98, 2016.

[23] M. Hovgard, O. Jonsson, N. Murgovski, M. Sanfridson, and J. Fredriksson, "Cooperative energy management of electrified vehicles on hilly roads," *Control Engineering Practice*, vol. 73, pp. 66–78, 2018.

[24] S. Uebel, N. Murgovski, C. Tempelhahn, and B. Bäker, "Optimal energy management and velocity control of hybrid electric vehicles," *IEEE Transactions on Vehicular Technology*, vol. 67, no. 1, pp. 327–337, 2017.

[25] B. Saerens, "Optimal control based eco-driving," *Theoretical Approach and Practical Applications. Heverlee: Katholieke Universiteit Leuven*, 2012.

[26] A. Hamednia, N. Murgovski, and J. Fredriksson, "Predictive velocity control in a hilly terrain over a long look-ahead horizon," *IFAC-PapersOnLine*, vol. 51, no. 31, pp. 485–492, 2018.

[27] A. Hamednia, N. K. Sharma, N. Murgovski, and J. Fredriksson, "Computationally efficient algorithm for eco-driving over long look-ahead horizons," *IEEE Transactions on Intelligent Transportation Systems*, 2021.

[28] J. A. Andersson, J. Gillis, G. Horn, J. B. Rawlings, and M. Diehl, "Casadi: A software framework for nonlinear optimization and optimal control," *Mathematical Programming Computation*, vol. 11, no. 1, pp. 1–36, 2019.

PAPER B

Computationally efficient algorithm for eco-driving over long look-ahead horizons

Ahad Hamednia, Nalin K.Sharma, Nikolce Murgovski, Jonas Fredriksson

IEEE Transactions on Intelligent Transportation Systems

The layout has been revised.

Abstract

This paper presents a computationally efficient algorithm for eco-driving along horizons of over 100 km. The eco-driving problem is formulated as a bi-level program, where the bottom level is solved offline, pre-optimising gear as a function of longitudinal velocity (kinetic energy) and acceleration. The top level is solved online, optimising a nonlinear dynamic program with travel time, kinetic energy and acceleration as state variables. To further reduce computational effort, the travel time is adjoined to the objective by applying necessary Pontryagin's Maximum Principle conditions, and the nonlinear program is solved using real-time iteration sequential quadratic programming scheme in a model predictive control framework. Compared to average driver's driving cycle, the energy savings of using the proposed algorithm is up to 11.60 %.

1 Introduction

Excessive energy consumption of vehicles is recently being regarded as a crucial concern for automotive industry leaders and transport service providers due to economic, ecological and environmental issues. For instance, the Organisation for Economic Co-operation and Development (OECD) forecasts a rapid growth in transport demand over the coming years, which may lead to 60 % increase in worldwide transport CO_2 emissions by 2050, due to increase in fossil fuel consumption [1]. One effective way to mitigate destructive consequences from ever growing energy consumption by vehicles is to improve *transport efficiency*. The transport efficiency can also be characterised as *tank-to-meter efficiency*, referred to as the conversion of energy stored in fuel into potential and kinetic energy required for displacement, and accompanied losses.

Eco-driving has been concerned widely as an approach for increasing the tank-to-meter efficiency by optimising velocity profile when considering road information and traffic flow [2]–[6]. When driving in a hilly terrain, it is preferable to vary the vehicle speed over a narrow interval while keeping the maximum allowed travel time, i.e., speeding up when driving downhill and

decreasing speed when climbing uphill, to have less energy waste at braking pads compared to a constant speed driving [7]. Implementing this behaviour over complex road topographies is generally achieved by model-based optimal control methods that maximise energy efficiency by optimally coordinating the energy use.

Dynamic programming (DP) [8] is the most commonly used algorithm to optimise the velocity profile of vehicles due to its potential to tackle non-convex, nonlinear and mixed-integer optimisation problems [9]–[14]. Fuel-optimal look-ahead control strategies have been proposed in [9] and [10] using DP, where in addition to optimising velocity, optimal gear shifting of conventional trucks is also investigated. Furthermore, a DP-based method is applied in [11] to minimise the energy consumption in fully electric vehicles (EVs) by optimising vehicle speed on short-range trips, e.g. driving between two consecutive traffic lights. A combined energy management and eco-driving approach using discrete DP is devised in [12] for hybrid electric vehicles (HEVs) driving over limited horizons, where the velocity profile is allowed to be optimised to further enhance fuel efficiency. Despite the promising contributions in solving optimal control problems (OCPs), DP-based methods suffer from the *curse of dimensionality*, which denotes to a fact that computational time increases exponentially with the number of state variables and control signals [8]. Several ways have been taken to decrease computational effort, for example by limiting the look-ahead horizon of cruise controllers for HEVs. At the current state, real-time capable DP-based control can only be applied for short prediction horizon scenarios of HEVs [13]. Other approaches focus on simplifying the powertrain model, by e.g. using a simplified internal combustion engine (ICE) model or discarding system states, such as travel time, ICE on/off and gear [14].

For high-dimensional optimisation problems, e.g. optimal control of HEVs with more energy states, several alternative approaches have been proposed. In [15] a mixed-integer quadratic program (MIQP) [16] has been applied for power allocation of HEVs. A way to diminish computational complexity of the high-dimensional problems is adjoining system dynamics to the cost function and neglecting constraints on state variables, as shown in [17]–[19]. In [19] Pontryagin's Maximum Principle (PMP) [20], [21] has been applied to optimise vehicle speed, gear selection and energy use of HEVs, where integer state variables have been neglected. Also, optimal speed and gear selection

of vehicles driving on highways have been addressed in [22] under varying parameters. Furthermore, in [23], [24] minimisation of energy consumption using PMP and considering varying speed requirements has been studied. Although PMP-based methods are computationally efficient for optimal velocity problems over long look-ahead horizons, they do not provide the same computational advantage for problems where state variables often activate their bounds. This is especially relevant for single shooting methods used for solving two-point boundary value problems (2PBVPs), as in e.g. [25].

Another portion of the conducted research benefits from the combination of DP and other methods. Such approaches have been proposed by [26]–[29], where real-valued decisions, e.g., planing optimal velocity, are made by sequential convex optimisation, while integer decisions are taken by DP. These strategies have also been shown to be effective when considering surrounding traffic [28], or cooperative energy management of multiple vehicles [26], [29]. In [30] a PMP-DP method has been proposed to solve the optimal control of vehicle speed, battery energy, gear selection and ICE on/off state. However, the computational effort of the control algorithms is still highly susceptible to long horizon lengths and high update frequencies.

High computational complexity may not be crucial when the eco-driving problem is implemented offline, since the problem solving is generally allowed to take a considerable amount of time. However, the offline implementation has drawbacks in situations where disturbances and/or constraints, for e.g. traffic situation, change unpredictably and the vehicle is no longer able to exactly follow the planned solution. Thus, the synergy among different optimisation methods is generally performed by splitting the problem into sub-problems arranged into multi-level or bi-level control architectures, where different tasks, for e.g. disturbance rejection, are delegated to distinct layers based on horizon length, time constants, sampling interval and updating frequency. To this end, multi-level and bi-level model predictive control (MPC) algorithms have been proposed for conventional vehicles (CVs), [31], and HEVs, [32]–[35], respectively. The multi-level architectures allow solving computationally intensive sub-problems, e.g. mixed-integer programs. When solving such programs in an MPC fashion, a certain reference or a target state are tracked, typically over look-ahead horizons of up to several of kilometers. Even though such horizons may appear long, there are problems that are naturally defined for even longer horizons.

Problems with very long look-ahead horizons, in the order of hundreds of kilometres, are typically addressed in electrified vehicles or logistics [36]. In the case of electrified vehicles, a target battery state of charge may be provided at charging locations along the route. For the logistics case, a target state over the long horizon is the travel time, which is often given at the end of the route by a logistics planner. Within the multi-level control architecture mentioned earlier, these problems are delegated to the highest supervisory level, generating reference travel time and battery state of charge trajectories over hundreds of kilometres. Early results on developing online implementable controllers that operate over long horizons, hereafter referred to as the eco-driving supervisors, have been published in our previous work for the case of CV, see [37].

In this paper, the eco-driving supervisor designed in [37] is generalised to both CVs and EVs. The purpose of the eco-driving supervisor is to generate optimal reference trajectories for the entire route, or for look-ahead horizons that may stretch over hundreds of kilometres, using road and traffic information compiled from look-ahead data and previous measurements. To do so, an online-capable algorithm is developed in an MPC framework that has the ability to anticipate future events and react to disturbances. For solving the eco-driving supervision problem online, reducing the computational complexity is the main concern, to allow the online solution to be obtained within the update frequency of real-time execution. Furthermore, having small computation time can strongly enhance the optimality, since the suggested optimal state of vehicle can be updated more frequently. Accordingly, the algorithm's computational effort is decreased in three steps: 1) a problem decomposition into two sub-problems, where velocity and travel-time trajectory are optimised online and gear shifting strategy is optimised offline; 2) a combination of an indirect PMP solution and a direct nonlinear programming for reducing the number of states in the online optimisation sub problem; 3) a real-time iteration (RTI) sequential quadratic programming (SQP) [38], which allows a single quadratic program (QP) to be solved in an MPC manner [39].

The outline of the paper is as follows. In Section 2, dynamic model of vehicle is presented. In Section 3, the energy minimisation problem is formulated. Section 4 describes the computationally efficient algorithm. In Section 5 the proposed algorithm is applied to a CV and an EV. In Section 6, the simulation results are demonstrated. Finally, Section 7 concludes the paper.

2 Physical Modelling

This section addresses vehicle dynamics, i.e. travel time and longitudinal vehicle dynamics. Furthermore, static relations are given that translate torque and rotational speed of actuator to traction force and longitudinal velocity. Finally, lower bounds and upper bounds on longitudinal velocity, traction force and acceleration are presented.

2.1 Travel time and longitudinal dynamics

According to Newton's law of motion, preliminary governing equations of a point mass vehicle model are

$$\dot{s}(t) = v(t) \tag{B.1}$$

$$\mathrm{m}\,\dot{v}(t) = F(t) + F_{\mathrm{brk}}(t) - F_{\mathrm{air}}(v) - F_{\alpha}(s) \tag{B.2}$$

where m is total lumped mass of the vehicle, t is travel time, s is travelled distance, v is longitudinal velocity, F is traction force at the wheel side of the vehicle generated by the actuator, and F_{brk} is a non-positive force that includes braking by the service brakes, a retarder, a compression release engine brake and/or an exhaust pressure governor. For the case of a conventional vehicle, more details on the braking force will be discussed later, in Section 5.1. Note that the travelled distance and longitudinal velocity are functions of travel time in (B.2). However, the explicit dependence is not shown for brevity, when these signals are input arguments to functions, such as $F_{\alpha}(s(t))$ and $F_{\mathrm{air}}(v(t))$. The nominal aerodynamic drag, F_{air}, and resistive forces that depend on road gradient α, $F_{\alpha}(s)$, are defined as

$$F_{\mathrm{air}}(v) = \frac{\rho_{\mathrm{a}} \mathrm{c_d} \mathrm{A_f} v^2}{2}, \tag{B.3}$$

$$F_{\alpha}(s) = \mathrm{mg}\left(\sin(\alpha(s)) + \mathrm{c_r}\cos(\alpha(s))\right), \tag{B.4}$$

where ρ_{a} is air density, $\mathrm{c_d}$ is aerodynamic drag coefficient, $\mathrm{A_f}$ is vehicle frontal area, g is the gravitational acceleration, and $\mathrm{c_r}$ is rolling resistance coefficient. The road gradient can be directly obtained from a standard global positioning system (GPS).

The vehicle longitudinal dynamics (B.1) and (B.2), are nonlinear due to

the quadratic dependency of longitudinal velocity in the aerodynamical drag function in (B.3) and the road gradient that can be an arbitrary nonlinear function of distance in (B.4). Such nonlinearities may increase computational complexity. To overcome this issue, it is possible to modify (B.1) and (B.2) by changing independent variables. Thus, distance s is used as independent variable instead of time t in (B.1), i.e. decisions are planned with respect to s, as presented in [40]–[43]. Subsequently, for a given road topography, the function F_α now becomes a fixed trajectory for the entire route. In addition, the nonlinearity in (B.3) can be removed by a change of state variable v to kinetic energy,

$$E(s) = \frac{\mathrm{m}v^2(s)}{2} \tag{B.5}$$

where E represents the kinetic energy of the vehicle. These transformations are non-approximate as long as the studied vehicle does not stop or change direction of its movement. Also, to study variations on speed and acceleration of the driving vehicle, we introduce acceleration, a, as an additional state variable. The change of acceleration in space coordinates, which resembles jerk, j, now becomes the input signal to the vehicle system. The resulting vehicle dynamics model becomes

$$t'(s) = \sqrt{\frac{\mathrm{m}}{2E(s)}} \tag{B.6}$$

$$E'(s) = \mathrm{m}a(s) \tag{B.7}$$

$$a'(s) = j(s) \tag{B.8}$$

where t' and a' are used as short hand notations for $\mathrm{d}t/\mathrm{d}s$ and $\mathrm{d}a/\mathrm{d}s$, respectively. The relation $E' = \mathrm{m}vv'$ is the product of mass and vehicle acceleration, and

$$a(s) = \frac{1}{\mathrm{m}}\left(-\mathrm{c_a}E(s) + F(s) + F_{\mathrm{brk}}(s) - F_\alpha(s)\right) \tag{B.9}$$

where $\mathrm{c_a} = \rho_\mathrm{a}\mathrm{c_d}\mathrm{A_f}/\mathrm{m}$, gathers the drag related coefficients.

It can be noticed that (B.6) is still nonlinear with respect to E. More information on how to tackle the nonlinearity in (B.6) is presented in Section 4.

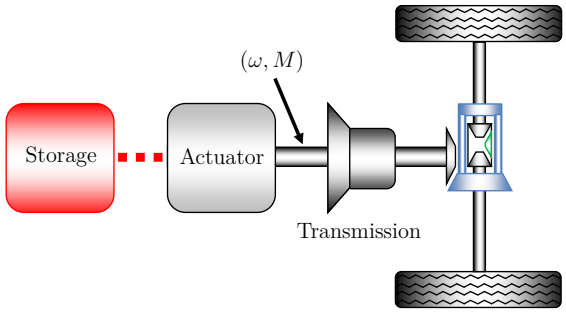

Figure 1: Schematic diagram of the studied powertrain. The powertrain consists of energy storage unit, actuator and transmission system, which transfers shaft torque, M, with rotating speed ω.

Throughout this paper, all constants, which are not dependent on s are shown in upright letters, e.g. $\mathrm{m}, \mathrm{A_f}, \mathrm{c_d}, \rho_\mathrm{a}$ do not depend on s. Also, all the states and control inputs are trajectories in terms of s, e.g. $t(s)$ and $E(s)$ are the trajectories dependent on s, where in several places the dependency is not displayed for simplicity.

2.2 Vehicle powertrain

A schematic diagram of the considered powertrain is illustrated in Fig. 1. The powertrain consists of an energy storage unit, an actuator, e.g. an ICE or an electric machine (EM), and a transmission system. The torque and speed at the shaft between the actuator and transmission are denoted by M and ω, respectively.

The transmission system is modelled considering the transmission and final gear ratios as

$$v(s) = \omega(s)R(\gamma), \quad F(s) = \frac{M(s)}{R(\gamma)}, \tag{B.10}$$

where γ denotes selected gear, and

$$R(\gamma) = \frac{\mathrm{r_w}}{\mathrm{r_{tg}}(\gamma)\mathrm{r_{fg}}} \tag{B.11}$$

where $\mathrm{r_w}$ is the wheel radius, $\mathrm{r_{tg}}$ and $\mathrm{r_{fg}}$ are transmission and final gear ratios, respectively.

The traction force is bounded

$$F(s) \in [F_{\gamma\min}(E), F_{\gamma\max}(E)], \tag{B.12}$$

where

$$F_{\gamma\min}(E) = \min_{\gamma} F_{\min}(E, \gamma), \tag{B.13}$$

$$F_{\gamma\max}(E) = \max_{\gamma} F_{\max}(E, \gamma). \tag{B.14}$$

The functions $F_{\min}(E, \gamma)$ and $F_{\max}(E, \gamma)$ are the traction force limits for a given pair of kinetic energy (longitudinal velocity) and gear.

In turn, the acceleration limits,

$$a(s) \in [a_{\min}(E), a_{\max}(E)],$$

can be derived using (B.9) as a function of kinetic energy (longitudinal velocity) and considering the limits on traction force, as

$$a_{\min}(E) = \max\left\{\underline{\mathrm{a}}, \frac{F_{\gamma\min}(E) - \mathrm{c_a}E + \underline{\mathrm{F_{brk}}} - F_\alpha}{\mathrm{m}}\right\} \tag{B.15}$$

$$a_{\max}(E) = \min\left\{\overline{\mathrm{a}}, \frac{F_{\gamma\max}(E) - \mathrm{c_a}E - F_\alpha}{\mathrm{m}}\right\} \tag{B.16}$$

where $\underline{\mathrm{a}}$ is the minimum and $\overline{\mathrm{a}}$ is the maximum allowed acceleration within a comfort zone and $\underline{\mathrm{F_{brk}}}$ denotes constant minimum total braking force. Here, $a_{\min}$ and $a_{\max}$ are not necessarily smooth functions, as $F_{\gamma\min}$ and $F_{\gamma\max}$ may not be smooth functions. This will be discussed in more details in Section 5.

In order to deliver a certain traction force, the actuator draws power from the energy storage unit. Let $P_{\mathrm{w}}(v, F, \gamma)$ denote the drawn power, which in the case of a combustion engine is a chemical, fossil fuel power, and in the case of an electric machine, it is an electric power. Explicit representations of the internal power in terms of the kinetic energy (longitudinal velocity) and traction force will be provided later, in Section 5.

3 Problem Statement

This section formulates the eco-driving OCP, which aims at planning an optimal velocity trajectory for the entire route such that the total energy consumption is minimised and the travel time is upper bounded by the target time given by a logistics planner.

3.1 Performance function

The performance function of the OCP is formulated as

$$\int_0^{\mathrm{s_f}} \left(\frac{\mathrm{c_{eg}} P_{\mathrm{w}}(v, F, \gamma)}{v(s)} + \mathrm{w}_1 a^2(s) + \mathrm{w}_2 j^2(s) \right) \mathrm{d}s \tag{B.17}$$

that incorporates total energy consumption by integrating the internal power drawn from the storage unit, and the driver's discomfort via the acceleration and jerk. Here, $\mathrm{c_{eg}}$ denotes the price of energy storage, and w_1 and w_2 are penalty factors associated with the acceleration and jerk. The division of the internal power with speed in (B.17) derives from the time to space transformation,

$$\int P_{\mathrm{w}}(v, F, \gamma) \mathrm{d}t = \int P_{\mathrm{w}}(v, F, \gamma)/v(s)\, \mathrm{d}s.$$

3.2 Speed limits and travel time

In order to increase feasibility in realistic driving situations, we consider speed limits that include not only legal, but also dynamic speed limits using available information about the road and traffic. Surrounding traffic can impose such dynamic constraints on the vehicle speed due to presence of e.g. traffic lights, intersections, ramps and junctions. Total speed limits are computed as

$$v_{\min}(s) = \min \left\{ v_{\min}^{\mathrm{legal}}(s), v_{\mathrm{fl}}(s) \right\}, \tag{B.18}$$

$$v_{\max}(s) = \min \left\{ v_{\max}^{\mathrm{legal}}(s), v_{\max}^{\mathrm{dyn}}(s) \right\}, \tag{B.19}$$

where $v_{\min}^{\mathrm{legal}}$ and $v_{\max}^{\mathrm{legal}}$ are legal speed limits, $v_{\max}^{\mathrm{dyn}}$ is maximum dynamic speed limit, and v_{fl} is a filtered speed that will be discussed later in this section. The legal and dynamic speed limits can be provided by new modern systems, e.g. e-horizon technologies [44]. An illustration of the speed limits are shown in

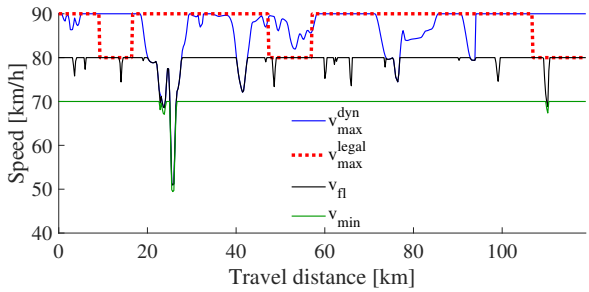

Figure 2: Examples of maximum legal and dynamic speed limits together with minimum allowed speed limit and filtered speed trajectory, v_{fl}. For calculating v_{fl} maximum power (acceleration) capability of the actuator has been considered.

Fig. 2, where the legal speed limits can generally change abruptly for different segments of the driving road, whereas the maximum dynamic speed limit vary smoothly in terms of travel distance. To avoid singularity in (B.6), the vehicle speed is not allowed to drop to zero. However, with the use of variable scaling, very small speed values are acceptable, and the speed may be rounded to zero after the optimisation is finished. This could be useful when short duration traffic stops are to be considered. For longer stops, it could be more convenient to split the trip into two distinct trips, and optimise each individually [45].

To compute the upper bound on travel time, $\mathrm{t_f}$, it is possible to obtain the velocity profile, $v_{\mathrm{fl}}(s) \in [v_{\min}(s), v_{\max}(s)]$, as the average driver's driving cycle, by filtering cruising speed, $\mathrm{v_{cru}} \in [v_{\min}(s), v_{\max}(s)]$. The logistics planner may send $\mathrm{v_{cru}}$ via a telemetry system, or it can be set manually by the driver. The rated power of the actuator and road/traffic limits on speed are taken into consideration in the cruise speed filtering [26], [27], [37]. When deriving v_{fl}, it is assumed that the vehicle will try to maintain $\mathrm{v_{cru}}$ unless instantaneous dynamic speed limit and/or actuator limit are reached.

$$v_{\mathrm{fl}}(s) = \min \left\{ v_{\max}^{\mathrm{dyn}}, \mathrm{v_{cru}}, \int_0^s \frac{a_{\max}(v_{\mathrm{fl}})}{v_{\mathrm{fl}}(\sigma)} \mathrm{d}\sigma \right\} \tag{B.20}$$

By computing maximum arrival time as

$$\mathrm{t_f} = \int_0^{\mathrm{s_f}} \frac{\mathrm{d}s}{v_{\mathrm{fl}}(s)}, \tag{B.21}$$

where $\mathrm{s_f}$ is the final position at the end of the route, a constraint can be imposed

$$t(\mathrm{s_f}) \leq \mathrm{t_f} \tag{B.22}$$

that requires finishing the route in the same time or sooner than what would be required when driving with v_{fl}.

3.3 MPC for minimising energy consumption

The problem (B.17) is optimised in an MPC framework with a prediction horizon of length s_{H}, aiming at anticipating future events and reacting to disturbances. The main goal of this paper is to develop a computationally efficient algorithm that allows horizons that cover the entire route. However, as computational resources are always limited, we impose an upper bound, $\mathrm{s_{Hmax}}$, hopefully in the range of hundreds of kilometres. The optimisation problem can then be solved in a moving horizon MPC (MHMPC) framework if $\mathrm{s_{Hmax}} < \mathrm{s_f}$, or in a shrinking horizon MPC (SHMPC) framework if $\mathrm{s_{Hmax}} \geq \mathrm{s_f}$. The optimisation variables are predicted at distance samples $s \in [\zeta, \zeta + s_{\mathrm{H}}]$, given information of the actual vehicle's states at ζ. Thus, the actual horizon length can be computed as

$$s_{\mathrm{H}}(\zeta) = \min\{\mathrm{s_{Hmax}}, \mathrm{s_f} - \zeta\}. \tag{B.23}$$

The problem can now be summarised as follows

$$\begin{aligned} \min_{j, F_{\mathrm{brk}}, \gamma} \int_{\zeta}^{\zeta + s_{\mathrm{H}}(\zeta)} \Bigg(& \frac{\mathrm{c_{eg}} P_{\mathrm{w}}(E, F, \gamma)}{\sqrt{\frac{2E(s|\zeta)}{\mathrm{m}}}} \\ & + \mathrm{w}_1 a^2(s|\zeta) + \mathrm{w}_2 j^2(s|\zeta) \Bigg) \mathrm{d}s, \end{aligned} \tag{B.24a}$$

subject to:

$$t'(s|\zeta) = \sqrt{\frac{\mathrm{m}}{2E(s|\zeta)}} \tag{B.24b}$$

$$E'(s|\zeta) = \mathrm{m}a(s|\zeta) \tag{B.24c}$$

$$a'(s|\zeta) = j(s|\zeta) \tag{B.24d}$$

$$F(s|\zeta) = \mathrm{m}a(s|\zeta) + \mathrm{c_a}E(s|\zeta) - F_{\mathrm{brk}}(s|\zeta) + F_\alpha(s) \tag{B.24e}$$

$$E(s|\zeta) \in \frac{\mathrm{m}}{2}[v^2_{\min}(s|\zeta), v^2_{\max}(s|\zeta)] \tag{B.24f}$$

$$a(s|\zeta) \in [a_{\min}(E), a_{\max}(E)] \tag{B.24g}$$

$$j(s|\zeta) \in [\underline{\mathrm{j}}, \bar{\mathrm{j}}] \tag{B.24h}$$

$$F_{\mathrm{brk}}(s|\zeta) \in [\underline{\mathrm{F_{brk}}}, 0] \tag{B.24i}$$

$$t(\zeta|\zeta) = t_0(\zeta), \quad E(\zeta|\zeta) = E_0(\zeta), \quad a(\zeta|\zeta) = a_0(\zeta) \tag{B.24j}$$

$$t(\zeta + s_{\mathrm{H}}|\zeta) \leq t_{\mathrm{H}}(\zeta) \tag{B.24k}$$

$$\gamma(s|\zeta) \in \{1, 2, \ldots, \gamma_{\max}\} \tag{B.24l}$$

where $\underline{\mathrm{j}}$ is the minimum and $\bar{\mathrm{j}}$ is the maximum allowed jerk within a comfort zone, t_0, E_0 and a_0 are the values of the system states at instance ζ, and $\gamma_{\max}$ is the highest gear. The constraints (B.24b)-(B.24l) are enforced for all $s \in [\zeta, \zeta + s_{\mathrm{H}}(\zeta)]$ and the problem is re-evaluated for all $\zeta \in [0, \mathrm{s_f}]$. The maximum allowed travel time over the prediction horizon, t_{H}, is computed as in (B.21) for the distance s_{H}. The problem (B.24) is a non-convex, mixed-integer and dynamic nonlinear program, where t, E and a are real-valued state variables, j and F_{brk} are real-valued control inputs, γ is an integer control input and F is an output variable. Although from a control point of view j is the control signal, in practice, a is applied to the vehicle. When solving such computationally complex problem online, reducing the computational time is the major bottleneck, since the online solution must be at least within the update frequency of real-time execution. Thus, we propose several reformulation steps in the following that break down the problem (B.24) into optimisation sub problems, which is solved with significantly reduced computational complexity compared to the original problem.

For the sake of simplicity, the dependence on ζ will not be shown in most following parts of the paper and the method is explained via a single MPC update, e.g. the one with $\zeta = 0$.

4 Computationally Efficient Algorithm

This section proposes three reformulation steps for reducing computational complexity of the problem (B.24). These steps are: 1) formulating a bi-level optimisation program that allows decoupling the integer variable, i.e. gear, from a nonlinear optimisation program (NLP); 2) adjoining nonlinear dynamics of travel time to the objective using necessary PMP conditions for optimality; 3) Removing a loop on finding optimal time costate and applying RTI SQP scheme.

4.1 Bi-level programming and gear optimisation

The mixed-integer problem (B.24) can be reformulated as a bi-level program:

$$\min_{j,F_{\mathrm{brk}}} \int_0^{s_{\mathrm{H}}} \left(\frac{\mathrm{c_{eg}} P_{\mathrm{w}}(E,F,\gamma^*)}{\sqrt{\frac{2E(s)}{\mathrm{m}}}} + \mathrm{w}_1 a^2(s) + \mathrm{w}_2 j^2(s) \right) \mathrm{d}s \tag{B.25a}$$

subject to:(B.24b)-(B.24k)

$$\gamma^*(s) = \arg\min_{\gamma} P_{\mathrm{w}}(E,F,\gamma) \tag{B.25b}$$

$$\text{subject to: } \gamma(s) \in \{1,2,...,\gamma_{\max}\} \tag{B.25c}$$

$$F(s) \in [F_{\gamma\min}(E), F_{\gamma\max}(E)] \tag{B.25d}$$

where the gear optimisation resides only in the bottom level program, while all the system dynamics reside in the top level program. Static modelling of the actuator and transmission system allows separating the bottom level and solving it offline, where v (or E) and F are regarded as parameters, and optimal gear is computed as a function of these parameters. To this end, the bottom level can be solved as

$$f^*_{\gamma}(E,F) = \arg\min_{\gamma} P_{\mathrm{w}}(E,F,\gamma) \tag{B.26a}$$

$$\text{subject to: } \gamma \in \{1,2,...,\gamma_{\max}\} \tag{B.26b}$$

$$F \in \mathcal{F}(E) = [F_{\gamma\min}(E), F_{\gamma\max}(E)] \tag{B.26c}$$

$$E \in \mathcal{E}(\gamma) = \frac{\mathrm{m}[\omega^2_{\mathrm{idle}}, \omega^2_{\max}]\mathrm{R}^2(\gamma)}{2} \tag{B.26d}$$

where $f^*_\gamma(E,F)$ is a two-dimensional function describing the optimal gear choices for all traction force versus speed (kinetic energy) combinations, $\mathcal{E}$ and $\mathcal{F}$ are the feasible sets for kinetic energy and traction force respectively, and ω_{idle} and $\omega_{\max}$ are rotational speed limits. By replacing the optimal gear with the parametric function, the internal power can be written as

$$P_\gamma(E,F) = P_{\text{w}}(E,F,f^*_\gamma(E,F)), \tag{B.27}$$

indicating power consumption when gear is optimally chosen. Note that for CV case study the offline-optimised gear selection algorithm is extended, which covers the negative force area originating from negative additional force. More details will be given later in Section 5.

4.2 Necessary PMP conditions for optimality

In the second step of the algorithm, the problem (B.25) is reformulated, which is facilitated by the necessary PMP conditions for optimality. The Hamiltonian is defined as

$$\begin{aligned}\mathcal{H}(\cdot) = {} & \text{c}_{\text{eg}} P_\gamma(E,F)\sqrt{\frac{\text{m}}{2E(s)}} + \text{w}_1 a^2(s) + \text{w}_2 j^2(s) + \\ & + \lambda_{\text{t}}(s)\sqrt{\frac{\text{m}}{2E(s)}} + \lambda_E(s)\text{m}a(s) + \lambda_a(s)j(s).\end{aligned} \tag{B.28}$$

where the symbol $\cdot$ is a compact notation for a function of multiple variables. Here, λ_{t}, λ_E and λ_a denote the costates of travel time, kinetic energy and acceleration, respectively. It can be observed that the Hamiltonian is not an explicit function of travel time, thus the optimal time costate, λ^*_t, i.e. the value for λ_{t} that satisfies the maximum travel time constraint (B.24k), is a constant value. Hence

$$\lambda'^*_t(s) = -\left(\frac{\partial \mathcal{H}(\cdot)}{\partial t}\right)^* = 0. \tag{B.29}$$

Furthermore, the travel time is a strictly monotonically increasing function that may activate constraint (B.24k) only at the final instance. Consequently, if λ^*_{t} is known, it will be possible to remove the nonlinear constraint on travel time (B.25) and adjoin the product of $\lambda^*_t(s)$ and the nonlinear function $\sqrt{\frac{\text{m}}{2E(s)}}$

to the objective function. This implies that the dynamic OCP can yet again be formulated as a bi-level program

$$\min_{\lambda_\mathrm{t}} \int_0^{s_\mathrm{H}} \left(\frac{\mathrm{c_{eg}} P_\gamma(E^*(\lambda_\mathrm{t}, s), F^*(\lambda_\mathrm{t}, s)) + \lambda_\mathrm{t}}{\sqrt{\frac{2E^*(\lambda_\mathrm{t}, s)}{\mathrm{m}}}} + \mathrm{w}_1 a^{*2}(\lambda_\mathrm{t}, s) + \mathrm{w}_2 j^{*2}(\lambda_\mathrm{t}, s) \right) \mathrm{d}s \tag{B.30a}$$

subject to:

$$t'^*(\lambda_\mathrm{t}, s) = \sqrt{\frac{\mathrm{m}}{2E^*(\lambda_\mathrm{t}, s)}} \tag{B.30b}$$

$$E'^*(\lambda_\mathrm{t}, s) = \mathrm{m} a^*(\lambda_\mathrm{t}, s) \tag{B.30c}$$

$$a'^*(\lambda_\mathrm{t}, s) = j^*(\lambda_\mathrm{t}, s) \tag{B.30d}$$

$$t^*(\lambda_\mathrm{t}, 0) = t_0, \quad t^*(\lambda_\mathrm{t}, s_\mathrm{H}) \leq t_\mathrm{H} \tag{B.30e}$$

$$[j^*(\lambda_\mathrm{t}, s), F^*_\mathrm{brk}(\lambda_\mathrm{t}, s), F^*(\lambda_\mathrm{t}, s)] = \arg\min_{j, F_\mathrm{brk}} \int_0^{s_\mathrm{H}} \left(\frac{\mathrm{c_{eg}} P_\gamma(E, F) + \lambda_\mathrm{t}}{\sqrt{\frac{2E(s)}{\mathrm{m}}}} + \mathrm{w}_1 a^2(s) + \mathrm{w}_2 j^2(s) \right) \mathrm{d}s \tag{B.30f}$$

subject to: (B.24c)-(B.24i), $\quad E(0) = E_0, \quad a(0) = a_0$

where all constraints involving travel time have been moved to the top level, while the bottom level, (B.30f), generates optimal control trajectories parameterised in λ_t. Similarly as before, the goal is to separate the two optimisation levels. One way to do this is by trying different values for λ_t and then using search methods, e.g. Newton or bisection, to find λ_t^* that minimises the top level's cost.

By assuming that problem (B.30f) is an NLP that can be solved with SQP, the procedure for solving the mixed-integer problem (B.24) will consist of three nested loops as illustrated in Fig. 3a. The outermost loop updates the MPC horizon, the middle loop finds the optimal value for λ_t and the innermost loop sequentially solves a QP in order to find the solution of problem (B.30f) for a given value of λ_t. The procedure is still computationally inefficient, as it requires solving multiple QPs for given multiple λ_t values in each MPC update. Our goal is to eliminate the inner most loops and for a given λ_t, solve

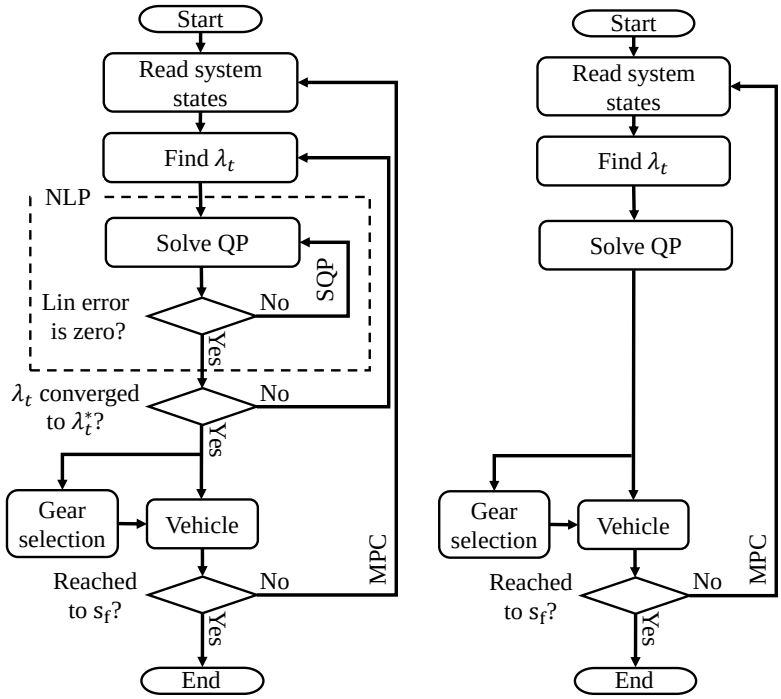

(a) With three nested loops.

(b) Without two innermost loops to solve NLP using SQP, and to find λ^*.

Figure 3: Flowchart of the proposed algorithm to solve NLP in MPC framework.

only a single QP in each MPC update, as illustrated in Fig 3b.

4.3 Updating the time costate over the MPC loop

To eliminate the loop on finding λ_t^*, it is considered that the optimal energy consumption corresponds in general to driving slow, so it can be assumed that the vehicle will use the entire travel time, i.e. $t^*(\lambda_\mathrm{t}, s_\mathrm{H}) \approx t_\mathrm{H}$. Hence, the objective of the top level program in (B.30) is transformed to minimising maximum travel time difference, as

$$\min_{\lambda_\mathrm{t}} ||t^*(\lambda_\mathrm{t}, s_\mathrm{H}|\zeta) - t_\mathrm{H}(\zeta)|| \tag{B.31}$$

where $||\cdot||$ may indicate any norm.

For the case that the problem (B.30) is solved in SHMPC framework, the final time instance and the final point of the horizon are fixed regardless of the update instance ζ, i.e. $t_{\mathrm{H}}(\zeta) = \mathrm{t_f}$ and $\zeta + s_{\mathrm{H}}(\zeta) = \mathrm{s_f}$, $\forall\zeta$.

Lemma 1: *If predicted disturbances do not change and there is no miss-match between the control and plant model, then for an SHMPC implementation of problem* (B.30) *and for a given* λ_{t}*, it holds,*

$$t^*(\lambda_{\mathrm{t}}, s_{\mathrm{H}}|\zeta) = t^*(\lambda_{\mathrm{t}}, s_{\mathrm{H}}|\zeta + \delta\zeta), \quad \forall\delta\zeta \in [0, \mathrm{s_f} - \zeta], \tag{B.32}$$

i.e. the optimal travel time at the end of the horizon does not change for different SHMPC updates.

Proof. The proof follows directly from Bellman's principle of optimality, i.e. *any tail of an optimal trajectory is an optimal solution as well* [8]. □

For an MHMPC, Lemma 1 does not hold even if disturbances are predicted exactly and there is no model miss-match. This is because new information is added as the prediction horizon moves forward at each MPC update. However, if the prediction horizon is much longer than the interval between two consecutive updates, then for different ζ, it can be assumed

$$t^*(\lambda_{\mathrm{t}}, s_{\mathrm{H}}|\zeta) - t_{\mathrm{H}}(\zeta) \approx t^*(\lambda_{\mathrm{t}}, s_{\mathrm{H}}|\zeta^+) - t_{\mathrm{H}}(\zeta^+) \tag{B.33}$$

where ζ^+ is the instance of the MHMPC update following that at ζ. Fig. 4 demonstrates the overlapped curves of the final time difference versus the time costate for a CV and an EV, where $\zeta = 0\,\mathrm{m}$ and $\zeta^+ = 300\,\mathrm{m}$. Thus, it is also possible for an MHMPC to update the time costate over the MPC loop.

Problem (B.31) is then solved by a derivative free Newton method, where the Newton iterates are spread across the MPC updates without waiting for a full convergence, i.e. by performing one Netwon step per update. A flowchart of the proposed algorithm is depicted in Fig. 3b, while more details on the Newton method is provided in Appendix 1.

4.4 Real-time iterations SQP over the MPC loop

For a given λ_{t} it remains to solve problem (B.30f). It will be shown later, in Section 5, that for the case of conventional and electric vehicle powertrians,

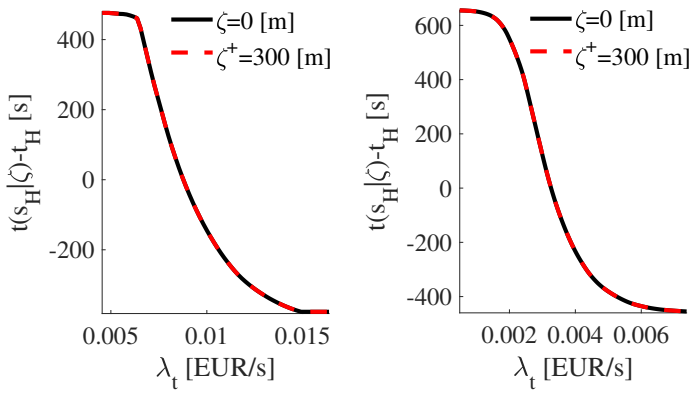

(a) For CV case study. (b) For EV case study.

Figure 4: Difference between calculated time at the end of horizon and the desired maximum time for varying time costate using MHMPC scheme, where $\zeta = 0\,\text{m}$ and $\zeta^+ = 300\,\text{m}$. Overlap of the curves for different ζ values shows that λ_t can be evaluated only once per each MPC update, rather than waiting for a full convergence.

problem (B.30f) is indeed a smooth NLP that can be solved by SQP. However, instead of sequentially solving a QP until linearization error is equal to zero, it is computationally efficient to spread the SQP over MPC updates, which is provided by RTI. The idea is to solve only a single QP per MPC update, without waiting for a full convergence. The obtained solution is possibly sub-optimal, but due to the contractivity of the RTI scheme as shown in [46], the real-time iterates quickly approach the optimal solution during the runtime of the process. Alternative algorithm for real-time solving of the NLPs has been presented in [47].

As the SQP is stopped prematurely, it is important to show that the obtained solution by solving a single QP is feasible in the original NLP. Feasibility can be guaranteed if the domain of the QP, obtained by linearizing the nonlinear constraints in problem (B.30f), is an inner approximation of the feasible set of the NLP (B.30f). This is indeed the case for conventional and electric vehicle powertrians, which will be shown in Section 5.

5 Application to CV and EV

This section proposes several steps that show how the computationally efficient algorithm proposed in Section 4 is applied to a CV and an EV.

5.1 Conventional vehicle

A conventional powertrain includes an ICE to transform chemical fuel energy to mechanical propulsion energy through a multiple-gear transmission.

A static fuel mass rate map for a given pair of rotational speed and engine torque is obtained by gathering steady-state data from a dynamic simulation model of a diesel engine, presented in [48]. Subsequently, efficiency map and torque limits are derived, see Fig. 5. According to the efficiency isolines, it is desirable to avoid operating the ICE at low speed and torque, where efficiency is low.

Fig. 5 also illustrates a negative torque limit for an additional braking system, including a retarder, a compression release engine brake and/or an exhaust pressure governor. The additional braking is preferred over the service braking in order to reduce wear and avoid lock up of the braking pads. Using (B.10), the negative torque is translated to negative force on the wheel side as

$$F_{\mathrm{brk}} = F_{\mathrm{A}} + F_{\mathrm{S}}, \tag{B.34}$$

where F_{S} and F_{A} are forces by the service brakes and the additional braking system. The minimum negative additional force limit for a given kinetic energy is

$$F_{\mathrm{Amin}}(E) = \min_{\gamma} F_{\gamma\mathrm{A}}(E, \gamma) \tag{B.35}$$

where $F_{\gamma\mathrm{A}}$ denotes the minimum negative additional force for each gear. The lower bound on the traction force is zero, i.e. $F_{\gamma\mathrm{min}}(E) = 0$.

The two-dimensional fuel mass rate map of the ICE translates to a three-dimensional map on the wheels side. This three-dimensional map, denoted as $\mu_{\mathrm{w}}(E, F, \gamma)$, can be expressed in terms of kinetic energy, traction force and gear using (B.5) and (B.10). Subsequently, a map, which represents the

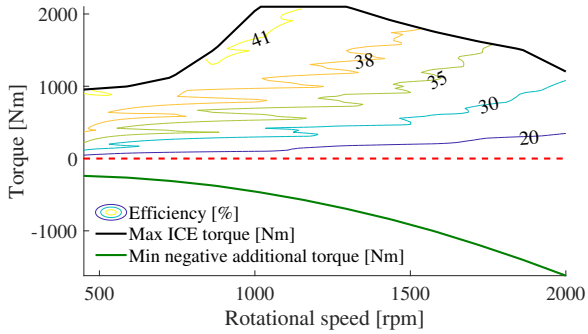

Figure 5: Steady-state efficiency map and maximum torque limit of the ICE. The negative torque limit illustrates the braking capability of the additional braking system that includes a retarder, an exhaust pressure governor and/or a compression release engine brake.

parametric internal power function, $P_{\mathrm{w}}(E, F, \gamma)$, can be derived as

$$P_{\mathrm{w}}(E, F, \gamma) = \mu_{\mathrm{w}}(E, F, \gamma) Q_{\mathrm{lhv}} \tag{B.36}$$

where Q_{lhv} is diesel heating value.

The bi-level program (B.25), can be extended for a CV case study, including the negative force region, which originates from the summation of negative additional force and service braking force, as

$$\min_{j, F_{\mathrm{brk}}} \int_0^{s_{\mathrm{H}}} \left(\frac{\mathrm{c_{eg}} P_{\mathrm{w}}(E, F, \gamma^*)}{\sqrt{\frac{2E(s)}{\mathrm{m}}}} + \mathrm{w}_1 a^2(s) + \mathrm{w}_2 j^2(s) \right) \mathrm{d}s \tag{B.37a}$$

subject to: (B.24b)-(B.24k)

$$\gamma^*(s) = \begin{cases} \arg\min_\gamma P_{\mathrm{w}}(E, F, \gamma), & \text{if } F + F_{\mathrm{brk}} \geq 0. \\ \arg\max_\gamma F_{\gamma \mathrm{A}}(E, \gamma), & \text{if } F_{\mathrm{Amin}}(E) \leq F + F_{\mathrm{brk}} < 0 \\ \arg\min_\gamma F_{\gamma \mathrm{A}}(E, \gamma), & \text{if } \underline{\mathrm{F_{brk}}} \leq F + F_{\mathrm{brk}} < F_{\mathrm{Amin}}(E) \end{cases} \tag{B.37b}$$

subject to: $\gamma(s) \in \{1, 2, ..., \gamma_{\max}\}$ (B.37c)

$$F(s) + F_{\mathrm{brk}}(s) \in [\underline{\mathrm{F_{brk}}}, F_{\gamma \max}(E)] \tag{B.37d}$$

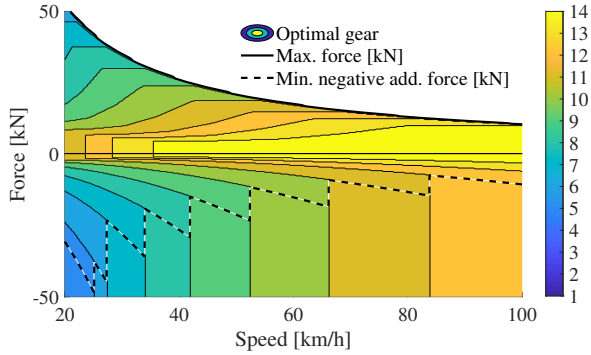

Figure 6: Offline-optimised gear map together with maximum traction force and minimum negative additional force. In the positive force region, the optimal selected gear is the one that minimises fuel consumption, which for the studied powertrain coincides with the highest feasible gear. In the negative force region, if the total force is lower than the minimum negative additional force, the lowest possible gear is selected, since it provides the most possible negative additional force. The remaining demanded negative force is covered by the service brakes. However, if the total force is higher than the minimum negative additional force, to avoid unnecessary down-shifting, the highest possible gear is selected.

Note that the traction force, F, and the total braking force, F_{brk}, cannot have non-zero values simultaneously, i.e. it is not the case that $F > 0$ and $F_{\text{brk}} < 0$ at the same time.

To approach the offline-optimal gear selection problem (B.37), it is possible to grid the feasible sets of kinetic energy and total force, i.e. $F + F_{\text{brk}}$. To this end, in the positive force region, for any feasible combination of longitudinal velocity (kinetic energy) and traction force, the optimal gear is the one that minimises energy consumption. In the negative force region, if the total demanded force is higher than the minimum negative additional force, the highest possible gear is selected, which avoids unnecessary down-shifting. However, if total demanded force is lower than the minimum negative additional force, the lowest possible gear is selected, since it provides the most possible negative additional force, see Fig. 6. The remaining demanded negative force is covered by the service brakes.

The optimal brake specific fuel consumption (BSFC) map and maximum traction force curve are depicted in Fig. 7. The optimal BSFC refers to the

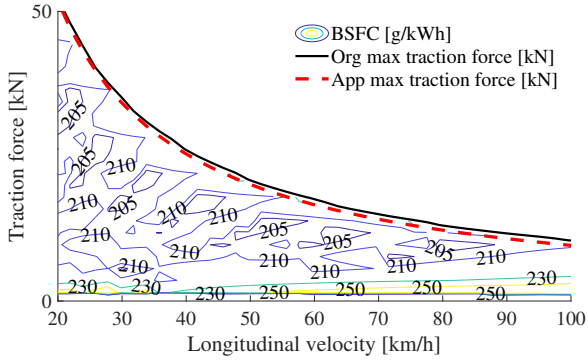

Figure 7: Offline-optimised BSFC map together with original and approximate maximum traction force as well as minimum negative additional force. The approximate limit is an inner approximation for the longitudinal velocities above 8 km/h.

minimum burnt fuel, which is obtained by optimising the internal power in (B.27).

The internal power drawn from fuel using (B.27), is approximated by the following expression

$$P_\gamma(v, F) \approx \mathrm{p_{e0}} + \mathrm{p_{e1}} v^3(s) + \mathrm{p_{e2}} v(s) F(s) \tag{B.38}$$

with $\mathrm{p_{e0}}, \mathrm{p_{e1}}, \mathrm{p_{e2}} \geq 0$. During a single driving mission, the parameters $\mathrm{p_{e0}}, \mathrm{p_{e1}}$ and $\mathrm{p_{e2}}$ are assumed constant, otherwise we will need to apply robust control methods to tackle possible uncertainties.

As illustrated in Fig. 8, for the studied engine model it is sufficient to use a first order term in F, although it is possible to include higher order terms as well, without significant increase in computational effort. Similar expressions for model abstraction of fuel mass rate are exploited in [26] and several references therein. Using (B.5) and (B.38), the stage cost (B.30f) transforms into

$$\begin{aligned} V_{\mathrm{CV}}(\cdot, \lambda_\mathrm{t}) \approx \frac{\mathrm{c_{eg}}(\mathrm{p_{e0}} + \lambda_\mathrm{t}^*)\sqrt{\mathrm{m}}}{\sqrt{2E(s)}} + \frac{2\mathrm{p_{e1}}}{\mathrm{m}} E(s) + \\ + \mathrm{p_{e2}} F(s) + \mathrm{w_1} a^2(s) + \mathrm{w_2} j^2(s) \end{aligned} \tag{B.39}$$

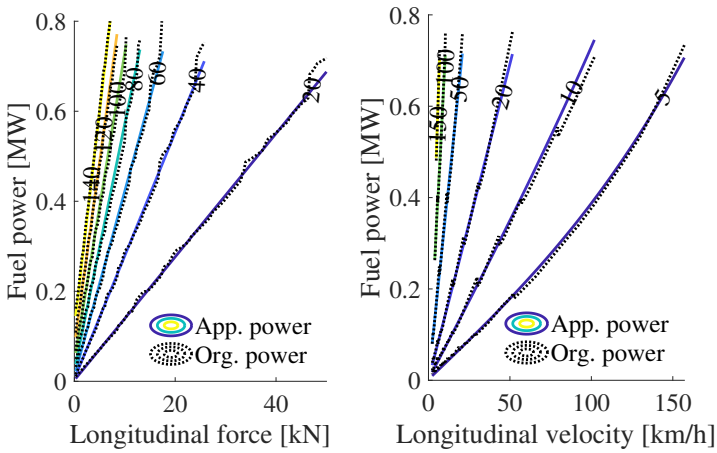

(a) Internal power versus longitudinal force for a given longitudinal velocity.

(b) Internal power versus longitudinal velocity for a given longitudinal force.

Figure 8: Original and approximated internal power drawn from fuel for a given longitudinal velocity and traction force.

which is a convex second order cone function in terms of E, a, j, F and F_{brk}.

The maximum traction force limit, see Fig. 7, is approximated by

$$F_{\gamma\max}(E) \approx \min\left\{\overline{F}, \mathrm{y}_0 + \frac{\mathrm{y}_1\sqrt{\mathrm{m}}}{\sqrt{2E(s)}}\right\} \tag{B.40}$$

where $\overline{F}$ is the maximum constant traction force, and y_1 resembles the maximum engine power, as it can be alternatively written as a division of power with vehicle speed. The coefficients y_0 and y_1 are obtained by solving a linear program, see Appendix 2 for details. The approximated force limit (B.40) is an inner approximation of the original force for speeds above 8 km/h, see Fig. 7, which is acceptable for the highway scenarios investigated in this paper.

The problem (B.30) with the stage cost (B.39) is non-convex nonlinear program, because of the nonlinear term $\mathrm{y}_1/\sqrt{E(s)}$ in (B.40). Due to the sign of $\mathrm{y}_1 \geq 0$, this term is a convex function (a convex problem, though, requires a concave function here). It is possible to transform (B.30) to a convex second order cone program (SOCP) by linearizing the maximum force limit in (B.40).

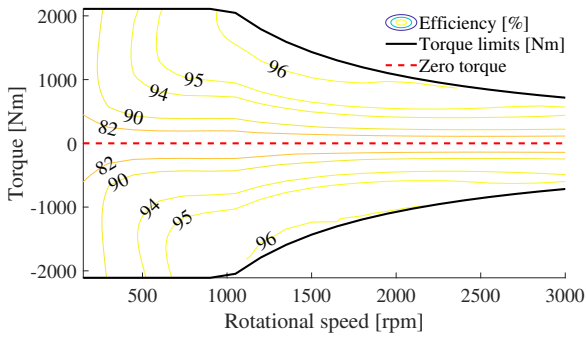

Figure 9: Steady-state efficiency map of EM together with shaft torque limits.

Note that linearizing any convex function about any trajectory, is always an inner approximation. Since the inner approximation is conservative, it is guaranteed that despite possibly being sub-optimal, all obtained solutions (if such solutions exist) are also feasible in the original non-convex problem. For more details, see Appendix 3.

5.2 Fully electric vehicle

In the fully electric powertrain, the EM converts electricity to mechanical power in motoring mode, whereas it converts mechanical power to electricity in generating mode of operation. In the generating mode, the energy is recuperated and stored in the electric battery, when decreasing kinetic energy by braking or decreasing potential energy while rolling downhill. Note that the electric powertrain is assumed to have a single-gear transmission system.

For a given pair of rotational speed and torque, EM efficiency map is shown in Fig. 9, using static internal electric battery power. In Fig. 9, positive and negative torque regions correspond to the motoring and the generating modes of operation, respectively.

It is assumed that a single-gear transmission system conveys the power from the battery to the wheels. Therefore, there is no need for offline gear optimisation, i.e. $P_\gamma(v, F) = P_{\mathrm{w}}(v, F, \gamma)$.

The internal power drawn from the electric battery is approximated by the

following expression

$$P_\gamma(v,F) \approx \mathrm{p_{m0}} + \mathrm{p_{m1}} v^3(s) + \mathrm{p_{m2}} v(s)F(s) + \\ + \mathrm{p_{m3}} v(s)F^2(s) \tag{B.41}$$

with $\mathrm{p_{m0}}, \mathrm{p_{m1}}, \mathrm{p_{m2}}, \mathrm{p_{m3}} \geq 0$. Fig. 10 demonstrates that the approximated model describes well the original internal battery power.

Using (B.5), (B.9) and (B.41), the stage cost (B.30f) transforms into

$$V_{\mathrm{EV}}(\cdot,\lambda_\mathrm{t}) \approx \frac{\mathrm{c_{eg}}(\mathrm{p_{m0}} + \lambda_\mathrm{t}^*)\sqrt{\mathrm{m}}}{\sqrt{2E(s)}} + \frac{2\mathrm{p_{m1}}}{\mathrm{m}} E(s) + \mathrm{p_{m2}} F(s) + \\ + \mathrm{p_{m2}} F^2(s) + \mathrm{w_1} a^2(s) + \mathrm{w_2} j^2(s). \tag{B.42}$$

The traction force limits, see Fig. 11, are approximated by

$$F_{\gamma\min}(E) \approx \max\left\{ \underline{F}, \mathrm{x_0} + \frac{\mathrm{x_1}\sqrt{\mathrm{m}}}{\sqrt{2E(s)}} \right\} \tag{B.43}$$

$$F_{\gamma\max}(E) \approx \min\left\{ \overline{F}, \mathrm{y_0} + \frac{\mathrm{y_1}\sqrt{\mathrm{m}}}{\sqrt{2E(s)}} \right\} \tag{B.44}$$

where $\underline{F}$ and $\overline{F}$ are constant traction force limits. The coefficients $\mathrm{x_0}$ and $\mathrm{x_1}$, similar to the $\mathrm{y_0}$ and $\mathrm{y_1}$, are the solution of the linear program given in Appendix 2.

According to the signs of $\mathrm{x_1} \leq 0$ and $\mathrm{y_1} \geq 0$, the term $\mathrm{x_1}/\sqrt{E(s)}$ is a concave function and $\mathrm{y_1}/\sqrt{E(s)}$ is a convex function. Thus, the area between the two force limits (B.43) and (B.44) include a concave force set, which leads the problem (B.30) with the stage cost (B.42) to be a non-convex nonlinear program. By linearizing the force limits, the problem (B.30) with the stage cost (B.42) can be formulated as a convex SOCP, see Appendix 3. Note that linearizing any convex function about any trajectory, is always an inner approximation, and linearizing any concave function about any trajectory, results in an outer approximation. Furthermore, the approximations are conservative, therefore, all obtained solutions are inside the feasible force area, see Fig. 11, and also feasible in the original non-convex problem.

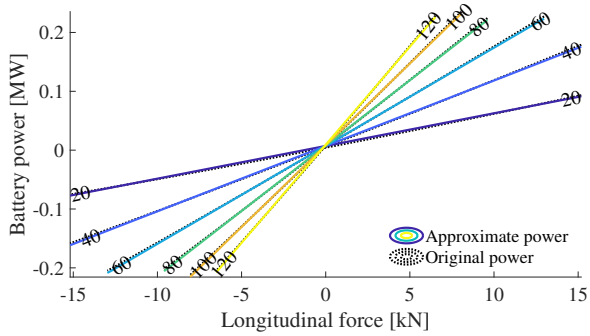

Figure 10: Original and approximated internal power drawn from the electric battery for a given longitudinal velocity and traction force.

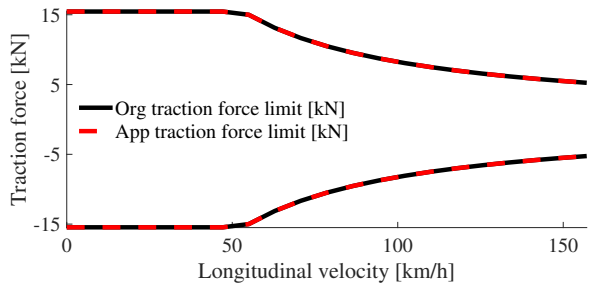

Figure 11: Original and approximated traction force limits of the EM.

Table 1: Simulation parameters

Gravitational acceleration	$g = 9.81\,m/s^2$
Air density	$\rho = 1.29\,kg/m^3$
Vehicle frontal area	$A_f = 10\,m^2$
Rolling resistance coefficient	$c_r = 0.006$
Vehicle mass	$m = 40\,000\,kg$
Aerodynamic drag coefficient	$c_d = 0.5$
Wheel radius	$r_w = 0.50\,m$
Final gear ratio	$r_{fg} = 3$
Cruising set speed	$v_{cru} = 80\,km/h$
Route length	$118\,km$
Number of samples	$N = 500$
Fuel cost	$c^f_{eg} = 1.51\,EUR/litre$
Electricity cost	$c^e_{eg} = 0.18\,EUR/kWh$

6 Results

In this paper, simulations are carried out for the CV and the EV over the 118 km long road from Södertälje to Norrköping in Sweden, which is the same route as considered in [49]. The problems (B.66) and (B.70) are discretized using the forward Euler method. The problems are solved in an SHMPC framework, i.e. $s_{Hmax} \geq s_f$, where travel time at the final position (end of the route) is upper bounded by t_f, using (B.21). The simulation parameters are given in Table 1.

Within the simulations we investigate: (1) sensitivity analysis to evaluate the impact of sampling interval on the solution of the proposed algorithm; (2) how optimisation cost and optimal speed profile change for different discomfort penalties; (3) convergence properties of the algorithm; (4) computation time as a function of the number of samples in the horizon.

6.1 Sampling interval impact on total cost

To investigate the sampling interval's impact on the total cost (B.25a), we calculate normalised relative cost error for varying number of samples, as

$$\text{rel}_{\text{error}} = \frac{\text{cost}_{\text{tot}}^{N} - \text{cost}_{\text{tot}}^{1200}}{\text{cost}_{\text{tot}}^{1200}}, \tag{B.45}$$

for $N \in [200, 1200]$ samples, where $\text{cost}_{\text{tot}}^{N}$ and $\text{cost}_{\text{tot}}^{1200}$ are the total cost calculated for a sampling number of N and 1200, respectively. Note that the obtained total cost value for the finest mesh, i.e. with $N = 1200$, is the most accurate among the investigated meshes. It is observed in Fig. 12 that the normalised relative cost error is less than 0.5 % for number of samples equal to or greater than 500. Thus, in the rest of the investigations we choose the number of samples equal to 500, i.e. the sampling interval is kept at 238 m as the finer mesh for most of the simulations, unless stated otherwise.

6.2 Energy consumption vs. drivability

To study the cost components, i.e. energy cost and the cost due to penalising discomfort, we compare three case studies: Case$^{\text{fl}}$ corresponds to a case with the filtered speed, v_{fl}, which corresponds to the average driver's driving cycle. For this case, the stage costs, (B.66) and (B.70) are calculated using (B.5),

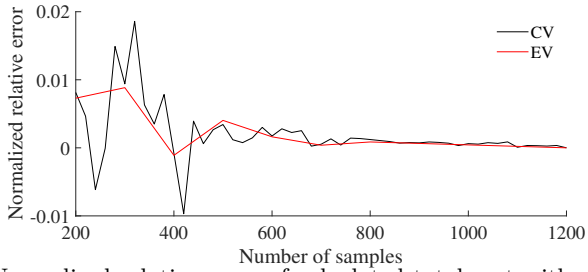

Figure 12: Normalised relative error of calculated total cost with varying number of samples. For number of samples equal to or greater than 500, the normalised relative cost error is less than 0.5 %.

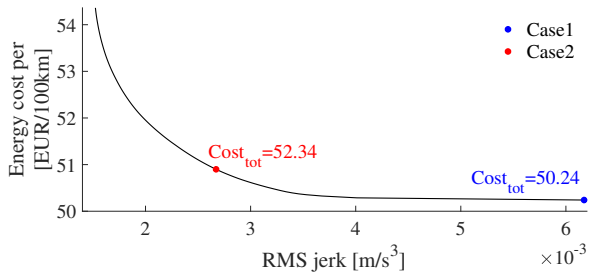

(a) Fuel cost vs. RMS jerk.

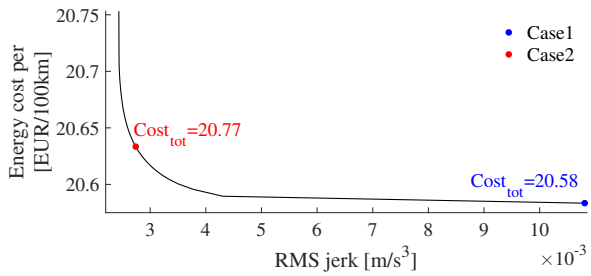

(b) Electricity cost vs. RMS jerk.

Figure 13: Energy cost investigation for different jerk penalty factors. For the large penalty factors, RMS jerk is saturated.

(B.7) and (B.8). In Case 1, i.e. performance drive, the jerk penalty term in (B.66) and (B.70) is kept to zero; and in Case 2, i.e. comfortable drive, non-

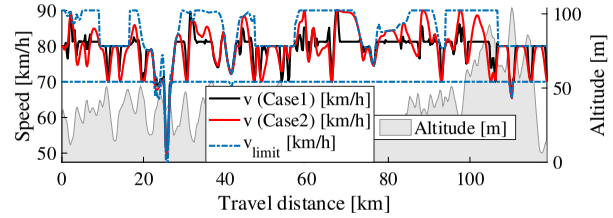

(a) Longitudinal velocity trajectories of CV.

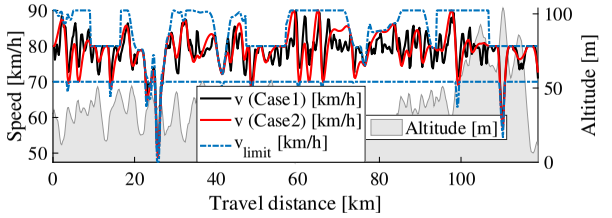

(b) Longitudinal velocity trajectories of EV.

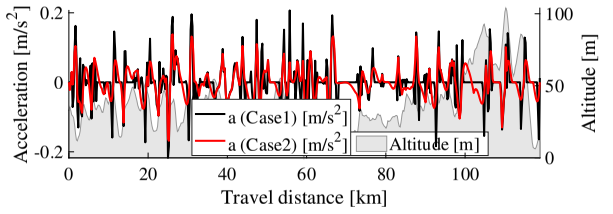

(c) Acceleration trajectories of CV.

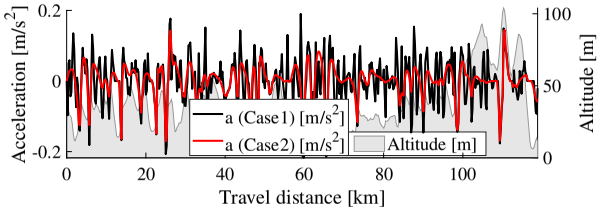

(d) Acceleration trajectories of EV.

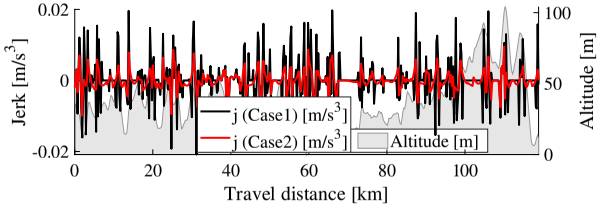

(e) Jerk trajectories of CV.

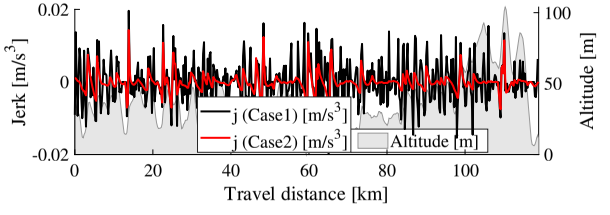

(f) Jerk trajectories of EV.

Figure 14: Optimal longitudinal velocity, acceleration and jerk trajectories for CV and EV. Case 2, i.e. which corresponds to comfortable drive, provides smoother profile and more comfortable driving. Thus, the amplitude of fluctuating acceleration and jerk is decreased.

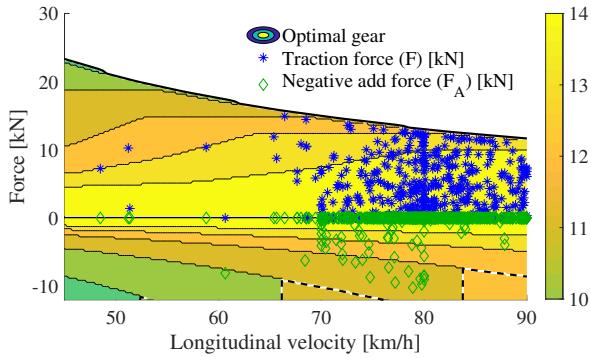

(a) Operating force-speed points of the CV and optimal gear as a contour map.

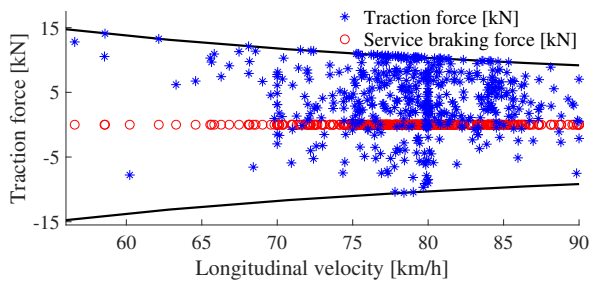

(b) Optimal force-speed points of the EV.

Figure 15: Optimal longitudinal forces vs. vehicle speed for Case 2, i.e. when jerk is penalised.

zero jerk penalty factor is used in (B.66) and (B.70). As an index to measure drivability, the root mean square (RMS) value of jerk

$$j_{\mathrm{RMS}} = \sqrt{\frac{1}{\mathrm{s_f}} \int_0^{\mathrm{s_f}} j^2(s) \mathrm{d}s} \tag{B.46}$$

is used. Note that we have observed the smooth speed profile could be achieved by only penalising jerk, thus the penalty coefficient on the acceleration, w_1, is always kept to be zero for all three cases.

There is a trade-off between the energy cost and comfort, i.e. lower values of RMS jerk yield higher energy cost, see Fig. 1.13(a) and Fig. 1.13(b) for such

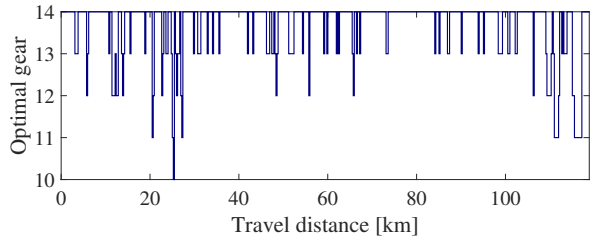

(a) Optimal gear trajectory.

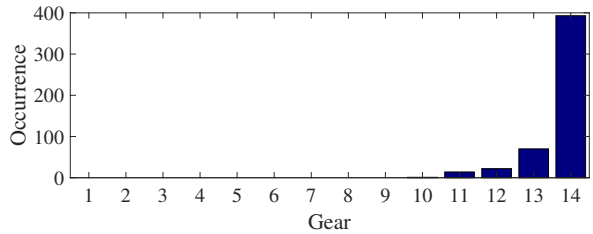

(b) Optimal gear occurrence.

Figure 16: Optimal gear profiles of CV for Case 2, i.e. which corresponds to comfortable drive. The most frequent selected gear is $\gamma = 14$.

trade-off for the CV and the EV respectively. Thus, vehicle manufacturers have wide range of choice to customise the vehicle's performance for a desired energy use and comfort. Note that RMS jerk saturates for large jerk penalty factors. Hereafter, the jerk penalty term in Case 2 is selected in a way that the RMS jerk is equal to $0.0027\,\mathrm{m/s^3}$ for the CV and the EV.

Optimal longitudinal velocity, acceleration and jerk profiles of Case 1 and Case 2 for the CV and the EV are demonstrated in Fig. 14. The velocity profiles without discomfort penalty, i.e. Case 1, are saw-tooth shaped and leads to more aggressive way of driving, however, the latter case provides smoother and more comfortable driving, see Fig. 1.14(a) and Fig. 1.14(b). Note that in addition to the RMS jerk, the RMS acceleration is also reduced in Case 2 compared to Case 1 for the CV and the EV, whereas the acceleration is not penalised in either cases, see Fig. 1.14(c), Fig. 1.14(d), 1.14(e) and Fig. 1.14(f).

Optimal traction and braking force points for the Case 2, i.e. comfortable drive, of CV and EV are shown in Fig. 15. Also, according to the optimal gear

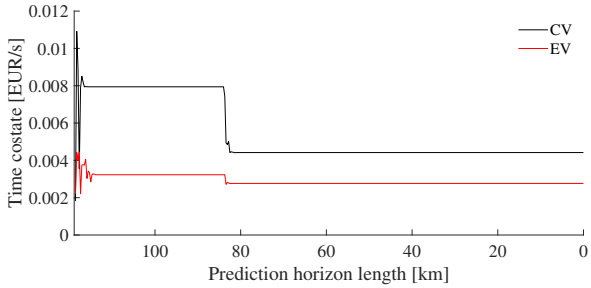

Figure 17: Travel time costate vs. prediction horizon length. The costate converges after few MPC updates, even after disturbance is introduced (at horizon length of 85 km) by suddenly increasing maximum travel time, e.g. due to traffic congestion.

map in Fig. 6, for a pair of total force and longitudinal velocity, the optimal gear is chosen. The optimised gear trajectory and distribution are shown in Fig. 16, where the most frequently selected gear is $\gamma = 14$. We have observed similar results for Case 1 as well.

The cost results of the whole driving mission and their corresponding RMS jerk values for all three case studies of the CV and the EV are given in Table 2.

For the CV, the most fuel-efficient case is Case 1. There is a benefit of 11.60 % to optimize the velocity profile compared to the Case$^{\text{fl}}$, whereas the discomfort of the performance drive is accepted. Furthermore, the results show 7.92 % reduction in total cost of Case 2 compared to the Case$^{\text{fl}}$, despite having 1.30% increase in fuel consumption compared to Case 1. As it has been expected, the proposed algorithm minimises the braking at the pads, i.e. the braking in Case 1 and Case 2 is significantly reduced compared to Case$^{\text{fl}}$.

For the EV, Case 1 provides 6.71% reduction of the total energy cost compared to Case$^{\text{fl}}$ and the total cost benefit of Case 2 is 5.87% compared to Case$^{\text{fl}}$. The comfortable drive, i.e. Case 2, leads to 0.20% increase in electricity usage compared to the performance drive, i.e. Case 1. The RMS jerk in Case 2 is reduced by 29% compared to Case$^{\text{fl}}$, i.e. the RMS jerk is reduced from 0.0038 m/s^3 to 0.0027 m/s^3.

Table 2: Simulation results, energy consumption vs. drivability

CV			
Variable	Case[fl]	Case 1	Case 2
Fuel cost [EUR]	65.33	59.72	60.50
Drivability cost [EUR]	2.23	0	1.71
Total cost [EUR]	67.56	59.72	62.21
Improvement [%]	-	11.60	7.92
j_{RMS} [m/s^3]	0.0026	0.0062	0.0027
$\|\|F_{\text{brk}}\|\|$ [kN]	49.46	35.27	34.07
EV			
Variable	Case[fl]	Case 1	Case 2
Electricity cost [EUR]	24.55	24.47	24.52
Drivability cost [EUR]	1.68	0	0.56
Total cost [EUR]	26.23	24.47	24.69
Improvement [%]	-	6.71	5.87
j_{RMS} [m/s^3]	0.0038	0.0108	0.0027
$\|\|F_{\text{brk}} + \min(F, 0)\|\|$ [kN]	49.15	34.25	40.94

6.3 Algorithm convergence

The convergence curve of the time costate versus shrinking prediction horizon length is shown in Fig. 17. According to the algorithm given in Appendix 1, the time costate is updated once per each MPC stage rather than waiting for the full costate convergence. It can be observed that after few initial MPC stages, the time costate converges to its optimum value. The disturbance rejection properties of the algorithm are verified in Fig. 17. At the prediction horizon of 85 km, maximum travel time changes due to e.g. traffic congestion. It can be seen in Fig. 17 that the travel time costate converges to its new value, which leads the vehicle to arrive to the final position within the updated maximum travel time.

The convergence profile of the SQP algorithm is depicted in Fig. 18, where the algorithm converges to an optimum obtained by solving (B.30) in 5 iterations for both CV and EV case studies. Note that the cost value drops to within 0.4% from the optimum value in the first iteration. We exploit this behaviour through RTI in SHMPC framework, where only one QP is solved in each MPC update rather than waiting for the full SQP convergence, since

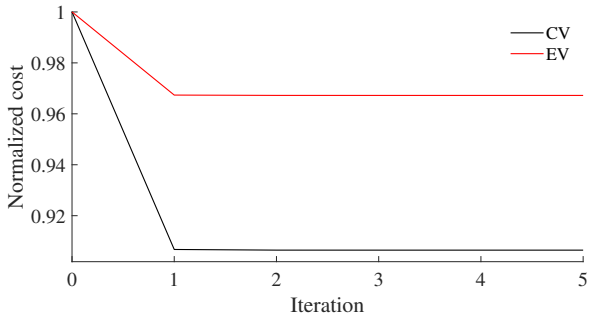

Figure 18: SQP convergence profile. The cost value drops to within 0.4% from optimum value in the first iteration. In iteration 0 the cost value is calculated when the vehicle is driving with the initial estimated trajectory, v_{fl}.

the cost value in the first iteration is very close to the local optimum. Note that the cost value in iteration 0 is calculated when the vehicle is driving with the initial estimated trajectory, v_{fl}.

6.4 Computation time

The computation time profile for various sampling intervals is depicted in Fig. 19, where each QP in the SQP scheme is solved using HPIPM, known as a high-performance tool for solving QPs [50]. Here, the entire route, 118 km, is considered as the prediction horizon. The optimisation was run on a laptop PC with 6600K CPU at 2.81GHz and 16GB RAM. The trend is that as the number of samples increases, the computation time also increases. For real-time applications, it is preferable to have small sampling interval, however the information on the topography should not be lost. In subsections 6.2 and 6.3, the number of samples is kept to 500 and the corresponding computation time for solving the problems (B.66) and (B.70) is less than 20ms, which is considerably low value for a horizon of 118 km with the sampling interval of 238 m.

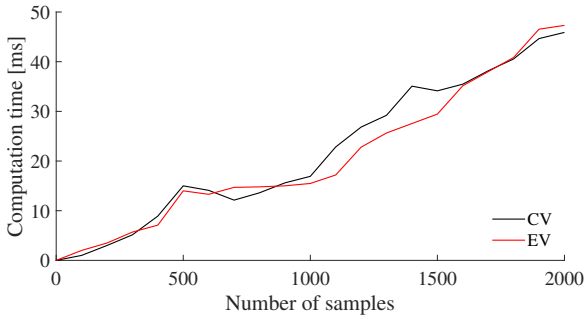

Figure 19: Computation time vs. prediction horizon length using HPIPM for various resolutions of the prediction horizon. The computation time increases linearly with the number of samples.

7 Conclusion

In this paper a computationally efficient algorithm is proposed for eco-driving over long look-ahead horizons. To this end, a bi-level program is formulated, where integer variable, i.e. gear, is decoupled from the real-valued variables. In the bottom level, the optimal gear map is derived in a way that the total energy consumption is minimised. In the top level, the remaining online implementable NLP is formulated. To provide more comfortable way of driving, acceleration and jerk of the vehicle are penalised in the top level's objective. In the NLP, the dynamics on travel time is adjoined to the objective function, using the necessary PMP conditions for optimality, since: 1) the Hamiltonian is not an explicit function of the travel time; 2) the travel time is strictly monotonically increasing function; and 3) the constraint on final time may activate at the final instance. The NLP is solved by applying RIT SQP scheme in MPC framework, i.e. the time costate and the linearization trajectory are updated once per each MPC update. The proposed algorithm is applied to a CV and an EV using SHMPC framework.

According to the simulation results, there is a trade-off between cost and comfort, i.e. driving comfortably is more expensive compared to the performance drive. The energy increase because of penalising the driver's discomfort is 1.30% and 0.20% for the CV and EV, respectively, where the RMS jerk is kept to $0.0027\,\mathrm{m/s^3}$. Also, by using the proposed algorithm, the total cost is reduced up to 11.60% and 7.92% for the CV and EV, respectively, compared

to the average driver's driving cycle. The computation time for the horizon of 118 km is 20 ms, the sampling interval is equal to 238 m. For on-line applications, the small computation time can enhance the optimality, since the suggested optimal state of vehicle can be updated more frequently. Also, in off-line analysis the small computation time can be applied to multi-path problems, where the optimal path of the driving vehicle in terms of energy consumption can be obtained within a small amount of time. The presented algorithm in this paper can also be applied to HEVs as well, where the battery discharge trajectory is generated by the eco-driving supervisor and delivered to lower control layers to charge depleting or charge sustaining operation.

1 Newton method for finding optimal time costate

In this paper, a modified Newton method is applied to find the λ_{t}^{*}. Let

$$f(\lambda_{\mathrm{t}}|\zeta) = t^{*}(\lambda_{\mathrm{t}}, s_{\mathrm{H}}|\zeta) - t_{\mathrm{H}}(\zeta). \tag{B.47}$$

The rule for updating λ_{t} is

$$\lambda_{\mathrm{t}}(\zeta^{+}) = \lambda_{\mathrm{t}}(\zeta) - \frac{f(\lambda_{\mathrm{t}}|\zeta)}{\tilde{f}^{'}(\lambda_{\mathrm{t}}|\zeta)} \tag{B.48}$$

with

$$\tilde{f}^{'}(\lambda_{\mathrm{t}}|\zeta) = \min_{\lambda_{\mathrm{t}}} \left\{ f^{'}(\lambda_{\mathrm{t}}|\zeta), f^{'}_{\max} \right\}, \tag{B.49}$$

$$f^{'}(\lambda_{\mathrm{t}}|\zeta) = \frac{f(\lambda_{\mathrm{t}}|\zeta) - f(\lambda_{\mathrm{t}}|\zeta^{+})}{\lambda_{\mathrm{t}}(\zeta) - \lambda_{\mathrm{t}}(\zeta^{+})}, \tag{B.50}$$

$$f^{'}_{\max} = \frac{f_{\max} - f_{\min}}{\lambda_{\mathrm{t}}^{\min} - \lambda_{\mathrm{t}}^{\max}} \tag{B.51}$$

where $\lambda_{\mathrm{t}}^{\min} = 0\mathrm{EUR}/s$ is the minimum and $\lambda_{\mathrm{t}}^{\max}$ is the maximum time costate. Also, $f_{\min}$ and $f_{\max}$ are

$$f_{\min} = t^{*}(\lambda_{\mathrm{t}}^{\max}, s_{\mathrm{H}}|\zeta) - t_{\mathrm{H}}(\zeta), \tag{B.52}$$

$$f_{\max} = t^{*}(\lambda_{\mathrm{t}}^{\min}, s_{\mathrm{H}}|\zeta) - t_{\mathrm{H}}(\zeta). \tag{B.53}$$

To speed up the convergence to λ_{t}^{*} in (B.48), it is possible to warm start the

algorithm by initialising λ_t at two consecutive instances $\zeta = 0$ and $\zeta = 0^+$, as

$$\lambda_\mathrm{t}(0) = \lambda_\mathrm{t}^{\min} - \frac{f_{\max}}{f'_{\max}} \tag{B.54}$$

$$\lambda_\mathrm{t}(0^+) = \lambda_\mathrm{t}(0) - \frac{f(\lambda_\mathrm{t}|0)}{f'_{\max}}. \tag{B.55}$$

where $\lambda_\mathrm{t}(0)$ is simply the intersection point of $f(\lambda_\mathrm{t}|0) = 0$ with a line connecting the two points $(\lambda_\mathrm{t}^{\min}, f_{\max})$ and $(\lambda_\mathrm{t}^{\max}, f_{\min})$.

2 Inner approximation of traction force limits

To approximate the force limits as inner approximations of the original nonlinear and non-smooth limits, a linear program is solved as:

$$\begin{aligned} &J = \min_x \left(f^T x\right) \\ &\text{subject to} \\ &Ax \leq b \end{aligned} \tag{B.56}$$

such that the area between actual force limits and their approximations is minimised. Therefore, the area between the approximated force limit and the line $F = 0$ is maximised. To this end, for the minimum force limit

$$J = \min_x \int_{\mathrm{v}_0}^{\mathrm{v}_{\max}} (\mathrm{x}_0 + \frac{\mathrm{x}_1}{v})\mathrm{d}v \tag{B.57}$$

and for the maximum force limit

$$J = \min_x \int_{\mathrm{v}_0}^{\mathrm{v}_{\max}} -(\mathrm{y}_0 + \frac{\mathrm{y}_1}{v})\mathrm{d}v. \tag{B.58}$$

Thus,

$$A = \begin{bmatrix} 1 & \frac{1}{v} \end{bmatrix}, \tag{B.59}$$

for the minimum force limit, f, b, x are defined as

$$f = -\begin{bmatrix} \mathrm{v}_{\max} - \mathrm{v}_0 \\ \ln(\mathrm{v}_{\max}) - \ln(\mathrm{v}_0) \end{bmatrix},\ b = F_{\gamma\min}(v),\ x = \begin{bmatrix} \mathrm{x}_0 \\ \mathrm{x}_1 \end{bmatrix} \tag{B.60}$$

and for the maximum force limit as

$$f = \begin{bmatrix} \mathrm{v}_{\max} - \mathrm{v}_0 \\ \ln(\mathrm{v}_{\max}) - \ln(\mathrm{v}_0) \end{bmatrix},\ b = F_{\gamma\max}(v), \quad x = \begin{bmatrix} \mathrm{y}_0 \\ \mathrm{y}_1 \end{bmatrix}. \tag{B.61}$$

The vehicle speed, v, is allowed to vary between two limits

$$v \in [\mathrm{v}_0, \mathrm{v}_{\max}]$$

where for CV v_0=8 km/h and for EV v_0=55 km/h, and $\mathrm{v}_{\max}$ is the maximum reachable speed by the vehicle. In this formulation, the idea is to minimize the area between the original force limit and the inner approximation.

3 Full statement of convex optimal energy consumption program

Here, the full statement of convex optimal energy consumption problem is given for CV and EV case studies. To this end, the nonlinear term $f(E) = 1/\sqrt{E(s)}$ in (B.40) is linearized about a trajectory $\hat{E}(s)$,

$$f^{\mathrm{lin}}(E, \hat{E}) \approx f(\hat{E}) + \left.\frac{\mathrm{d}f(E)}{\mathrm{d}E}\right|_{\hat{E}} (E(s) - \hat{E}(s)). \tag{B.62}$$

Thus, (B.40) is transformed into

$$F^{\mathrm{lin}}_{\gamma\max}(E) = \min\left\{\overline{F}, \mathrm{y}_0 + \mathrm{y}_1\sqrt{\frac{m}{2}} f^{\mathrm{lin}}(E, \hat{E})\right\} \tag{B.63}$$

and by using (B.16),

$$a^{\mathrm{lin}}_{\max}(E) = \min\left\{\overline{\mathrm{a}}, \frac{F^{\mathrm{lin}}_{\gamma\max}(E) - \mathrm{c_a}E - F_\alpha}{\mathrm{m}}\right\}. \tag{B.64}$$

Also by having $F^{\text{lin}}_{\gamma\text{min}}(E) = 0$ for the CV case study,

$$a^{\text{lin}}_{\text{min}}(E) = \max\left\{\underline{\text{a}}, \frac{-\text{c}_\text{a}E + \underline{\text{F}_\text{brk}} - F_\alpha}{\text{m}}\right\}. \tag{B.65}$$

The convex dynamic optimisation problem for the CV case study is now formulated as

$$\min_{j, F_\text{brk}} \int_0^{s_\text{H}} V_\text{CV}(\cdot, \lambda_\text{t}, \hat{E})\text{d}s \tag{B.66a}$$

subject to:

$$E'(s) = \text{m}a(s) \tag{B.66b}$$

$$a'(s) = j(s) \tag{B.66c}$$

$$F(s) = \text{m}a(s) + \text{c}_\text{a}E(s) - F_\text{brk}(s) + F_\alpha(s) \tag{B.66d}$$

$$E(s) \in \frac{\text{m}}{2}[v^2_\text{min}(s), v^2_\text{max}(s)] \tag{B.66e}$$

$$a(s) \in [a^{\text{lin}}_{\text{min}}(E), a^{\text{lin}}_{\text{max}}(E)] \tag{B.66f}$$

$$j(s) \in [\underline{\text{j}}, \bar{\text{j}}] \tag{B.66g}$$

$$F_\text{brk}(s) \in [\underline{\text{F}_\text{brk}}, 0] \tag{B.66h}$$

$$E(0) = E_0, \quad a(0) = a_0 \tag{B.66i}$$

After each SQP iteration, which occurs at each distance step forward, the trajectory about which that the problem is linearized is updated by moving towards the direction of the current optimal solution, i.e.

$$\hat{E}^{(i+1)}(k) = \hat{E}^{(i)}(k) + \beta(E^{*(i)}(k) - \hat{E}^{(i)}(k)). \tag{B.67}$$

where β is the step size that regulates the convergence rate.

For the EV case study, (B.43) is transformed into

$$F^{\text{lin}}_{\gamma\text{min}}(E) = \max\left\{\underline{F}, f^{\text{lin}}(E, \hat{E})\right\} \tag{B.68}$$

using the linearized function, $f^{\text{lin}}(E, \hat{E})$. Therefore, by using (B.16)

$$a^{\text{lin}}_{\text{min}}(E) = \max\left\{\overline{\text{a}}, \frac{F^{\text{lin}}_{\gamma\text{min}}(E) - \text{c}_\text{a}E - F_\alpha}{\text{m}}\right\}. \tag{B.69}$$

Note that the maximum traction force limit for EV is approximated by (B.40). Accordingly, the maximum linearized acceleration is calculated by (B.64).

The convex dynamic optimisation problem for the EV case study is formulated as

$$\min_{j, F_{\text{brk}}} \int_0^{s_{\text{H}}} V_{\text{EV}}(\cdot, \lambda_{\text{t}}, \hat{E}) \mathrm{d}s \tag{B.70a}$$

$$\text{subject to: (B.66b)-(B.66i).} \tag{B.70b}$$

Acknowledgment

This work has been financed by the Swedish Energy Agency (project number: 32226312). The authors would also like to acknowledge Martin Sivertsson from Volvo Cars, Mikael Askerdal from Volvo Truck, and Henrik Svärd and Karl Redbrandt from Scania for the support and helpful discussions during the project.

References

[1] I. T. Forum, *ITF Transport Outlook 2019*. OECD Publishing/ITF, Paris, France, Tech, Rep., 2019, p. 200, ISBN: 9789282103937.

[2] M. A. S. Kamal, M. Mukai, J. Murata, and T. Kawabe, "Ecological vehicle control on roads with up-down slopes," *IEEE Transactions on Intelligent Transportation Systems*, vol. 12, no. 3, pp. 783–794, 2011.

[3] ——, "Model predictive control of vehicles on urban roads for improved fuel economy," *IEEE Transactions on control systems technology*, vol. 21, no. 3, pp. 831–841, 2012.

[4] M. Vajedi and N. L. Azad, "Ecological adaptive cruise controller for plug-in hybrid electric vehicles using nonlinear model predictive control," *IEEE Transactions on Intelligent Transportation Systems*, vol. 17, no. 1, pp. 113–122, 2015.

[5] Y. Luo, T. Chen, S. Zhang, and K. Li, "Intelligent hybrid electric vehicle acc with coordinated control of tracking ability, fuel economy, and ride comfort," *IEEE Transactions on Intelligent Transportation Systems*, vol. 16, no. 4, pp. 2303–2308, 2015.

[6] G. Padilla, S. Weiland, and M. Donkers, "A global optimal solution to the eco-driving problem," *IEEE control systems letters*, vol. 2, no. 4, pp. 599–604, 2018.

[7] J. N. Barkenbus, "Eco-driving: An overlooked climate change initiative," *Energy Policy*, vol. 38, no. 2, pp. 762–769, 2010.

[8] R. Bellman, *Dynamic Programming*. New Jersey: Princeton Univ Pr, 1957.

[9] E. Hellström, M. Ivarsson, J. Åslund, and L. Nielsen, "Look-ahead control for heavy trucks to minimize trip time and fuel consumption," *Control Engineering Practice*, vol. 17, no. 2, pp. 245–254, 2009.

[10] E. Hellström, J. Åslund, and L. Nielsen, "Design of an efficient algorithm for fuel-optimal look-ahead control," *Control Engineering Practice*, vol. 18, no. 11, pp. 1318–1327, 2010.

[11] W. Dib, L. Serrao, and A. Sciarretta, "Optimal control to minimize trip time and energy consumption in electric vehicles," in *2011 IEEE Vehicle Power and Propulsion Conference*, IEEE, 2011, pp. 1–8.

[12] G. Heppeler, M. Sonntag, U. Wohlhaupter, and O. Sawodny, "Predictive planning of optimal velocity and state of charge trajectories for hybrid electric vehicles," *Control Engineering Practice*, vol. 61, pp. 229–243, 2016.

[13] H.-G. Wahl, K.-L. Bauer, F. Gauterin, and M. Holzäpfel, "A real-time capable enhanced dynamic programming approach for predictive optimal cruise control in hybrid electric vehicles," in *16th International IEEE Conference on Intelligent Transportation Systems (ITSC 2013)*, IEEE, 2013, pp. 1662–1667.

[14] L. Bühler, *Fuel-efficient platooning of heavy duty vehicles through road topography preview information*, 2013.

[15] P. Themann, A. Zlocki, and L. Eckstein, "Energieeffiziente fahrzeuglängsführung durch v2x-kommunikation," in *Fahrerassistenzsysteme und Effiziente Antriebe*, W. Siebenpfeiffer, Ed. Wiesbaden: Springer Fachmedien Wiesbaden, 2015, pp. 27–33, ISBN: 978-3-658-08161-4.

[16] S. Boyd and L. Vandenberghe, *Convex Optimization*. Cambridge University Press, 2004.

[17] E. Hellström, J. Åslund, and L. Nielsen, "Management of kinetic and electric energy in heavy trucks," *SAE International Journal of Engines*, vol. 3, no. 1, pp. 1152–1163, 2010.

[18] T. van Keulen, B. de Jager, D. Foster, and M. Steinbuch, "Velocity trajectory optimization in hybrid electric trucks," in *American Control Conference*, Marriott Waterfront, Baltimore, MD, USA, 2010, pp. 5074–5079.

[19] T. van Keulen, B. de Jager, and M. Steinbuch, "Optimal trajectories for vehicles with energy recovery options," in *IFAC World Congress*, Milan, Italy, 2011, pp. 3831–3836.

[20] L. S. Pontryagin, V. G. Boltyanskii, R. V. Gamkrelidze, and E. F. Mishchenko, *The Mathematical Theory of Optimal Processes*. Interscience Publishers, 1962.

[21] R. F. Hartl, S. P. Sethi, and R. G. Vickson, "A survey of the maximum principles for optimal control problems with state constraints," *SIAM review*, vol. 37, no. 2, pp. 181–218, 1995.

[22] C. R. He, H. Maurer, and G. Orosz, "Fuel consumption optimization of heavy-duty vehicles with grade, wind, and traffic information," *Journal of Computational and Nonlinear Dynamics*, vol. 11, no. 6, 2016.

[23] M. Held, O. Flärdh, and J. Mårtensson, "Optimal speed control of a heavy-duty vehicle in urban driving," *IEEE Transactions on Intelligent Transportation Systems*, vol. 20, no. 4, pp. 1562–1573, 2018.

[24] M. Held, "Fuel-efficient look-ahead control for heavy-duty vehicles with varying velocity demands," Ph.D. dissertation, KTH Royal Institute of Technology, 2020.

[25] T. van Keulen, J. Gillot, B. de Jager, and M. Steinbuch, "Solution for state constrained optimal control problems applied to power split control for hybrid vehicles," *Automatica*, vol. 50, no. 1, pp. 187–192, 2014.

[26] N. Murgovski, B. Egardt, and M. Nilsson, "Cooperative energy management of automated vehicles," *Control Engineering Practice*, vol. 57, pp. 84–98, 2016.

[27] L. Johannesson, N. Murgovski, E. Jonasson, J. Hellgren, and B. Egardt, "Predictive energy management of hybrid long-haul trucks," *Control Engineering Practice*, vol. 41, pp. 83–97, 2015.

[28] L. Johannesson, M. Nilsson, and N. Murgovski, "Look-ahead vehicle energy management with traffic predictions," in *IFAC Workshop on Engine and Powertrain Control, Simulation and Modeling (E-COSM)*, vol. 48, Columbus, Ohio, USA, 2015, pp. 244–251.

[29] M. Hovgard, O. Jonsson, N. Murgovski, M. Sanfridson, and J. Fredriksson, "Cooperative energy management of electrified vehicles on hilly roads," *Control Engineering Practice*, vol. 73, pp. 66–78, 2018.

[30] S. Uebel, N. Murgovski, C. Tempelhahn, and B. Bäker, "Optimal energy management and velocity control of hybrid electric vehicles," *IEEE Transactions on Vehicular Technology*, vol. 67, no. 1, pp. 327–337, 2017.

[31] L. Guo, H. Chen, Q. Liu, and B. Gao, "A computationally efficient and hierarchical control strategy for velocity optimization of on-road vehicles," *IEEE Transactions on Systems, Man, and Cybernetics: Systems*, vol. 49, no. 1, pp. 31–41, 2018.

[32] V. Turri, B. Besselink, and K. H. Johansson, "Cooperative look-ahead control for fuel-efficient and safe heavy-duty vehicle platooning," *IEEE Transactions on Control Systems Technology*, vol. 25, no. 1, pp. 12–28, 2016.

[33] L. Guo, B. Gao, Y. Gao, and H. Chen, "Optimal energy management for HEVs in eco-driving applications using bi-level MPC," *IEEE Transactions on Intelligent Transportation Systems*, vol. 18, no. 8, pp. 2153–2162, 2016.

[34] N. Stroe, S. Olaru, G. Colin, K. Ben-Cherif, and Y. Chamaillard, "A two-layer predictive control for hybrid electric vehicles energy management," *IFAC-PapersOnLine*, vol. 50, no. 1, pp. 10 058–10 064, 2017.

[35] S. Uebel, N. Murgovski, B. Baker, and J. Sjoberg, "A 2-level MPC for energy management including velocity control of hybrid electric vehicle," *IEEE Transactions on Vehicular Technology*, 2019.

[36] B. B. Hanson and T. E. Hanson, *Systems and methods for multi-mode unmanned vehicle mission planning and control*, US Patent 9,669,904, Jun. 2017.

[37] A. Hamednia, N. Murgovski, and J. Fredriksson, "Predictive velocity control in a hilly terrain over a long look-ahead horizon," *IFAC-PapersOnLine*, vol. 51, no. 31, pp. 485–492, 2018.

[38] M. Diehl, "Real-time optimization for large scale nonlinear processes," Ph.D. dissertation, University of Heidelberg, 2001.

[39] M. M. Thomas, J. Kardos, and B. Joseph, "Shrinking horizon model predictive control applied to autoclave curing of composite laminate materials," in *Proceedings of 1994 American Control Conference-ACC'94*, IEEE, vol. 1, 1994, pp. 505–509.

[40] N. Murgovski, X. Hu, L. Johannesson, and B. Egardt, "Filtering driving cycles for assessment of electrified vehicles," in *Workshop for new energy vehicle dynamic system and control technology*, Beijing, China, 2013.

[41] T. Lipp and S. Boyd, "Minimum-time speed optimization along a fixed path," *International Journal of Control*, vol. 87, no. 6, pp. 1297–1311, 2014.

[42] N. Murgovski, L. Johannesson, X. Hu, B. Egardt, and J. Sjöberg, "Convex relaxations in the optimal control of electrified vehicles," in *American Control Conference*, Chicago, USA, 2015.

[43] R. de Castro, M. Tanelli, R. E. Araújo, and S. M. Savaresi, "Minimum-time path-following for highly redundant electric vehicles," *IEEE Transactions on Control Systems Technology*, vol. 24, no. 2, pp. 487–501, 2016.

[44] O. Lindgärde, M. Söderman, A. Tenstam, and L. Feng, "Optimal complete vehicle control for fuel efficiency," *Transportation Research Procedia*, vol. 14, pp. 1087–1096, 2016.

[45] A. Hamednia, N. Murgovski, and J. Fredriksson, "Time optimal and eco-driving mission planning under traffic constraints," in *Intelligent Transportation Systems (ITSC)*, Rhodos, Greece, 2020.

[46] M. Diehl, H. G. Bock, and J. P. Schlöder, "A real-time iteration scheme for nonlinear optimization in optimal feedback control," *SIAM Journal on control and optimization*, vol. 43, no. 5, pp. 1714–1736, 2005.

[47] T. Ohtsuka, "A continuation/GMRES method for fast computation of nonlinear receding horizon control," *Automatica*, vol. 40, no. 4, pp. 563–574, 2004.

[48] J. Wahlström and L. Eriksson, "Modelling diesel engines with a variable-geometry turbocharger and exhaust gas recirculation by optimization of model parameters for capturing non-linear system dynamics," *Sage journals*, vol. 225, no. 7, pp. 960–986, 2012.

[49] L. Eriksson, A. Larsson, A. Thomasson, and S. C. Ab, "Heavy duty truck on open road–the aac2016 benchmark," in *IFAC Symposium on Advances in Automotive Control*, 2016.

[50] G. Frison and M. Diehl, "HPIPM: A high-performance quadratic programming framework for model predictive control," *arXiv preprint*, 2020.

PAPER C

Electric vehicle eco-driving under wind uncertainty

Ahad Hamednia, Maryam Razi, Nikolce Murgovski, and Jonas Fredriksson

24rd *IEEE International Conference on Intelligent Transportation Systems (ITSC)*

The layout has been revised.

Abstract

This paper addresses eco-driving of an electric vehicle driving in a hilly terrain under stochastic wind speed uncertainty. The eco-driving problem has been formulated as an optimisation problem, subject to road and traffic information. To enhance the computational efficiency, the dimension of the formulated problem has been reduced by appending trip time dynamics to the problem objective, which is facilitated by necessary Pontryagin's Maximum Principle conditions. To cope with the wind speed uncertainty, stochastic dynamic programming has been applied to solve the problem. Moreover, soft constraints on speed limits (kinetic energy) have been considered in the problem by enforcing sharp penalties in the objective. To benchmark the results, a deterministic controller has also been obtained with the aim of investigating possible constraints violations due to the wind speed uncertainty. For the proposed stochastic controller the optimised speed trajectories always remain within the limits and the violation on the trip time limit is only 8%. On the other hand, the speed and trip time constraints violations for the deterministic controller are 21% and 25%, respectively.

1 Introduction

Electrification of the powertrain is gaining in popularity by vehicle manufacturers worldwide, due to its numerous advantages over conventional powertrain, such as higher energy efficiency, zero local emissions, reduced operating and maintenance costs and lower level of noise [1]. These advantageous factors as well as recent advances in battery technology substantially contribute to the development of more sustainable transportation system, especially with presence of renewable power generation systems and less dependency on oil and fossil fuels [2].

To improve the transportation sustainability, there exist considerable issues that are associated with growth and market penetration of electric vehicles (EVs), namely high initial investments, limited charging infrastructure, long

recharging periods and most notably the vehicle's range limit [1], [3]. Also, imprecise range estimation is another concern that causes the customers or drivers to lose their trust in the displayed range value, and builds up an anxiety of not reaching their destination. This in turn, leads to retention of about 20 % of battery capacity as a safety margin by the drivers [4]. Thus, it is essential to not only increase the range and battery capacity, but also enhance the accuracy of range predictions and energy efficiency of the driving vehicle [5], [6].

Aiming at achieving more accurate range estimation and relieve the anxiety, more realistic conditions have been considered in energy cost models, e.g. battery aging, efficiency model, auxiliary power, road topography and traffic information [7], [8]. In [7] an estimation method has been developed, by providing appropriate information through in-vehicle information systems. In [8] a refined battery state of charge (SoC) estimation algorithm has been devised that yields an enhanced range estimation.

Increasing the vehicular energy efficiency has also been identified as another approach that considerably influences the transportation sustainability development. Thus, it is possible to follow the principles of energy-efficient driving, referred to as eco-driving [9], [10], by optimally planning the velocity profile of the vehicle, subject to road and traffic flow information. The traffic situation can be translated into dynamic speed limits, which indirectly reflect the speed drop due to the presence of e.g. intersections, traffic lights, junctions and ramps [11], [12]. The optimal velocity usually varies, when driving in a hilly terrain. In other words, the vehicle accelerates when climbing uphill, and increases its speed when driving downhill, thus reducing the waste of non-recuperable energy compared to driving with constant speed [13]. To implement this behaviour over complex topographies, advanced control strategies can be applied [14]. Majority of these control strategies can be summarised into: dynamic programming (DP) [15]–[18], Pontryagin's Maximum Principle (PMP) [19], [20], a combination of DP and other methods [21], [22], and multi-level control algorithms [23]–[25].

The major portion of the research being conducted so far, addresses deterministic analysis of the vehicle energy usage. However, the nature of the vehicle driving is stochastic and subject to a vast number of factors that bring uncertainty to the system [1]. In [26] authors identify weather conditions such as wind and temperature as the influencing factors. Furthermore, it is known

that the relative change in energy consumption of EVs due to the environmental factor is much greater than conventional vehicles, because of the EVs' high energy efficiency [27], [28]. Thus, it is crucial to consider the weather conditions in designing the energy-efficient driving of vehicles, especially EVs.

In this paper, eco-driving of an EV has been presented by formulating an optimisation problem under stochastic wind speed uncertainty. Also, with the aim of increasing feasibility in realistic driving situations, the legal and dynamic speed limits have been considered in the problem formulation, using the road and traffic information. The dimension of the formulated problem has been reduced by adjoining the trip time dynamics to the objective. This can considerably boost the computational efficiency. Furthermore, to cope with the stochastic wind disturbance, stochastic dynamic programming (SDP) has been applied to find the global optimum of the problem. To approach the SDP method, the problem in continuous spatial domain has been discretized, and the feasible sets of state variable (kinetic energy) and control input (traction acceleration) are gridded. Moreover, soft constraints on speed limits (kinetic energy) have been imposed to the problem by including sharp penalties to the objective, in order to study potential constraints violations. To this end, a deterministic controller and a stochastic controller have been obtained. The deterministic controller has been derived by considering a deterministic (average) wind speed, whereas for the stochastic controller, the wind speed can have a value from a bounded and discretized normal distribution. Both controllers have been evaluated later on stochastic wind profiles.

This paper is organised as follows: Section 2 addresses the vehicle modelling. In Section 3, the optimal energy consumption problem has been formulated. Section 4 describes the algorithm applied to solve the formulated problem. Section 5 is about the case studies and simulation results. Finally, Section 6 concludes the paper.

2 Vehicle modelling

In this section, trip time, longitudinal dynamics and powertrain dynamics of an EV are presented. Also, the static equations that translate the electric machine's rotational speed and torque into longitudinal velocity and traction acceleration are given.

2.1 Longitudinal dynamics

Consider a vehicle driving on a planned route in a hilly terrain with no stop or direction change of the vehicle's movement. Thus, it is valid to choose travel distance, s, as an independent variable, i.e. decisions are taken with respect to s. The dynamics on trip time is

$$t'(s) = \frac{1}{v(s)}, \tag{C.1}$$

where v is longitudinal velocity.

Originating from the Newton's law of motion, the longitudinal dynamics of the EV considered as a lumped mass is

$$E'(s) = a_{\mathrm{t}}(s) - a_{\alpha}(s) - a_{\mathrm{air}}(E(s), v_{\mathrm{w}}(s)), \tag{C.2}$$

where v_{w} is wind speed, and $E' = \mathrm{d}E/\mathrm{d}s$ is the space derivative of kinetic energy of a unit mass, E, defined as

$$E(s) = \frac{1}{2}v^2(s). \tag{C.3}$$

Also, a_{t} is traction acceleration at the wheel side of the vehicle generated by the EM, and a_{α} and a_{air} are the accelerations associated with roll and aerodynamic drags, respectively. They are defined as

$$a_{\alpha}(s) = \mathrm{g}\left(\sin(\alpha(s)) + \mathrm{c_r}\cos(\alpha(s))\right), \tag{C.4}$$

$$a_{\mathrm{air}}(E(s), v_{\mathrm{w}}(s)) = \frac{\rho_{\mathrm{a}}\mathrm{c_d}\mathrm{A_f}}{2\mathrm{m}}(\sqrt{2E(s)} - v_{\mathrm{w}}(s))^2, \tag{C.5}$$

where g is the gravitational acceleration, α is road gradient, $\mathrm{c_r}$ is rolling resistance coefficient, ρ_{a} is air density, $\mathrm{c_d}$ is nominal aerodynamic drag coefficient, $\mathrm{A_f}$ is frontal area of the vehicle, and m is total lumped mass of the vehicle. Note that all constants, i.e. non-dependent on s, are displayed in upright letters throughout this paper. Also, in several places of the paper, the dependency of the variables that are trajectories in terms of s is not shown for simplicity.

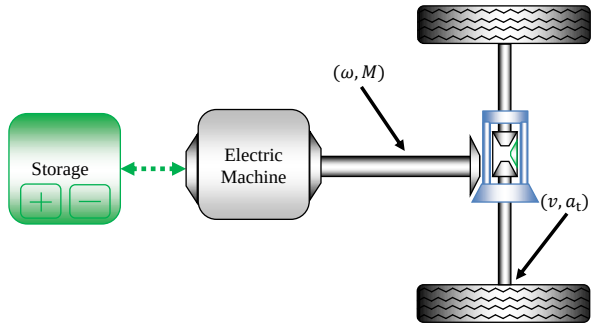

Figure 1: A schematic diagram of an electric powertrain, which includes energy storage unit, i.e. electric battery, electric machine and transmission. The transmission system transfers shaft torque, M, with rotating speed ω, to the wheels with longitudinal speed v and traction acceleration a_t [12].

2.2 Powertrain dynamics

A schematic diagram of the electric powertrain is depicted in Fig. 1. The powertrain includes an energy storage unit, i.e. electric battery, an electric machine (EM) and a transmission. The EM's torque and rotational speed are denoted by M and ω, respectively. The EM is modelled with static relations based on steady state measurements. Accordingly, the steady-state efficiency map of the EM for a given pair of rotational speed and torque is demonstrated in Fig. 2. Within this map, positive and negative torque regions indicate the motoring and the generating modes of operation, respectively. This map has been derived in our earlier work [12]. To provide a certain traction acceleration at the wheels, the EM draws electric power P_b from the storage unit (electric battery). The electric battery power P_b can therefore be written as a function of longitudinal velocity (kinetic energy) and traction acceleration.

The EM torque and rotational speed are translated to traction acceleration and longitudinal velocity respectively, via the transmission system with solely a final gear ratio and wheel radius, using the static equations

$$a_t(s) = \frac{M(s)}{mR}, \quad v(s) = \omega(s)R, \quad R = \frac{r_w}{r_{fg}} \tag{C.6}$$

where r_w is wheel radius and r_{fg} is final gear ratio respectively.

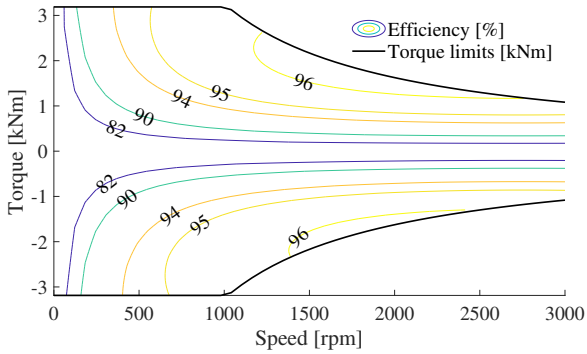

Figure 2: Steady-state efficiency map and torque limits of the electric machine [12].

3 Problem formulation

This section addresses the formulation of an optimisation problem, which aims at optimal velocity planning for the vehicle's entire mission and preserving the trip time within a bound, under the uncertainty of wind speed.

3.1 Objective function

Objective of the formulated problem is to minimise total energy consumption, as

$$\int_{s_0}^{s_f} \frac{P_b(v, a_t)}{v} \mathrm{d}s, \tag{C.7}$$

where the division of the battery power with speed in (C.7) derives directly from the time to space transformation, i.e.

$$\int P_b(v, a_t)\mathrm{d}t = \int \frac{P_b(v, a_t)}{v}\, \mathrm{d}s.$$

3.2 Constraints on longitudinal velocity and traction acceleration

In the problem formulation, we incorporate both legal and dynamic speed limits using the road and traffic information, in order to increase credibility in realistic driving conditions. Such dynamic speed limits can be set due to

the speed drops in different situations, e.g. traffic lights, intersections, ramps and junctions. Thus, total speed limits are computed as

$$v_{\min}(s) = \min\left\{v_{\min}^{\text{legal}}(s), v_{\max}^{\text{dyn}}(s)\right\}, \tag{C.8}$$

$$v_{\max}(s) = \min\left\{v_{\max}^{\text{legal}}(s), v_{\max}^{\text{dyn}}(s)\right\}, \tag{C.9}$$

where $v_{\min}^{\text{legal}}$ and $v_{\max}^{\text{legal}}$ are legal speed limits, and $v_{\max}^{\text{dyn}}$ is maximum dynamic speed limit. The legal and dynamic speed limits can be communicated to the driving vehicle by new modern intelligent speed assistant (ISA) systems, e.g. e-horizon technologies [29]. The traffic constraints' influence on trip time and vehicular energy efficiency has been studied in [12].

The traction acceleration limits are modelled as piecewise functions

$$a_{\text{t}}^{\min}(E) \approx \max\left\{\underline{a_{\text{t}}}, \text{p}_0 + \frac{\text{p}_1}{\sqrt{2E(s)}}\right\} \tag{C.10}$$

$$a_{\text{t}}^{\max}(E) \approx \min\left\{\overline{a_{\text{t}}}, \text{q}_0 + \frac{\text{q}_1}{\sqrt{2E(s)}}\right\} \tag{C.11}$$

where $\underline{a_{\text{t}}}$ and $\overline{a_{\text{t}}}$ are constant minimum and maximum traction acceleration limits, respectively. The coefficients p_1 and q_1 represent maximum and minimum power limits, respectively.

3.3 Energy minimisation problem

Using the relation (C.3) between longitudinal velocity and unit mass kinetic energy, the optimal energy consumption problem is summarised as

$$\pi^*(E, s) = \arg\min_{a_{\text{t}}(s)} \int_{\text{s}_0}^{\text{s}_{\text{f}}} \frac{P_{\text{b}}(E, a_{\text{t}})}{\sqrt{2E(s)}} \text{d}s \tag{C.12a}$$

subject to:

$$t'(s) = \frac{1}{\sqrt{2E(s)}} \tag{C.12b}$$

$$E'(s) = a_{\text{t}}(s) - a_\alpha(s) - a_{\text{air}}(E, v_{\text{w}}) \tag{C.12c}$$

$$E(s) \in \frac{1}{2}[v_{\min}^2(s), v_{\max}^2(s)] \tag{C.12d}$$

$$a_{\text{t}}(s) \in [a_{\text{t}}^{\min}(E), a_{\text{t}}^{\max}(E)] \tag{C.12e}$$

$$t(0) = \mathrm{t}_0, \quad E(0) = \mathrm{E}_0 \tag{C.12f}$$

$$t(\mathrm{s_f}) \leq \mathrm{t_f} \tag{C.12g}$$

where $\pi^*(E, s)$ is the optimal policy for a given pair of unit mass kinetic energy and distance, s_0 and $\mathrm{s_f}$ are initial and final vehicle's positions respectively, t_0 and $\mathrm{t_f}$ are initial and maximum allowed trip times respectively, E_0 is initial unit mass kinetic energy, $E_{\min}$ and $E_{\max}$ are the unit mass kinetic energy limits, and $a_{\mathrm{t}}^{\min}(E)$ and $a_{\mathrm{t}}^{\max}(E)$ are traction acceleration limits. The wind speed v_{w} is modelled as an uncertain variable that is normally distributed, i.e. $v_{\mathrm{w}} \sim \mathcal{N}(\mu, \sigma)$, with unbounded probability density function

$$f(v_{\mathrm{w}}) = \frac{1}{\sigma\sqrt{2\pi}} e^{-\frac{1}{2}(\frac{v_{\mathrm{w}}-\mu}{\sigma})^2}, \tag{C.13}$$

where μ is the mean or expected value and σ is standard deviation of the distribution. The constraints (C.12b)-(C.12e) are enforced for all $s \in [\mathrm{s}_0, \mathrm{s_f}]$. The signs of $\mathrm{p}_1 \leq 0$ and $\mathrm{q}_1 \geq 0$ lead the functions $\mathrm{p}_1/\sqrt{2E(s)}$ and $\mathrm{q}_1/\sqrt{2E(s)}$ to be concave and convex respectively. Accordingly, the area between the two acceleration limits (C.10) and (C.11) is a concave set. Thus, the problem (C.12) is a non-convex nonlinear and stochastic program. This problem has two state variables, t and E, one control input, a_{t}, and a stochastic disturbance v_{w}. We apply SDP method to solve this problem.

4 Energy optimal algorithm

This section addresses two reformulation steps in order to reduce computational complexity of the problem (C.12), and to make it possible to apply the SDP method while incorporating the wind speed uncertainty. Then, the SDP algorithm has been explained. The two reformulation steps are:

1. **Necessary PMP conditions of optimality:** This step aims at reducing the dimension of the problem (C.12), which is done by adjoining the product of the trip time dynamics (C.12b) and optimal time costate to stage cost function.
2. **Problem discretization with soft-constrained kinetic energy limits:** In this step, the problem (C.12) in continuous spatial domain is discretized, then the SDP algorithm can be applied to find the global optimum of the problem. Also, the hard constraints on the kinetic en-

ergy limits (C.12d) are softened by including sharp penalties for the constraints violations to the objective. The incentive for such transformation in the kinetic energy limits is to investigate possible constraint violations on kinetic energy due to the wind speed uncertainty. This will be discussed later in Section 5.

4.1 Necessary PMP conditions of optimality

Here, the problem (C.12) is reformulated by following the necessary PMP conditions for optimality [19]. The Hamiltonian for (C.12) is defined as

$$\begin{aligned}\mathcal{H}(\cdot) = \frac{\lambda_{\mathrm{t}}(s) + P_{\mathrm{b}}(E, a_{\mathrm{t}})}{\sqrt{2E(s)}} + \\ \lambda_{\mathrm{E}}(s)\Big(a_{\mathrm{t}}(s) - a_{\alpha}(s) - a_{\mathrm{air}}(E, v_{\mathrm{w}})\Big),\end{aligned} \tag{C.14}$$

where the symbol $\cdot$ is a compact notation representing multiple variables of the Hamiltonian function, λ_{t} is the costate of trip time, and λ_{E} is the costate of unit mass kinetic energy. It is obvious that the Hamiltonian is not an explicit function of trip time. Thus, according to the necessary PMP conditions for optimality

$$\lambda_{\mathrm{t}}'^{*}(s) = -\left(\frac{\partial \mathcal{H}(\cdot)}{\partial t}\right)^{*} = 0, \tag{C.15}$$

where optimal costate λ_{t}^{*} is a constant value. The optimal costate refers to a value for which the maximum trip time constraint (C.12g) is satisfied. In addition, the constraint (C.12g) may only be activated at the final instance of the driving road, since the trip time (C.12b) is a strictly monotonically increasing function. Note that the maximum trip time limit can be violated at the final instance because of the wind speed uncertainty. This will be discussed later in the Section 5. Thus, considering λ_{t}^{*} to be known, the nonlinear constraint on trip time (C.12b) is removed, and instead the objective function (C.12a) is replaced with

$$\min_{\pi(E,s)} \int_{\mathrm{s_0}}^{\mathrm{s_f}} \frac{\lambda_{\mathrm{t}}^{*}(s) + P_{\mathrm{b}}(E, a_{\mathrm{t}})}{\sqrt{2E(s)}} \mathrm{d}s. \tag{C.16}$$

It is possible to compute the value of λ_{t}^* by numerically solving a two point boundary value problem (TPBVP). To approach this, one can consider that the energy minimisation problem is associated with driving slow, i.e the vehicle would spend the maximum allowed trip time $\mathrm{t_f}$. Thus, $t^*(\lambda_{\mathrm{t}}, \mathrm{s_f}) \approx \mathrm{t_f}$, where t^* represents the optimised trip time. Accordingly, different values can be tried for λ_{t} followed by applying a search method, e.g. Newton [24] or bisection [23], in order to minimise the objective

$$\min_{\lambda_{\mathrm{t}}} ||t^*(\lambda_{\mathrm{t}}, \mathrm{s_f}) - \mathrm{t_f}|| \tag{C.17}$$

where $||\cdot||$ indicates any norm.

4.2 Problem discretization with soft-constrained kinetic energy limits

Using the first order Euler method with a sampling interval of h meters, the discretized optimisation problem with distance samples $s = k\mathrm{h},\ k = 0, \ldots, \mathrm{N}$, is summarised as

$$\begin{aligned}\pi^*(E,k) = \arg\min_{a_{\mathrm{t}}(s)} & \frac{\lambda_{\mathrm{t}}^*}{\sqrt{2E(\mathrm{N})}} + \sum_{k=0}^{\mathrm{N}-1} \frac{\lambda_{\mathrm{t}}^* + P_{\mathrm{b}}(E, a_{\mathrm{t}})}{\sqrt{2E(k)}} \\ & + \mathrm{w}_1 \left(\max\left\{ \frac{1}{2} v_{\min}^2(k) - E(k), 0 \right\} \right) + \\ & + \mathrm{w}_2 \left(\max\left\{ E(k) - \frac{1}{2} v_{\max}^2(k), 0 \right\} \right)\end{aligned} \tag{C.18a}$$

subject to:

$$E(k+1) = \Big(a_{\mathrm{t}}(k) - a_\alpha(k) - a_{\mathrm{air}}(E, v_{\mathrm{w}}) \Big)\mathrm{h} + E(k) \tag{C.18b}$$

$$a_{\mathrm{t}}(k) \in [a_{\mathrm{t}}^{\min}(E), a_{\mathrm{t}}^{\max}(E)] \tag{C.18c}$$

$$E(0) = \mathrm{E}_0 \tag{C.18d}$$

where N is number of samples, h is sampling interval and w_1 and w_2 are the penalty factors, respectively for the lower and upper constraints violations on kinetic energy. Note that the target cost $\lambda_{\mathrm{t}}^*/\sqrt{2E(\mathrm{N})}$ is only applicable

to the trip time. The constraints (C.18b)-(C.18d) are imposed for all $k \in [0, \ldots, \mathrm{N}]$. Also notice that the normal distribution of wind speed is bounded, and discretized in (C.18).

To approach the SDP algorithm, the feasible sets of the state variable (kinetic energy), $\mathcal{E}$, and control input (traction acceleration), $\mathcal{A}$, are gridded as

$$E \in \mathcal{E} = \{e_1, e_2, \ldots, e_n\}, \tag{C.19}$$

$$a_\mathrm{t} \in \mathcal{A} = \{a_{\mathrm{t},1}, a_{\mathrm{t},2}, \ldots, a_{\mathrm{t},m}\}. \tag{C.20}$$

Using the SDP method, the problem (C.18) has been broken down into a sequence of decision steps over s. According to the Proposition 1.1 stated in Appendix 1, the value function V_k and optimal policy map π^* at any state E for the instances $k = \mathrm{N}-1, \ldots, 1$ are calculated by proceeding backwards, using the recursive equation (C.21b). Also, the value function at final instance V_N includes the target cost $\lambda_\mathrm{t}/\sqrt{2E(\mathrm{N})}$. Note that the optimal policy refers to a deterministic controller (DC) if the wind speed is a fixed value, or a stochastic controller (SC) if the wind speed is a variable chosen from the bounded and discretized normal distribution. For obtaining the DC, the expected value and actual value are equal in (C.21b), due to the fixed wind speed value. The optimal control (traction acceleration) values are retrieved from the optimal policy map, proceeding forward by rolling out the dynamical equation (C.18b), starting from the initial kinetic energy value E_0.

5 Results

In this section, simulations are carried out for the EV driving in a 7 km long road with a hilly terrain. Within the simulations, we investigate possible constraint violations on speed (kinetic energy) limits and maximum trip time for the DC and SC. The energy consumption and average trip time for both controllers are equal and fixed. Vehicle and simulation parameters are given in Table 1.

The DC has been obtained, where the wind speed always has a fixed value of 5 m/s. However, the SC has been calculated in a way that the wind speed can take the values between 0 to 10, i.e. $v_\mathrm{w} \in \{0, 1, \ldots, 10\}$, which are normally distributed with $\mu = 5\,\mathrm{m/s}$ and $\sigma = 2$, see Fig. 3.

Table 1: Simulation parameters

Gravitational acceleration	$g = 9.81\,m/s^2$
Air density	$\rho = 1.29\,kg/m^3$
Vehicle frontal area	$A_f = 10\,m^2$
Rolling resistance coefficient	$c_r = 0.006$
Vehicle mass	$m = 40\,000\,kg$
Aerodynamic drag coefficient	$c_d = 0.5$
Wheel radius	$r_w = 0.50\,m$
Final gear ratio	$r_{fg} = 3$
Route length	$7\,km$
Sampling interval	$h = 100\,m$
Penalty factors	$w_1 = w_2 = 80$

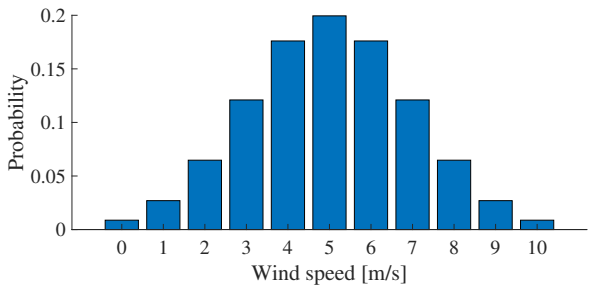

Figure 3: Bounded and discretized normal distribution of wind speed with $\mu = 5\,m/s$ and $\sigma = 2$.

In order to evaluate the performance of both controllers in the face of wind uncertainty, 100 random sequences of wind speed sampled from its distribution with $\mu = 5\,m/s$ and $\sigma = 2$ have been generated for the entire driving road. Thus, the speed trajectory and trip time that are corresponding to each sequence can be calculated, using the recovered optimal control values from each controller's optimal policy map.

For a given combination of longitudinal velocity (kinetic energy) and travel distance, the value functions for the DC and SC are depicted in Fig. 4. Also, optimal policy for the controllers are demonstrated in Fig. 4. It is noticed that the optimal traction acceleration for low speed areas has usually positive values, and for high speed areas it is vice versa. The energy consumption,

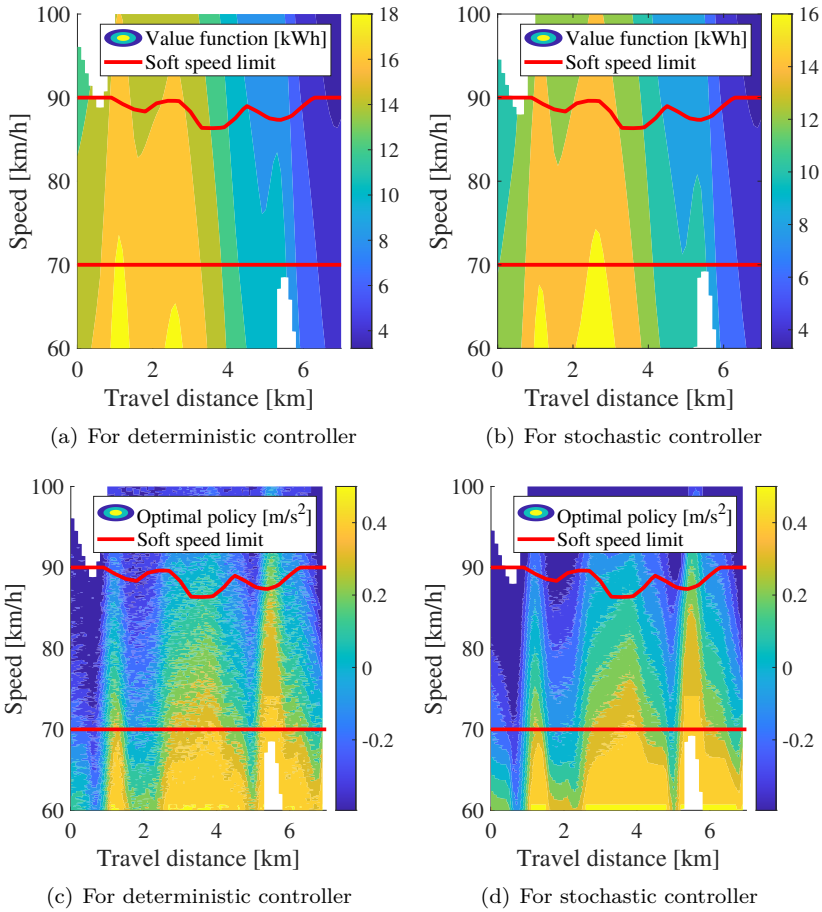

(a) For deterministic controller

(b) For stochastic controller

(c) For deterministic controller

(d) For stochastic controller

Figure 4: Value function (top row) and optimal policy (bottom row) for a given pair of longitudinal velocity and travel distance.

average trip time and time costate for this scenario have been reported in Table 2. The bisection method has been applied for finding λ_t^*, where the algorithm's stopping criterion is (C.17).

Optimal longitudinal velocity trajectory corresponding to each wind speed sequence is shown in Fig. 5 for the controllers. It is observed that for the DC, 21% of the optimised speed trajectories violate the speed limits, while

Table 2: Time costate, average trip time and energy consumption

Variable	**Det. control**	**Sto. control**
λ_{t}^{*} [kW]	39.5	62.75
Average trip time [s]	336	336
Eng. consumption [kWh]	6.29	6.29

the system with SC is always robust against the wind speed changes, and the speed trajectories stay within the bounds. The SC also reduces optimal speed variations, while there are larger speed variations provided by DC. Also, the histograms demonstrating the trip times associated with the wind speed sequences are given in Fig. 6 for the controllers. Similar to the speed limits, the maximum allowed trip time, i.e. $\mathrm{t_f} = 336\,\mathrm{s}$, is violated 25% of all for the DC, whereas for the SC this percentage is simply 8%. These behaviours in speed limits and trip time are reasonable, since the stochasticity in the wind speed has been already taken into account, when obtaining the SC, however, the wind speed is fixed in the DC's design.

6 Conclusion

In this paper, eco-driving of an electric vehicle, under wind speed uncertainty and driving in a hilly terrain, is formulated as an optimisation problem. In the problem formulation, the legal and dynamic speed limits are incorporated, which enhance the credibility in realistic driving conditions. Also, the problem is reformulated by adjoining trip time dynamics to the problem objective, having insights from necessary PMP conditions for optimality. This reduces the dimension of the optimisation problem, which reduces computational complexity. Furthermore, to deal with the wind speed uncertainty, stochastic dynamic programming is employed to solve the problem. Moreover, soft constraints on speed limits (kinetic energy) are considered in the problem by imposing sharp penalties in the problem objective. To study potential constraints violations on speed limits and trip time, a deterministic controller and a stochastic controller are designed. For a fixed energy consumption and average trip time, the constraint violation on speed due to the wind speed uncertainty is 21% for the deterministic controller, whereas the stochastic controller is robust against such violations. Also, the percentage of

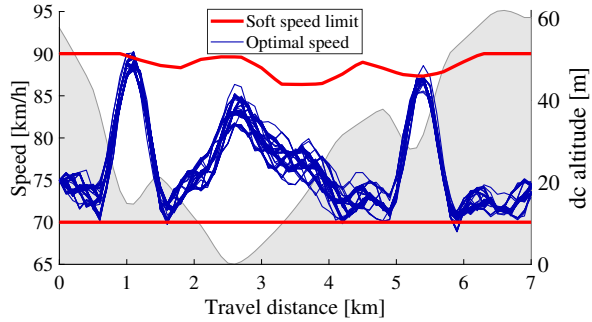

(a) For deterministic controller

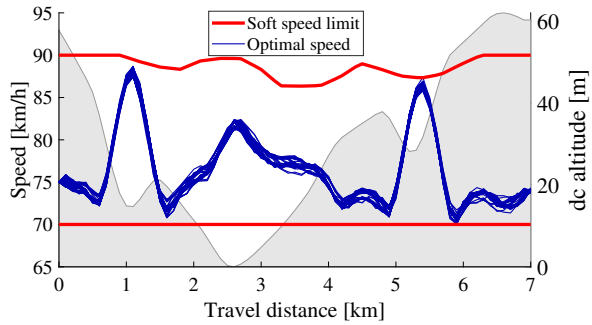

(b) For stochastic controller

Figure 5: Optimal longitudinal velocity trajectories associated with each wind speed sequence.

violated maximum allowed trip time is 25% for the deterministic controller, however, this value for the stochastic controller is simply 8%. Such behaviour on the speed and trip time constraints violations correspond to the fact that within the deterministic controller's design, the wind speed has a fixed value, while in the stochastic controller wind speed can be taken from a vector of normally distributed values.

Acknowledgment

The authors would like to acknowledge Johan Kjellgren, Petter Lindesson, Tove Sohlman, and Hanna Winblad for their endeavour to produce early re-

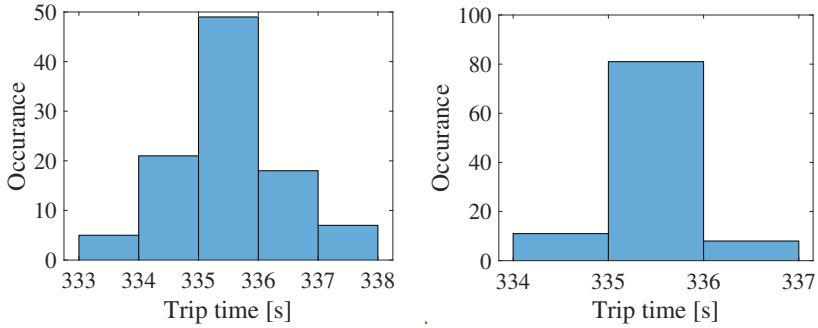

(a) For deterministic controller (b) For stochastic controller

Figure 6: Histogram of trip times corresponding to wind speed sequences.

sults for this project.

1 Stochastic dynamic programming

SDP [30] lies on the *principle of optimality*, i.e. *any tail of an optimal trajectory is an optimal solution as well* [15]. The procedure is to break the optimization problem into a sequence of simpler sub-problems, and derive a policy that optimally acts in the face of stochasticity, as it is explained in the following proposition from [30].

Proposition 1.1. *For the problem* (C.18)*, the last step of following algorithm computes the optimal cost* $V_0(\mathrm{E}_0)$ *for each initial state* E_0*. This algorithm continues backward in distance from instance N-1 to instance 0, as*

$$V_N(E(\mathrm{N})) = \frac{\lambda_\mathrm{t}\mathrm{h}}{\sqrt{2E(\mathrm{N})}}, \tag{C.21a}$$

$$\begin{aligned} V_k(E(k)) = \min_{a_\mathrm{t}(k)\in\mathcal{A}} \mathop{\mathbf{E}}_{v_\mathrm{w}(k)} \Big\{ & g_k\big(E(k), a_\mathrm{t}(k), v_\mathrm{w}(k)\big) + \\ & + V_{k+1}\Big(f_k\big(E(k), a_\mathrm{t}(k), v_\mathrm{w}(k)\big)\Big)\Big\}, \\ & k = \mathrm{N}-1, \ldots, 1, 0, \end{aligned} \tag{C.21b}$$

where g_k is the running cost at instance k defined as

$$g_k = \frac{h\Big(\lambda_\mathrm{t} + P_\mathrm{b}\Big(E(k), a_\mathrm{t}(k)\Big)\Big)}{\sqrt{2E(k)}},$$

and f_k is a function describing the state dynamics at instance k defined as

$$f_k = \Big(a_\mathrm{t}(k) - a_\alpha(k) - a_\mathrm{air}(\sqrt{2E(k)}, v_\mathrm{w}(k))\Big)\mathrm{h} + E(k).$$

Note that the expectation $\mathbf{E}$ *is calculated with respect to probability distribution of v_w. Furthermore, the policy $\pi^*(E,k) = \{\mu_0^*(E), \ldots, \mu_{N-1}^*(E)\}$ is optimal if for each E and k, $a_\mathrm{t}^*(k) = \mu_k^*(E)$ minimises the right hand side of* (C.21b) *[30].*

References

[1] S. Pelletier, O. Jabali, and G. Laporte, "The electric vehicle routing problem with energy consumption uncertainty," *Transportation Research Part B: Methodological*, vol. 126, pp. 225–255, 2019.

[2] Z. Yi and P. H. Bauer, "Optimal stochastic eco-routing solutions for electric vehicles," *IEEE Transactions on Intelligent Transportation Systems*, vol. 19, no. 12, pp. 3807–3817, 2018.

[3] A. Ahmadi, P. H. Bauer, and Y.-F. Huang, "Estimating environmental parameters in connected electric powertrains using set-membership filtering," in *2020 IEEE 91st Vehicular Technology Conference (VTC2020-Spring)*, IEEE, 2020, pp. 1–5.

[4] S. Sautermeister, M. Falk, B. Bäker, F. Gauterin, and M. Vaillant, "Influence of measurement and prediction uncertainties on range estimation for electric vehicles," *IEEE Transactions on Intelligent Transportation Systems*, vol. 19, no. 8, pp. 2615–2626, 2017.

[5] A. Bouscayrol, D. Hissel, R. Trigui, and A. Emadi, "Guest editorial special section on advanced transportation systems," *IEEE Transactions on Vehicular Technology*, vol. 60, no. 9, pp. 4102–4105, 2011.

[6] A. Khaligh, M. Krishnamurthy, and Z. Nie, "Special section on sustainable transportation systems," *IEEE Transactions on Vehicular Technology*, vol. 61, no. 8, pp. 3362–3364, 2012.

[7] M. Eisel, I. Nastjuk, and L. M. Kolbe, "Understanding the influence of in-vehicle information systems on range stress–insights from an electric vehicle field experiment," *Transportation research part F: traffic psychology and behaviour*, vol. 43, pp. 199–211, 2016.

[8] V. R. Tannahill, D. Sutanto, K. M. Muttaqi, and M. A. Masrur, "Future vision for reduction of range anxiety by using an improved state of charge estimation algorithm for electric vehicle batteries implemented with low-cost microcontrollers," *IET Electrical Systems in Transportation*, vol. 5, no. 1, pp. 24–32, 2014.

[9] M. Vajedi and N. L. Azad, "Ecological adaptive cruise controller for plug-in hybrid electric vehicles using nonlinear model predictive control," *IEEE Transactions on Intelligent Transportation Systems*, vol. 17, no. 1, pp. 113–122, 2015.

[10] J. Felipe, J. C. Amarillo, J. E. Naranjo, F. Serradilla, and A. Diaz, "Energy consumption estimation in electric vehicles considering driving style," in *2015 IEEE 18th international conference on intelligent transportation systems*, IEEE, 2015, pp. 101–106.

[11] R. Basso, P. Lindroth, B. Kulcsár, and B. Egardt, "Traffic aware electric vehicle routing," in *2016 IEEE 19th International Conference on Intelligent Transportation Systems (ITSC)*, IEEE, 2016, pp. 416–421.

[12] A. Hamednia, N. Murgovski, and J. Fredriksson, "Time optimal and eco-driving mission planning under traffic constraints," in *Intelligent Transportation Systems (ITSC)*, Rhodos, Greece, 2020.

[13] J. N. Barkenbus, "Eco-driving: An overlooked climate change initiative," *Energy Policy*, vol. 38, no. 2, pp. 762–769, 2010.

[14] A. Sciarretta, G. D. Nunzio, and L. L. Ojeda, "Optimal ecodriving control: Energy-efficient driving of road vehicles as an optimal control problem," *IEEE Control Systems Magazine*, vol. 35, no. 5, pp. 71–90, 2015.

[15] R. Bellman, *Dynamic Programming*. New Jersey: Princeton Univ Pr, 1957.

[16] E. Hellström, J. Åslund, and L. Nielsen, "Design of an efficient algorithm for fuel-optimal look-ahead control," *Control Engineering Practice*, vol. 18, no. 11, pp. 1318–1327, 2010.

[17] H.-G. Wahl, K.-L. Bauer, F. Gauterin, and M. Holzäpfel, "A real-time capable enhanced dynamic programming approach for predictive optimal cruise control in hybrid electric vehicles," in *16th International IEEE Conference on Intelligent Transportation Systems (ITSC 2013)*, IEEE, 2013, pp. 1662–1667.

[18] G. Heppeler, M. Sonntag, U. Wohlhaupter, and O. Sawodny, "Predictive planning of optimal velocity and state of charge trajectories for hybrid electric vehicles," *Control Engineering Practice*, vol. 61, pp. 229–243, 2016.

[19] L. S. Pontryagin, V. G. Boltyanskii, R. V. Gamkrelidze, and E. F. Mishchenko, *The Mathematical Theory of Optimal Processes*. Interscience Publishers, 1962.

[20] M. Held, "Fuel-efficient look-ahead control for heavy-duty vehicles with varying velocity demands," Ph.D. dissertation, KTH Royal Institute of Technology, 2020.

[21] N. Murgovski, B. Egardt, and M. Nilsson, "Cooperative energy management of automated vehicles," *Control Engineering Practice*, vol. 57, pp. 84–98, 2016.

[22] S. Uebel, N. Murgovski, C. Tempelhahn, and B. Bäker, "Optimal energy management and velocity control of hybrid electric vehicles," *IEEE Transactions on Vehicular Technology*, vol. 67, no. 1, pp. 327–337, 2017.

[23] A. Hamednia, N. Murgovski, and J. Fredriksson, "Predictive velocity control in a hilly terrain over a long look-ahead horizon," *IFAC-PapersOnLine*, vol. 51, no. 31, pp. 485–492, 2018.

[24] A. Hamednia, N. K. Sharma, N. Murgovski, and J. Fredriksson, "Computationally efficient algorithm for eco-driving over long look-ahead horizons," *IEEE Transactions on Intelligent Transportation Systems*, 2021.

[25] L. Guo, B. Gao, Y. Gao, and H. Chen, "Optimal energy management for HEVs in eco-driving applications using bi-level MPC," *IEEE Transactions on Intelligent Transportation Systems*, vol. 18, no. 8, pp. 2153–2162, 2016.

[26] Z. Yi and P. H. Bauer, "Effects of environmental factors on electric vehicle energy consumption: A sensitivity analysis," *IET Electrical Systems in Transportation*, vol. 7, no. 1, pp. 3–13, 2016.

[27] ——, "Optimal speed profiles for sustainable driving of electric vehicles," in *2015 IEEE Vehicle Power and Propulsion Conference (VPPC)*, IEEE, 2015, pp. 1–6.

[28] B. Bilgin, P. Magne, P. Malysz, *et al.*, "Making the case for electrified transportation," *IEEE Transactions on Transportation Electrification*, vol. 1, no. 1, pp. 4–17, 2015.

[29] O. Lindgärde, M. Söderman, A. Tenstam, and L. Feng, "Optimal complete vehicle control for fuel efficiency," *Transportation Research Procedia*, vol. 14, pp. 1087–1096, 2016.

[30] D. P. Bertsekas, *Dynamic programming and optimal control*, 2. Athena scientific Belmont, MA, 1995, vol. 1.

PAPER D

Optimal thermal management, charging, and eco-driving of battery electric vehicles

Ahad Hamednia, Nikolce Murgovski, Jonas Fredriksson, Jimmy Forsman, Mitra Pourabdollah, and Viktor Larsson

Re-submitted the revised version to IEEE Transactions on Vehicular Technology in Oct 2022

The layout has been revised.

Abstract

This paper addresses optimal battery thermal management (TM), charging, and eco-driving of a battery electric vehicle (BEV) with the goal of improving its grid-to-meter energy efficiency. Thus, an optimization problem is formulated, aiming at finding the optimal trade-off between trip time and charging cost. The formulated problem is then transformed into a hybrid dynamical system, where the dynamics in driving and charging modes are modeled with different functions and with different state and control vectors. Moreover, to improve computational efficiency, we propose modeling the driving dynamics in a spatial domain, where decisions are made along the traveled distance. Charging dynamics are modeled in a temporal domain, where decisions are made along a normalized charging time. The actual charging time is modeled as a scalar variable that is optimized simultaneously with the optimal state and control trajectories, for both charging and driving modes. The performance of the proposed algorithm is assessed over a road with a hilly terrain, where two charging possibilities are considered along the driving route and the battery is soaked to the ambient before departure. According to the results, trip time including driving and charging times, is reduced by 44 %, compared to a case without active heating/cooling of the battery.

ELECTRIC vehicles (EVs) have recently emerged as a viable technology to fulfill the increasingly stringent legislation against greenhouse gas emissions, and to counteract the drawbacks associated with combustion engine vehicles, such as air pollution, climate change, high operating and maintenance costs, and high oil prices [1], [2]. These issues as well as recent advances in battery technology propel vehicle manufacturers towards electromobility, aiming at developing more sustainable vehicles [3], [4]. However, electromobility must confront several issues hindering the widespread use of EVs. Among them, the limited electric range of EVs is a major concern, which emphasizes the significance of reducing total energy consumption [5]. Also, lithium-ion (Li-ion) batteries, as a dominant cell chemistry in the market, are

highly temperature sensitive, i.e. Li-ions have reduced performance at sub-zero and very high temperatures, e.g. $45\,^{\circ}\mathrm{C} - 60\,^{\circ}\mathrm{C}$ [6]. Thus, developing a suitable battery thermal management (TM) for the electric powertrain is another hindrance to ponder on.

One promising way to reduce the EVs' total energy consumption is by improving *grid-to-meter* efficiency, referred to as the conversion of electrical energy drawn from the electrical grid into kinetic and potential energies required for the vehicle's movement, and accompanied losses. To do so, a suggested way in the literature is to follow the principles of *eco-driving*, [7]. Eco-driving can be achieved by optimizing the velocity profile of the vehicle given the road conditions and traffic situation. In case of driving in a hilly terrain, the optimal speed has a varying behaviour, where the vehicle typically decelerates when climbing uphill, and accelerates when rolling downhill. This reduces non-recuperable energy waste at the braking pads, compared to driving with a constant speed [8]. To obtain an eco-driving velocity profile over complex road topographies, model-based optimal control strategies are employed to optimally coordinate energy use, see e.g., [9]–[12]. Dynamic programming (DP) [13] is a widely used approach in eco-driving applications [14]–[16] due to its capability of solving mixed-integer, non-convex, and nonlinear optimization problems. However, main drawback of the DP method is the *curse of dimensionality*, i.e. computational time increases exponentially with the dimension of the optimal control problem (OCP). For high-dimensional OCPs, it is possible to reduce computational complexity by adjoining system state dynamics to the cost function and neglecting the state constraints [17], as suggested by Pontryagin's Maximum Principle (PMP) [18], [19]. In [20] PMP is used for solving an OCP describing the driving mission with incorporated real-world considerations, e.g. speed limits and safety. A PMP-DP method is devised for optimal speed control and energy management of hybrid electric vehicles (HEVs) in [21]. Nonlinear programming (NLP) is another approach employed to investigate the eco-driving problem and trip time under various traffic situations [22]. In this context, several strategies are proposed in [23]–[29], aiming at improving computational efficiency. Different tasks, for e.g. gear optimization or disturbance rejection, are assigned to distinct layers according to time constants, updating frequency, horizon length, and sampling interval. Also, eco-driving can be used within the model predictive control (MPC) framework for heavy-duty platooning, as shown in [30]. Despite ex-

tensive contributions to the topic of eco-driving, the conducted research does not address the limited driving range of EVs.

Another challenge impeding the deployment of EVs is the development of a battery management system that satisfies strict requirements on durability, performance, and safety. At high battery temperatures, the battery performance is deteriorated due to overexposure to heat, i.e. excessive battery temperatures can create sparks, flames, bulge and bubbles, and lead to battery corrosion and even explosion [31]. This raises the importance of studying battery life, as well as the energy efficiency, being especially relevant for heavy-duty vehicles, where the battery temperature is increased due to frequent use of fast charging [32]–[34]. At sub-zero temperatures, the electro-chemical process is severely slowed due to an increase in internal impedance of the battery cell. This leads to a drastic loss of the cell's available power and energy [35]. Thus, it is essential to develop an adequate TM system, especially in places where temperature drops to sub-zero values for a considerable period of time in a year [36]–[41]. Within the TM system, several components, e.g. heating, ventilation, and air conditioning (HVAC) and high-voltage coolant heater (HVCH), are utilised for controlling the battery pack's temperature. As these components draw power from the battery, it is pivotal to consider the TM when optimizing the EV's grid-to-meter energy efficiency. This increases the awareness on total demanded power of the vehicle to achieve a more energy efficient drive [42], [43]. Thus, various research efforts have been carried out on developing a TM system based on optimal control techniques. In [44] a DP algorithm is applied for the TM of an electrified vehicle parked outside at low temperatures, and unplugged from the electrical grid. The algorithm's objective is to maximise the available energy in the battery pack prior to vehicle departure, and minimise the cell degradation stemming from low temperatures. Also, PMP is used in [45] to find an optimal compromise between battery life expectancy and energy cost. Furthermore, several TM strategies are developed within an MPC framework for achieving energy savings due to optimal cooling/heating [6], [46]–[48]. Moreover, the TM is addressed in [42], [49], where the vehicle speed profile is known a priori [49], or future speed prediction is included into the energy efficiency improvement OCP [42]. Although a vast portion of research has been carried out on TM systems, to the best of our knowledge, the optimal coordination of eco-driving, TM, and charging for a BEV has not been explored, especially for long driving missions

where optimal trade-off has to be made between travel time, energy efficiency and charging cost and trip time.

This paper considers a BEV over long-distance trips with a hilly terrain, where the vehicle's electric range is not sufficient to reach the destination. This necessitates multiple intermediate (and terminal) charging options along the driving route. In addition to the battery temperature, the maximum available cell power is also dependent on the battery state of charge (SoC), i.e. as SoC increases, charging power capability decreases and discharging power capability increases. Furthermore, constraints on state variables and control inputs as well as governing dynamics describing the vehicle's behaviour in driving and charging modes, generally differ. If not formulated with care, the optimal control problem for optimizing eco-driving, charging, and TM may suffer several computational issues. These include: (1) the time instants that belong to the charging and driving modes are not known prior to the vehicle's mission. Thus, there is no explicit clue of using the state variables, control inputs, constraints, and governing dynamics of each mode; (2) the vehicle longitudinal dynamics is nonlinear with respect to trip time, as the aerodynamic drag has quadratic dependency to the vehicle speed. Also, the road slope can be an arbitrary nonlinear function of distance. Furthermore, the speed limits can have abrupt changes for some segments of the road. Accordingly, the speed limits may be non-smooth and non-differentiable functions of travel distance.

To overcome above-mentioned computational drawbacks and achieve optimal TM, charging, and eco-driving, we propose an optimization problem formulated as a hybrid dynamical system. Within the problem formulation, the dynamics in driving and charging modes are modeled with different state and control vectors, and with different functions. The driving dynamics are modeled in a spatial domain, i.e. decisions are made along the traveled distance. Also, charging dynamics are modeled in a temporal domain, i.e. decisions are made along a normalized charging time. The actual charging time is optimized together with the optimal state and control trajectories, for both charging and driving modes. Within the problem formulation, multiple intermediate (and terminal) charging possibilities are included along the route, to increase scalability and feasibility of the developed algorithm in expressing more realistic driving situations. Note that the developed algorithm is capable of addressing both cold and hot ambient operations. However, here we have focused on the impact of cold ambient temperatures on the energy efficiency and trip time,

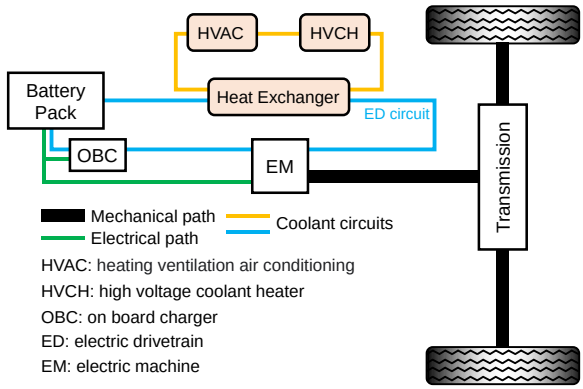

Figure 1: Schematic diagram of the studied electric powertrain, which consists of a battery, an EM, a transmission system, a thermal management system, and an on board charger. The thermal management system includes HVCH and HVAC, which are actively regulating the battery pack and cabin compartment temperatures. HVCH is used for heating and HVAC is used for cooling of the battery and cabin.

when the battery is soaked to ambient before departure.

The rest of the paper is organized as follows. Section 1 addresses the overall vehicle model including longitudinal dynamics and multi-domain powertrain structure. Section 2 corresponds to the problem formulation in a temporal domain. Section 3 proposes the hybrid dynamical system with the goal of alleviating computational drawbacks. In Section 4 simulation results are presented. Finally, Section 5 concludes the paper and outlines the possible future research directions.

1 Modeling

In this section, the dynamics of a BEV is addressed. A multi-domain configuration of an electric powertrain is described, including powertrain components connecting via electrical, thermal, and mechanical paths.

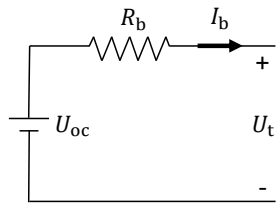

Figure 2: Equivalent circuit of the battery pack, where U_{oc} is open circuit voltage, R_b is internal resistance, I_b is battery discharge current and U_t is battery terminal voltage

1.1 Vehicle as a Lumped Mass System

According to Newton's law of motion, the longitudinal dynamics of the vehicle is described by

$$\dot{v}(t) = a_t(t) - a_{air}(v(t)) - a_\alpha(s(t)), \tag{D.1}$$

where v is the vehicle's speed, a_t is traction acceleration at the wheel side of the vehicle, and a_{air} and a_α are the accelerations associated with air drag (drag force normalized by vehicle mass), rolling resistance, and gravitational load, respectively, as

$$a_{air}(v(t)) = \frac{\rho_a c_d A_f v^2(t)}{2m}, \tag{D.2}$$

$$a_\alpha(s(t)) = g\Big(\sin\big(\alpha(s(t))\big) + c_r \cos(\alpha(s(t)))\Big), \tag{D.3}$$

where ρ_a is air density, c_d is aerodynamic drag coefficient, A_f is the vehicle's frontal area, m is the vehicle's total lumped mass, g is gravitational acceleration, c_r is rolling resistance coefficient, and α is road gradient.

The vehicle's travelled distance, s, is given by integrating the vehicle speed:

(D.4)

where t is trip time.

1.2 Multi-domain Powertrain Structure

Fig. 1 depicts the schematic diagram of the studied electric powertrain. The powertrain consists of an electric machine (EM) as an actuator, a transmission system and a battery for energy supply or storage. Apart from the propulsion components the powertrain also consists of a thermal management system, and an on board charger (OBC). As demonstrated in Fig. 1, the electric power flow through an electrical path is bidirectional depending on operating mode of the EM. Thus, the battery receives energy from the EM in generating mode, or delivers energy to the EM in motoring mode. HVAC and HVCH are the components used for the thermal management of cabin compartment and battery pack, i.e. HVCH and HVAC are mainly used for heating and cooling, respectively. The OBC is a device that is employed for regulating the flow of electricity from the electrical grid to the battery, monitoring the charging rate and for protection purposes. Note that the OBC is assumed to be ideal in this paper.

Electrical Domain

The battery is modeled using an equivalent circuit shown in Fig. 2. The circuit includes a voltage source U_{oc} and an internal resistance R_{b}, which are mainly influenced by SoC and battery temperature, respectively. The internal resistance is generally proportional to the inverse of battery temperature [6]. Thus, the internal resistance has been modeled as a monotonically nonlinear decreasing function of the battery temperature in this paper. Also, a slight mismatch between the internal resistance while charging and discharging has been neglected here. Open-circuit voltage is commonly a nonlinear monotonically increasing function of SoC, which is usually derived via offline experiments at different battery aging stages and ambient temperatures. The change of SoC, soc, is given by

$$\dot{\mathrm{soc}}(t) = -\frac{P_{\mathrm{b}}(t)}{C_{\mathrm{b}} U_{\mathrm{oc}}(\mathrm{soc}(t))}, \tag{D.5}$$

where P_{b} is battery power including internal resistive losses, and C_{b} is maximum capacity of the battery. P_{b} is positive when discharging, and is negative while charging.

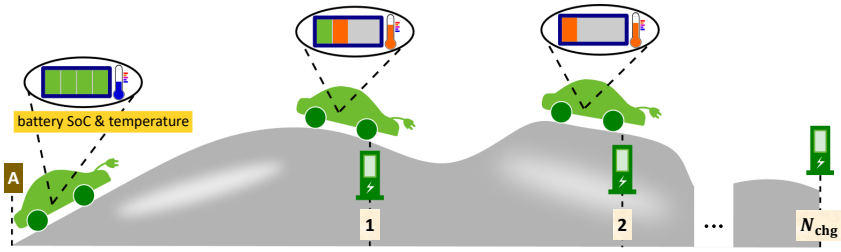

Figure 3: Studied scenario; a BEV is driving in a hilly terrain, where the vehicle starts its mission from point A with a fully charged battery with sub-zero ambient and initial battery temperatures. The indices 1, 2, and N_{chg} denote to the intermediate (an terminal) charging stations.

Thermal Domain

An energy balance is used to describe the battery pack's thermal dynamics. Following the fundamental thermodynamic principle, a lumped-parameter thermal model describing the dynamical variations of the battery pack's temperature is given by

$$\dot{T}_{\text{b}}(t) = \frac{1}{c_{\text{p}} m_{\text{b}}} \big(Q^{\text{gen}}_{\text{pass}}(\cdot) + Q_{\text{act}}(P^{\text{b}}_{\text{hvch}}(t), P^{\text{b}}_{\text{hvac}}(t)) + Q_{\text{exh}}(T_{\text{b}}(t), T_{\text{amb}}(t), v(t)) \big), \tag{D.6}$$

where c_{p} is specific heat capacity of the battery pack, m_{b} is total battery mass, the symbol $\cdot$ is a compact notation for a function of multiple variables, $Q^{\text{gen}}_{\text{pass}}$ is the rate of generated heat by sources that passively affect the battery temperature, Q_{act} is the heat rate due to components that can actively adjust the battery pack temperature, $P^{\text{b}}_{\text{hvch}}$ and $P^{\text{b}}_{\text{hvac}}$ are HVCH and HVAC powers, respectively, and Q_{exh} is the heat exchange rate among the battery pack, ambient air and/or the chassis of the vehicle.

The passive generated heat includes: 1) irreversible ohmic Joule heat induced by the battery internal resistive losses; and 2) heat Q_{ed} generated by electric drivetrain (ED) power losses, including the excess heat from power electronic devices and EM. For a given pair of vehicle speed and traction

acceleration; the passive generated heat rate can be written as

$$Q_{\text{pass}}^{\text{gen}}(\cdot) = R_{\text{b}}(T_{\text{b}}(t))\frac{P_{\text{b}}^2(t)}{U_{\text{oc}}^2(\text{soc}(t))} + Q_{\text{ed}}(v(t), a_{\text{t}}(t)). \tag{D.7}$$

Note that the heat losses can generally originate from two types of conductive and convective heat transfers. In this paper, the uneven conductive distribution of the battery pack temperature associated with the diffusion is overlooked to avoid increasing complexity of the thermal model. Thus, the core and crust battery pack temperatures are assumed to be identical.

The active heat rate

$$Q_{\text{act}}(P_{\text{hvch}}^{\text{b}}(t), P_{\text{hvac}}^{\text{b}}(t)) = \eta_{\text{hvch}} P_{\text{hvch}}^{\text{b}}(t) - \eta_{\text{hvac}} P_{\text{hvac}}^{\text{b}}(t) \tag{D.8}$$

corresponds to the power conversion of the HVCH and HVAC systems, respectively, with the battery pack's heating with efficiency of η_{hvch}, and its cooling with efficiency of η_{hvac}. Note that cabin temperature is not treated as a dynamic state, but rather as a disturbance, irrespective if there is a cooling or heating need for the cabin.

The convective heat exchange rate between the battery pack and ambient air is modeled as

$$Q_{\text{exh}}(T_{\text{b}}(t), t) = \gamma(v(t))(T_{\text{amb}}(t) - T_{\text{b}}(t)), \tag{D.9}$$

where T_{amb} is ambient temperature, and γ is a speed dependent function representing parasitic heat transfer between the battery and the ambient air, i.e. if the battery temperature is higher than the ambient temperature, heat is conveyed from the battery to the ambient air.

Mechanical Domain

The EM when operated in motoring mode, provides propulsive power, which is delivered via the transmission system to the wheels through a mechanical path, see Fig. 1. To do so, the EM torque and rotational speed are translated by the transmission system to traction acceleration and vehicle speed, respectively. Speed dependent bounds on EM torque are translated as limits on traction

acceleration via

$$a_{\mathrm{t}}(t) \in [a_{\min}(v(t)), a_{\max}(v(t))]. \tag{D.10}$$

2 Problem Statement

Consider a BEV driving in a hilly terrain, as in Fig. 3. The trip starts from point **A** with a cold initial battery temperature and a fully-charged battery, where the ambient temperature is also low during the vehicle's trip. As the vehicle continues its drive, the battery depletes and its temperature may increase due to the passive and/or active heating sources. The vehicle's travelled distance is greater than its range and intermediate (and terminal charging) possibilities have to be considered along the driving route.

2.1 Bounds on Vehicle Speed, Battery Power and Grid Power

Using available information about the road and traffic situation, the vehicle speed limits are defined as

$$v(t) \in \begin{cases} [v_{\min}(s(t)), v_{\max}(s(t))], & t \in \mathcal{T}_{\mathrm{drv}} \\ \{0\}, & t \in \mathcal{T}^{i}_{\mathrm{chg}} \end{cases} \tag{D.11}$$

where $0 < v_{\min} \leq v_{\max}$, $\mathcal{T}_{\mathrm{drv}}$ and $\mathcal{T}_{\mathrm{chg}}$ denote the sets of driving and charging time instants, respectively, $i \in \mathcal{I} = \{1, 2, \ldots, N_{\mathrm{chg}}\}$ is charger index, and N_{chg} is total number of charging stations along the route.

The speed limits include legal and dynamic speed limits that resemble realistic driving situations. New modern technologies, e.g. e-horizon systems, can provide the information about legal and dynamic speed limits and the road slope [50]. The dynamic speed limits are enforced due to presence of e.g. intersections, ramps, junctions and traffic lights. The legal speed limits may have abrupt changes for different segments of the driving road, where such variations can lead to computational issues that are discussed later in this Section 2 and Section 3. Note that the vehicle speed is equal to zero when the vehicle stops at the charging station.

For a given pair of battery temperature and SoC, the battery power limits

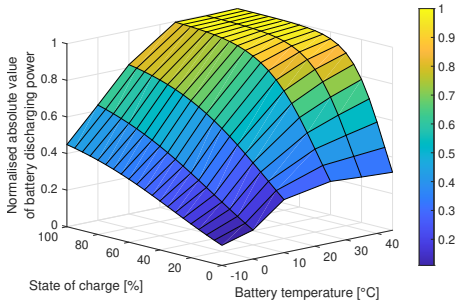

(a) Battery discharge power limit.

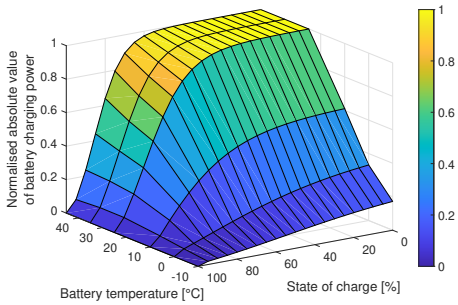

(b) Battery charge power limit.

Figure 4: Normalised absolute value of battery charge and discharge power limit for a given combination of battery temperature and SoC.

corresponding to driving and charging modes for $i \in \mathcal{I}$ are given by

$$P_{\mathrm{b}}(t) \in \begin{cases} [P^{\min}_{\mathrm{b,chg}}(\mathrm{soc}(t), T_{\mathrm{b}}(t)), P^{\max}_{\mathrm{b,dchg}}(\mathrm{soc}(t), T_{\mathrm{b}}(t))], & t \in \mathcal{T}_{\mathrm{drv}} \\ [P^{\min}_{\mathrm{b,chg}}(\mathrm{soc}(t), T_{\mathrm{b}}(t)), 0], & t \in \mathcal{T}^{i}_{\mathrm{chg}} \end{cases} \tag{D.12}$$

where $P^{\max}_{\mathrm{b,dchg}} > 0$ and $P^{\min}_{\mathrm{b,chg}} < 0$ are the battery discharge and charge power limits, respectively. It can be deduced from (D.12) that the battery power during driving can also be negative due to regenerative braking, referred to as a mechanism that transforms the vehicle's kinetic energy into electrical energy to be stored in the battery. Note that the charging power limit may differ in

driving and charging modes. Here, we assume that the same bound is applied, for simplicity, and without loss of generality.

Normalised absolute values of the battery discharge and charge power limits versus battery temperature and SoC are illustrated in Fig. 1.4(a) and Fig. 1.4(b), respectively. These figures are derived from a vehicle original equipment manufacturer (OEM) data to form a representative but generic data set describing the battery power for a given pair of the battery temperature and SoC. As shown in Fig. 1.4(a), the battery discharge power limit is proportional to the battery temperature and SoC level. Also, the charge power limit is proportional to the battery temperature and inverse of SoC level, according to Fig. 1.4(b). For the studied battery, the desirable SoC range for the discharge and charge power limits are about $25\,\% - 100\,\%$ and $0\,\% - 60\,\%$, respectively. Also, the battery temperature window for attaining high power availability is about $25\,^{\circ}\mathrm{C} - 45\,^{\circ}\mathrm{C}$, when both charging and discharging. Thus, for a cold battery it is generally favourable to perform battery *pre-conditioning*, referred to as heating up a cold battery prior to charging in order to charge the battery with a high power, thereby reducing the charging time.

The power P^i_{grid} provided by the ith charger is limited by

$$P^i_{\text{grid}}(t) \in \begin{cases} \{0\}, & t \in \mathcal{T}_{\text{drv}}, \\ [0, P^{i,\max}_{\text{grid}}], & t \in \mathcal{T}^i_{\text{chg}} \end{cases} \tag{D.13}$$

where $P^{i,\max}_{\text{grid}}$ is rated power of the ith charger. It is here assumed that grid charging power is not supplied to the vehicle during the driving mode, although the method presented later can directly be applied to the vehicles driving on an electric road, e.g. when charging lanes are installed on the road [51].

2.2 Objective Function

In order to achieve an optimal compromise between trip time and charging cost, an optimization problem is formulated with the performance function J,

as

$$J(\cdot) = \sum_{i=1}^{N_{\text{chg}}} \Big(\int_{t \in \mathcal{T}^i_{\text{chg}}} c^i_{\text{e}} P^i_{\text{grid}}(t) \mathrm{d}t + c^i_{\text{T}} \max\left(0, t^i_{\text{chg}} - t^i_{\text{occ}}\right) \Big) + \int_{t \in \mathcal{T}} c_{\text{t,trip}} \mathrm{d}t, \tag{D.14}$$

where the charging cost can be expressed as energy and/or time, depending on the pricing plan of each charging station. Thus, J includes:

- Electrical energy supplied to the vehicle by chargers, as

$$\sum_{i=1}^{N_{\text{chg}}} \int_{t \in \mathcal{T}^i_{\text{chg}}} c^i_{\text{e}} P^i_{\text{grid}}(t) \mathrm{d}t, \tag{D.15}$$

  where c_{e} is currency per-kilowatt-hour charging electrical energy cost.
- The time based cost for occupying the charging spot, as

$$\sum_{i=1}^{N_{\text{chg}}} c^i_{\text{occ}} \max\left(0, t^i_{\text{chg}} - t^i_{\text{occ}}\right), \tag{D.16}$$

  where c_{occ} is currency per-minute cost due to occupying the charger for longer time than $t_{\text{occ}} \geq 0$, and t_{chg} is a scalar variable representing charging time.
- A penalty on total trip time, as

$$\int_{t \in \mathcal{T}} c_{\text{t,trip}} \mathrm{d}t, \tag{D.17}$$

  where $c_{\text{t,trip}}$ is the penalty factor and $\mathcal{T} = \bigcup_{i \in \mathcal{I}} \mathcal{T}^i_{\text{chg}} \bigcup \mathcal{T}_{\text{drv}}$. Note that the trip time includes the charging time; thus, charging time may need to be paid twice, due to a longer trip and/or occupying the charger.

2.3 Optimization Problem with Respect to Trip Time

For $i \in \mathcal{I}$, the optimization problem can now be summarised, as

$$\min_{P^{\text{b}}_{\text{hvch}}, P^{\text{b}}_{\text{hvac}}, P_{\text{b}}, P^i_{\text{grid}}, a_{\text{t}}, t^i_{\text{chg}}} J(\cdot) \tag{D.18a}$$

subject to: (D.11)-(D.13) and

$$\dot{T}_{\mathrm{b}}(t) = \frac{1}{c_{\mathrm{p}} m_{\mathrm{b}}}\big(Q^{\mathrm{gen}}_{\mathrm{pass}}(\cdot) + Q_{\mathrm{act}}(P^{\mathrm{b}}_{\mathrm{hvch}}(t), P^{\mathrm{b}}_{\mathrm{hvac}}(t)) + Q_{\mathrm{exh}}(T_{\mathrm{b}}(t), T_{\mathrm{amb}}(t), v(t))\big), \quad t \in \mathcal{T} \tag{D.18b}$$

$$\dot{\mathrm{soc}}(t) = -\frac{P_{\mathrm{b}}(t)}{C_{\mathrm{b}} U_{\mathrm{oc}}(\mathrm{soc}(t))}, \quad t \in \mathcal{T} \tag{D.18c}$$

$$\dot{s}(t) = v(t), \quad t \in \mathcal{T}_{\mathrm{drv}} \tag{D.18d}$$

$$\dot{v}(t) = a_{\mathrm{t}}(t) - a_{\mathrm{air}}(v(t)) - a_{\alpha}(s(t)), \quad t \in \mathcal{T}_{\mathrm{drv}} \tag{D.18e}$$

$$P^{i}_{\mathrm{grid}}(t) + P_{\mathrm{b}}(t) = R(T_{\mathrm{b}}(t))\frac{P^2_{\mathrm{b}}(t)}{U^2_{\mathrm{oc}}(\mathrm{soc}(t))} + P_{\mathrm{prop}}(v(t), a_{\mathrm{t}}(t)) + P^{\mathrm{b}}_{\mathrm{hvch}}(t) + P^{\mathrm{b}}_{\mathrm{hvac}}(t) + P^{\mathrm{c}}_{\mathrm{hvch}}(t) + P_{\mathrm{aux}}(t), \quad t \in \mathcal{T} \tag{D.18f}$$

$$s(t) = s^{i}_{\mathrm{chg}}, \quad t \in \mathcal{T}^{i}_{\mathrm{chg}} \tag{D.18g}$$

$$T_{\mathrm{b}}(t) \in [T^{\min}_{\mathrm{b}}(t), T^{\max}_{\mathrm{b}}(t)], \quad t \in \mathcal{T} \tag{D.18h}$$

$$\mathrm{soc}(t) \in [\mathrm{soc}_{\min}(t), \mathrm{soc}_{\max}(t)], \quad t \in \mathcal{T} \tag{D.18i}$$

$$P^{\mathrm{b}}_{\mathrm{hvch}}(t) \in [0, P^{\max}_{\mathrm{hvch}} - P^{\mathrm{c}}_{\mathrm{hvch}}(t)], \quad t \in \mathcal{T} \tag{D.18j}$$

$$P^{\mathrm{b}}_{\mathrm{hvac}}(t) \in [0, P^{\max}_{\mathrm{hvac}}], \quad t \in \mathcal{T} \tag{D.18k}$$

$$a_{\mathrm{t}}(t) \in [a_{\min}(v(t)), a_{\max}(v(t))], \quad t \in \mathcal{T}_{\mathrm{drv}} \tag{D.18l}$$

$$t^{i}_{\mathrm{chg}} \in [0, t^{\max}_{\mathrm{chg}}] \tag{D.18m}$$

$$T_{\mathrm{b}}(0) = T_{\mathrm{b0}},\ \mathrm{soc}(0) = \mathrm{soc}_0,\ s(0) = s_0,\ v(0) = v_0 \tag{D.18n}$$

$$T_{\mathrm{b}}(t_{\mathrm{f}}) \geq T_{\mathrm{bf}},\ \mathrm{soc}(t_{\mathrm{f}}) \geq \mathrm{soc}_{\mathrm{f}},\ s(t_{\mathrm{f}}) = s_{\mathrm{f}} \tag{D.18o}$$

where T_{b0} and T_{bf} are initial and final battery temperatures, respectively, soc_0 and $\mathrm{soc}_{\mathrm{f}}$ are initial and final SoC values, respectively, s_0 and s_{f} are initial and final travel distances, respectively, v_0 is initial vehicle speed, P_{prop} is propulsion power including the internal losses of the powertrain for a given pair of vehicle speed and traction acceleration, P_{aux} is given auxiliary load demand, $T^{\min}_{\mathrm{b}}$ and $T^{\max}_{\mathrm{b}}$ are the bounds on battery temperature, $\mathrm{soc}_{\min}$ and $\mathrm{soc}_{\max}$ are SoC limits, $P^{\max}_{\mathrm{hvch}}$ and $P^{\max}_{\mathrm{hvac}}$ are the maximum deliverable HVCH and HVAC power values, respectively, s_{chg} is the charging position that is known prior to starting the vehicle's driving mission, $t^{\max}_{\mathrm{chg}}$ is the maximum allowed charging time, and $P^{\mathrm{c}}_{\mathrm{hvch}}$ is the HVCH power demand for heating the cabin compartment. Note that the $P^{\mathrm{c}}_{\mathrm{hvch}}$ is assumed to be a function of the known ambient temperature.

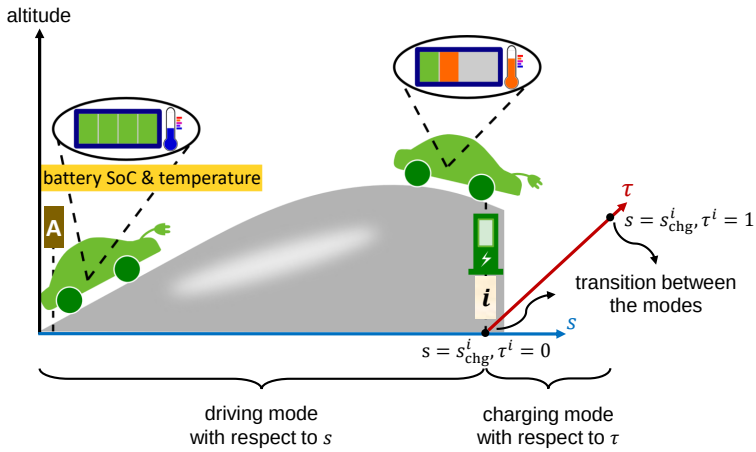

Figure 5: Schematic illustration of a hybrid dynamical system; driving mode, charging mode, and transition between these two modes. During the driving mode decisions are taken in terms of s, and in charging mode the decisions are planned with respect to τ^i, $i \in \mathcal{I}$.

The full problem (D.18), including the formulations of both driving and charging modes with respect to t is difficult to solve due to the following reasons:

- The sets including charging mode and driving mode time instants, $\mathcal{T}_{\text{chg}}$ and $\mathcal{T}_{\text{drv}}$, respectively, are unknown prior to the optimization. Thus, imposing the right dynamics/values/bounds in (D.18) may require introducing integer variables, which would make the problem intractable.
- The vehicle longitudinal dynamics (D.1) is nonlinear with respect to t, as the aerodynamic drag is quadratically dependent to vehicle speed in (D.2), the road gradient can be any arbitrary nonlinear function of t in (D.3), and the speed limits (D.11) may also be non-smooth functions of s, i.e. the speed limits can generally change abruptly for different segments of the driving road. This may require additional integer variables, or smoothing techniques.

The aforementioned issues can severely increase computational complexity. Thus, we propose several reformulation steps in Section 3 that transform the problem (D.18) into a hybrid dynamical system that can be solved in a minute or less on a standard computer.

3 Hybrid Dynamical System Formulation

In this section, the highlighted issues in Section 2 are resolved by exact reformulations of driving and charging modes:

- **Driving mode**: During driving mode, s is chosen as an independent variable instead of t, i.e. decisions are made with respect to s, as depicted in Fig. 5. Such transformation is valid throughout the driving mode, as the vehicle does not stop or change its direction of movement, i.e. $v > 0$. Accordingly, for a certain road topography, the function a_α becomes a fixed trajectory covering the entire route. Also, the speed limits directly turn into position dependent limits; thus, the sudden legal speed limit change is no longer an issue. Furthermore, to remove the nonlinearity in (D.2), kinetic energy of unit mass E with respect to s is selected instead of v, as

$$E(s) = \frac{v^2(s)}{2}. \tag{D.19}$$

  Thus, the aerodynamic drag (D.2) becomes a linear function of unit mass kinetic energy. Note that the decision making in the spatial coordinate is promising, since the charging positions are given. Subsequently, driving and charging distance instances are known prior to optimization.
- **Charging mode**: Despite fixed position of the vehicle at the charging station, battery temperature and SoC will change during charging. Thus, the battery temperature and SoC dynamics cannot be described with respect to s for the charging mode. Instead, the decisions are planned with respect to a variable $\tau^i \in [0, 1]$, defined, as

$$\tau^i = \frac{t}{t^i_{\text{chg}}}, \quad t \in \mathcal{T}^i_{\text{chg}}, i \in \mathcal{I}. \tag{D.20}$$

Following this selection of independent variables, problem (D.18) is transformed into a hybrid dynamical system, see Fig. 5. Note that state variables, control inputs and governing dynamics describing each mode may differ with those from the other mode, which will be explained later in this Section. By repeating the combination of driving and charging modes, it is possible to investigate multiple charging scenarios along the vehicle's trip. Hereafter, the variables with subscripts or superscripts 'drv' or 'chg', are the previously intro-

duced variables that now belong specifically to the driving mode or charging mode, respectively.

3.1 Driving Mode: Dynamics and Performance Function

Governing dynamics during driving mode include the vehicle's longitudinal dynamics, and the dynamical variations of battery temperature and SoC. To group the state variables and control inputs belonging to driving mode, it is possible to introduce state and control vectors, respectively $\mathrm{x}_{\mathrm{drv}}$ and $\mathrm{u}_{\mathrm{drv}}$, with respect to s, as

$$\mathrm{x}_{\mathrm{drv}}(s) = \begin{bmatrix} E(s) \\ \mathrm{soc}^{\mathrm{drv}}(s) \\ T_{\mathrm{b}}^{\mathrm{drv}}(s) \end{bmatrix}, \ \mathrm{u}_{\mathrm{drv}}(s) = \begin{bmatrix} P_{\mathrm{hvch}}^{\mathrm{b,drv}}(s) \\ P_{\mathrm{hvac}}^{\mathrm{b,drv}}(s) \\ a_{\mathrm{t}}(s) \end{bmatrix}.$$

Accordingly, the relation between the time and space derivatives is given as

$$\frac{\mathrm{d}\mathrm{x}_{\mathrm{drv}}(t)}{\mathrm{d}t} = v(s)\frac{\mathrm{d}\mathrm{x}_{\mathrm{drv}}(s)}{\mathrm{d}s}, \quad t \in \mathcal{T}_{\mathrm{drv}}, s \in \mathcal{S}_{\mathrm{drv}}, \tag{D.21}$$

where $\mathcal{S}_{\mathrm{drv}}$ is a set including driving distance instances.

Following (D.21), the longitudinal dynamics (D.1) is now described in the space coordinate s, as

$$\frac{\mathrm{d}E(s)}{\mathrm{d}s} = a_{\mathrm{t}}(s) - c_{\mathrm{a}}E(s) - a_{\alpha}(s), \tag{D.22}$$

where $\frac{\mathrm{d}E}{\mathrm{d}s} = v\frac{\mathrm{d}v}{\mathrm{d}s}$ represents longitudinal acceleration in s domain, and the coefficient $c_{\mathrm{a}} = \rho_{\mathrm{a}}c_{\mathrm{d}}A_{\mathrm{f}}/m$ contains the air drag related factors.

Using the relations (D.19) and (D.21), the dynamical change of battery SoC with respect to s is given by

$$\frac{\mathrm{dsoc}^{\mathrm{drv}}(s)}{\mathrm{d}s} = -\frac{P_{\mathrm{b}}^{\mathrm{drv}}(s)}{C_{\mathrm{b}}U_{\mathrm{oc}}(\mathrm{soc}^{\mathrm{drv}}(s))\sqrt{2E(s)}}. \tag{D.23}$$

Similarly, the position dependent dynamical change of the battery pack

temperature is given by

$$\frac{\mathrm{d}T_{\mathrm{b}}^{\mathrm{drv}}(s)}{\mathrm{d}s} = \frac{1}{c_{\mathrm{p}} m_{\mathrm{b}} \sqrt{2E(s)}} \big(Q_{\mathrm{pass}}^{\mathrm{gen}}(\cdot) + Q_{\mathrm{act}}(P_{\mathrm{hvch}}^{\mathrm{b,drv}}(s), P_{\mathrm{hvac}}^{\mathrm{b,drv}}(s)) + Q_{\mathrm{exh}}(T_{\mathrm{b}}^{\mathrm{drv}}(s), T_{\mathrm{amb}}(s), v(s))\big). \tag{D.24}$$

The power balance equation (D.18f) can also be summarized throughout the driving mode, as

$$P_{\mathrm{b}}^{\mathrm{drv}}(s) = R(T_{\mathrm{b}}^{\mathrm{drv}}(s)) \frac{\big(P_{\mathrm{b}}^{\mathrm{drv}}(s)\big)^2}{U_{\mathrm{oc}}^2(\mathrm{soc}^{\mathrm{drv}}(s))} + P_{\mathrm{prop}}^{\mathrm{drv}}(v(s), a_{\mathrm{t}}(s)) + P_{\mathrm{hvch}}^{\mathrm{b,drv}}(s) + P_{\mathrm{hvac}}^{\mathrm{b,drv}}(s) + P_{\mathrm{hvch}}^{\mathrm{c}}(s) + P_{\mathrm{aux}}^{\mathrm{drv}}(s). \tag{D.25}$$

The governing dynamics during driving mode can be summarized as

$$\frac{\mathrm{dx}_{\mathrm{drv}}(s)}{\mathrm{d}s} = f_{\mathrm{drv}}(\mathrm{x}_{\mathrm{drv}}(s), \mathrm{u}_{\mathrm{drv}}(s), s),$$

where f_{drv} is a vector function including nonlinear scalar functions illustrating each state variable's dynamical change, according to (D.22)-(D.24). We also define a vector $\mathrm{x}_{\mathrm{drv}}^{\mathrm{ts}}$, as

$$\mathrm{x}_{\mathrm{drv}}^{\mathrm{ts}}(s) = \begin{bmatrix} \mathrm{soc}^{\mathrm{drv}}(s) \\ T_{\mathrm{b}}^{\mathrm{drv}}(s) \end{bmatrix},$$

which will be used later for describing the transition between the modes.

The performance function during driving mode includes the penalty on trip time, as

$$J_{\mathrm{drv}}(\cdot) = \int_{s \in \mathcal{S}_{\mathrm{drv}}} \frac{c_{\mathrm{t,trip}}}{\sqrt{2E(s)}} \mathrm{d}s, \tag{D.26}$$

which is directly obtained from the trip time to travel distance transformation, i.e. $\int c_{\mathrm{t,trip}} \mathrm{d}t = \int c_{\mathrm{t,trip}} / \sqrt{2E(s)}\, \mathrm{d}s$. The set $\mathcal{S}_{\mathrm{drv}}$ includes the driving distance instances.

3.2 Charging Mode: Dynamics and Performance Function

The governing dynamics during charging mode corresponds to the dynamical changes of battery temperature and SoC. The state variables and control inputs of charging mode for $i \in \mathcal{I}$ are stacked, respectively, in vectors $\mathrm{x}^i_{\mathrm{chg}}$ and $\mathrm{u}^i_{\mathrm{chg}}$, as

$$\mathrm{x}^i_{\mathrm{chg}}(\tau^i) = \begin{bmatrix} \mathrm{soc}^{i,\mathrm{chg}}(\tau^i) \\ T_{\mathrm{b}}^{i,\mathrm{chg}}(\tau^i) \end{bmatrix}, \ \mathrm{u}^i_{\mathrm{chg}}(\tau^i) = \begin{bmatrix} P_{\mathrm{hvch}}^{i,\mathrm{b,chg}}(\tau^i) \\ P_{\mathrm{hvac}}^{i,\mathrm{b,chg}}(\tau^i) \\ P^i_{\mathrm{grid}}(\tau^i) \end{bmatrix}, \ i \in \mathcal{I}.$$

Also, the charging time associated with each charging station is considered as a scalar variable, which is optimized simultaneously with the optimal state and control trajectories of both driving and charging modes. According to (D.5) and (D.20), the relation between the time derivative and the derivative with respect to $\tau^i \in [0,1]$, $i \in \mathcal{I}$, is

$$\frac{\mathrm{dx}^i_{\mathrm{chg}}(t)}{\mathrm{d}t} = \frac{1}{t^i_{\mathrm{chg}}} \frac{\mathrm{dx}^i_{\mathrm{chg}}(\tau^i)}{\mathrm{d}\tau^i}, \quad t \in \mathcal{T}^i_{\mathrm{chg}}, s(t) = s^i_{\mathrm{chg}}. \tag{D.27}$$

Following (D.27), the dynamical variation of battery SoC with respect to τ^i for $i \in \mathcal{I}$ is given by

$$\frac{\mathrm{dsoc}^{i,\mathrm{chg}}(\tau^i)}{\mathrm{d}\tau^i} = -\frac{t^i_{\mathrm{chg}} P_{\mathrm{b}}^{i,\mathrm{chg}}(\tau^i)}{C_{\mathrm{b}} U_{\mathrm{oc}}(\mathrm{soc}^{i,\mathrm{chg}}(\tau^i))}. \tag{D.28}$$

Similarly, the τ^i dependent dynamical change of the battery pack temperature for $i \in \mathcal{I}$ is given by

$$\begin{aligned} \frac{\mathrm{d}T_{\mathrm{b}}^{i,\mathrm{chg}}(\tau^i)}{\mathrm{d}\tau^i} = \frac{t^i_{\mathrm{chg}}}{c_{\mathrm{p}} m_{\mathrm{b}}} \big(& Q^{\mathrm{gen}}_{\mathrm{pass}}(\cdot) + Q_{\mathrm{act}}(P_{\mathrm{hvch}}^{i,\mathrm{b,chg}}(\tau^i), P_{\mathrm{hvac}}^{i,\mathrm{b,chg}}(\tau^i)) \\ & + Q_{\mathrm{exh}}(T_{\mathrm{b}}^{i,\mathrm{chg}}(\tau^i), T_{\mathrm{amb}}(\tau^i))\big), \end{aligned} \tag{D.29}$$

using (D.5) and (D.20).

For $i \in \mathcal{I}$, the power balance equation (D.18f) during the charging modes is

$$P^i_{\text{grid}}(\tau^i) + P^{i,\text{chg}}_{\text{b}}(\tau^i) = R(T^{i,\text{chg}}_{\text{b}}(\tau^i))\frac{\left(P^{i,\text{chg}}_{\text{b}}(\tau^i)\right)^2}{U^2_{\text{oc}}(\text{soc}^{i,\text{chg}}(\tau^i))} + P^{i,\text{b,chg}}_{\text{hvch}}(\tau^i) + P^{i,\text{b,chg}}_{\text{hvac}}(\tau^i) + P^{i,\text{chg}}_{\text{aux}}(\tau^i). \tag{D.30}$$

Note that propulsion power is equal to zero during charging in (D.30). Also, the power demand for heating the cabin compartment during charging is assumed to be zero in (D.30), without loss of generality in the formulated problem later in 3.3. Such assumption is reasonable for the case when the driver/passengers stay outside the vehicle during charging.

The governing dynamics during charging mode for $i \in \mathcal{I}$ can be summarized as

$$\frac{\mathrm{dx}^i_{\text{chg}}(\tau^i)}{\mathrm{d}\tau^i} = f_{\text{chg}}(\mathrm{x}^i_{\text{chg}}(\tau^i), \mathrm{u}^i_{\text{chg}}(\tau^i), t^i_{\text{chg}}, \tau^i),$$

where f_{chg} is a vector function including nonlinear scalar functions describing each state variable's dynamical variation, according to (D.28) and (D.29).

The performance function associated with charging mode for $i \in \mathcal{I}$, is the compromise among charging energy cost, charging time and charger occupying time cost, as

$$J_{\text{chg}}(\cdot) = \sum_{i=1}^{N_{\text{chg}}} \Big(t^i_{\text{chg}} \int_0^1 \big(c_{\text{t,trip}} + c^i_{\text{e}} P^i_{\text{grid}}(\tau^i)\big)\mathrm{d}\tau^i + c^i_{\text{occ}} \max\left(0, t^i_{\text{chg}} - t^i_{\text{occ}}\right)\Big). \tag{D.31}$$

3.3 Hybrid Dynamical System Formulation

The hybrid dynamical system's formulation for $i \in \mathcal{I}$, can now be summarized as

$$\min_{\mathrm{u}_{\text{drv}}(s), \mathrm{u}^i_{\text{chg}}(\tau^i), t^i_{\text{chg}}} J_{\text{drv}}(\cdot) + J_{\text{chg}}(\cdot) \tag{D.32a}$$

for $\tau^i \in [0,1]$ subject to:

$$\frac{\mathrm{dx}_{\text{drv}}(s)}{\mathrm{d}s} = f_{\text{drv}}(\mathrm{x}_{\text{drv}}(s), \mathrm{u}_{\text{drv}}(s), s), \quad s \in \mathcal{S}_{\text{drv}} \tag{D.32b}$$

$$\frac{\mathrm{d}\mathrm{x}^i_{\mathrm{chg}}(\tau^i)}{\mathrm{d}\tau^i} = f_{\mathrm{chg}}(\mathrm{x}^i_{\mathrm{chg}}(\tau^i), \mathrm{u}^i_{\mathrm{chg}}(\tau^i), \tau^i), \quad s \in s^i_{\mathrm{chg}} \tag{D.32c}$$

$$g_{\mathrm{drv}}(\mathrm{x}_{\mathrm{drv}}(s), \mathrm{u}_{\mathrm{drv}}(s), s) \leq 0, \quad s \in \mathcal{S}_{\mathrm{drv}} \tag{D.32d}$$

$$g_{\mathrm{chg}}(\mathrm{x}^i_{\mathrm{chg}}(\tau^i), \mathrm{u}^i_{\mathrm{chg}}(\tau^i), \tau^i) \leq 0, \quad s \in s^i_{\mathrm{chg}} \tag{D.32e}$$

$$\mathrm{x}_{\mathrm{drv}}(s) \in \mathcal{X}_{\mathrm{drv}}(s), \quad \mathrm{u}_{\mathrm{drv}}(s) \in \mathcal{U}_{\mathrm{drv}}(s), \quad s \in \mathcal{S}_{\mathrm{drv}} \tag{D.32f}$$

$$\mathrm{x}^i_{\mathrm{chg}}(\tau^i) \in \mathcal{X}^i_{\mathrm{chg}}(\tau^i), \quad \mathrm{u}^i_{\mathrm{chg}}(\tau^i) \in \mathcal{U}^i_{\mathrm{chg}}(\tau^i), \quad s \in s^i_{\mathrm{chg}} \tag{D.32g}$$

$$t^i_{\mathrm{chg}} \in [0, t^{\max}_{\mathrm{chg}}] \tag{D.32h}$$

$$\mathrm{x}^i_{\mathrm{chg}}(0) = \mathrm{x}^{\mathrm{ts}}_{\mathrm{drv}}(s^i_{\mathrm{chg}}) \tag{D.32i}$$

$$\mathrm{x}^{\mathrm{ts}}_{\mathrm{drv}}(s^{i^+}_{\mathrm{chg}}) = \mathrm{x}^i_{\mathrm{chg}}(1) \tag{D.32j}$$

$$\mathrm{x}_{\mathrm{drv}}(s_0) \in \mathcal{X}_{\mathrm{drv0}}, \quad \mathrm{x}_{\mathrm{drv}}(s_{\mathrm{f}}) \in \mathcal{X}_{\mathrm{drvf}} \tag{D.32k}$$

where t^i_{chg} is treated as a design parameter, $s^{i^+}_{\mathrm{chg}}$ is an instance where the vehicle is leaving the charging station, $t^{\max}_{\mathrm{chg}}$ is maximum allowed charging time, g_{drv} and g_{chg} denote the system general constraints, respectively during driving and charging modes, including the bounds on battery power and traction acceleration, as

$$g_{\mathrm{drv}}(\cdot) = \left\{ \begin{array}{c} P^{\min}_{\mathrm{b,chg}}(\mathrm{soc}^{\mathrm{drv}}(s), T^{\mathrm{drv}}_{\mathrm{b}}(s)) - P^{\mathrm{drv}}_{\mathrm{b}}(s), \\ P^{\mathrm{drv}}_{\mathrm{b}}(s) - P^{\max}_{\mathrm{b,dchg}}(\mathrm{soc}^{\mathrm{drv}}(s), T^{\mathrm{drv}}_{\mathrm{b}}(s)), \\ a_{\min}(E(s)) - a_{\mathrm{t}}(s), \\ a_{\mathrm{t}}(s) - a_{\max}(E(s)) \end{array} \right\} \tag{D.33a}$$

$$g_{\mathrm{chg}}(\cdot) = \left\{ \; P^{\min}_{\mathrm{b,chg}}(\mathrm{soc}^{i,\mathrm{chg}}(\tau^i)), T^{i,\mathrm{chg}}_{\mathrm{b}}(\tau^i)) - P^{i,\mathrm{chg}}_{\mathrm{b}}(\tau^i). \; \right\} \tag{D.33b}$$

Also, $\mathcal{X}_{\mathrm{drv}}$ and $\mathcal{X}_{\mathrm{chg}}$ denote the feasible sets of state variables, and $\mathcal{U}_{\mathrm{drv}}$ and $\mathcal{U}_{\mathrm{chg}}$ represent the feasible sets of control inputs for each mode. Furthermore, $\mathcal{X}_{\mathrm{drv0}}$ and $\mathcal{X}_{\mathrm{drvf}}$ denote allowed initial states at s_0, and target states at s_{f}, respectively. The constraints (D.32i) and (D.32j) denote the transition between the modes. Thus, the battery temperature and SoC at the arrival of charging station must be equal to the corresponding variables when charging begins. Similarly, the battery temperature and SoC when charging is just finished must be equal to the corresponding variables when the vehicle resumes its drive.

4 Results

In this section, we evaluate the performance of the proposed algorithm to achieve optimal thermal management, eco-driving, and charging of a BEV in the presence of existing constraints. The simulation setup is given in Section 4.1.

4.1 Simulation Setup

The simulations are performed for a BEV over a 440 km long road with a hilly terrain. The BEV starts its mission with 80 % SoC and cold battery, where ambient temperature is also low during the vehicle's entire mission, i.e. $T_{\mathrm{b0}}(s_0) = T_{\mathrm{amb}}(s) = -10\,^{\circ}\mathrm{C}, s \in [s_0, s_{\mathrm{f}}]$. Followed by the constant ambient temperature, the HVCH power demand for heating the cabin compartment during the vehicle's driving mode is also a fixed value. As the driving distance is greater than the vehicle's electric range, one intermediate charging station is visited at $s = 240\,\mathrm{km}$, and a terminal charging station is also considered at the end of the route. The terminal battery SoC is set to be the same percentage as the initial SoC, i.e. 80 %. Also, the rated grid power provided by the chargers as well as the rated battery charging power are 150 kW. Note that the time based cost for occupying the charging spot is not considered in the studied scenario, i.e. $c_{\mathrm{occ}} = 0$. The vehicle and simulation parameters are provided in Table 1.

The NLP (D.32) is discretized using the Runge-Kutta 4^{th} order method [52], with a distance sampling interval of 2 km. Subsequently, the discretized problem is solved in Matlab with the solver IPOPT, using the open source nonlinear optimization tool CasADi [53]. IPOPT is an open-source tool used for solving large-scale NLPs, by implementing an interior-point algorithm for continuous, nonlinear, nonconvex, constrained optimization problems [54]. The optimization was run on a laptop PC with 6600K CPU at 2.81GHz and 16GB RAM, where the solving time is less than a minute.

4.2 Energy Efficiency versus Time

To investigate the trade-off between total charging energy cost versus trip time, the Pareto frontier is derived, as shown in Fig. 6, where the total charging cost includes the electrical energy cost during the intermediate and termi-

Table 1: Vehicle and Simulation Parameters

Gravitational acceleration	$g = 9.81\,\mathrm{m/s^2}$
Air density	$\rho_\mathrm{a} = 1.29\,\mathrm{kg/m^3}$
Vehicle frontal area	$A_\mathrm{f} = 1.36\,\mathrm{m^2}$
Rolling resistance coefficient	$c_\mathrm{r} = 0.013$
Total vehicle mass	$m = 2200\,\mathrm{kg}$
Aerodynamic drag coefficient	$c_\mathrm{d} = 0.6$
Maximum battery capacity	$C_\mathrm{p} = 200\,\mathrm{Ah}$
Specific heat capacity and battery mass product	$c_\mathrm{p} m_\mathrm{b} = 375\,\mathrm{kJ/(K)}$
Route length	$480\,\mathrm{km}$
Distance sampling interval	$2\,\mathrm{km}$
Number of charging along the route	$N_\mathrm{chg} = 2$
Electrical energy cost while charging	$c_\mathrm{e} = 5\,\mathrm{SEK/kWh}$
EM max power	$350\,\mathrm{kW}$
Max. battery power (discharging)	$P^\mathrm{max}_\mathrm{b,dchg} = 350\,\mathrm{kW}$
Min. battery power (charging)	$P^\mathrm{min}_\mathrm{b,chg} = -150\,\mathrm{kW}$
Charger rated power	$P^\mathrm{max}_\mathrm{grid} = 150\,\mathrm{kW}$
Auxiliary load	$P_\mathrm{aux} = 0.5\,\mathrm{kW}$
HVCH power for heating cabin	$P^\mathrm{c}_\mathrm{hvch} = 1.5\,\mathrm{kW}$
HVCH power to heat rate efficiency	$\eta_\mathrm{hvch} = 87\,\%$
HVAC power to heat rate efficiency	$\eta_\mathrm{hvac} = 87\,\%$
Initial battery temperature	$T_\mathrm{b0} = -10\,^\circ\mathrm{C}$
Ambient temperature	$T_\mathrm{amb} = -10\,^\circ\mathrm{C}$
Initial battery state of charge	$\mathrm{soc}_0 = 80\,\%$
Terminal battery state of charge	$\mathrm{soc}_\mathrm{f} = 80\,\%$
Minimum speed limit	$v_\mathrm{min} = 65\,\mathrm{km/h}$
Maximum speed limit	$v_\mathrm{max} = 110\,\mathrm{km/h}$

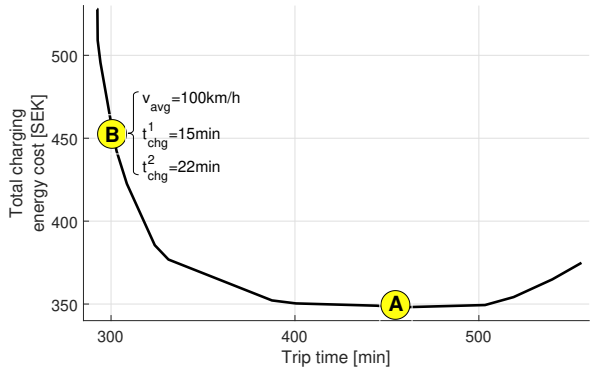

Figure 6: Pareto frontier describing the trade-off between total charging energy cost versus trip time.

nal charging modes. Also, the trip time covers both the driving and charging times. The driving time variations can be characterised as changing the vehicle's average speed. The demonstrated Pareto frontier provides a wide range of choices for various types of car users to customise their trip. In Fig. 6, point A denotes the vehicle's most energy efficient trip, where $c_{\mathrm{t,trip}} = 0$. The trip time can be increased further by letting $c_{\mathrm{t,trip}}$ be negative, where this leads to an increase in the energy cost. Thus, there is a low average speed v_{avg} threshold, here about $v_{\mathrm{avg}} \approx 70\,\mathrm{km/h}$, below which the increased time of accumulating auxiliary loads prevails the benefit of reduced air drag. Point B in Fig. 6 corresponds to the trade-off between trip time and energy, where $v_{\mathrm{avg}} = 100\,\mathrm{km/h}$.

In the remainder of the paper, we will only consider the vehicle's operation in point B. In this point, Case 1, i.e. with active heating/cooling, is compared to Case 2, i.e. without active heating/cooling, to evaluate the impact of *battery pre-conditioning* on the charging time and energy cost. Battery pre-conditioning is characterized as bringing the battery temperature to (or closer to) its desired range, where discharging/charging power availability is increased considerably.

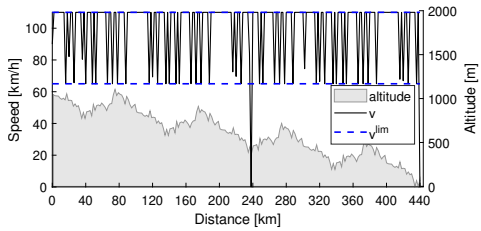

(a) Road topography together with vehicle speed profile and speed limits.

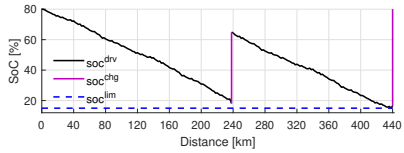

(b) Battery state of charge trajectory together with its bounds.

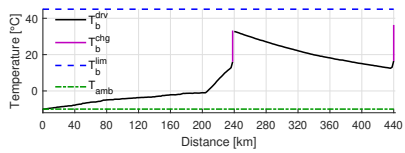

(c) Battery temperature trajectory together with its upper bound and ambient temperature.

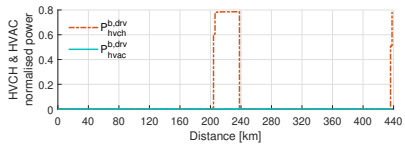

(d) Trajectories of HVCH and HVAC power for battery heating.

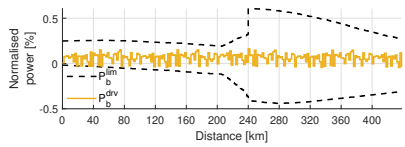

(e) Trajectory of optimal battery power together with its limits (normalised with the maximum battery discharge power).

Figure 7: Case 1; optimal trajectories versus travelled distance. The step changes in battery temperature and SoC at $s = 240\,\text{km}$ and $s = 440\,\text{km}$ in (a) and (b), denote the increase in the corresponding variables during charging mode.

4.3 Case 1: Time Efficient Trip with Active Heating/Cooling

Here, the results are categorized into the optimal trajectories versus travelled distance, and versus charging time during the intermediate and terminal charging events. Total charging cost and trip time are given in Table 2.

Table 2: Charging Cost versus Trip Time

Case	Trip Time (Total Chg. Time) [min]	Chg. Cost [SEK]
Case 1	294 (37)	453
Case 2	323 (66)	444

Optimal Trajectories versus Travelled Distance

Optimal vehicle speed profile together with the speed limits and road topography are depicted in Fig. 1.7(a), where the zero speed values at travel distances $s = 240\,\text{km}$ and $s = 440\,\text{km}$ indicates the vehicle stops at the charging stations. The battery depletes gradually as the vehicle continues its drive, where at the arrival of the charging stations at $s = 240\,\text{km}$ and $s = 440\,\text{km}$, the SoC levels are about 20 % and 15 %, respectively as demonstrated in Fig. 1.7(b). The battery temperature increases primarily due to only the passive heat generation resources, i.e. Joule heat and ED losses, from $s = 0\,\text{km}$ to $s = 205\,\text{km}$, according to Fig. 1.7(c). Later, the HVCH, jointly with the passive heat resources, further raise the battery temperature (from $s = 205\,\text{km}$ to $s = 240\,\text{km}$, and from $s = 435\,\text{km}$ to $s = 440\,\text{km}$). Such battery temperature increase by the HVCH demonstrates the battery pre-conditioning. As shown in Fig. 1.4(b), the charging battery power availability is high for low SoC and high battery temperature region. This leads to a reduced charging time, but higher charging cost instead. Note that the decreasing battery temperature from $s = 240\,\text{km}$ to $s = 435\,\text{km}$ is due to an increased heat transfer to the ambient air, as the temperature difference between the battery pack and ambient air is large for this distance segment. In the intermediate and terminal charging stations, the battery is charged to 63 % and 80 % SoC levels, respectively. The propulsion power, battery discharge power and its limit are shown in Fig. 1.7(e). The battery discharge power limit has a step increase at $s = 240\,\text{km}$, due to the steep rise in SoC and battery temperature due to charging.

Intermediate Charging

During the intermediate charging, in addition to the SoC level increase, the battery temperature also rises steadily, as shown in Fig. 1.8(a) and Fig. 1.8(b).

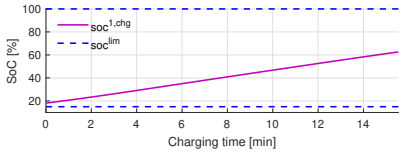

(a) Battery state of charge trajectory together with its bounds.

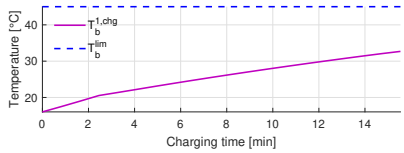

(b) Battery temperature trajectory together with its bounds.

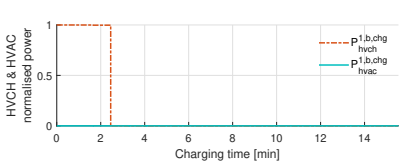

(c) Trajectories of HVCH and HVAC power for battery heating.

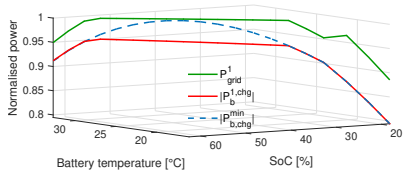

(d) Grid power together with absolute values of battery charging power and its limit, versus battery temperature and SoC.

Figure 8: Case 1; optimal trajectories associated with the vehicle's intermediate charging mode at $s = 240\,\text{km}$.

The SoC level throughout the intermediate charging is always in a range with high charging power availability. Also, HVCH stays on for about 2.5 min from the beginning of charging, in order to further raise the battery temperature above 20 °C. This allows charging with high power and for a short time period, which is about 15 min here. Fig. 1.8(d) illustrates a 3D plot including grid power as well as the absolute values of battery charging power and its limit versus SoC and battery temperature values. The difference between the grid power and battery power is due to the Joule heat losses and the HVCH power demand for heating the battery pack.

Terminal Charging

The battery SoC and temperature during terminal charging at $s = 440\,\text{km}$, have similar behaviours as they had during the intermediate charging. In the beginning of charging, initial battery SoC and temperature, respectively, are about 15 % and 17 °C. HVCH stays on for about a minute from the beginning of charging, and the battery temperature rises up to about 20 °C accordingly.

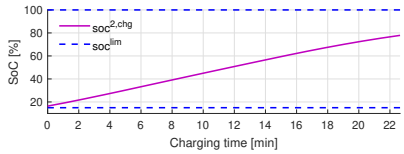

(a) Battery state of charge trajectory together with its bounds.

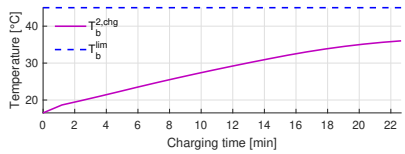

(b) Battery temperature trajectory together with its bounds.

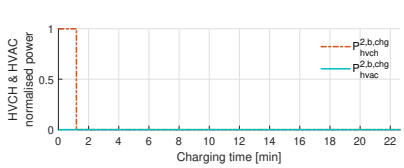

(c) Trajectories of HVCH and HVAC power for battery heating.

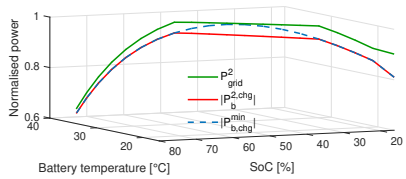

(d) Grid power together with absolute values of battery charging power and its limit, versus battery temperature and SoC.

Figure 9: Case 1; optimal trajectories associated with the vehicle's terminal charging mode at $s = 440\,\text{km}$.

Fig. 1.9(d) shows a 3D plot including grid power together with the absolute values of battery charging power and its limit for a given combination of SoC and battery temperature. As expected, the charging power availability drops for high SoC values. The charging time is about 22 min.

4.4 Case 2: Time Efficient Trip without Active Heating/Cooling

Similar to Section 4.3, the simulation results are summarized into the distance based and time based trajectories. Here, the HVCH and HVAC are not used, respectively for the battery heating and cooling throughout the vehicle's entire trip.

Optimal Trajectories versus Travelled Distance

Optimal vehicle speed profile as well as the speed limits and road topography are depicted in Fig. 1.10(a). The battery depletion profile, shown in

Fig. 1.10(b), follows a similar trend as the one in Case 1, since in both cases in addition to the identical simulation parameters and the driving behaviour are similar, i.e. $v_{\text{avg}} = 100km/h$. The SoC levels at the arrival of the charging stations at $s = 240\,\text{km}$ and $s = 440\,\text{km}$, are respectively about 17 % and 15 %, as depicted in Fig. 1.10(b). The battery temperature increase is simply due to Joule heat and ED losses, according to Fig. 1.10(c), where at the arrival of the intermediate and terminal charging stations, the battery temperature is 0 °C and 5 °C, respectively. These battery temperature values are lower compared to Case 1, as no active heating is applied in Case 2. In the intermediate and terminal charging stations, the battery is charged to about 60 % and 80 % SoC levels, respectively. The propulsion power together with the battery discharge power and its limit are shown in Fig. 1.10(d), where the limit is generally lower compared to the one in Case 1, due to the battery's operation in the lower temperature region.

Intermediate and Terminal Charging

During both intermediate and terminal charging periods, the battery temperature and SoC increase monotonically, as demonstrated in Fig. 1.11(a) and Fig. 1.11(b), and Fig. 1.12(a) and Fig. 1.12(b), respectively. Also, the grid power together with the absolute values of battery charging power and its limit versus battery temperature and SoC, are shown in Fig. 1.11(c) and Fig. 1.12(c), respectively for the intermediate and terminal charging modes. The charging power availability for Case 2 is lower compared to Case 1, which leads to a higher charging time. According to the results reported in Table 2, total charging time for Case 2 is 66 min, which is increased by 44 % compared to the Case 1 with optimal battery pre-conditioning. Instead, the charging cost is simply reduced by 2 %.

5 Discussion, Conclusion, and Future Work

In this paper, optimal TM, charging, and eco-driving problems are jointly solved for a BEV over a long-distance trip. To do so, an optimization problem in the form of a hybrid dynamical system is formulated, in which the objective function includes total trip time (including driving and charging times) and charging cost. The propose an algorithm that is capable of addressing both cold and hot ambient operations, as in the TM system the components for

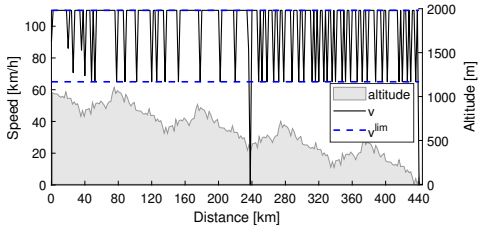

(a) Road topography together with vehicle speed profile and speed limits.

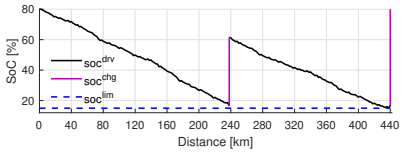

(b) Battery state of charge trajectory together with its bounds.

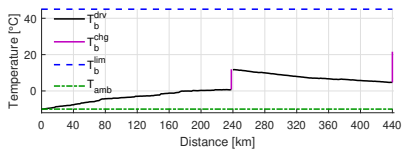

(c) Battery temperature trajectory together with its upper bound and ambient temperature.

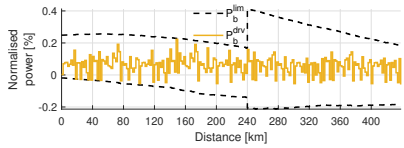

(d) Trajectory of optimal battery power together with its limits (normalised with the maximum battery discharge power).

Figure 10: Case 2; optimal trajectories versus travelled distance in Case 2. The step changes in battery temperature and SoC at $s = 240\,\text{km}$ and $s = 440\,\text{km}$ in (a) and (b), denote the increase in the corresponding variables during charging mode.

both heating and cooling of the battery/cabin are incorporated. However, in this paper we have focused on cold ambient operation, as the limited battery power affects the optimal solution in terms of energy efficiency and charging time. The vehicle's drivability in terms of maximum acceleration capability is another factor that is limited in the cold ambient operation. To enhance the drivability, the battery can be pre-heated before the vehicle's departure, using the electrical grid power, as this may reduce the Joule heat losses throughout

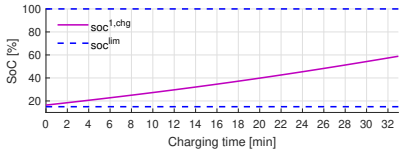

(a) Battery state of charge trajectory together with its bounds.

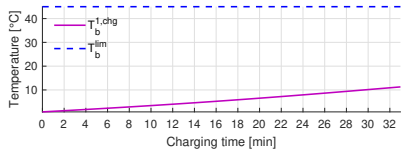

(b) Battery temperature trajectory together with its bounds.

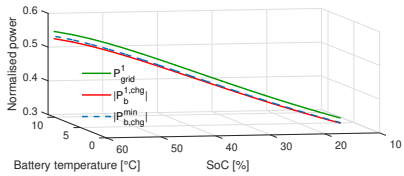

(c) Grid power together with absolute values of battery charging power and its limit, versus battery temperature and SoC.

Figure 11: Case 2; optimal trajectories associated with the vehicle's intermediate charging mode at $s = 240\,\text{km}$.

the trip and the need for pre-conditioning before fast charging. However, the disadvantage is the leakage of thermal energy to the ambient. Furthermore, it is often assumed in literature that the departure time is known when pre-heating is performed before departure. This will not always be the case, as not all car users plan far ahead. In general, pre-heating before departure may be more beneficial only if it yields skipping the charging occasion along the route, by less need for battery pre-conditioning and lower Joule heat losses.

The performance of the proposed algorithm is evaluated for a vehicle driving on a route, along which two charging possibilities are considered. To study the trade-off between trip time and charging energy cost, the Pareto frontier is derived for different driving scenarios of the vehicle. According to the results, trip time is reduced by 44 %, in case the optimal battery pre-conditioning is applied to the vehicle. Low charging time, high charging power availability, and the preservation of the vehicle's potential range are the knock-on effects of the battery pre-conditioning.

The proposed algorithm for eco-driving and TM of BEVs can also be extended in several ways, such as:

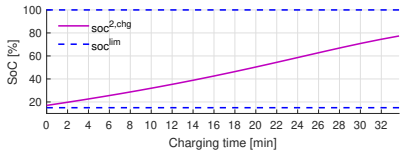

(a) Battery state of charge trajectory together with its bounds.

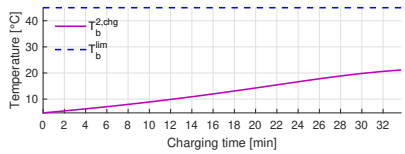

(b) Battery temperature trajectory together with its bounds.

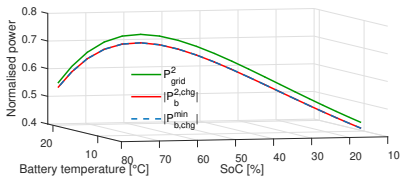

(c) Grid power together with absolute values of battery charging power and its limit, versus battery temperature and SoC.

Figure 12: Case 2; optimal trajectories associated with the vehicle's intermediate charging mode at $s = 440\,\text{km}$.

1. A heat pump can be incorporated in the TM system to include heating/cooling the battery. In case of the battery cooling, the excess heat from the battery can be transferred to the cabin compartment and/or ambient air. Also, heat pumps are able to transfer the heat from ambient air to the cabin.
2. It is possible to optimally select the charging stops, in a way to achieve optimality in time, energy, or their trade-off.
3. An online-implementable algorithm can be developed based on the current algorithm that is capable of reacting to potential disturbances, considering model-plant mismatches, and anticipating future events.
4. Performance of the control actions provided by the developed algorithm can be verified, using a more detailed thermal model.

Acknowledgment

The authors would like to acknowledge Mats Bohman, Anand Ganesan, and Ole-Fredrik Dunderberg from Volvo Car Corporation for the support and helpful discussions during this research. This work is part of a project titled “Predictive Energy and Thermal management of Electric Vehicles with Connectivity to Infrastructure" funded by Swedish Electromobility Center.

References

[1] J. Y. Yong, V. K. Ramachandaramurthy, K. M. Tan, and N. Mithulananthan, “A review on the state-of-the-art technologies of electric vehicle, its impacts and prospects,” *Renewable and sustainable energy reviews*, vol. 49, pp. 365–385, 2015.

[2] A. M. Andwari, A. Pesiridis, S. Rajoo, R. Martinez-Botas, and V. Esfahanian, “A review of battery electric vehicle technology and readiness levels,” *Renewable and Sustainable Energy Reviews*, vol. 78, pp. 414–430, 2017.

[3] H. Löbberding, S. Wessel, C. Offermanns, *et al.*, “From cell to battery system in bevs: Analysis of system packing efficiency and cell types,” *World Electric Vehicle Journal*, vol. 11, no. 4, p. 77, 2020.

[4] N. Rietmann, B. Hügler, and T. Lieven, “Forecasting the trajectory of electric vehicle sales and the consequences for worldwide co2 emissions,” *Journal of Cleaner Production*, vol. 261, p. 121 038, 2020.

[5] I. T. Forum, *ITF Transport Outlook 2019*. OECD Publishing/ITF, Paris, France, Tech, Rep., 2019, p. 200, ISBN: 9789282103937.

[6] C. Zhu, F. Lu, H. Zhang, and C. C. Mi, “Robust predictive battery thermal management strategy for connected and automated hybrid electric vehicles based on thermoelectric parameter uncertainty,” *IEEE Journal of Emerging and Selected Topics in Power Electronics*, vol. 6, no. 4, pp. 1796–1805, 2018.

[7] M. A. S. Kamal, M. Mukai, J. Murata, and T. Kawabe, “Ecological vehicle control on roads with up-down slopes,” *IEEE Transactions on Intelligent Transportation Systems*, vol. 12, no. 3, pp. 783–794, 2011.

[8] J. N. Barkenbus, "Eco-driving: An overlooked climate change initiative," *Energy Policy*, vol. 38, no. 2, pp. 762–769, 2010.

[9] N. Murgovski, B. Egardt, and M. Nilsson, "Cooperative energy management of automated vehicles," *Control Engineering Practice*, vol. 57, pp. 84–98, 2016.

[10] L. Johannesson, N. Murgovski, E. Jonasson, J. Hellgren, and B. Egardt, "Predictive energy management of hybrid long-haul trucks," *Control Engineering Practice*, vol. 41, pp. 83–97, 2015.

[11] M. Hovgard, O. Jonsson, N. Murgovski, M. Sanfridson, and J. Fredriksson, "Cooperative energy management of electrified vehicles on hilly roads," *Control Engineering Practice*, vol. 73, pp. 66–78, 2018.

[12] A. Hamednia, M. Razi, N. Murgovski, and J. Fredriksson, "Electric vehicle eco-driving under wind uncertainty," in *2021 IEEE International Intelligent Transportation Systems Conference (ITSC)*, IEEE, 2021, pp. 3502–3508.

[13] R. Bellman, *Dynamic Programming*. New Jersey: Princeton Univ Pr, 1957.

[14] G. Heppeler, M. Sonntag, U. Wohlhaupter, and O. Sawodny, "Predictive planning of optimal velocity and state of charge trajectories for hybrid electric vehicles," *Control Engineering Practice*, vol. 61, pp. 229–243, 2016.

[15] F. Ding and H. Jin, "On the optimal speed profile for eco-driving on curved roads," *IEEE Transactions on Intelligent Transportation Systems*, vol. 19, no. 12, pp. 4000–4010, 2018.

[16] D. Maamria, K. Gillet, G. Colin, Y. Chamaillard, and C. Nouillant, "Optimal predictive eco-driving cycles for conventional, electric, and hybrid electric cars," *IEEE Transactions on Vehicular Technology*, vol. 68, no. 7, pp. 6320–6330, 2019.

[17] T. van Keulen, B. de Jager, and M. Steinbuch, "Optimal trajectories for vehicles with energy recovery options," in *IFAC World Congress*, Milan, Italy, 2011, pp. 3831–3836.

[18] L. S. Pontryagin, V. G. Boltyanskii, R. V. Gamkrelidze, and E. F. Mishchenko, *The Mathematical Theory of Optimal Processes*. Interscience Publishers, 1962.

[19] R. F. Hartl, S. P. Sethi, and R. G. Vickson, "A survey of the maximum principles for optimal control problems with state constraints," *SIAM review*, vol. 37, no. 2, pp. 181–218, 1995.

[20] D. Shen, D. Karbowski, and A. Rousseau, "A minimum principle-based algorithm for energy-efficient eco-driving of electric vehicles in various traffic and road conditions," *IEEE Transactions on Intelligent Vehicles*, vol. 5, no. 4, pp. 725–737, 2020.

[21] S. Uebel, N. Murgovski, C. Tempelhahn, and B. Bäker, "Optimal energy management and velocity control of hybrid electric vehicles," *IEEE Transactions on Vehicular Technology*, vol. 67, no. 1, pp. 327–337, 2017.

[22] A. Hamednia, N. Murgovski, and J. Fredriksson, "Time optimal and eco-driving mission planning under traffic constraints," in *Intelligent Transportation Systems (ITSC)*, Rhodos, Greece, 2020.

[23] V. Turri, B. Besselink, and K. H. Johansson, "Cooperative look-ahead control for fuel-efficient and safe heavy-duty vehicle platooning," *IEEE Transactions on Control Systems Technology*, vol. 25, no. 1, pp. 12–28, 2016.

[24] H. Chen, L. Guo, H. Ding, Y. Li, and B. Gao, "Real-time predictive cruise control for eco-driving taking into account traffic constraints," *IEEE Transactions on Intelligent Transportation Systems*, vol. 20, no. 8, pp. 2858–2868, 2018.

[25] S. Uebel, N. Murgovski, B. Baker, and J. Sjoberg, "A 2-level MPC for energy management including velocity control of hybrid electric vehicle," *IEEE Transactions on Vehicular Technology*, 2019.

[26] A. Hamednia, N. K. Sharma, N. Murgovski, and J. Fredriksson, "Computationally efficient algorithm for eco-driving over long look-ahead horizons," *IEEE Transactions on Intelligent Transportation Systems*, 2021.

[27] D. Maamria, K. Gillet, G. Colin, Y. Chamaillard, and C. Nouillant, "Which methodology is more appropriate to solve eco-driving optimal control problem for conventional vehicles?" In *2016 IEEE Conference on Control Applications (CCA)*, IEEE, 2016, pp. 1262–1267.

[28] A. Biswas and A. Emadi, "Energy management systems for electrified powertrains: State-of-the-art review and future trends," *IEEE Transactions on Vehicular Technology*, vol. 68, no. 7, pp. 6453–6467, 2019.

[29] Y. Jia, R. Jibrin, and D. Görges, "Energy-optimal adaptive cruise control for electric vehicles based on linear and nonlinear model predictive control," *IEEE Transactions on Vehicular Technology*, vol. 69, no. 12, pp. 14 173–14 187, 2020.

[30] N. K. Sharma, A. Hamednia, N. Murgovski, E. R. Gelso, and J. Sjöberg, "Optimal eco-driving of a heavy-duty vehicle behind a leading heavy-duty vehicle," *IEEE Transactions on Intelligent Transportation Systems*, vol. 22, no. 12, pp. 7792–7803, 2020.

[31] M. A. Hannan, M. M. Hoque, A. Hussain, Y. Yusof, and P. J. Ker, "State-of-the-art and energy management system of lithium-ion batteries in electric vehicle applications: Issues and recommendations," *Ieee Access*, vol. 6, pp. 19 362–19 378, 2018.

[32] T. H. Pham, J. T. Kessels, P. P. Van Den Bosch, and R. G. Huisman, "Analytical solution to energy management guaranteeing battery life for hybrid trucks," *IEEE Transactions on Vehicular Technology*, vol. 65, no. 10, pp. 7956–7971, 2015.

[33] B. Gao, L. Guo, Q. Zheng, B. Huang, and H. Chen, "Acceleration speed optimization of intelligent evs in consideration of battery aging," *IEEE Transactions on Vehicular Technology*, vol. 67, no. 9, pp. 8009–8018, 2018.

[34] L. De Pascali, F. Biral, and S. Onori, "Aging-aware optimal energy management control for a parallel hybrid vehicle based on electrochemical-degradation dynamics," *IEEE Transactions on Vehicular Technology*, vol. 69, no. 10, pp. 10 868–10 878, 2020.

[35] J. Jeffs, "An investigation into the optimal operation of a complex heat pump for the complete thermal management of an electric vehicle in cold climates," Ph.D. dissertation, University of Warwick, 2019.

[36] J. Jaguemont, L. Boulon, P. Venet, Y. Dubé, and A. Sari, "Lithium-ion battery aging experiments at subzero temperatures and model development for capacity fade estimation," *IEEE Transactions on Vehicular Technology*, vol. 65, no. 6, pp. 4328–4343, 2015.

[37] G. Zhang, S. Ge, X.-G. Yang, Y. Leng, D. Marple, and C.-Y. Wang, "Rapid restoration of electric vehicle battery performance while driving at cold temperatures," *Journal of Power Sources*, vol. 371, pp. 35–40, 2017.

[38] T. Wang, X. Wu, S. Xu, *et al.*, "Performance of plug-in hybrid electric vehicle under low temperature condition and economy analysis of battery pre-heating," *Journal of Power Sources*, vol. 401, pp. 245–254, 2018.

[39] X. Hu, Y. Zheng, D. A. Howey, H. Perez, A. Foley, and M. Pecht, "Battery warm-up methodologies at subzero temperatures for automotive applications: Recent advances and perspectives," *Progress in Energy and Combustion Science*, vol. 77, p. 100 806, 2020.

[40] S. Wu, R. Xiong, H. Li, V. Nian, and S. Ma, "The state of the art on preheating lithium-ion batteries in cold weather," *Journal of Energy Storage*, vol. 27, p. 101 059, 2020.

[41] Y. Wang, X. Zhang, and Z. Chen, "Low temperature preheating techniques for lithium-ion batteries: Recent advances and future challenges," *Applied Energy*, vol. 313, p. 118 832, 2022.

[42] M. R. Amini, H. Wang, X. Gong, D. Liao-McPherson, I. Kolmanovsky, and J. Sun, "Cabin and battery thermal management of connected and automated hevs for improved energy efficiency using hierarchical model predictive control," *IEEE Transactions on Control Systems Technology*, vol. 28, no. 5, pp. 1711–1726, 2019.

[43] B. Chen, X. Li, S. A. Evangelou, and R. Lot, "Joint propulsion and cooling energy management of hybrid electric vehicles by optimal control," *IEEE Transactions on Vehicular Technology*, vol. 69, no. 5, pp. 4894–4906, 2020.

[44] J. Jaguemont, L. Boulon, Y. Dube, and F. Martel, "Thermal management of a hybrid electric vehicle in cold weather," *IEEE Transactions on Energy Conversion*, vol. 31, no. 3, pp. 1110–1120, 2016.

[45] S. Bauer, A. Suchaneck, and F. P. León, "Thermal and energy battery management optimization in electric vehicles using pontryagin's maximum principle," *Journal of Power Sources*, vol. 246, pp. 808–818, 2014.

[46] C. Zhu, F. Lu, H. Zhang, J. Sun, and C. C. Mi, "A real-time battery thermal management strategy for connected and automated hybrid electric vehicles (cahevs) based on iterative dynamic programming," *IEEE Transactions on Vehicular Technology*, vol. 67, no. 9, pp. 8077–8084, 2018.

[47] J. Lopez-Sanz, C. Ocampo-Martinez, J. Alvarez-Florez, *et al.*, "Nonlinear model predictive control for thermal management in plug-in hybrid electric vehicles," *IEEE Transactions on Vehicular Technology*, vol. 66, no. 5, pp. 3632–3644, 2016.

[48] ——, "Thermal management in plug-in hybrid electric vehicles: A real-time nonlinear model predictive control implementation," *IEEE transactions on vehicular technology*, vol. 66, no. 9, pp. 7751–7760, 2017.

[49] B. Chen, X. Li, S. A. Evangelou, and R. Lot, "Joint propulsion and cooling energy management of hybrid electric vehicles by optimal control," *IEEE Transactions on Vehicular Technology*, vol. 69, no. 5, pp. 4894–4906, 2020.

[50] O. Lindgärde, M. Söderman, A. Tenstam, and L. Feng, "Optimal complete vehicle control for fuel efficiency," *Transportation Research Procedia*, vol. 14, pp. 1087–1096, 2016.

[51] B. J. Limb, Z. D. Asher, T. H. Bradley, *et al.*, "Economic viability and environmental impact of in-motion wireless power transfer," *IEEE Transactions on Transportation Electrification*, vol. 5, no. 1, pp. 135–146, 2018.

[52] J. C. Butcher, "On the implementation of implicit runge-kutta methods," *BIT Numerical Mathematics*, vol. 16, no. 3, pp. 237–240, 1976.

[53] J. A. Andersson, J. Gillis, G. Horn, J. B. Rawlings, and M. Diehl, "Casadi: A software framework for nonlinear optimization and optimal control," *Mathematical Programming Computation*, vol. 11, no. 1, pp. 1–36, 2019.

[54] L. T. Biegler and V. M. Zavala, "Large-scale nonlinear programming using ipopt: An integrating framework for enterprise-wide dynamic optimization," *Computers & Chemical Engineering*, vol. 33, no. 3, pp. 575–582, 2009.

PAPER E

Optimal thermal management and charging of battery electric vehicles over long trips

Ahad Hamednia, Victor Hanson, Jiaming Zhao, Nikolce Murgovski, Jimmy Forsman, Mitra Pourabdollah, Viktor Larsson, and Jonas Fredriksson

Submitted to IEEE Transactions on Vehicular Technology in Sep 2022

The layout has been revised.

Abstract

This paper studies optimal thermal management (TM) and charging of a battery electric vehicle (BEV) driving over long distance trips. Here, the focus is on the potential benefits of including a heat pump (HP) in the TM system for waste heat recovery (WHR), and charging point planning, in a way to achieve optimality in time, energy, or their trade-off. An optimal control problem (OCP) is formulated, in which the objective function includes the energy delivered by the charger(s), and total charging time including the actual charging time and the detour time to and from the charging stop. To reduce the computational complexity, the formulated problem is then transformed into a hybrid dynamical system (HDS), where charging dynamics are modelled in the domain of normalized charging time. Driving dynamics can be modelled in either of the trip time or travel distance domains, as the vehicle speed is assumed to be known a priori, and the vehicle is only stopping at charging locations. Within the HDS, a binary variable is introduced for each charging location, in order to decide to use or skip a charger. This problem is solved numerically, and simulations are performed to evaluate the performance in terms of energy efficiency and time. The simulation results indicate that the time required for charging and total energy consumption are reduced up to 30.6 % and 19.4 %, respectively, by applying the proposed algorithm.

1 Introduction

RECENTLY electric vehicles (EVs) have gained considerable attention among researchers, manufacturer, and users, due to their advanced and sustainable technologies for counteracting drawbacks by convectional vehicles, for e.g. limited fuel resource, severe environmental impact, and high maintenance and operating costs [1]. Accordingly, the EV market has grown rapidly over the last few years, and several car companies have stated that they will only produce electric vehicles in near future [2]. In particular, battery electric

vehicles (BEVs) are identified as a promising choice for achieving the decarbonized light duty vehicle fleet. However, there still exist several challenges impeding the widespread deployment of BEVs, mostly related to energy cost, limited driving range, charging time, and thermal management. These issues become even more important to consider when planning for long-distance trips, i.e. exceeding the vehicle's range [3].

Although the range can vary over a large distance window [4], still the majority of cost-effective BEV models fail to fully meet the range requirement of long trips, highlighting the significance of reducing total energy consumption as well as improving fast charging technology, for higher customer acceptance of BEVs. Lately, a high-power fast charging technology has been introduced, aiming at recharging a battery up to 80 % state of charge (SoC) within 15 min, in order to provide more convenient long-trip experiences [5].

Apart from the charger's rated power, the charging time is also highly influenced by fast charging properties of the battery. This is mainly characterised as the battery's chemistry, SoC, temperature, and health state, which may negatively affect the charging rate [6]. Thus, solutions associated with the BEV's fast charging are required to incorporate various aspects rather than just focusing on increasing the maximum power provided by the charger [7], [8].

One crucial factor that can significantly improve charging time, total energy consumption, and passenger comfort, especially in harsh climates, is to develop an adequate thermal management (TM) [9], [10]. Lithium-ion (Li-ion) batteries, known as a widely used alternative in the market, are highly temperature sensitive [11]. Excessive battery temperatures can cause corrosion and even explosion by creating bubbles, bulge, sparks, and flames [12]. Furthermore, at sub-zero Celsius temperatures, the battery performance is severely deteriorated due to a considerably slowed electro-chemical process within the battery cells [13], [14]. This yields a severe reduction in the cell's available power and energy, thereby significantly increasing the charging time [15]. Moreover, to minimize the total energy consumption of the vehicle, it is essential to incorporate the TM when optimising grid-to-meter energy efficiency of the BEV [16]–[18]. In this context, several research works have been conducted, mainly by formulating an optimal control problem (OCP) that can be solved by different optimization tools.

Dynamic programming (DP) [19] is used in [20] for developing an algo-

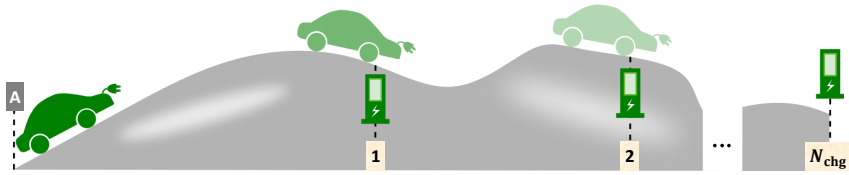

Figure 1: A BEV starts its trip from point A, and drives in a hilly terrain. The indices 1, 2,... represent the charging stations, and N_{chg} denotes the total number of charging locations.

rithm for the TM of a vehicle that is unplugged from the electrical grid and parked outside at a low ambient temperature. The goal within this study is to find an optimal trade-off between contained energy in the battery pack, and the cell degradation of being exposed to a cold weather. However, the main disadvantage of the DP approach is expressed as *curse of dimensionality*, which refers to exponential growth of computational time with the dimension of the OCP. Accordingly, Pontryagin's Maximum Principle (PMP) [21], [22], with a potential of enhancing the computational efficiency, is applied as an alternative strategy for maximising the expected battery life with minimum energy consumed. Furthermore, several TM strategies have been proposed using model predictive control (MPC) scheme for increasing the energy efficiency via optimal cooling/heating [23]–[25]. Moreover, the TM is studied for vehicles with a given drive cycle [17], or with future speed prediction, to be incorporated into the energy efficiency analysis [16]. In the context of the TM of electrified vehicles, several research efforts have been carried out with a focus on waste heat recovery (WHR), see In [26] and the references therein. In [27], a multi-level WHR system with an improved heat transfer capacity is developed, where the battery temperature is maintained within an appropriate range. Also, a novel HP system is designed for electric buses in [28], where the heating performance of the TM system is enhanced in cold environments. Despite the contributions provided by developing numerous TM strategies for vehicles, the technical literature lacks investigation on joint optimal charging and TM over long trips, with a WHR ability and charge point planning.

As an extension to our earlier work [29], this paper addresses a BEV driving on a road with a hilly terrain. The vehicle's travelled distance is greater than its range; there is thus a need for at least one charging stop along the route. In this paper, the following goals are addressed:

- Develop an algorithm to achieve optimal charging and TM of a BEV on long trips, capturing both driving and charging modes of the vehicle.
- Quantify the trade-off between charging time and energy efficiency.
- Investigate the benefits of including a heat pump (HP) in the TM system for WHR.
- Plan the charging locations, in favour of obtaining optimality in time, energy, or their trade-off.

To achieve the above-mentioned goals, an OCP is formulated for charging and TM of a BEV. The objective of the OCP is to find the optimal compromise between the energy delivered by the charger(s), and *total charging time* referred to as the actual charging time and the detour time to and from the charging locations. Within the TM system, an HP is included for WHR purposes, in addition to a high-voltage coolant heater (HVCH) for the heating of battery/cabin, and heating, ventilation, and air conditioning (HVAC) for the battery/cabin cooling. The driving dynamics can be described in either of the space or trip time domains. However, charging dynamics is modelled in terms a normalized charging time. Thus, the OCP transforms into a hybrid dynamical system (HDS). Note that the actual charging time is treated as a scalar variable, which is optimized simultaneously with the optimal state and control trajectories that belong to the driving and charging modes. Also, for each charging location a binary variable is defined to optimally plan the charging stops, in favour of further optimising the energy efficiency and/or trip time. Such formulation procedure turns the HDS into a mixed-integer optimisation problem.

The rest of the paper is outlined as follows. In Section 2, electrical and thermal modelling of the electric powertrain are addressed. Section 3 illustrates the constrains on the battery and grid power values. In Section 4, the HDS is formulated, covering the vehicle's operation during both driving and charging modes. In Section 5 simulation results are presented. Section 6 discuses the obtained results. Finally, Section 7 includes conclusion of the paper and the suggestions regarding the possible future research directions.

2 Modelling

This section addresses the vehicle driving mission and a multi-domain configuration of an electric powertrain, describing connection of the powertrain

components via electrical, thermal, and mechanical paths.

2.1 Vehicle driving mission

Consider a BEV that starts its trip from point A, and drives in a hilly terrain, as depicted in Fig. 1. As the vehicle moves forward, the battery is depleted. The battery temperature may be adjusted by different heating/cooling sources within the powertrain. Along the driving route, multiple charging possibilities are considered, as the vehicle's trip length is greater than its range. In realistic driving situations it is preferable to plan the charging stops, to achieve optimal trip time and/or charging cost.

In this paper, we assume the vehicle speed to be known a priori, in which the vehicle stops only during charging (and not during driving). This allows to identically formulate the driving dynamics, in either of space or trip time domains, without adding any complexity to the algorithm developed later in Section 4. Here, we freely choose the spatial domain to associate the system trajectories with space-defined events, such as speed limits and charging locations. Thus, the vehicle's driving time, t, is calculated by integrating the vehicle speed, as

$$t(s) = \int_0^s \frac{\mathrm{d}x}{v(x)}, \tag{E.1}$$

where s and v denote travelled distance and the vehicle speed, respectively. The formulation of charging dynamics is postponed to Section 4.

2.2 Multi-domain Powertrain Configuration

Schematic diagram of the studied electric powertrain is demonstrated in Fig. 2. The powertrain includes propulsion components, i.e. a battery for energy supply/storage, an electric machine (EM), and a transmission system. In addition to the propulsion components, the powertrain is equipped with an on board charger (OBC), as a device to regulate the electricity flow from the electrical grid to the battery, monitor charge rate, and protect the battery from over-current charging. Furthermore, the electric powertrain includes a thermal management system, comprising HVAC, HVCH, and HP. The HVAC and HVCH are mainly used, respectively for cooling and heating of the battery pack and cabin compartment. Also, an HP is generally employed for trans-

ferring heat from heat source at low temperature, i.e. the battery, to heat sink at higher temperature, for e.g. the cabin compartment and/or ambient air. To achieve this, work is required, as heat cannot spontaneously flow from a colder place to a warmer location, according to the second law of thermodynamics [30]. As depicted in Fig. 2, the operating principle of HPs can be summarized into a *refrigeration cycle*, which consists of five major components: evaporator, compressor, condenser, expansion valve, and a refrigerant. Thus, the evaporator absorbs heat from the battery pack and turns the refrigerant from liquid mode into a low-pressure gas that is delivered to the compressor. Then the compressor pressurises the gas and dispatches it to the condenser. Later, the condenser cools down the hot gas, turns it into a liquid, and expels the extracted heat from the refrigerant to the cabin compartment and/or ambient air. Finally, the high-pressure liquid refrigerant departed from the condenser becomes a low-pressure liquid by passing through the expansion valve; and the cycle starts over again. The merit of an HP is specified by a parameter called the coefficient of performance (CoP), defined as a ratio of useful heating provided (for the cabin compartment) to the net work required, as

$$\mathrm{cop}(T_{\mathrm{b}}(s), P_{\mathrm{hp}}(s)) = \frac{Q^{\mathrm{b}}_{\mathrm{hp}}(T_{\mathrm{b}}(s)) + P_{\mathrm{hp}}(s)}{P_{\mathrm{hp}}(s)}, \tag{E.2}$$

where T_{b} is the battery pack's temperature, P_{hp} is the rate of the net work put into the cycle, and $Q^{\mathrm{b}}_{\mathrm{hp}}$ is rate of the heat removed from the battery pack and electric drivetrain (ED). Hereafter, P_{hp} is called HP power. The three domains of the powertrain configuration are elaborated in Sections 2.2-2.2.

Electrical Domain

Depending on the EM's operating mode, i.e. generating or motoring, the electric power flow through the electrical path is bidirectional, as shown in Fig. 2. Accordingly, electrical energy is charged to the battery during the generating mode, or supplied to the EM during the motoring mode. The battery is modelled using an equivalent circuit, which includes a voltage source U_{oc}, known as open-circuit voltage, and an internal resistance R_{b}. The open-circuit voltage is usually proportional to the battery SoC. Also, as the battery temperature is raised, the ions inside the battery cells get more energized, which results in a reduced resistance against the ions' displacement. Thus, the

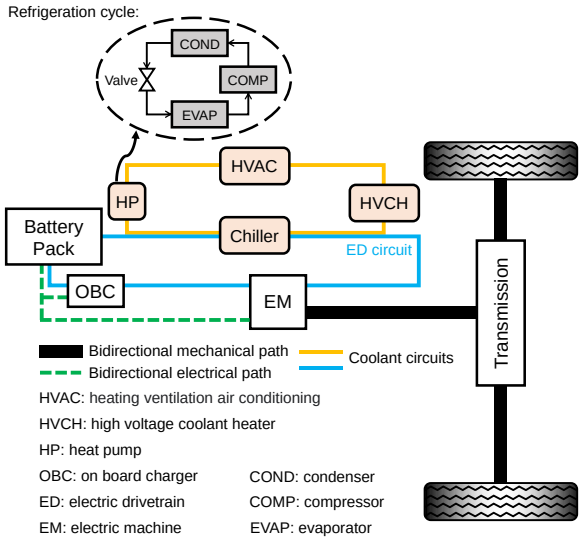

Figure 2: Schematic diagram of the studied electric powertrain, which consists of propulsion components, i.e. a battery, an EM, and a transmission system, on board charger, and a thermal management system. The thermal management system consists of HVCH, HVAC, and a heat pump, which are used for actively adjusting the battery pack and cabin compartment temperatures.

internal resistance is commonly a nonlinear monotonically decreasing function of the battery temperature [23]. Note that the slight mismatch between the internal resistance while charging and discharging is overlooked in this paper. The battery SoC dynamics is calculated by

$$\mathrm{soc}'(s) = -\frac{P_\mathrm{b}(s)}{C_\mathrm{b} U_\mathrm{oc}(\mathrm{soc}(s)) v(s)}, \tag{E.3}$$

where P_b is battery power, including internal resistive losses, and C_b is maximum capacity of the battery pack. P_b is negative while charging, and is positive when discharging. Note that throughout this paper, x' represents the space derivative of an arbitrary variable x, i.e. $x' = \mathrm{d}x/\mathrm{d}s$.

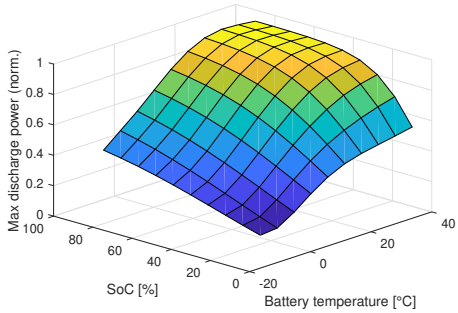

(a) Battery discharge power limit.

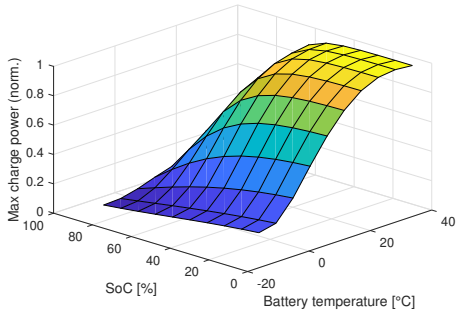

(b) Battery charge power limit.

Figure 3: Normalised absolute value of discharge and charge power bounds versus battery temperature and SoC for the studied battery in this paper.

Thermal Domain

According to the fundamental thermodynamic principle [30], the changing rate of the battery pack's temperature T_{b} is modelled using a lumped-parameter thermal model, as

$$T'_{\mathrm{b}}(s) = \frac{1}{c_{\mathrm{p}} m_{\mathrm{b}} v(s)} \big(Q_{\mathrm{pass}}(\cdot) + Q_{\mathrm{act}}(\cdot) + Q_{\mathrm{exh}}(\cdot) \big), \tag{E.4}$$

where c_{p} and m_{b} are the battery pack's specific heat capacity and total mass, respectively, Q_{pass} is the rate of induced heat by passive heat sources affecting the battery temperature, Q_{act} is the active heat rate from or removed by components, e.g. HVAC, HVCH, and HP, that can actively affect the battery

pack temperature, Q_{exh} is rate of the heat exchanged among the battery pack, ambient air and/or the chassis of the vehicle, and the symbol $\cdot$ is a compact notation used for expressing multiple variables of a function. Note that the nonuniform distribution of the battery pack temperature due to the heat diffusion is neglected in this paper, which reduces the complexity of the thermal model. Accordingly, crust and core battery pack temperatures are assumed to be identical.

The passive heat generation rate

$$Q_{\mathrm{pass}}(\mathrm{soc}(s), T_{\mathrm{b}}(s), v(s), a_{\mathrm{t}}(s)) = R_{\mathrm{b}}(T_{\mathrm{b}}(s)) \frac{P_{\mathrm{b}}^2(s)}{U_{\mathrm{oc}}^2(\mathrm{soc}(s))} + Q_{\mathrm{ed}}(v(s), a_{\mathrm{t}}(s)), \tag{E.5}$$

includes: 1) the produced heat due to the battery internal resistive losses, referred to as *irreversible ohmic Joule heat*; and 2) the heat produced by the ED power losses, Q_{ed}, which is dependent on the vehicle speed and traction acceleration a_{t}.

The active heat generation rate

$$Q_{\mathrm{act}}(P_{\mathrm{hvch}}^{\mathrm{b}}(s), P_{\mathrm{hvac}}^{\mathrm{b}}(s), P_{\mathrm{hp}}(s)) = \eta_{\mathrm{hvch}} P_{\mathrm{hvch}}^{\mathrm{b}}(s) - \eta_{\mathrm{hvac}} P_{\mathrm{hvac}}^{\mathrm{b}}(s) - Q_{\mathrm{hp}}(s). \tag{E.6}$$

includes: 1) HVCH power conversion for heating the battery pack, $P_{\mathrm{hvch}}^{\mathrm{b}}$, with efficiency of η_{hvch}, HVAC power conversion for cooling the battery pack, $P_{\mathrm{hvac}}^{\mathrm{b}}$, with efficiency of η_{hvac}, and rate of the heat removed from the battery pack by HP.

The convective heat exchange rate between the battery pack and ambient air depends on the ambient temperature T_{amb}, battery temperature, and vehicle speed, as

$$Q_{\mathrm{exh}}(T_{\mathrm{amb}}(s), T_{\mathrm{b}}(s), v(s)) = \gamma(v(s))(T_{\mathrm{amb}}(s) - T_{\mathrm{b}}(s)), \tag{E.7}$$

where $\gamma > 0$ is a speed dependent coefficient of heat exchange.

Mechanical Domain

Similar to the electrical path, the mechanical path is also bidirectional, as depicted in Fig. 2. The EM when operated in motoring mode, provides propul-

sion power, which is delivered to the wheels through the mechanical path via the transmission system. Thus, the EM rotational speed and output torque are translated by the transmission system into vehicle speed and traction acceleration, respectively. Furthermore, the EM when operated in generating mode, transforms the vehicle's kinetic energy at the wheels via the mechanical path into electrical energy to be stored in the battery.

3 Bounds on Battery and Grid Power Values

The bounds on available battery power during discharging and charging are formulated as functions of battery temperature and SoC as

$$P_{\mathrm{b}}(s) \in \begin{cases} [P^{\min}_{\mathrm{b,chg}}(\mathrm{soc}(s), T_{\mathrm{b}}(s)), P^{\max}_{\mathrm{b,dchg}}(\mathrm{soc}(s), T_{\mathrm{b}}(s))], & s \in \mathcal{S}_{\mathrm{drv}} \\ [\zeta_i P^{\min}_{\mathrm{b,chg}}(\mathrm{soc}(s), T_{\mathrm{b}}(s)), 0], & s \in \mathcal{S}^i_{\mathrm{chg}} \end{cases} \tag{E.8}$$

where $P^{\max}_{\mathrm{b,dchg}} > 0$ and $P^{\min}_{\mathrm{b,chg}} < 0$ are the bounds on the battery discharge and charge power, respectively, $i \in \mathcal{I} = \{1, 2, \ldots, N_{\mathrm{chg}}\}$ is charger index, N_{chg} is total number of charging locations along the driving route, and $\mathcal{S}_{\mathrm{drv}}$ and $\mathcal{S}_{\mathrm{chg}}$ represent sets of driving and charging distance instances, respectively. Also, $\zeta \in \mathbb{Z} = \{0, 1\}$ is a binary variable defined for each charging location, in order to decide whether to skip the charger, i.e. $\zeta = 0$, or use it, i.e. $\zeta = 1$. Note that $P^{\min}_{\mathrm{b,chg}}$ may differ in driving and charging modes, whereas it is here assumed that the same bound is imposed for simplicity, and without loss of generality. The negative power limit during driving is due to regenerative braking, within which the kinetic energy at the wheels is transformed into electrical energy to be stored in the battery. As demonstrated in Fig. 1.3(a), the studied battery discharge power limit is proportional to both the battery temperature and SoC level. However, the battery charge power limit is proportional to the battery temperature and inverse of SoC level, as depicted in Fig. 1.3(b).

For $i \in \mathcal{I}$ and $\zeta \in \mathbb{Z}$, the bound on the ith charger's provided power is given

by

$$P^i_{\text{grid}}(s) \in \begin{cases} \{0\}, & s \in \mathcal{S}_{\text{drv}}, \\ [0, \zeta_i P^{i,\max}_{\text{grid}}], & s \in \mathcal{S}^i_{\text{chg}} \end{cases} \tag{E.9}$$

where $P^{i,\max}_{\text{grid}}$ is rated power of the ith charger. Although it is assumed that the vehicle power demand is not supplied by the grid power during the driving mode, it is possible to do so on a road with charging lanes installed [31], by directly applying a method developed earlier in [29] in combination with the method provided later in Section 4.

Considering the battery and grid power limits (E.8) and (E.9), the power balance equation can be written as

$$\begin{aligned} &P^i_{\text{grid}}(s) + P_{\text{b}}(s) = R(T_{\text{b}}(s)) \frac{P^2_{\text{b}}(s)}{U^2_{\text{oc}}(\text{soc}(s))} + P_{\text{prop}}(v(s), a_{\text{t}}(s)) \\ &+ P^{\text{b}}_{\text{hvch}}(s) + P^{\text{b}}_{\text{hvac}}(s) + P^{\text{c}}_{\text{hvch}}(T_{\text{amb}}(s)) + P_{\text{hp}}(s) + P_{\text{aux}}(s), \end{aligned} \tag{E.10}$$

where P_{prop} is propulsion power including the internal powertrain losses, $P^{\text{c}}_{\text{hvch}}$ is the HVCH power consumed for heating the cabin compartment, and P_{aux} is auxiliary power demand used for lights, infotainment, etc.

System state variables and control inputs can be stacked into state and control vectors, respectively x and u, as

$$\text{x}(s) = \begin{bmatrix} \text{soc}(s) \\ T_{\text{b}}(s) \end{bmatrix}, \ \text{u}(s) = \begin{bmatrix} P^{\text{b}}_{\text{hvch}}(s) \\ P^{\text{b}}_{\text{hvac}}(s) \\ P^{\text{hp}}_{\text{b}}(s) \\ P_{\text{grid}}(s) \end{bmatrix}. \tag{E.11}$$

Thus, according to (E.3) and (E.4), the governing dynamics describing the battery SoC and temperature variations in the spatial domain can be summarized as

$$\frac{\text{dx}(s)}{\text{d}s} = \frac{1}{v(s)} h(\text{x}(s), \text{u}(s), s), \tag{E.12}$$

with h defined as a vector function.

4 Problem Statement

Despite the vehicle's fixed position at the charging stop, there will still be dynamical variations in the battery temperature and SoC while charging. Thus, to find the optimal trade-off between time and energy cost during both the driving and charging modes, it is not possible to formulate a single optimisation problem, within which decisions are always made with respect to s. Subsequently, we propose modelling of the charging dynamics in a temporal domain, where decisions are planned along a normalized charging time, $\tau^i \in [0, 1]$, defined, as

$$\tau^i = \frac{t}{t^i_{\text{chg}}}, \quad t \in \mathcal{T}^i_{\text{chg}}, i \in \mathcal{I}, \tag{E.13}$$

where t is trip time, and $\mathcal{T}^i_{\text{chg}}$ and t^i_{chg} denote respectively a set of charging time instants and charging time, at the i^{th} charging station. Thus, with choosing a distinct independent variable describing each mode, i.e. s for the driving mode and τ^i for the charging modes, as well as considering the binary variable ζ, a mixed-integer HDS can be formulated. A demonstration of the HDS including the driving and charging modes as well as transition between the modes is shown in Fig. 4, where by repeating such combination, it is possible to incorporate multiple charging locations within the system.

Following (E.13) and the derivative chain rule, the relation between the space derivative and the derivative with respect to $\tau^i \in [0, 1]$, $i \in \mathcal{I}$ is given by

$$\frac{\mathrm{dx}}{\mathrm{d}s} = \frac{\mathrm{dx}}{\mathrm{d}\tau} \frac{1}{t_{\text{chg}} v(s)}, \tag{E.14}$$

where $\frac{1}{t_{\text{chg}} v(s)} = \frac{\mathrm{d}\tau}{\mathrm{d}t} \frac{\mathrm{d}t}{\mathrm{d}s}$. Hereafter, the variables notated with subscripts/superscripts 'drv' or 'chg', correspond to the previously introduced variables that now belong specifically to the driving mode or charging mode, respectively. Note that the charging cost can be defined as the cost of electrical energy provided by the charger and/or the time spent for occupying the charging spot, depending on the pricing policy of a charger.

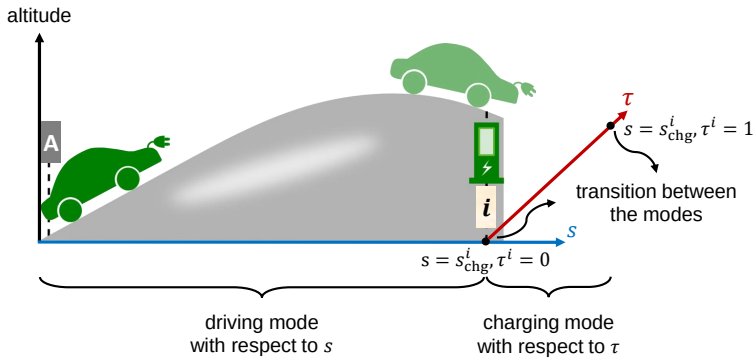

Figure 4: Hybrid dynamical system demonstration including driving mode, charging mode and transition between these two modes. During the driving and charging modes decisions are planned with respect to s and τ^i, $i \in \mathcal{I}$, respectively.

4.1 Objective Function

The objective function of the optimisation problem is defined as

$$J(\cdot) = \sum_{i=1}^{N_{\text{chg}}} \Big(\int_0^1 c_{\text{e}}^i P_{\text{grid}}^i(\tau^i) \mathrm{d}\tau^i + c_{\text{t,chg}} t_{\text{chg}}^i + c_{\text{occ}}^i \max\left(0, t_{\text{chg}}^i - t_{\text{occ}}^i\right) + c_\zeta \zeta_i \Big), \tag{E.15}$$

where J includes

- A charger's supplied electrical energy to the vehicle, where c_{e} denotes currency per-kilowatt-hour cost of the charged energy.
- A penalty on charging time with $c_{\text{t,chg}}$ as the penalty coefficient.
- A cost of occupying the charger for longer time than $t_{\text{occ}} \geq 0$, where c_{occ} is currency per-minute cost, and a scalar variable t_{chg} represents the charging time. Note that with non-zero value of c_{T}, the charging time is penalized twice, due to an occupied charger and/or a longer charging time.
- Detour cost by penalising the number of the charging occasions, where c_ζ is the penalty factor.

4.2 Mixed-integer Hybrid Dynamical System Formulation

Using (E.12) and (E.14), the mixed-integer HDS formulation for $i \in \mathcal{I}$, $\tau^i \in [0,1]$, and $\zeta \in \mathbb{Z}$ can now be summarized as

$$\min_{\mathrm{u_{drv}}(s),\mathrm{u}^i_{\mathrm{chg}}(\tau^i),t^i_{\mathrm{chg}},\zeta_i} J(\cdot) \tag{E.16a}$$

subject to:

$$\frac{\mathrm{dx_{drv}}(s)}{\mathrm{d}s} = \frac{1}{v(s)} h(\mathrm{x_{drv}}(s), \mathrm{u_{drv}}(s), s), \quad s \in \mathcal{S}_{\mathrm{drv}} \tag{E.16b}$$

$$\frac{\mathrm{dx}^i_{\mathrm{chg}}(\tau^i)}{\mathrm{d}\tau^i} = t^i_{\mathrm{chg}} h(\mathrm{x}^i_{\mathrm{chg}}(\tau^i), \mathrm{u}^i_{\mathrm{chg}}(\tau^i), \tau^i), \quad s \in s^i_{\mathrm{chg}} \tag{E.16c}$$

$$g_{\mathrm{drv}}(\mathrm{x_{drv}}(s), \mathrm{u_{drv}}(s), s) \leq 0, \quad s \in \mathcal{S}_{\mathrm{drv}} \tag{E.16d}$$

$$g_{\mathrm{chg}}(\mathrm{x}^i_{\mathrm{chg}}(\tau^i), \mathrm{u}^i_{\mathrm{chg}}(\tau^i), \tau^i) \leq 0, \quad s \in s^i_{\mathrm{chg}} \tag{E.16e}$$

$$\mathrm{x_{drv}}(s) \in \mathcal{X}_{\mathrm{drv}}(s), \quad \mathrm{u_{drv}}(s) \in \mathcal{U}_{\mathrm{drv}}(s), \quad s \in \mathcal{S}_{\mathrm{drv}} \tag{E.16f}$$

$$\mathrm{x}^i_{\mathrm{chg}}(\tau^i) \in \mathcal{X}^i_{\mathrm{chg}}(\tau^i), \quad \mathrm{u}^i_{\mathrm{chg}}(\tau^i) \in \mathcal{U}^i_{\mathrm{chg}}(\tau^i), \quad s \in s^i_{\mathrm{chg}} \tag{E.16g}$$

$$t^i_{\mathrm{chg}} \in [0, t^{\max}_{\mathrm{chg}}] \tag{E.16h}$$

$$\mathrm{x}^i_{\mathrm{chg}}(0) = \mathrm{x_{drv}}(s^i_{\mathrm{chg}}) - \zeta_i \mathrm{x_{detour}} \tag{E.16i}$$

$$\mathrm{x_{drv}}(s^{i^+}_{\mathrm{chg}}) = \mathrm{x}^i_{\mathrm{chg}}(1) - \zeta_i \mathrm{x_{detour}} \tag{E.16j}$$

$$\mathrm{x_{drv}}(s_0) \in \mathcal{X}_{\mathrm{drv0}}, \quad \mathrm{x_{drv}}(s_{\mathrm{f}}) \in \mathcal{X}_{\mathrm{drvf}} \tag{E.16k}$$

where t^i_{chg} and ζ_i are considered as design parameters, s_0 and s_{f} denote initial and final vehicle position, respectively, $t^{\max}_{\mathrm{chg}}$ is maximum allowed charging time, g_{drv} and g_{chg} represent the battery power limits (E.8) during driving and charging modes, respectively, and $s^{i^+}_{\mathrm{chg}}$ is an instance denoting the vehicle's position when charging is done and the vehicle is leaving the charging station. Also, $\mathcal{X}_{\mathrm{drv}}$ and $\mathcal{U}_{\mathrm{drv}}$ are the feasible sets of states and control inputs for the driving mode, and $\mathcal{X}_{\mathrm{chg}}$ and $\mathcal{U}_{\mathrm{chg}}$ are the corresponding feasible sets for the charging mode. Furthermore, $\mathcal{X}_{\mathrm{drv0}}$ and $\mathcal{X}_{\mathrm{drvf}}$ denote allowed initial and target states, respectively. Moreover, $\mathrm{x_{detour}}$ corresponds to the change in battery temperature and SoC during the detour periods. The constraints (E.16i) and (E.16j) represent the transition between the modes. Accordingly, the battery temperature and SoC in the beginning of charging event must be equal to the corresponding variables at the arrival of charging station. Similarly, the battery temperature and SoC when the vehicle resumes its drive after charging

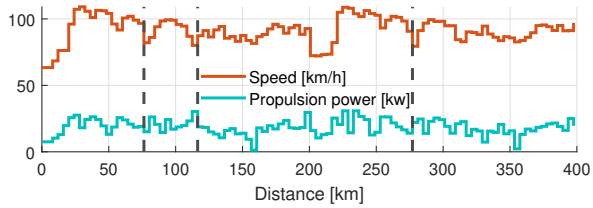

Figure 5: Vehicle drive cycle including the vehicle speed and propulsion power trajectories. Dashed vertical lines indicate available charging locations.

must be equal to the corresponding variables at the end of the charging event. The problem (E.16) is a mixed-integer nonlinear program (MINLP), due to the binary variable ζ and nonlinear relations in the constraints and cost function.

5 Results

In this section, simulation results are provided for the BEV demonstrated in Fig. 1. Within the simulations, we investigate the benefits of including a heat pump in the TM system. Also, we concern the charge point planning, in favour of achieving an optimal compromise between time and energy cost. The simulation setup and the results are given in Section 5.1 and Sections 5.2 to 5.5, respectively.

5.1 Simulation Setup

As depicted in Fig. 5, the simulations are conducted on a 400 km long drive cycle, which is based on real-world measurements. Three available charging locations along the driving route are marked by dashed vertical lines. The used charging stops are indicated with a solid vertical line hereafter. The vehicle starts its drive with a battery soaked in the ambient temperature, i.e. $T_{\mathrm{b}0} = T_{\mathrm{amb}}$. Also, cabin climate and auxiliary load demand are supplied during both the driving and charging modes. Furthermore, the cost for occupying the charging spot is assumed to be zero, i.e. $c_{\mathrm{T}} = 0$. The results shown in the remainder of the paper use those vehicle and simulation parameters reported in Table 1, unless stated otherwise.

The MINLP (E.16) is discretised with a distance sampling interval of 4 km, using the Runge-Kutta 4^{th} order method [32]. The discretised problem is

Table 1: Vehicle and Simulation Parameters

Maximum battery capacity	$C_\mathrm{b} = 195\,\mathrm{Ah}$
Product of specific heat and battery mass	$c_\mathrm{p} m_\mathrm{b} = 375\,\mathrm{kJ/(K)}$
Route length	$400\,\mathrm{km}$
Distance sampling interval	$4\,\mathrm{km}$
Number of charging along the route	$N_\mathrm{chg} = 3$
Detour time for each charging stop	$t_\mathrm{d} = 300\,\mathrm{s}$
Detour energy for each charging stop	$E_\mathrm{d} = 450\,\mathrm{Wh}$
Electrical energy cost while charging	$c_\mathrm{e} = 8.7\,\mathrm{SEK/kWh}$
Charger rated power	$P_\mathrm{grid}^\mathrm{max} = 200\,\mathrm{kW}$
Auxiliary load	$P_\mathrm{aux} = 0.5\,\mathrm{kW}$
Maximum HVCH power	$P_\mathrm{hvch}^\mathrm{max} = 7\,\mathrm{kW}$
Maximum HVAC power	$P_\mathrm{hvac}^\mathrm{max} = 3\,\mathrm{kW}$
Maximum HP power	$P_\mathrm{hp}^\mathrm{max} = \{0, 1, 3\}\mathrm{kW}$
HVCH power to heat rate efficiency	$\eta_\mathrm{hvch} = 87\,\%$
Ambient temperature	$T_\mathrm{amb} = \{-10, 0, 10\}^\circ\mathrm{C}$
Initial battery temperature	$T_\mathrm{b0} = T_\mathrm{amb}$
Initial battery state of charge	$\mathrm{soc}_0 = 90\,\%$
Terminal battery state of charge	$\mathrm{soc}_\mathrm{f} = 10\,\%$

solved with the solver BONMIN, using the open source nonlinear optimisation tool CasADi [33] in Matlab.

5.2 Time vs. Energy Efficiency

For different HP power limits and ambient temperatures, the Pareto frontiers are derived describing the trade-off between total charged energy versus combined charging and detour time, as depicted in Fig. 6. The HP is either disabled, or activated with maximum power of 1 kW or 3 kW, hereafter referred to as *smaller* HP or *larger* HP, respectively. To obtain the Pareto graphs, the time cost $c_\mathrm{t,chg}$ is varied over a large span to obtain solutions that vary respectively from energy optimal to time optimal.

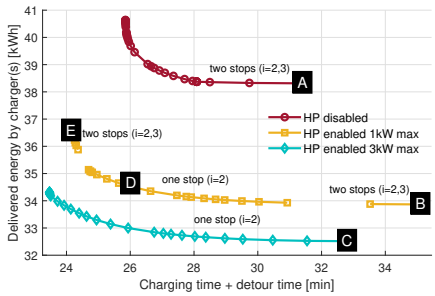

(a) Ambient temperature of −10 °C.

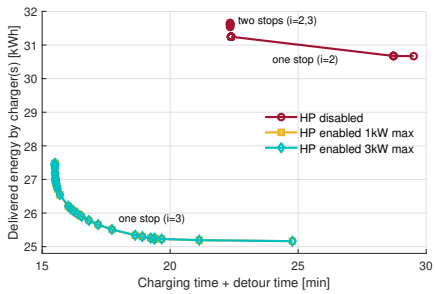

(b) Ambient temperature of 0 °C.

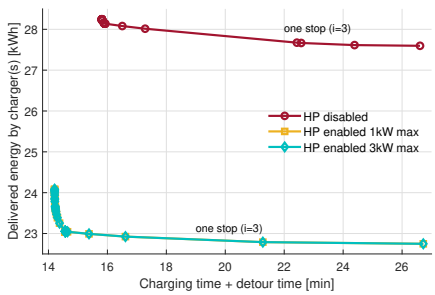

(c) Ambient temperature of 10 °C.

Figure 6: Pareto frontier describing the trade-off between total charging energy versus time including charging and detour times for various ambient temperatures and heat pump power limits.

Table 2: Energy reduced solution at different ambient temperatures

-10 °C ambient temperature			
Variable	HP disabled	smaller HP	larger HP
Energy (at 28 min) [kWh]	38.4	34.1	32.7
Reduction [%]	-	11.1	14.9
0 °C ambient temperature			
Variable	HP disabled	smaller HP	larger HP
Energy (at 22 min) [kWh]	31.3	25.2	25.2
Reduction [%]	-	19.4	19.4
10 °C ambient temperature			
Variable	HP disabled	smaller HP	larger HP
Energy (at 16 min) [kWh]	28.0	22.3	22.3
Reduction [%]	-	18.4	18.4

5.3 Energy Optimal Trip

From the Pareto frontiers shown in Fig. 1.6(a)-Fig. 1.6(c), it is observable that activating HP generally leads to a reduced energy consumption. For instance, at $-10\,^{\circ}$C ambient temperature and 28 min of combined charging and detour time, the charger(s) delivered energy is decreased by 11 % for the 1 kW limited HP and 15 % for the larger HP, compared to the similar scenario but with the HP disabled. Such energy reduction is due to the HP being used to move the heat from the battery loop into the cabin compartment, thus reducing the need for the HVCH to be used for cabin heating. The detailed results of charged energy together with the energy reduction percentage for different ambient temperatures and HP power limits are given in Table 2. Furthermore, at a given ambient temperature, the number of charging stops may change for different HP maximum power values. Also, it is observed that a more powerful HP is more beneficial compared to the smaller HP, at low ambient temperatures. However, at high ambient temperature there is no noticeable advantage of using the larger HP rather than the smaller HP. This will be discussed in more details later in Section 5.5.

According to Fig. 1.6(a), we look more closely at the energy optimal cases at $-10\,^{\circ}$C ambient temperature, as:

- Case A: energy optimal solution with HP disabled
- Case B: energy optimal solution with 1 kW HP power limit

- Case C: energy optimal solution with 3 kW HP power limit

Case A

States and control inputs trajectories versus travelled distance and charging time are depicted in Fig. 7, where the power is normalised with the maximum HVCH power. In this case, it is optimal to select two charging occasions ($i = 2, 3$) along the trip. The battery temperature increases significantly over the course of the trip and levels out between 25 °C and 30 °C at the destination, whereas no active battery heating is done with the HVCH. Such battery temperature increase is only due to the passively generated heat, which is mainly kept within the battery pack, and not pumped to the cabin by HP. Active cooling by HVAC is not used in this case, since the battery is kept below the maximum allowed temperature of 40 °C, by just exchanging the heat to the ambient air. The battery discharge power limit is kept at reasonable levels, as shown in Fig. 1.7(b), which is due to the overall high battery temperature throughout the trip.

Case B

States and control inputs trajectories versus travelled distance and charging time are shown in Fig. 8. The solution for Case B also involves charging twice ($i = 2, 3$). This implies that the cost associated with the detour of stopping twice is less than the cost of stopping once at charger $i = 2$. Performing only a single charging stop would in this case mean charging in a high SoC region with reduced charging speed at the second charging location. This leads to a longer charging time and more energy spent on maintaining cabin climate and supplying auxiliary load. The HP is switched off right before each charging stop and stays off during a portion of the charging period, as demonstrated in Fig. 1.8(c), Fig. 1.8(f), and Fig. 1.8(i). This means that the Joule and ED losses are prioritised for battery heating right before and in the beginning of the charging periods. The HVCH is not used at all for battery heating in this case in order to minimise unnecessary heat losses to the ambient environment.

Case C

Fig. 9 demonstrates states and control inputs trajectories versus travelled distance and charging time. Changing the HP maximum power from 1 kW

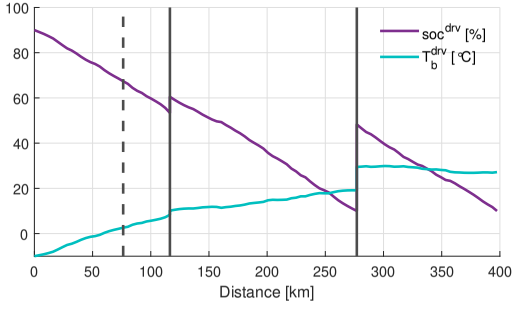

(a) Battery temperature and SoC trajectories vs. travelled distance.

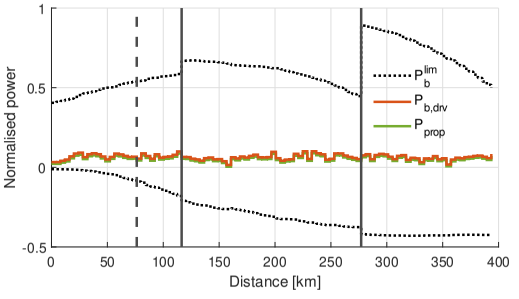

(b) Trajectories of battery power and propulsion power together with battery power limits vs. travelled distance.

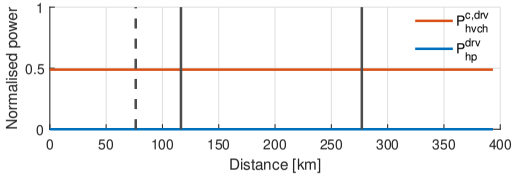

(c) Trajectories of HVCH and HP power for cabin heating, vs. travelled distance.

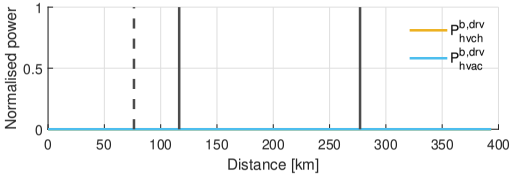

(d) Trajectories of HVCH and HVAC power, respectively for battery heating and cooling, vs. travelled distance.

(e) Battery temperature and SoC trajectories vs. charging time (second charging stop).

(f) Trajectories of HVCH and HP power for cabin heating, vs. charging time (second charging stop).

(g) Trajectories of HVCH and HVAC power, respectively for battery heating and cooling, vs. charging time (second charging stop).

(h) Battery temperature and SoC trajectories vs. charging time (third charging stop).

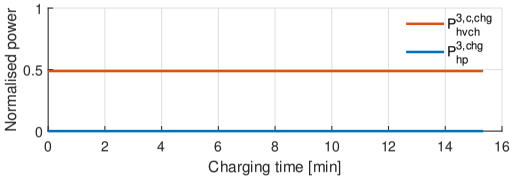

(i) Trajectories of HVCH and HP power for cabin heating, vs. charging time (third charging stop).

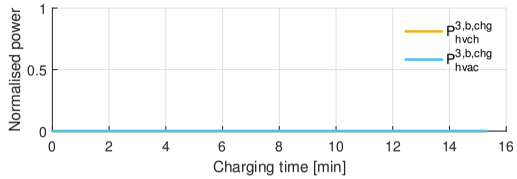

(j) Trajectories of HVCH and HVAC power, respectively for battery heating and cooling, vs. charging time (third charging stop).

Figure 7: Case A: Energy optimal case with heat pump disabled.

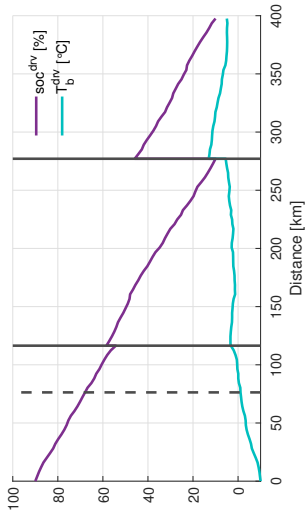

(a) Battery temperature and SoC trajectories vs. travelled distance.

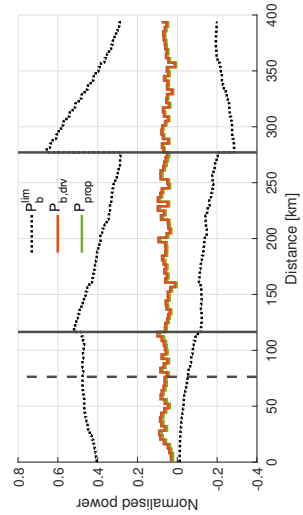

(b) Trajectories of battery power and propulsion power together with battery power limits vs. travelled distance.

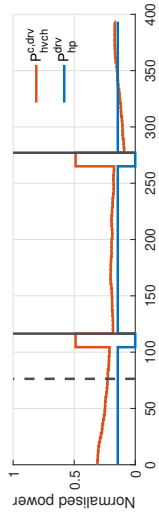

(c) Trajectories of HVCH and HP power for cabin heating, vs. travelled distance.

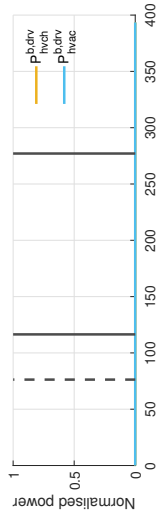

(d) Trajectories of HVCH and HVAC power, respectively for battery heating and cooling, vs. travelled distance.

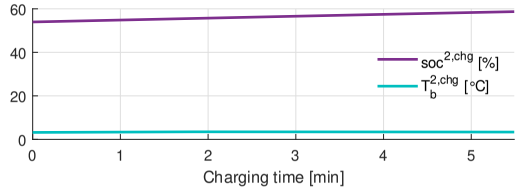

(e) Battery temperature and SoC trajectories vs. charging time (second charging stop).

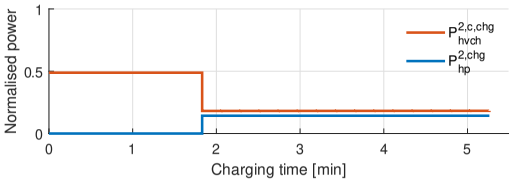

(f) Trajectories of HVCH and HP power for cabin heating, vs. charging time (second charging stop).

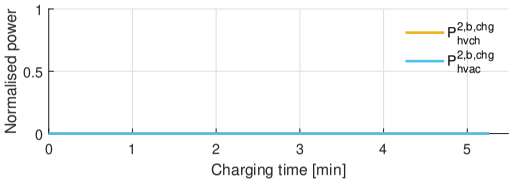

(g) Trajectories of HVCH and HVAC power, respectively for battery heating and cooling, vs. charging time (second charging stop).

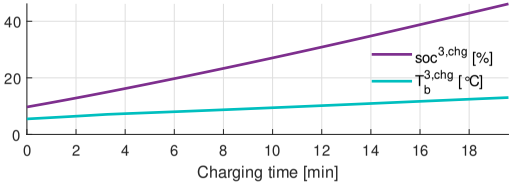

(h) Battery temperature and SoC trajectories vs. charging time (third charging stop).

(i) Trajectories of HVCH and HP power for cabin heating, vs. charging time (third charging stop).

(j) Trajectories of HVCH and HVAC power, respectively for battery heating and cooling, vs. charging time (third charging stop).

Figure 8: Case B: Energy optimal case with 1 kW heat pump power limit.

Table 3: Time optimal solution at different ambient temperatures

-10 °C ambient temperature			
Variable	HP disabled	smaller HP	larger HP
Time [min]	25.9	24.2	23.5
Reduction [%]	-	6.5	9.2
0 °C ambient temperature			
Variable	HP disabled	smaller HP	larger HP
Time [min]	22.3	15.5	15.5
Reduction [%]	-	30.6	30.6
10 °C ambient temperature			
Variable	HP disabled	smaller HP	larger HP
Time [min]	15.8	14.2	14.2
Reduction [%]	-	10.1	10.1

to 3 kW can considerably influence the energy optimal solution. Accordingly, only one charging stop is performed during the whole trip. Also, HVCH is used for battery heating before the charging stop and several minutes at the beginning of the charging period. As only the HP is used for cabin heating after the charging stop, the battery temperature is kept low and even drops below 0 °C when approaching the destination. This combined with low SoC from the last 50 km of the trip, results in a limited discharge power availability, which is a challenge for more aggressive driven cycles.

5.4 Time Optimal Trip

Looking more closely at the time optimal solutions for different ambient temperatures illustrated in Fig. 1.6(a)-Fig. 1.6(c), reveals that the HP allows for shorter combined charging and detour time, compared to the case with HP disabled. For instance, the observed time reduction at −10 °C ambient temperature is 6.5 % and 9.2 % for the smaller and larger HP cases, respectively. Such time reduction is primarily due to a more efficient cabin heating during driving, leading to an improved grid-to-wheel efficiency; and thus reducing the amount of energy required to be supplied at a given charging stop. Furthermore, it may be infeasible to finish the trip with just one charging stop with the HP disabled. However, the number of charging stops can generally be reduced by having HP activated, which yields a lower total detour time.

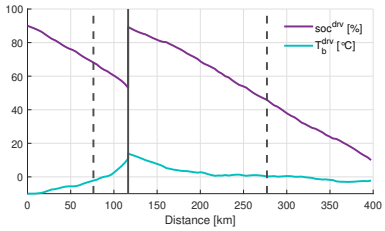

(a) Battery temperature and SoC trajectories vs. travelled distance.

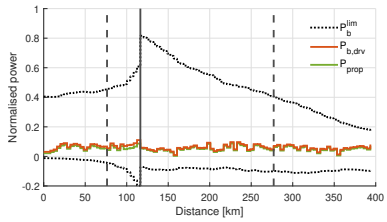

(b) Trajectories of battery power and propulsion power together with battery power limits vs. travelled distance.

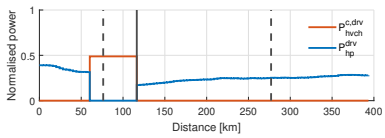

(c) Trajectories of HVCH and HP power for cabin heating, vs. travelled distance.

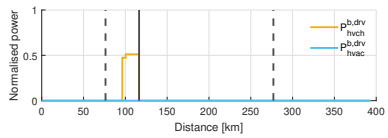

(d) Trajectories of HVCH and HVAC power, respectively for battery heating and cooling, vs. travelled distance.

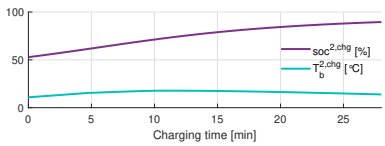

(e) Battery temperature and SoC trajectories vs. charging time (second charging stop).

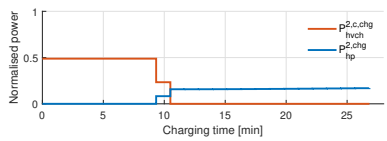

(f) Trajectories of HVCH and HP power for cabin heating, vs. charging time (second charging stop).

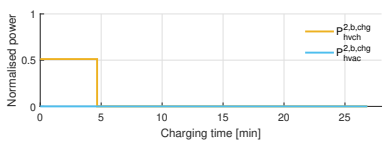

(g) Trajectories of HVCH and HVAC power, respectively for battery heating and cooling, vs. charging time (second charging stop).

Figure 9: Case C: Energy optimal case with 3 kW heat pump power limit.

The detailed results about combined charging and detour time for different ambient temperatures and HP power limits are reported in Table 3. In the

following Section 5.3, the results of Case E, i.e. time optimal solution with 1 kW HP power limit at −10 °C ambient temperature, are demonstrated.

Case E

States and control inputs trajectories versus travelled distance and charging time are shown in Fig. 1.10(a)-Fig. 1.10(j). Similar to the energy optimal Case B, two charging stops are also performed in the time optimal Case E. However, in contrast to the energy optimal case, the battery is pre-heated before the charging stops, to the point with optimal temperature, i.e. $\approx 25\,^{\circ}\mathrm{C}$, for fast charging. During charging, the use of HVCH at full power for battery heating and only HP for cabin heating at the same time is an effort to maximise the amount of heat possible to be within the battery pack. This implies that, the HP frees up the HVCH for maximum battery heating, while maintaining cabin heating demand.

5.5 Charged Energy vs. Ambient Temperature

Fig. 1.11(a) illustrates the charger(s) delivered energy versus ambient temperature values for different HP maximum power limits, and with the time cost fixed at 40 SEK/h, which corresponds to point D in Fig. 1.6(a). In Fig. 1.11(a), number of charging stops for a given HP power limit and ambient temperature is also given. Accordingly, at high ambient temperatures between 7 °C and 21 °C, both the HP enabled and disabled cases are able to complete the trip with one late charging stop, i.e. ($i = 3$). However, the HP enabled cases demand between 6 % to 18 % less energy from the charger compared to the HP disabled case, as depicted in Fig. 1.11(b). At 6 °C, two charging stops are needed for the HP disabled case to complete the trip. Thus, a jump in energy reduction of about 19.5 % for the HP enabled cases is observed, which is due to the increased detour energy and time associated with stopping twice ($i = 2, 3$). As the ambient temperature is reduced further, the energy difference between the smaller and larger HP cases is more noticeable. This is due to a combination of high cabin heating demand and reduced CoP at low battery temperatures, resulting in the need for more than 1 kW of HP compressor power to maintain the cabin climate. Thus, the more limited power case has to supplement cabin heating with the HVCH, while the other case is able to supplement less or not at all by the HVCH. Once the ambient temperature is

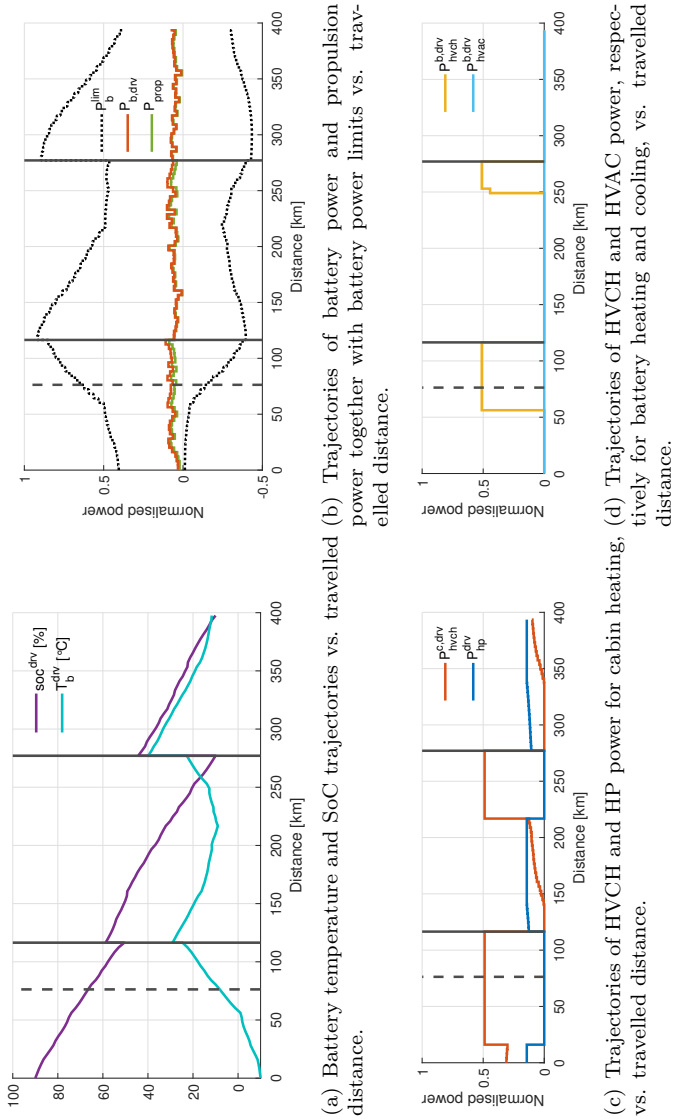

(a) Battery temperature and SoC trajectories vs. travelled distance.

(b) Trajectories of battery power and propulsion power together with battery power limits vs. travelled distance.

(c) Trajectories of HVCH and HP power for cabin heating, vs. travelled distance.

(d) Trajectories of HVCH and HVAC power, respectively for battery heating and cooling, vs. travelled distance.

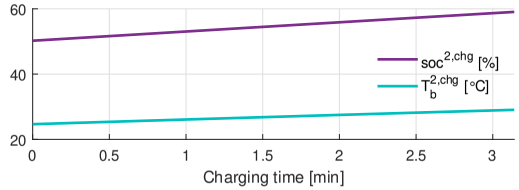

(e) Battery temperature and SoC trajectories vs. charging time (second charging stop).

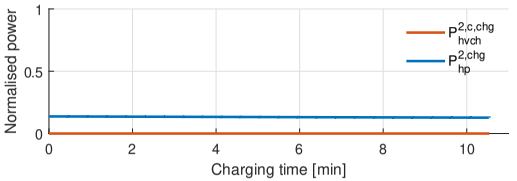

(f) Trajectories of HVCH and HP power for cabin heating, vs. charging time (second charging stop).

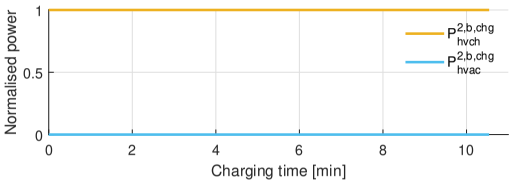

(g) Trajectories of HVCH and HVAC power, respectively for battery heating and cooling, vs. charging time (second charging stop).

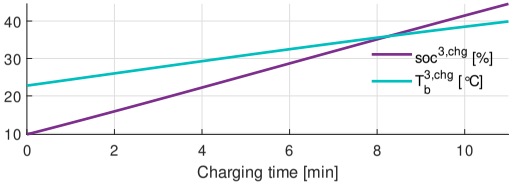

(h) Battery temperature and SoC trajectories vs. charging time (third charging stop).

(i) Trajectories of HVCH and HP power for cabin heating, vs. charging time (third charging stop).

(j) Trajectories of HVCH and HVAC power, respectively for battery heating and cooling, vs. charging time (third charging stop).

Figure 10: Case E: Time optimal case with 1 kW heat pump power limit.

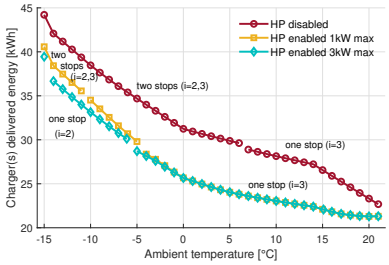

(a) Charged energy vs. ambient temperature for different maximum HP power values.

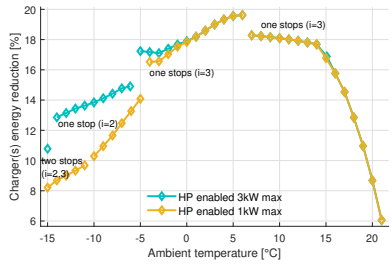

(b) Relative energy benefit of HP activated cases compared to HP disabled case over ambient temperature.

Figure 11: Comparison of energy delivered by charger(s) over ambient temperature.

dropped to $-5\,^{\circ}\mathrm{C}$ and $-6\,^{\circ}\mathrm{C}$, the smaller and larger HP cases, respectively, start switching to perform one early stop at the second charge location ($i = 2$). When this switch occurs, the energy reduction percentage drops, even though the detour time or detour energy has not changed. This is due to the low charging power in the high SoC region, which leads to a longer charging time; and accordingly an increased energy demand by the auxiliary and TM system components. With the temperature reduced to $-11\,^{\circ}\mathrm{C}$, the smaller HP case starts to perform two charging stops, the same way as the HP disabled case. Such switch occurs for the 3 kW limit case at $-15\,^{\circ}\mathrm{C}$.

6 Discussion

Here the benefits of including HP in the TM system and optimally planning the charging points are discussed.

6.1 Improved Energy Efficiency and Trip Time by a Heat Pump

According to the results given in Section 5, the reduction in terms of both energy consumption as well as combined charging and detour time is significant, when an HP is considered in the TM system of BEVs for waste heat recovery. Although the improvement varies noticeably with ambient temperature, as

long as there is a heating demand for the cabin compartment, the case with an HP activated has better performance compared to the one without. This is true even when the HP compressor power is limited, especially in milder climates.

Using an HP in the TM system may be less advantageous in cases where the waste heat available within the battery pack is limited, or there are constraints on discharge power capability of the battery at low SoC and temperature regions.

6.2 Effects of Charge Point Optimisation

Optimal charge point planning allows for a holistic solution of a long trip in a BEV in terms of energy consumption and total trip time. At warmer ambient temperatures, i.e. $T_{\mathrm{amb}} \geq 0\,^{\circ}\mathrm{C}$, minimum possible number of charging stops is favourable, regardless of priorities in terms of time or energy, suggested by Fig. 1.6(b) and Fig. 1.6(c). On the other hand, at colder ambient temperatures, e.g. $T_{\mathrm{amb}} = -10\,^{\circ}\mathrm{C}$, two charging stops are identified to be energy and/or time optimal for HP disabled and smaller HP, as shown in Fig. 1.6(a). This implies that the increased consumption due to higher demand for cabin heating outweighs the energy and time cost associated with stopping frequently. Thus, there is a merit to the strategy of initially driving as far as possible to a stop, in which charging is performed enough to make it to the next charging station. However, as demonstrated by the trade-off between the two extremes, energy and time optimal, with the 1 kW limit, there are cases where that strategy is not the optimal solution. For e.g. in Case D only one charging stop is performed, where the optimal strategy suggests to minimise the detour energy and time by reducing the number of stops.

7 Conclusion and Future Work

In this paper, a mixed-integer nonlinear optimisation problem is formulated for optimal thermal management and charging of a BEV, in order to capture its long trip including both driving and charging. Within this problem, Pareto frontiers describing the trade-off between energy efficiency and time are derived versus different features, e.g. a heat pump, charging stops, and ambient temperature. Such graphs provide wide range of choices for car man-

ufacturers as well as grid service providers to gain more insight into design and development of TM and charging systems. Furthermore, various car users can customise their trip according to the information given within these graphs. According to the obtained results, energy consumption and the time needed for charging are reduced by up to 19.4 % and 30.6 %, respectively, by including an HP in the TM system. By including optimal charge point planning in the form of binary decision variables, the solution depends on factors such as the priority between time and energy, the availability of an HP, and ambient temperature.

The current study can readily be extended by the inclusion of speed optimisation in favour of an energy efficient driving, so called *eco-driving*, where the vehicle's longitudinal dynamics is required to be incorporated in the problem formulation, in addition to the dynamics on battery temperature and SoC. Note that similar analysis has been conducted in [29], but without charge point planning and without an HP. Thus, a nonuniform sampling could be introduced, or speed could be optimized in a separate level. With such extension in the developed algorithm, the solution would represent a more complete route optimisation, aiming at enhancing energy and/or time efficiency. For instance, the short charging periods at the second location in Case B and Case E may be avoided if the vehicle eco-drives, leading to a direct reduction in time and energy.

In order to implement the proposed algorithm online in a vehicle, it is crucial to reduce the computational burden. To do so, the knowledge gained by the current results is highly beneficial. For instance, in case of active battery pre-heating, the solution always involves running the HVCH at maximum power for some period right before the charging stop and at the beginning of the charging interval. According to such knowledge, one effort may be to reformulate the problem to control the average power or energy used for battery heating instead. This may allow for significant reduction in discretised samples to imitate the non-simplified system behaviour, with a small or non-existent loss in optimality.

Acknowledgment

The authors would like to acknowledge Mats Bohman from Volvo Car Corporation for the support and fruitful discussions during this research. This work

is part of a project titled “Predictive Energy and Thermal management of Electric Vehicles with Connectivity to Infrastructure" funded by the Swedish Electromobility Center.

References

[1] R. R. Kumar and K. Alok, “Adoption of electric vehicle: A literature review and prospects for sustainability,” *Journal of Cleaner Production*, vol. 253, p. 119 911, 2020.

[2] A. M. Andwari, A. Pesiridis, S. Rajoo, R. Martinez-Botas, and V. Esfahanian, “A review of battery electric vehicle technology and readiness levels,” *Renewable and Sustainable Energy Reviews*, vol. 78, pp. 414–430, 2017.

[3] J. A. Sanguesa, V. Torres-Sanz, P. Garrido, F. J. Martinez, and J. M. Marquez-Barja, “A review on electric vehicles: Technologies and challenges,” *Smart Cities*, vol. 4, no. 1, pp. 372–404, 2021.

[4] C. Suarez and W. Martinez, “Fast and ultra-fast charging for battery electric vehicles–a review,” in *2019 IEEE Energy Conversion Congress and Exposition (ECCE)*, IEEE, 2019, pp. 569–575.

[5] M. M. Mahfouz and M. R. Iravani, “Grid-integration of battery-enabled dc fast charging station for electric vehicles,” *IEEE Transactions on Energy Conversion*, vol. 35, no. 1, pp. 375–385, 2019.

[6] J. Jaguemont, M. Abdel-Monem, N. Omar, J. Van Mierlo, and P. Van Den Bossche, “Thermal effect of fast-charging profiles on lithium-ion batteries,” in *2018 21st International Conference on Electrical Machines and Systems (ICEMS)*, IEEE, 2018, pp. 2127–2132.

[7] M. Keyser, A. Pesaran, Q. Li, *et al.*, “Enabling fast charging–battery thermal considerations,” *Journal of Power Sources*, vol. 367, pp. 228–236, 2017.

[8] M. A. H. Rafi and J. Bauman, “A comprehensive review of dc fast-charging stations with energy storage: Architectures, power converters, and analysis,” *IEEE Transactions on Transportation Electrification*, vol. 7, no. 2, pp. 345–368, 2020.

[9] J. Jaguemont, L. Boulon, P. Venet, Y. Dubé, and A. Sari, "Lithium-ion battery aging experiments at subzero temperatures and model development for capacity fade estimation," *IEEE Transactions on Vehicular Technology*, vol. 65, no. 6, pp. 4328–4343, 2015.

[10] G. Zhang, S. Ge, X.-G. Yang, Y. Leng, D. Marple, and C.-Y. Wang, "Rapid restoration of electric vehicle battery performance while driving at cold temperatures," *Journal of Power Sources*, vol. 371, pp. 35–40, 2017.

[11] T. Wang, X. Wu, S. Xu, *et al.*, "Performance of plug-in hybrid electric vehicle under low temperature condition and economy analysis of battery pre-heating," *Journal of Power Sources*, vol. 401, pp. 245–254, 2018.

[12] M. A. Hannan, M. M. Hoque, A. Hussain, Y. Yusof, and P. J. Ker, "State-of-the-art and energy management system of lithium-ion batteries in electric vehicle applications: Issues and recommendations," *Ieee Access*, vol. 6, pp. 19 362–19 378, 2018.

[13] S. Wu, R. Xiong, H. Li, V. Nian, and S. Ma, "The state of the art on preheating lithium-ion batteries in cold weather," *Journal of Energy Storage*, vol. 27, p. 101 059, 2020.

[14] Y. Wang, X. Zhang, and Z. Chen, "Low temperature preheating techniques for lithium-ion batteries: Recent advances and future challenges," *Applied Energy*, vol. 313, p. 118 832, 2022.

[15] J. Jeffs, "An investigation into the optimal operation of a complex heat pump for the complete thermal management of an electric vehicle in cold climates," Ph.D. dissertation, University of Warwick, 2019.

[16] M. R. Amini, H. Wang, X. Gong, D. Liao-McPherson, I. Kolmanovsky, and J. Sun, "Cabin and battery thermal management of connected and automated hevs for improved energy efficiency using hierarchical model predictive control," *IEEE Transactions on Control Systems Technology*, vol. 28, no. 5, pp. 1711–1726, 2019.

[17] B. Chen, X. Li, S. A. Evangelou, and R. Lot, "Joint propulsion and cooling energy management of hybrid electric vehicles by optimal control," *IEEE Transactions on Vehicular Technology*, vol. 69, no. 5, pp. 4894–4906, 2020.

[18] X. Hu, Y. Zheng, D. A. Howey, H. Perez, A. Foley, and M. Pecht, "Battery warm-up methodologies at subzero temperatures for automotive applications: Recent advances and perspectives," *Progress in Energy and Combustion Science*, vol. 77, p. 100 806, 2020.

[19] R. Bellman, *Dynamic Programming*. New Jersey: Princeton Univ Pr, 1957.

[20] J. Jaguemont, L. Boulon, Y. Dube, and F. Martel, "Thermal management of a hybrid electric vehicle in cold weather," *IEEE Transactions on Energy Conversion*, vol. 31, no. 3, pp. 1110–1120, 2016.

[21] L. S. Pontryagin, V. G. Boltyanskii, R. V. Gamkrelidze, and E. F. Mishchenko, *The Mathematical Theory of Optimal Processes*. Interscience Publishers, 1962.

[22] R. F. Hartl, S. P. Sethi, and R. G. Vickson, "A survey of the maximum principles for optimal control problems with state constraints," *SIAM review*, vol. 37, no. 2, pp. 181–218, 1995.

[23] C. Zhu, F. Lu, H. Zhang, and C. C. Mi, "Robust predictive battery thermal management strategy for connected and automated hybrid electric vehicles based on thermoelectric parameter uncertainty," *IEEE Journal of Emerging and Selected Topics in Power Electronics*, vol. 6, no. 4, pp. 1796–1805, 2018.

[24] J. Lopez-Sanz, C. Ocampo-Martinez, J. Alvarez-Florez, *et al.*, "Nonlinear model predictive control for thermal management in plug-in hybrid electric vehicles," *IEEE Transactions on Vehicular Technology*, vol. 66, no. 5, pp. 3632–3644, 2016.

[25] ——, "Thermal management in plug-in hybrid electric vehicles: A real-time nonlinear model predictive control implementation," *IEEE transactions on vehicular technology*, vol. 66, no. 9, pp. 7751–7760, 2017.

[26] R. Rodriguez, M. Preindl, J. S. Cotton, and A. Emadi, "Review and trends of thermoelectric generator heat recovery in automotive applications," *IEEE Transactions on Vehicular Technology*, vol. 68, no. 6, pp. 5366–5378, 2019.

[27] S. Lee, Y. Chung, Y. Jeong, and M. S. Kim, "Experimental study on an electric vehicle heat pump system with multi-level waste heat recovery using a vapor injection technique at low ambient temperatures," *Energy Conversion and Management*, vol. 267, p. 115 935, 2022.

[28] X. Han, H. Zou, J. Wu, C. Tian, M. Tang, and G. Huang, "Investigation on the heating performance of the heat pump with waste heat recovery for the electric bus," *Renewable Energy*, vol. 152, pp. 835–848, 2020.

[29] A. Hamednia, N. Murgovski, J. Fredriksson, J. Forsman, M. Pourabdollah, and V. Larsson, "Optimal thermal management, charging, and eco-driving of battery electric vehicles," *arXiv preprint arXiv:2205.01560*, 2022.

[30] M. J. Moran, H. N. Shapiro, D. D. Boettner, and M. B. Bailey, *Fundamentals of engineering thermodynamics*. John Wiley & Sons, 2010.

[31] B. J. Limb, Z. D. Asher, T. H. Bradley, *et al.*, "Economic viability and environmental impact of in-motion wireless power transfer," *IEEE Transactions on Transportation Electrification*, vol. 5, no. 1, pp. 135–146, 2018.

[32] J. C. Butcher, "On the implementation of implicit runge-kutta methods," *BIT Numerical Mathematics*, vol. 16, no. 3, pp. 237–240, 1976.

[33] J. A. Andersson, J. Gillis, G. Horn, J. B. Rawlings, and M. Diehl, "Casadi: A software framework for nonlinear optimization and optimal control," *Mathematical Programming Computation*, vol. 11, no. 1, pp. 1–36, 2019.